# EXTREMELY EXTENDED DUST SHELLS AROUND EVOLVED INTERMEDIATE MASS STARS: PROBING MASS LOSS HISTORIES,THERMAL PULSES AND STELLAR EVOLUTION

---

A Thesis presented to

the Faculty of the Graduate School

at the University of Missouri

---

In Partial Fulfillment

of the Requirements for the Degree

Doctor of Philosophy

---

by

BASIL MENZI MCHUNU

Dr. Angela K. Speck

December 2011

The undersigned, appointed by the Dean of the Graduate School, have examined the dissertation entitled:

EXTREMELY EXTENDED DUST SHELLS AROUND EVOLVED INTERMEDIATE MASS STARS PROBING MASS LOSS HISTORIES, THERMAL PULSES AND STELLAR EVOLUTION USING FAR-INFRARED IMAGING PHOTOMETRY

presented by Basil Menzi Mchunu,
a candidate for the degree of Doctor of Philosophy and hereby certify that, in their opinion, it is worthy of acceptance.

---

Dr. Angela K. Speck

---

Dr. Sergei Kopeikin

---

Dr. Adam Helfer

---

Dr. Bahram Mashhoon

---

Dr. Haskell Taub

# DEDICATION

This thesis is dedicated to my family, who raised me to be the man I am today under challenging conditions: my grandfather Baba (Samuel Mpala Mchunu), my grandmother (Ma Magasa, Nonhlekiso Mchunu), my aunt Thembeni, and my mother, Nombso Betty Mchunu. I would especially like to thank my mother for all the courage she gave me, bringing me chocolate during my undergraduate days to show her love when she had little else to give, and giving her unending support when I was so far away from home in graduate school. She passed away, when I was so close to graduation. To her, I say, ″Ulale kahle Macingwane.″ I have done it with the help from your spirit and courage. I would also like to thank my wife, Heather Shawver, and our beautiful children, Rosemary and Brianna , for making me see life with a new meaning of hope and prosperity.

I also thank my long - term child-hood friend, Tholinhlanhla Henry Ngcobo for helping me during trying times and furthermore for his encouragement repeat grade 11 that I already passed in order to do physical science at Mqhakama high school in South Africa. These early periods marked the beginning of my science career that has led to this position I am in today. During heavy moments while writing this thesis, I got encouraged by looking back in time when my friend and I used stones and the sticks arguing about space geometry from our mathematics class, while taking our long walks back from school. This has been / still is a long journey worth taking as I am begining to realize that there is still a lot to learn concerning the physics of the stars and their recycling of their material in space, all of which is connected to the science of our well being.

# ACKNOWLEDGMENTS

I would like to thank Dr. Peter. Abrahams at Kolonky observatory / Max–Planck Insitute for Physics for helping me with ISO data analysis, and also his useful comments about the PHT32 data; especially, the reduction and analysis of Omi Cet - Mira observations. I am also thankful to the Spitzer help desk for assistance on MIPS data especially with PSF subtraction. I recieved very useful comments from Dr Tuan Do, Professor Mark Morris at UCLA on Mips data. I would not have done this thesis without my adviser Dr. Angela Speck for making this research the whole success.

# TABLE OF CONTENTS

# LIST OF TABLES

Table Page

# LIST OF FIGURES

Figure Page

# ABSTRACT

Intermediate mass stars ($0.8-8M_{\odot}$) at the asymptotic giant branch phase (AGB) suffer intensive mass loss, which leads to the formation of a circumstellar shell (s) of gas and dust in their circumstellar envelope. At the end of the AGB phase, the mass-loss decreases or stops and the circumstellar envelope begins to drift away from the star. If the velocity of the AGB phase wind has been relatively constant, then dust or molecular emission furthest from the star represents the oldest mass loss, while material closer to the star represents more recent mass loss. Therefore, the history of mass loss during the AGB phase is imprinted on the dust shells of the post-AGB envelope. Thus, by studying the distribution of matterial in the form of dust emission in the circumstellar shells of late evolved stars (i.e. the post AGB phases are pre - planetary nebula (PPN) and the planetary nebula (PN)) we can gain a better understanding of the mass-loss processes involved in the evolution of intermediate mass stars. I studied two groups of intermediate mass stars, namely six oxygen rich and six carbon rich candidates. In this thesis a study of evolution of intermadiate mass stars is confronted by means of observations, in which far - infrared (FIR) images, are used to study the physical properties and the material distribution of dust shells of AGB and post AGB circumstellar envelope. Infrared radiation from thermal dust emission can be used to probe the entire dust shell because, near to mid-infrared radiation arises solely from the hotest regions close to the star; while the outer regions away from the star are cool such that they emitt at longer infrared wavelengths. Essentially, radiation in the FIR to submillimiter wavelengths is emittted by the entire dust shell and hence can be used to probe the entire dusty envelope. Therefore far-infrared emission by late evolved stars can be used to probe the large scale - structure of AGB and post - AGB circumstellar shells.

Our results from space observations indicated the folowing: The sizes of the cir-

cumstellar dust shell observed in oxygen rich stars are within >1 pc. We derived the dust masses derived from far infrared ISO PHT 32 observation of oxygen rich stars that are between 1.7 – 4 $\times 10^{-4}$ $M_{\odot}$. These results provides us with a lower limit in the progenitor masses of stars estimated to be within 0.56 – 0.76 $M_{\odot}$. The time scales derived since the oldest mass was ejected during the evolution of oxygen rich stars are 4 - 13 $\times 10^{4}$ years. The size of the circumstellar circumstellar dust shells for carbon rich stars are within 1 - 1.6 pc. The masses of dust are a approximated to be within 0.1 - 1.44 $\times 10^{-4}$ $M_{\odot}$. These results provides a lower limit to the progenitor masses of carbon rich stars that are between 0.61 – 0.9 $M_{\odot}$ suggesting that these stars evolved from the main sequence masses between 1.5 – 3.5 $M_{\odot}$.

# Chapter 1

# Introduction

The universe started as a very uniform, hot and dense primordial state of matter and radiation that was created explosively from a singular point (often referred to the Big Bang). Big Bang theory suggests that universe has been expanding in time since its inception. Current observations, e.g. Wilkinson Microwave Anisotropy Probe; Bennett et al.2003 [7] give an age for the universe of approximately 13.7 billion years.

Immediately after the Big Bang, elementary particles of matter, i.e. protons, electrons, neutrons and their antimatter were created. The universe was so hot and dense that photons could spontaneously convert into material particles, while simultaneously matter-antimatter pairs would annihilate to create photons. By the end of this particle era, protons and neutrons left over from the annihilation of antimatter began to fuse into more massive nuclei resulting in a cosmic composition of $\sim$75% hydrogen (i.e. protons) and $\sim$25% helium by mass, with traces of other elements such as deuterium and lithium. The elemental abundances have remained approximately the same for the entire observable universe, except that a small fraction of hydrogen ($\sim$5%) has been reprocessed inside by stars, forming all the heavier elements.

The main aim of the research presented here is to test hypotheses related to how

stars generate and eject new elements. In particular low- and intermediate mass stars are major contributors of new material to the ISM but we still do not understand the detailed mechanisms.

The stars form from the gravitational collapse of molecular clouds of gas and dust in interstellar space. For most of their lives, stars shine by continuously fusing hydrogen to make helium. As they evolve, stars fuse heavier elements and create new elements by other processes (e.g. neutron capture). The elements synthesized inside the stars, are eventually dispersed back into the interstellar medium (ISM). For massive stars this process is explosive (supernovae) and efficiently makes heavy elements. However, even a sun-like star will disintegrate and return much of its material to the ISM. The heavy-element enriched material becomes part of the new generation of stars and planets.

Stars come in a variety of different masses that depends on mass of the cloud from which they collapsed. The massive stars live fast, die young and leave extremely bright corpses, ejecting newly-formed elements explosively along the way, lower mass stars evolve slowly and die gently. They lose mass over hundred of millenia leading to the formation of shells of dust that contains elements made inside the star. This work focuses on intermediate mass stars with initial stellar masses between 0.8 and 8 $M_{\odot}$ [1]. Intermediate mass stars do not explode, but rather die slowly via gentle mass ejection during the late stage of their stellar evolution.

Stellar evolution can be tracked in terms of changes in a star's effective temperature and luminosity, and can be plotted on the Hertzsprung–Russell (HR) diagram (Hertzsprung 1905 & Russell 1915 [112]). The evolution of an AGB star is is illustrated schematically in Figure 1.1.

Intermediate mass stars evolve off the main-sequence and go through a red giant phase known as the asymptotic giant branch (AGB, Iben 1995), during which they lose

[1] $M_{\odot}$ is the mass of the sun, $1.99 \times 10^{30}$ kg

a large fraction of their mass to the surrounding space. An AGB star is characterized by a small (and dense) carbon-oxygen (CO) core that is surrounded by helium (He) and hydrogen (H) fusion shells followed by an extended mantle of non-fusing H/He convective envelope where radial pulsation originate; and then an atmosphere that is dynamical with respect to its extent above the stellar surface. The energy heating the outer layers of the atmosphere comes from the instabilities in hydrogen and helium burning shells. These shells heat the mantle interchangeable such that the star begin to pulsate and expel material which leads to the formation of circumstellar dust shells (CDs) away from the star's surface.

The dust grains tap into the tremendous luminosity power of the star $(10^3 - 10^4)$ $L_\odot$[2] and drive a radiation-pressured wind. The wind created this way cause AGB stars to lose mass at tremendous rates $(10^{-6} - 10^{-4})$ $M_\odot$ per year such that entire mantle of the star gets blown away causing the core to be exposed and the star remnant becomes a white dwarfs (WDs) rather than explode as supernovae (Iben & Renzini 1993; Blöcker & Schöbener 1991).

As AGB stars shed their outer circumstellar envelope (CSE) they move up towards the post AGB called proto-planetary nebula (PPN) phase for a short time ($\sim$ 1000 years). After the PPN phase, the star evolves towards the blue side of the HR-diagram with high enough effective temperatures to produces photo-ionizing radiation that leads to the ejection of the circumstellar envelope called a planetary nebula (PN). After the outer shell of matter has been removed these stars become white dwarfs.

The mass loss and the acceleration efficiencies vary depending on the properties of the mass losing star, so the properties of the circumstellar envelope that contains the dust shell vary considerable e.g. in terms of opaqueness,[3] geometry, kinematics and

[2] $L_\odot$ is the luminosity of the sun whose value is $3.939 \times 10^{26}$ W

[3] opaqueness is a measure /degree of obscurity for the passage of light (intensity) coming inside the star to emerge to the interstellar space. In this case the density, mass absorption of the emitting species (dust and gas molecules) and the size of the dust shell determines the degree of transparency or the opacity of light. See of Chapter 4 section **??** for more details.

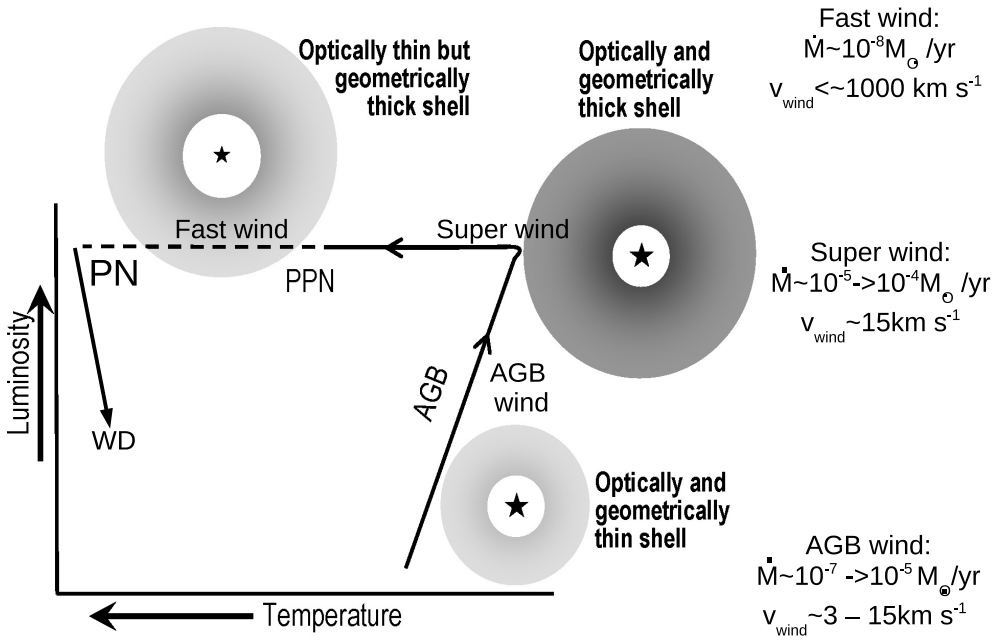


Figure 1.1: Schematic evolutionary track of intermediate mass star on the Hertzsprung - Russel (H-R) diagram.

chemistry. The schematic diagrams of the circumstellar dust shell at different stages of stellar evolution shown in Figure 1.1 indicates this effect. From an early AGB E-AGB: the dust shell is assumed to be small, less dense (geometrically thin), and is also optically thin at visible and at infrared wavelengths. When more dust forms closer to the center and the star looses more mass and evolves from AGB and toward becoming a PPN with increasing mass loss rate, the size of the the circumstellar dust shell becomes larger in size, that is it become geometrically thick and dense. At the very same time, the dust shell becomes optically thick at visible wavelengths but optically thin to allow to be 'seen' in the infrared wavelengths. The reason is that dust particles absorbs photons at all wavelengths and as they heat, they release their radiation at long-ward wavelengths that peaks at the infrared. Thus, the star is inside a cocoon of dust that blocks all radiation coming from the star. Therefore when the

star enters PPN phase, most of its emitted radiation can only be seen at infrared, sub-millimeter and radio wavelengths. As the star transcends towards becoming a Planetary Nebula, the shell becomes transparent again, it becomes optically thin again both at visible and at infrared wavelengths and beyond; at the very same time it becomes geometrical thick with respect to size and it is still dense in dust and molecular composition. As the star evolves on the PN, the core heats the circumstellar envelope eventually, it gets disperse into the ISM by strong radiation field from the star as the core becomes exposed.

Observational evidence e.g. Chu et al. 1991 [21] suggests that three winds are involved in stripping the outer envelope of an AGB star on its way in becoming the white PN (Marten et al. 1993 [89]; Frank et al. 2004 [31]).

1. **AGB wind** is characterized by lower mass loss rates (the minimum mass loss is the Red giant branch mass loss rate given by Reimers law) that increases up to $10^{-5} M_{\odot} yr^{-1}$, the wind speed maybe be in the orders of $10 kms^{-1}$ (Speck & Meixner & Knapp et al. 2000[125], hereafter SMK00). AGB stellar winds are slow by astronomical standards; the large majority are found in the range $3 - 30 kms^{-1}$ while typical molecule's velocities lie in the range $5 - 15 kms^{-1}$ (e.g. [51])

2. **Superwind** : At the tip of the AGB, the star enters a PPN phase that is characterized by an increase in mass loss rate in the orders of $\sim (10^{-4} - 10^{-3}) M_{\odot} yr^{-1}$ called the superwind, still the wind speeds are $\sim 10 kms^{-1}$ (e.g. SMK00). The need for a super wind is required for the for the post AGB dust shells because they have higher densities than when a star is in the AGB phase.

3. **Fast Wind** After the superwind has exhausted most of the outer circumstellar envelope; the star evolves off the AGB and becomes a proto-planetary nebula. At this stage the mass loss has significantly decreased or stopped, the star enters the Fast wind characterized by low mass loss rates $\sim 10^{-8} M_{\odot} yr^{-1}$ but very high out wind speeds $\sim 1000\, kms^{-1}$. This causes the central star to shrink raising the effective

temperatures from 3000K (typical at AGB) to higher temperatures ($T_{eff} \leq 10^4$ K) responsible to photo-ionize the base of the circumstellar envelope e.g. Meixner et al. 2006 [92].

The dust that forms around AGB stars is believed be one of the driving mechanism for mass loss. Dust grains can absorb all energies of photons, whereas atoms and molecules can only absorb specific wavelengths associated with atomic energy levels. This means that dust can capture the momentum of stellar photons more effective than can gas particles. The collisions between dust and gas particles then transfer the captured momentum and the gas can be dragged along in the outflow e.g. Gilman 1972 [40]. This mechanism of mass loss by dust driven winds is shown schematically in Figure 1.2.

As the star lose its mass, gas drifts or is pushed away from the star; at some distance dust forms (something refractory like $Al_2O_3$). The dust gains momentum by absorbing photons (through radiation pressure) and accelerates away from the star, because the dust grains hit the gas molecules, momentum is transferred to the gas and the gas is dragged along with the dust. This creates a low pressure zone in the atmosphere into which gas will 'flow in' (from the star's surface).

As the refractory dust and gas moves outwards it cools because of low temperature, as a result under good conditions that favor dust condensation, more dust can form. The more dust that forms is also acted upon by radiation pressure and thus we should get increasing mass loss. Eventually these stellar winds (gas and microscopic dust grains) will lead to the formation of an expanding dusty circumstellar envelope around AGB stars. Stellar evolution calculations that predicts the motion of gas and dust molecules in the atmosphere of AGB stars couples mass loss with dust formation e.g. Höfner, 2006 [58]. Therefore, the dust formation has its influences on the structure and dynamics of the atmosphere and eventually the whole star. Since the dust grains often interact more efficiently with radiation than molecules and atoms, the dust

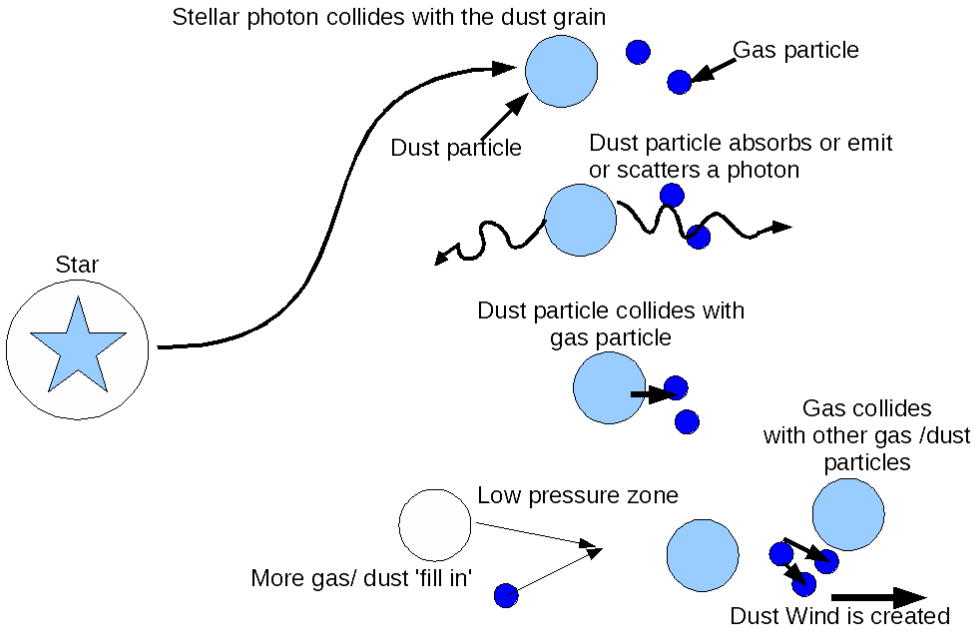


Figure 1.2: Dust grains acquire momentum from stellar photons and transfer it to the surrounding gas via kinetic collisions.

opacity actually dominates the total opacity of the star, as a result this gives rise to a radiation pressure that is sufficient to overcome gravity in the outer layers of the extended atmosphere.

In the atmosphere of a pulsating star, shock waves may also develop. The propagating shock waves will cause levitation of the outer atmospheric layers, creating a temporary reservoir of relatively dense gas at a certain distance from the photosphere and thus increasing the efficiency of dust formation. Most AGB stars are radial pulsating stars, and their periods vary and also grow with time during the star's evolution. This variation in in period also causes the radius of the star to vary. The growth time scales of dust formation associated with the stellar winds are of orders$10^7$ seconds, which is comparable to typical radial pulsation periods of $10^6 - 10^7$ seconds of these stars e.g.Gustafsson and Höfner, 2006 [58]. The combination of pulsation and dust formation can produce very large mass loss rates up to $10^{-5}\mathrm{M}_\odot$ $\mathrm{yr}^{-1}$ e.g. Lamers & Cassinelli 1999 [77]. Models of this type of mass loss scenario have attained a highest level of consistency because there are a few parameters that are used to predict the dependence of mass loss rates on stellar parameters. Therefore, this is the most promising hypothesis for a mass loss mechanism to date.

Theoretical calculations of Vassiliadis and Wood 1993 [137], Steffen, Szcerba and Shoenberner (1998) [126], Blöcker, (1995) [10] have produced models of evolution of AGB stars including the effect of thermal pulse[4]. on mass-loss. The variable parameters include pulsation period, luminosity, initial stellar mass and effective (surface) temperature. These authors e.g.Vassiliadis &Wood [137] suggest that the changes in surface luminosity of the star as a result of thermal pulses should lead to the variation in mass-loss, that is defined by an episodic mass loss rate. An episodic mass loss rate defined by [137] depends on the period and the mass of the star. The

[4]A thermal pulse is peak in the luminosity that occurs as a result of the He-shell heating the H-shell causing it to decline or extinguish in burning its left over hydrogen, therefore the total surface luminosity of the star is pulse-like during this runaway short period, and it is given by He-luminosity layer, hence the pulse often called the He-shell flash

pulsation period grows with time a star spends at AGB. The periods observed from stars in the our galaxy e.g. Knapp et al. 1986 [74] the Large Magellanic Clouds (LMC) e.g. Wood et. al 1992 [152], and the Galactic Bulge (Whitelock, Feast, & Catchpole 1991 [143]) increases exponentially at an onset of AGB from a few hundreds of days up to a maximum period of approximately 500 days as the star enters the superwind phase towards the end of AGB. The superwind phase is characterized by a dramatic increase in mass loss rate while the wind speed the star had at the AGB stays at about a constant value. The need for a supper wind is based on observations of PN objects versus those of AGB stars. PN dust shells have higher densities than the AGB winds (Renzini 1981). The mass loss-rate can increase from approx $10^{-5} - 10^{-3}\mathrm{M}_{\odot}$ per year e.g. Vassiliadis 1993 [137]. Because the period depends on the mass and the radius, so its distribution is affected by the interior evolution of the star in a complex way. As the star evolves the super wind phase models by Vassiliadis 1993 [137] predicts that the star may go through brief increase in mass loss rates (episodes). The narrow circumstellar dust shells found around some AGB stars are probably produced by these brief increase in mass loss rate e.g. Lattanzio & Wood at [51]. In such a scenario, it maybe possible to observe enhanced emission (bumps) in the surface brightness that indicates the occurrence multiple shells around our evolved AGB stars due to the effects of thermal pulses e.g. Speck et al. 2000b [125].

The aim of the work proposed here is to test these hypothesis by studying the dust in the circumstellar envelopes of AGB and post-AGB stars. For instance, if mass loss is truly driven by radiation pressure on the dust grains, then we should see evidence for this in the structure (spatial and temporal) of the circumstellar shell. The mass-loss rate could be constant, varying, episodic or steadily increasing (e.g. van der Veen & Habing 1998 [49], Vassiliadis & Wood, 1993 [137]), but there is little observational evidence for to clarify the situation e.g. Speck et al. 2000a, [124].

By detecting the surface brightness variations imprinted on the circumstellar dust

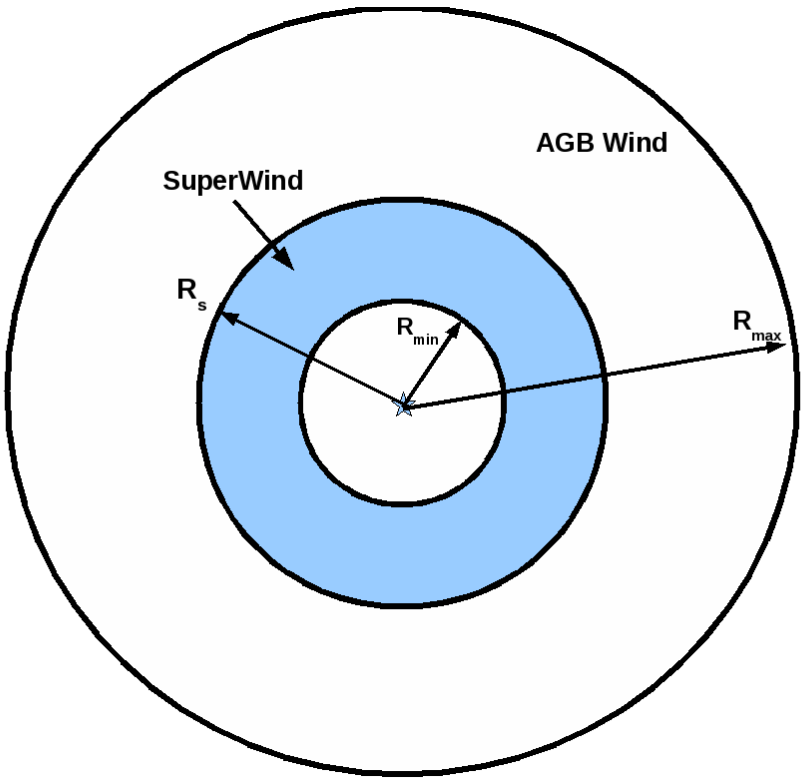


Figure 1.3: Geometric view of a fossil dust shell of a post AGB circumstellar envelope.

shells we can address whether such variations are related to time-dependent stellar properties such as pulsations (and an approximately annual timescale) and/or thermal pulses. Thermal pulses are expected to significantly increase a star's luminosity for $\propto 10^3 - 10^4$ years, and they recur on a time-scale of $10^5$ years.

The circumstellar dust shells (CDS) around AGB stars and post-AGB stars are the direct outcome of AGB mass loss. The circumstellar envelope of post-AGB stars contain the fossil record of the previous AGB mass loss. The structure of the post AGB - dust shell is shown schematically in Figure 1.3.

In this diagram, the dust farthest from the central star at $R_{max}$ represents the oldest mass loss that was caused by an earlier AGB wind. The material closer to star represents the more recent mass-loss after the onset of the superwind events at $R_s$. The inner radius of the dust shell (at $R_{in}$) represent the end of heavy mass loss by the superwind, which marks the begining of the PN stage. This model structure

presented assumes that the outer region has spherical geometry symmetric because AGB stars appear to have spherically symmetric dust outflows e.g. Habing & Bloummaert 1993 [48]. The inner regions is often modeled by toroidal geometry because the observations of planetary nebulae in the mid infrared suggest that they exhibit axi-symmetric geometry (e.g. Meixner et al. 1999 [94]) and further out, the outer shells have spherical halos (e.g. Schwarz 1992 [119]). This geometrical model is good representation of the dust shell structure expected to observed in the far-infrared.

When mass - loss first becomes significant, during the AGB phase, stellar mass loss appears to be mostly spherically symmetric in nature, as we might expect from more or less spherical pulsations. However, towards the end of AGB phase when these stars become post-AGB stars there is evidence that they develop at least some axisymmetric structure (e.g. Meixner et al. 1999 [94]; Ueta et al. 2000 [131]; Gledhill et al. 2001 [42]; Su et al. 2003[128]; Ueta et al. 2005 [132]). Planetary nebulae (PNe), the end products of AGB mass-loss, are usually axisymmetric (bipolar in structure) while the early AGBs are spherically symmetric. Hence, something must have triggered the development of the aspherical shell structure prior to the late AGB phase, but this mechanism remains a mystery. By looking for asphericity in the 2-dimensional structures of circumstellar dust shells we attempt to address when this phase begins and therefore achieve a better understanding of its origin.

As circumstellar dust forms and is pushed away from its parent AGB star, it achieves a terminal velocity that is approximately constant throughout the AGB phase of stellar evolution. Consequently the distance of the dust from the dying star is proportional to its time of ejection. In this way a pristine fossil record of this mass loss is imprinted on these shells (much like tree rings).

The duration of the mass loss in the transition phase (AGB - PN) can be estimated by the assessment of the extent of the dust emitting region in the circumstellar envelope, that is, if the velocities of the emitting particle′s were known, we can calcu-

late the time scale responsible for the expansion of the shell. Unfortunately infrared mapping observations does not predict the wind speeds, so we rely on what molecular emission lines that are use to expansion velocities. The molecular wind velocities often employed in determining the expansion velocities are measured by using line emission profiles that are abundant in the CSE's e.g.CO rotational transitions that dominates the circumstellar envelops. This method, though cumbersome, because we don't know exactly the wind speeds of particles at a particular region around the tar, has been widely applied in determining the time scales of the duration of mass loss. For example, Gillett & Bachman et al. 1986 [39] (hereafter GB86) used infrared photometry to study of the history of mass loss on an extreme carbon star R Coronae Borealis. GB86 results showed that, a straight forward explanation for an inverse law ($r^{-2}$ spherical density distribution responsible for the extended to proceed at a uniform mass loss rate ($\dot{M}$) with a constant velocity, under the assumption that the mass loss is driven by the radiation pressure, the mass loss rate can be expressed as

$$\dot{M} = \frac{M_t V_{exp}}{R_{max} - R_{in}} \tag{1.1}$$

where $M_t$ is the total mass of the extended shell (by both dust and gas),$V_{exp}$ is the assumed constant expansion velocity. The time scale over which mass loss occurred can be estimated by

$$t_{shell} = \frac{R_{max} - R_{in}}{V_{exp}} \tag{1.2}$$

and the terminating time at $R_{in}$ is about

$$t_{term} = \frac{R_{in}}{V_{exp}} \tag{1.3}$$

Thus in order to get an estimate of the time scales associated with mass loss

events, the radial extent can be divided by the expansion velocity measured from line emission profiles e.g. SKM00. This idealism was employed in obtaining the time scales reported in this thesis, and the results obtained were compared to the time scales predicted by stellar evolution models e.g models by Vassiliadis & Wood 1993, Blöker 1995 that derive the time scales for intermediate mass stars during and after the AGB phase. The are already several reports about the existence of large dust shells around some evolved stars in which far infrared emission has been used, e.g. on the basis of Infrared Astronomical Satellite IRAS [99], Gillet et.al 1986 [39] found that R Coronae Borealis, a late type carbon star have a very large shell with a radius of 4 pc, Hawkins 1990 [53] reported a 1-pc shell around W - Hya, Speck, Meixner & Knapp 2000, hereafter SMK00, reported 2 - 3 pc concentric shells whose identify have been associated with thermal pulsation on two late carbon-rich Pre-Planetary Nebulae (PPNe) AFGL 2688 and AFGL 618 on the basis of European Space Agency Infrared space Observatory (ISO), Do & Morris 2007 [24] reported the presence of 4pc shell of thickness 1pc around IRAS 16342 - 3814 on the basis of infrared satellite Spitzer (Werner et al. 2007 [36]).

The dust grains in these shells absorb radiation from the star at all wavelengths and re-emit the energy in the far-infrared (far-IR). Therefore we use far-IR imaging to detect and investigate circumstellar dust shells.

In order to detect thermal infrared emission from the cold dust in the extended circumstellar dust shells we used far-IR imaging photometry. The images presented in this thesis were observed using wave band filters between $60\mu$m – $160\mu$m, using the archival data from infrared space telescope (ISO; Kessler et al. 1996[70]) and were compared with IRAS (Neugebauer et al. 1984 [99]). In order to establish the size and density distribution of the entire structure we use cold dust emission as a primary tracer. In the inner regions of the circumstellar shell molecular gas is a good tracer of the density and spatial structures. However, in the outer parts of the shell, these

molecules are photo-dissociated by high energy photons from interstellar radiation field (ISRF) in the outer parts of the shell (e.g. Meixner et al. 1998), making the dust the only tracer of the outer reaches of the CDS's, and thus the tracer of the oldest mass loss. The ISRF heats the outermost regions of the extended CDS's and keeps the dust temperature around $20 - 40$K[5].

When gas and dust plows into the ISM there may exist the pile-up material causing the increase in shell density and thus an increase in surface brightness as models suggest e.g. Zijlstra & Weinberg 2002 [155], this is expected to be observable from our data. In such a situation the material lost from the star collides with the interstellar medium (ISM) that leads to the densty increase in the direction of the motion of the star. Bow shocks are created due to the increase in surface brightness. The dust emission due to the formation of bow shocks is observable in far infrared e.g. Gillett et al. 1986 [39]; Zijlstra & Weinberger 2002 [155]. The bow shock structures have been identified and reported to occur in two PPNs objects in our sample of stars, e.g. Mira and Rhya by Ueta et al. 2006 [133], 2008 [130] (see also Wareing et al. 2007 [139] and a review by Stencel 2009[127]). Moreover, the interfaces through which AGB stars interact with their environments have remained poorly studied observationally. One problem is that CSEs can be enormously extended ( >1 pc), and their chemical composition changes as a function of distance from the star, as densities drop and molecules become dissociated by the interstellar radiation field or by other radiation sources. The result is that the some of the most frequently used observational tracers of CSEs (e.g., CO; SiO, H2O, and OH masers) do not probe the outermost CSE or its interaction zone with the ISM. Thus the more extended material can be traced via imaging observations in the infrared (Zijlstra & Weinberger 2002; Ueta et al. 2006, Ueta et al 2010 [134]; Ladjal et al. 2010[76]) or in the far-ultraviolet (Martin et al. 2007 [90]; Sahai & Chronopoulos 2010 [114]). Though such

[5]According to Wien's Law (see equation A.3) i.e. for 20K < T < 40K the emission will peak at $70 - 150$ $\mu$ m

data does not provide any direct kinematic information of extended structures such as bow shocks, however it does provide a well defined evidence a bout their presence around some evolved AGB stars.

For each object in the sample we used photometric images at more than one far-IR wavelengths. The advantage of using multiple filter bands is that one can independently determine the size of the shell as well as the energy flux (Jy) it contains. Measuring size and flux of the circumstellar shell allows the determination of the mass of the dust contained within, provided that the local dust temperature and emissivity or the nature of dust species are known. Multiple wavelength observations allow derivation of the dust temperature/emissivity profiles. Calculating the total mass of the dust shells together with an estimate of the core mass sets a lower limit on progenitor masses of stars (i.e. prior to AGB mass loss). The progenitor mass found this way, can give us clues on what mass the star began with before entering the AGB phase. This study has an impact on initial - final mass relations that predicts how much mass a star started as a main sequence star to what the final the end product in mass a star should be. Most intermediate mass stars become white dwarfs whose masses can essentially be found in old clusters. Therefore a comparison of masses derived by IMF relations and what the theories suggest can be clarified provided that the dust masses are found with fair accuracy.

The proto-planetary nebulae (PPN) or planetary nebulae(PN) circumstellar shells potentially have complete history of their progenitor AGB star′s mass loss. Since AGB stars suffer high mass loss rates at AGB phase, the mass loss rates during at this phase has an in impact on the distribution of matter. That is, the mass the generic form of the loss rates is expressed in-terms of density, radial distance and outflow velocity inside the wind. If for example we take a constant mass loss rate such that the local mass density does not vary over a long time (AGB phase $10^5$ years) , this mass loss will give rise to an inverse law ($\rho \sim 1/r^2$) density distribution if we also assume that

the velocity of the expanding shell is a constant (e.g. Huggins et. al. 1998[60], Fong et al. 2003 [29]). An episodic mass loss should result should appear as discrete dust shell enhancements at particular radii from the star, while accelerated mass loss rate would appear to drop faster that (maybe like $\rho \sim 1/r$) in dust density. This is what theories of stellar evolutions currently suggest as far as mass lose rate and density are related, however there needs to be observational evidence to show that such claims actually occurs in AGB stars. In attempt to work on this matter the density profiles derived from far infra-red observations images are presented in order to show if there is any surface brightness variation in flux of the circumstellar dust shells. The radial profiles are cut through scan from a photometric image that shows the flux variation a function of distance in 1-dimension. Therefore the radial profiles derived from infrared photometric observations provides a record of mass loss which should test the theories of mass loss. AGB stars can be broadly divided into two chemical groups on basis of spectroscopic observations of molecules in their atmospheres. The stars that have more carbon atoms than oxygen atoms in their atmospheres are termed carbon-rich AGB stars or simply carbon stars, whose spectra are dominated by C-rich molecular bands such as $C_2$ and Cyanide (CN) molecules. There are also those with more oxygen molecules (e.g. TiO) and they are called oxygen-rich AGB stars. There are also S-stars, which have approximately equal amount of carbon and oxygen atoms. The cause of this chemical dichotomy is carbon monoxide (CO), which is one of the most strongly bound molecules in the atmospheres of cool stars. If C/O<1 there is a surplus of oxygen atoms available to form oxygen-rich molecules whereas if C/O>1 all oxygen is bound up in CO, and surplus carbon atoms are available to form molecules e.g. C2, and CN, by Harbing and Olofsson 2003 [51]. AGB stars are born from oxygen-rich environments because interstellar space has more oxygen than carbon. Therefore the atmospheres of newly-born AGB stars are by default oxygen-rich. However, AGB stars create carbon atoms through helium fusion, and

those carbon atoms are dredged-up to the stellar surface by convection currents. The presence of excess carbon in an AGB star $'$ atmosphere indicates that efficient dredge up must have occurred. The study of the history of mass loss of evolved or aging AGB stars presented in this chapter uses infra-red photometry in order to detect the presence of extended emission around the star.

Mechanisms for the evolution of these stars is still not well understood. There are several issues still to be resolved that are listed below:

1. The existence of the extended emission due to the presence of circumstellar dust around most intermediate mass stars is not well contrained by observations. We lack knowledge about how big the emitting region is that contains the circumstellar dust. And also the location and the structures of the emitting regions that constitute a dust shell or multiple dust shells are still not well defined due to the resolution issues of infrared telescopes. IRAS Hires (Neugebauer et al. 1984 [99]) mapped a number of AGB stars including the ones in our sample, however, due to the large IRAS beam and its low angular resolution, the origin of infrared emission (circumstellar disks, or small spherical, or dust off-centered dust clumps) were not reliable identified. ISOPHOT (Lemke et al. 1996 [84]) has the mapping capability in the far infrared that can be use to derive the information about the location and the size of the emitting regions. The initial goal for this project was to determine and understand the origin of the extended far-infrared emission around intermediate mass stars, and to separate the radiation surrounding the star.

The physical mechanisms for intensive mass - loss experienced by AGB stars can be addressed by investigating the extended emission through localizing the emitting regions and constrain the presence of the circumstellar shell. In imaging photometry, this is achieved by first deriving the linear scans of surface brightness variation versus the radial distance from the the star location, the emerging profile is called the radial profiles. The radial profile from observations is then compared with point spread

function (PSF)of a point source profile (the PSF) in order to make an assessment of the size and the nature of the emitting region. For any structure to be identifiable and resolved by a telescope, the full width half max (FWHM) representing the diameter of emitting region have to match with the FWHM of the footprint psf of the telescope detector. If the FWHM of the observation matches that of the footprint, the measured radial profile from observation represents a point source. On the other hand, if the FWHM of the footprint falls outside that of the emitting region, it means that the emitting region was unable to be resolved at that particular filter band. If the resolved source has an extended clump, we can estimate the extent of the source clump by fitting the Gaussian profile in order to estimate its size from the FWHM of the Gaussian distribution. The diameter of extended emission is assumed to fall at 3 - 4 times the FWHM of the fitted Gaussian distribution. The reason for estimating the sizes of the shell using this method, is a because the surface sky background for ISOPHOT detectors is very uncertain and it varies per wavelength– filter used and the pixels used to construct the maps. Our Gaussian profiles indicated that the extended clumps fall far below the sky background level, indicating that radius of extended source might be larger than that derived by using one FWHM.

2. It is not well established what are the initial masses intermediate mass stars which evolve into planetary nebula. In the infrared, we can calculate the mass of dust contained in the emitting region e.g. Hilderbrand et al. 1983 [57], hereafter Hiderbrand 1983. Hiderbrand 1983 showed that in order to obtain the mass of the dust, the emissivity and the dust temperature have to be known. These properties were derived from our observations by performing surface area photometry in order to get the flux emitted by the same emitting region at more than one filter bands. We used the fluxes derived at different filters to measure the total mass of circumstellar dust by assuming spherical geometry; and we calculated the total mass of the dusty envelope by using the canonical dust-to-gas ratio (using the literature values as well

as laboratory data) from which estimated the total mass lost by the star. The mass of the core was estimated by using luminosity - core mass relation given by Paczynski et al. 1970 [102]. Thus, using the core mass estimate of the star, together with the total mass lost by the star we were able to get a lower limit to the initial mass of the the progenitor star.

3. Intermediate mass stars are classified according to the chemistry i.e. some are oxygen - rich with C/O $< 1$ and carbon rich (C/O $> 1$) and S-stars (assumed to have C/O $= 1$), in this study we also wanted to find out under what conditions does mass - loss process depends on chemistry. For instance, the objects already studied in details using infrared photometry are the two carbon rich PPNe (AFGL 2688 and AFGL 618) and oxygen-rich PPNe HD 16796 by Speck. et al. 2000. Speck. et al. 2000 was able to show that that (a) the dust emission by O-rich object is much fainter in brightness than any of each of the two C-rich objects they studied. (b) the oxygen rich surface brightness did no show any surface brightness variations associated with mas loss events (maybe due to thermal pulse on their report) that were seen on both carbon rich objects. As a result of this dichotomy, it was not clear how significant does chemistry in intermediate mass stars will have on mass loss. So it was worth expanding the sample representing both classes of stars in order to investigate further if the evolution of intermediate mass stars are affected by their chemistry.

In theory, the time-dependent changes expected in the luminosity and temperature of a star should be manifested in the radial distribution of the dust in the far infrared (e.g. Vassiliadis & Wood 1993; Steffen et al. 1998). Converse to say, from an observational perspective, the easement of the radial profiles show the surface brightness variations imprinted on the CDSs by mass loss, and thus can be used as a tool to investigate mass loss. As a result it is essential to compare the radial profiles of both oxygen and carbon rich stars and address there are any variations in surface brightness related to time-dependent stellar properties that are linked to the

differences in chemistry of intermediate mass stars.

The other important aspect of this study, is estimation of dust mass loss rates from the monochromatic fluxes derived by our observations. We assume that the flux density is obtained in the optically thin limit and the source emitting region is unresolved. In such a case the mass loss rate can be determined from the flux, the distance to the source, mass absorption coefficient (depends on derived emission index) and the dust temperature of the shell. The mass loss rate estimated this way requires the knowledge of dust velocity that can be estimated by expansion velocity of the resolved CO emission lines profiles. The total mass loss rates derived this way depends on the assumed dust to gas ratios, and in general they are accurate to within an order of magnitude (e.g.Habing & Olofsson 2003 [51]) The mass loss rates can be derived from far-IR emission, therefore by knowing the history of the dust shells we can also trace the mass loss rates associated with the evolution of the star.

In summary this thesis focuses on using observations of far-IR emission from AGB and post-AGB stars to determine whether dust shells are seen, and if so, what are their sizes, masses and radial density profiles. These derived parameters are then used trace the history of mass loss of the observed stars as well as the masses of the progenitor stars. I then compare the results to theoretical models in order to test, constrain and refine these models and gain a better understanding of the factors that affect the details of stellar evolution.

Since this work deals with the evolution of the stars at late stages of their lives, it is important to first understand how stars evolve, this is covered in Chapter 2. Chapter 3 deals with the formalism behind the formation of Asymptotic Giant Branch Stars (AGB). Chapter 4 covers mass loss and dust formation around AGB stars. Chapter 5 covers thermal emission by dust around AGB stars. Chapter 6 discusses far infrared observations by ISOPHOT photo-polarimetry used in this thesis. Chapter 7 covers probing the history of mass loss of oxygen - rich AGB star using imaging photometry

by ISOPHOT PHT32 Observations. Chapter 7 covers probing the history of mass loss of carbon - rich AGB star using imaging photometry by ISOPHOT PHT32 observations. Chapter 9 gives the summary.

# Chapter 2

# Intermediate Mass Stars and their Evolution

## 2.1 Intermediate Mass Stars and the Hertzsprung-Russell Diagram

For countless generations, humans have gazed up in at sky to see that it is full of many stars. Even with the naked eye we can see that as many stars as there are, they vary in appearance; some are bright, others are dim; some are blue, others white and others red. We now know that the differences in apparent brightnesses of stars occur because of the large ranges in both intrinsic stellar brightnesses and distances to stars.

Because astronomy has been pursued over millennia, we have developed ways to look at the heavens that are historical, and based on the response of human eye to light, but which remain used in our technologically-advanced state today. A detailed discussion leading to our current methods for measuring stars brightnesses and temperatures can be found in Appendix A.

In the early 19th century Hertzsprung [56] and Russell [112] independently dis-

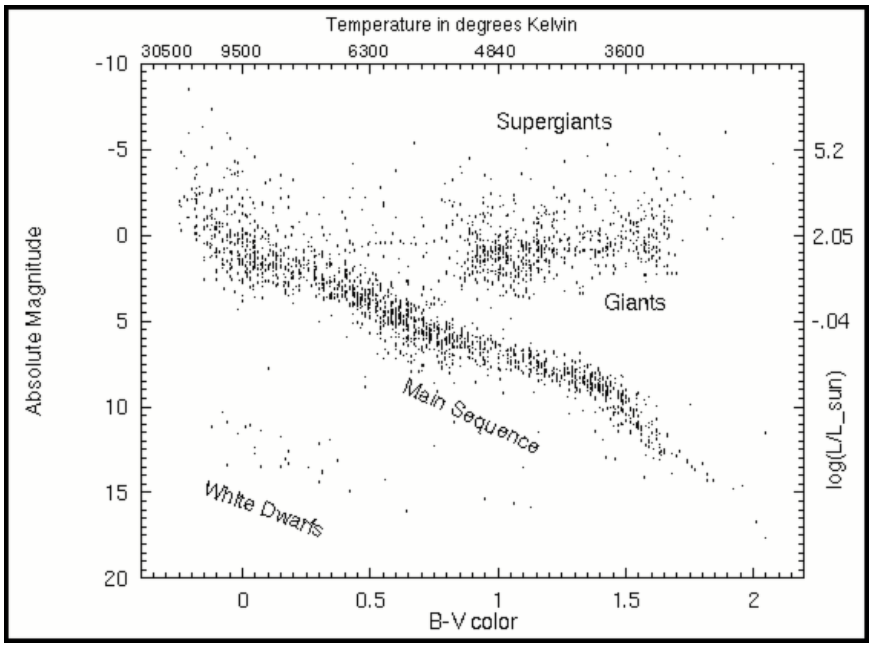


Figure 2.1: The Hertzsprung-Russell Diagram: a plot of the Luminosity or Absolute magnitude (vertical axis) vs. Surface temperature, Spectral type or color (e.g. B−V color band; horizontal axis). Both scales are logarithmic (except in magnitudes, which is intrinsically logarithmic) and temperature is increasing to the left. This plot contains stars in the local neighborhood. The dots shown in this plot represents the stars from Hipparcos catalog [107]. Common groups seen in HR diagrams are labeled.

covered that when they compared the absolute magnitudes (or the luminosities) with the spectral types (i.e. surface temperatures) that patterns emerge. In recognition of their originators, graphs of absolute magnitudes against the spectral type are called Hertzsprung-Russell (HR) diagrams, an example of which is shown in Figure 2.1

The majority of stars (∼90%) fall on a diagonal band that extends from hot stars of high luminosity in the upper left corner to cool stars of low luminosity in the lower right corner. This band is called the Main Sequence which is now understood to be where stars spend most of their lifes performing hydrogen-fusion in their cores. There is also a group of stars that are abnormally faint with their white-hot surface temperatures, they lie sparsely scattered on the lower left corner in the HR diagram and they are called White Dwarfs (they must be small because they are both hot and faint; see Equation A.4. Giant stars have high luminosity and form a thick, approxi-

mately horizontal band that joins the main sequence near the middle of the diagonal band. Above the giant stars, there is another sparse horizontal band consisting of the even more luminous 'supergiant′ stars.

The significance of the H-R diagram is that stars are concentrated in certain distinct regions instead of being distributed at random. This distribution is an indication that definite laws govern stellar structure. The existence of fundamentally different types (groups) of stars in the HR diagram is the most important tool in understanding stars.

Our understanding of stellar evolution suggests that stars should change in luminosity and temperature throughout their lives as they evolve and thus move around on the H-R diagram. This means that the stars within the same group share essentially the same characteristics, and as they evolve something must have caused changes in surface temperature and luminosity that we observe on the H-R diagram. Thus the evolution of stars can be tracked through H-R diagram since it represents stars at different stages of their evolution.

For main sequence stars with high temperature, and high luminosities stars have the highest mass, while the mass decreases as we move down the Main Sequence to the cooler, lower luminosity stars. We now understand that stars will evolve off the main sequence according to their initial mass such that high mass stars ($\geq$12 $M_\odot$) become supergiants and explode as supernovae. There is some ambiguity about what happens in the mass range $8 \leq M_\star \leq 12\ M_\odot$, but that topic is beyond the scope of the present work.

Models of stellar evolution theories suggests that, stars with initial mass less than $0.08 M_\odot$ never reach central temperatures high enough to ignite hydrogen burning thus they become Brown dwarf stars at the end of their evolution. Very low mass stars (0.08–0.8 $M_\odot$) never ignite helium, and die as helium white dwarfs. The focus of this thesis is on the intermediate mass stars (0.8–8 $M_\odot$) which do not explode, but

do fuse helium to make heavier elements. The evolution of stars of all masses can be plotted on the HR diagram, but I concentrate on only the intermediate masses. In the following discussion, the evolution of intermediate mass stars of $1\,M_{\odot}$ and $5\,M_{\odot}$ respectively are presente. These masses were selected because there are subtle difference in their structures that govern how these stars evolve on the HR diagram. At various times, nuclear fusion events (known as "burning") are accompanied by readjustments of the structure of the star.

The evolutionary tracks shown in Figure 2.2 demonstrate the changes in luminosity and temperature that the star will go through as it evolves. Throughout their lives the structures of stars are dictates by the interplay between gravity and pressure. Pressure acts in all directions, trying to push the stallar mass in every which way. Gravity acts towards the center of masses, pulling materials inwards. When pressure and gravity exactly balance the system is in hydrostatic equilibrium. The changes stars experience can be explained in terms of the battle between pressure and gravity. Prior to ignition of fusion in a star gravity tends to win out over pressure because constant radiation of energy prevents the pressure from rising to balance gravity. At point 1, known as the Zero-Age Main Sequence (ZAMS), stars begin hydrogen (H) fusion in their cores and begin their lives as fully-fledged stars. H-burning provides the energy supply to drive pressue to balance gravity and hydrostatic equilibrium in achieved. All stars spend most (90%) of their lifetime fusing hydrogen into helium (He) in their cores. As the star develops a He-core, the central temperature increases because the conversion of 4 H particles into one He particle reduces the pressure; gravity causes the core to shrink; potential energy is converted to kinetic energy. During the main sequence evolution (points 1-4 in Figure 2.2), theoretical models predicts that the mass fraction of hydrogen in the core decreases as indicated by insert (a) on both panels.

Once the core exhausts its supply of H fuel, core fusion stops and the star evolves

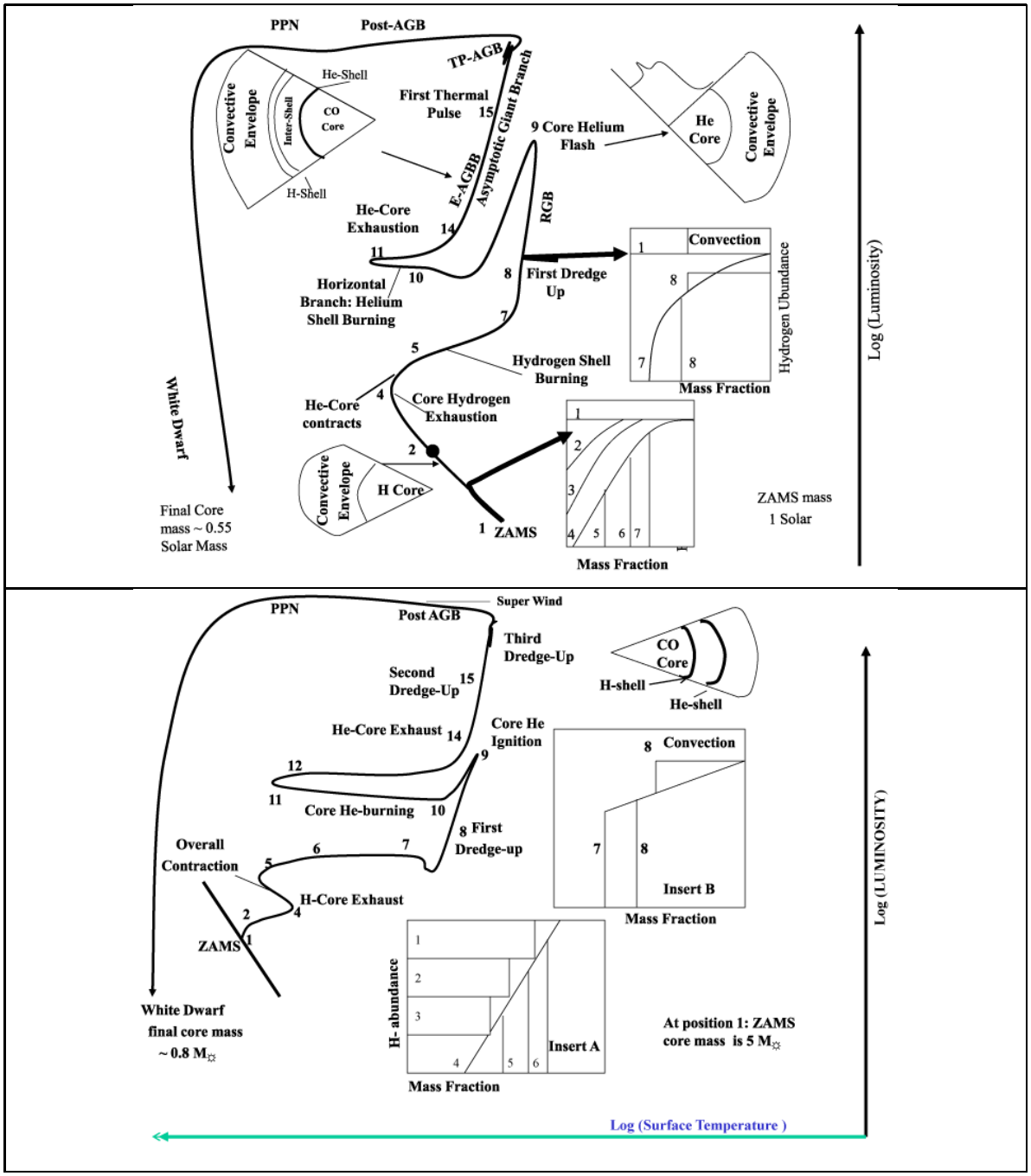


Figure 2.2: Stellar evolutionary tracks on the HR Diagram: the evolution of intermediate mass stars from birth onto the zero age main sequence (ZAMS) to death as a white dwarf. *Top Panel*: track for a "low" intermediate mass star (initial mass = $1M_{\odot}$; final mass $\sim$0.55M$_{\odot}$). *Bottom Panel*: track for a "high" intermediate mass star (initial mass = 5M$_{\odot}$; final mass $\sim$0.8$M_{\odot}$). The inset panels show the mass fractional changes in composition of hydrogen relative to the other elements during the evolution of both stars on HR diagram.

off the main sequence (at stage 4). For "low"-intermediate-mass stars ($0.8 \leq 1.8$), H-exhaustion is followed by contraction of the He-core that does not involve the whole star. The He-core begins to contract while thick H-shell continues to burn hydrogen, the collapse of the core (release of gravitational energy) causes the temperature of the H-shell to rise,which increases the rate of H-burning and thus the H-burning shell produces more energy than did the whole core during the main sequence phase. The H-shell heats the surrounding (non-fusing) stellar envelope, which absorbs some of the energy, therefore expands and cools. As a result, the luminosity increases, the star expands while the effective temperature decreases, thus the evolutionary track moves up to the right. In higher mass stars (>1.8), the whole star contracts (overall contraction) in response to core-H-exhaustion, causing the luminosity to increase slightly, the stellar radius to decrease while the effective temperature increases, as result, the evolutionary track moves to the left as the star enters stage 5. The differences in tracks 3 - 5 indicates this evolution.

Stars enter the subgiant branch (SGB) at stage 5, with H-burning well established in the shell that surrounds the He-core. The differences in structural changes with stellar mass occur because the nuclear processes depend sensitively on the temperature of the He-core, high mass stars gain more energy during formation and thus have higher temperature cores than their low mass counterparts.

For both the $1\,M_\odot$ and $5\,M_\odot$ stars subgiant branch evolution proceeds similarly Hydrogen shell burning creates and deposits He onto the core causing it to grow and become isothermal. During this phase, contraction of the isothermal core releases gravitational energy that causes the whole envelope to expand while the effective temperature cools. Therefore the luminosity remains at a constant value while the effective temperature decreases, resulting in a redward evolution for until stage 7 is reached. The consumption of hydrogen during the SGB phase are shown by insert (b).

When the star reaches stage 7, the temperature and density of the narrowing H-shell has increased, the rate at which it generates energy rises rapidly, depositing more helium onto the core forcing it to contract and release energy that expands the envelope while cooling. The process is similar to that occurred in stages 4–5. The star ascends the red giant branch with increasing luminosity and decreasing effective temperature while the stellar envelope expands.

As the star climbs up the red giant branch phase, the He-core continues to contract and heat (increasing in central temperature), such that a non-zero temperature gradient is re-established between the ' narrowing H-shell and the core. As a result , a convection zone is established between the core and the envelope where H-shell is located. The convective envelope penetrates deep into a region where H-burning once occurred earlier in the stars evolution, this is called First Dredge-Up, as a result material rich in H-burning products, e.g. steps in the CNO cycle (see Figure A.2.2) are mixed into the stellar envelope. The effect of convection is noticeable by observable changes in chemical composition of the photosphere of intermediate mass stars, such as the the decrease of $^{12}$C / $^{13}$C from $\sim$90 to $\sim$20, decrease in $^{12}$C / $^{14}$N.

Further collapse of the core provides more conversion of potential energy to kinetic energy and will trigger He-burning at stage 9. For low mass stars, the H-burning shell eats its way outward leaving behind more helium ash. As the helium piles up, the core becomes more massive and contracts. The contraction heats the core as it becomes more dense. The density of the core increases to the point where the electrons become degenerate and therefore incompressible (see § A.1.4). Contraction stops. As the hydrogen shell continues burning, the degenerate core grows hotter and hotter, and eventually the triple alpha-processes (He-fusion) is ignited is a fierce He-core flash.

The evolution of a high mass stars between stages 8 - 9 is a little different because they begin He-burning under non-degenerate conditions. There is no helium flash,

just a gradual shift to a core He-burning region surrounded by a H-burning shell. After helium burning begins (either explosively with a flash, or gradually for more massive stars), the star has two sources of energy, H-fusion in a shell around the core and He- fusion in the core. Helium burns into carbon, and carbon combines with helium to make oxygen. The core of the star becomes rich in carbon and oxygen nuclei.

During the horizontal branch phase, stars pass through the Instability Strip (points 11-13) where they begin to pulsate in a regular fashion. The amplitude and period of the pulsation is dictated by the star's mass such that a low mass star will become a RR Lyrae star, while a high mass star evolves to become Cepheid variables. In this part of the H-R diagram, the structure of any star is such that the non-burning gassy envelope is cool enough and dense enough to become opaque to the radiation passing through it from the core. Thus the envelope absorbs the radiation and energy is transported convectively. The absorbed energy increases the temperature of the envelope gas which then expands. Expansion decreases the opacity and thus energy can escape radiatively and envelope cools again. Pressure drops and the envelope has to shrink under gravity. As it shrinks the envelope becomes more opaque again and again traps energy and the cyce repeats. For Cepheid and RR Lyrae variables this process produces extremely regular pulsations.

When the star enters stage 14, He-core-burning stops, and a He-burning shell will develop underneath the H-burning shell (in much the same way that a H-burning shell develop after H-burning eneded in the core). Above both these shells remains an envelope of non-fusing gas which has strong and deep convection currents (see inserts (f) for a hypothetical structure).

The electrons in the C-O core again become degenerate (see section § A.1.4) and the star expands and cools to become an asymptotic giant branch (AGB) star. As the star ascends up the AGB, the luminosity of star is provided by both the H-

and He-burning shells, so that it increases, but the effective temperature decreases because of the expanding envelope. The star evolves redward and up on the HR.

At first the luminosity of the star is dominated by the luminosity from the He-burning shell, because the H-burning shell is partially dormant. As the He-interlayer that separates these fusion shells narrows, the H-burning shell will begins to dominate the luminosity while there is a decline in He-urning shell. Eventually there is as oscillation between He-burning and H-burning as the dominant luminosity producer. This oscillation is caused by the thermal sensitivity of the He-burning process. The star has entered a thermally pulsating phase[1], indicated by stage 15. Thermal pulses occur as He-burning switches on which is accompanied by an increase in luminosity (due to extra energy production in He-burning shell). A thermal pulse ends when the He-burning switches off due to shell expansion and accompanying temperature drop. This leads to a drop in luminosity as the He-burning shell reduces its contribution to the overall stellar luminosity. Just like the loss and gain of hydrostatic equilibrium due to core nuclear processes gives rise to changes in surface brightness and temperature of a star, so the He-shell oscillation between fusion and non-fusion is manifested the same way. The timescales associated with Thermal Pulses are much longer ($\sim 10^4 - 10^5$ years) that those associated with the usual LPV/instability strip pulsation (which is $\sim$1 yr).

For high intermediate mass stars (>4M) depending on the metallicity, model by Vassiliadis 1993 [137] suggest that a second dredge-up may occur before a star begins to thermally-pulsate leading to a further mix of material H-burning products; while, for lower mass (<4M) the second dredge-up does not occur before the star begins to thermally-pulsate.

AGB stars are also known to lose mass as they radially pulsate due to their position in the instability strip. Mass-loss rates of $10^{-8} - 10^{-6}$ $M_\odot$/yr (e.g. van

[1]Thermal pulses are due to different mechanism and have different timescales compared to the pulsations that are seen for all stars in the instability strip and described above.

Loon et al. 1999 [136]) leads to the formation of circumstellar of predominantly molecular gas that leaves the star in the form of stellar winds. Dust grains form with this outflowing material giving rise to circumstellar dust shells (CDS) as part of the ejected circumstellar material. This mass-loss process will be discussed in more detail in Chapter 3. At the tip of AGB phase the star is expected to enter a superwind stage characterized by an increase in mass loss and invoked to explain the high densities seen in Planetary Nebulae (Renzini 1981). Mass-loss rates can exceed $\sim 10^{-4} M_{\odot}/yr$ e.g.van Loon et al. 1999 [136]. The velocity of the material in the stellar wind material is $\sim 5 - 30 \mathrm{km\,s^{-1}}$ (e.g. Marshal et al. 2004 [88]) throughout the AGB mass-loss phase. During the superwind phase the circumstellar envelope becomes so dense with dust that it is opaque to visible light; the dust shell absorbs all starlight incident upon it. The reprocessed starlight is emitted by dust at infrared wavelengths and sub-millimeter wavelengths making these objects observable at very long wavelengths.

The high mass-loss rates during the superwind phase reduce the mass of the non-burning envelope above the H-burning shell to such a degree that the gas pressure drops and is unable to compete with the effect of gravity. The star is no longer able to maintain its size and begins to shrink. The mass loss rates decreases dramatically ($\sim 10^{-8} M_{\odot}/yr$), while the wind speeds increases ($\sim 1000 km^{-1}$ e.g. [125]). The star leaves the superwind phase and enters the so called a Fast-wind phase. Meanwhile, the collapse of the stars envelope under gravity causes an increase in effective stellar temperature as potential energy is converted to kinetic energy. The star evolves to the left on the H-R diagram with increasing surface temperature, shrinking in size to maintain constant luminosity.

The star is now a post-AGB star alsoknown as a proto- or pre-planetary nebula (PPN) at stage 16, a transitional stage between the AGB phase and a planetary nebula (PN) phase. PPNe objects are composed of a central star with detached cir-

cumstellar shells of dust and gas. The effective temperature of a star is increasing but still low enough that the the circumstellar envelope 'the mantle' remains neutral (un-ionized; e.g. Meixner et al. 1998 [93], Kwok et al. 1993 [75]). The evolution of intermediate mass stars during this phase is poorly known, however observations of dust shells around these stars indicate that their inner shells already show some axisymetric structures. For example, bipolar structures are seen in images of PPNe AFGL 2688, CRL 618, Zuckerman & Aller 1986[156]). The departure from spherical symmetry must take place towards the end of the AGB phase or early in the PPNe phase. Shaping effects that lead to these axisymmetric structures remain controversial (see Dijkstra & Speck 2006 [23] and references therein). For instance, axisymmetry can be imposed by introducing an equatorial density enhancement in the mass-loss ejecta (Kahn & West 1985 [68]) and distinct morphological groups can be created by varying the degree of equatorial enhancement in red giant or AGB ejecta (e.g., Balick 1987 [5]; Habing, te Lintel Hekkert, & van der Veen 1989 [50] ; Mellema & Frank 1995 [95]). Although there has been a number of suggestions for the source of equatorial density enhancement, which include magnetic fields, binary companions and conservation of angular momentum (e.g., Soker 1998[123]; Mastrodemos & Morris 1999 [91], Dijkstra & Speck 2006), there is no definite solution to the problem. Whichever the true scenario may be, a significant portion of the entire mass-loss history is imprinted on the PPN circumstellar shell of gas and dust: the innermost edge defines the termination of mass loss and the mass-loss history can be traced back in time as one probes outer regions of the circumstellar shell. Therefore, one can investigate when and how geometry of mass loss departs from spherical symmetry by sampling dust/gas distribution at various radial locations in a PPN circumstellar shell.

As the star evolves towards the left of the H-R the effective temperature of the star continues to increase. Once it reaches temperatures around (T>30,000K), the

stellar photon can ionizes the circumstellar shell and the star becomes a planetary nebula. The timescale for the transition from AGB to PN is very short $\sim 10^3$ years (Ueta & Meixner 1999 [94]). The ultra-violet photons from the central star excite and ionize gas atoms in the envelope. As a result when the electrons cascade back to the lower energy levels they emit visible light. Thus, most PN are visually observable and are dominated by green light ($\lambda$=500.7 nm) due to $O^{2+}$ and red light due to H-$\alpha$ and N II (at $\lambda$= 656 nm and 658 nm respectively).

Eventually the consumption of the H-rich envelope means that there is not enough mass left above the H-shell to maintain the temperature required to burn hydrogen, and the star runs out of fuel after it reaches a peak temperature close to 200,000 K With no energy source, the central star (which is essentially the remnant core of the original star) declines rapidly in luminosity. As the circumstellar material drifts away, the PN evolves to become a white dwarf at stage 18. At this stage, all that is left of a star with initial mass $M_\star$= 1 $M_\odot$ is a C-O white dwarf with $M_{WD} \approx 0.6 M_\odot$; wheareas a 5 $M_\odot$ leaves a white dwarf of with $M_{WD} \approx 0.8 M_\odot$; these values depend on the models and also they are constrained by the observations of AGB stars found in globular clusters.

According to stellar evolutionary models (e.g.Vassiliadis &Wood 1993 [137], Steffen 1998 [126], Blöcker 1995 [10]), intermediate mass stars lose most of their circumstellar matter near or at the end of AGB phase because of the increase in mass loss rates e.g.( Wood, Bessel & Fox 1983 [8]). A 1 $M_\odot$ star in Figure 2.2 loses ~40% of its mass between stages 15 (AGB) and 17 (PPN) and most of this mass is lost during the superwind phase. For the 5 $M_\odot$ star, 80% mass is lost during stages 15–17.

# Chapter 3

# Asymptotic Giant Branch Stars

## 3.1 Early Asymptotic Giant Branch

Following helium exhaustion and core contraction, the surface luminosity is increasing while the surface temperature is decreasing because the whole star is expanding. As a result the star begins to climb again the red giant phase for the second time. The luminosity comes from the Helium burning shell and the Hydrogen burning shell is partially dormant, the core has become degenerate as the star is approaching the new stage called Early Asymptotic Giant branch (E-AGB). The degeneracy of the core ensures that no carbon burning occurs in the center of the star because the core temperatures is still high enough to allow such processes to occur so the core cools by emitting neutrinos. As the star is swelling and burning helium in the He-shell, the convective envelope starts to deepen inside the interface between the hydrogen shell burning region and the helium layer. As a result Second Dredge-up of materials rich in He burning layer gets transported into the surface of the star through convection. Current models (Lattanzio and Wood on Habing & Olofsson, 2004 [45]) suggests that in the first dredge the convective zone mixes up to the regions

that have undergone only partial H-shell burning whereas the in the case of second dredge-up, the convective zone can penetrate the entire H-shell reaching material up to the He-shell; therefore the products of the second dredged-up maybe essentially similar to the first one with the additional Helium burning products.

## 3.2 Structure of an AGB Star

As the star arrives on the AGB phase it has a very tiny degenerate core, for stars like our sun the core will be about Earth size. Most of the volume of the star is taken by a huge convective envelope. The envelope can pulsate or change in composition as a result of what goes on inside the star, while the central small and very dense region around the core is where nuclear processes and stellar evolution occurs. Most models Tuchman et al. 1983 [129] like the idea that the evolution of the intermediate mass stars at the AGB phase depends on how the mass of the core change or evolves, and in such a situation the core mass evolves independently from the envelope mass. Therefore hydrogen and helium shell-layers near the core are very important when modeling the structure of an AGB star, because it is in these areas near the core where most of the energy is generated drives entire evolution of an AGB star. The structural appearance of an AGB star resembles like the one shown below in figure 3.1. As we can see in figure 3.1; AGB stars have very extended envelopes that takes up the whole star volume, while the inner regions are dense hot and small. The envelopes of AGB stars develop convective currents because they are cool, while the inner regions are hot, this causes hot material to rise while the colder material sinks. Looking further on figure 3.1 we can immediately notice that about half of the of the mass of the star is contained inside a small region that is as small as 10% the size of the whole star. The radius of the star at the base of the convective core at radius is about $2.5R_{\odot}$ with the mass the core that is about $0.6M_{\odot}$; The total mass ($1M_{\odot}$) is

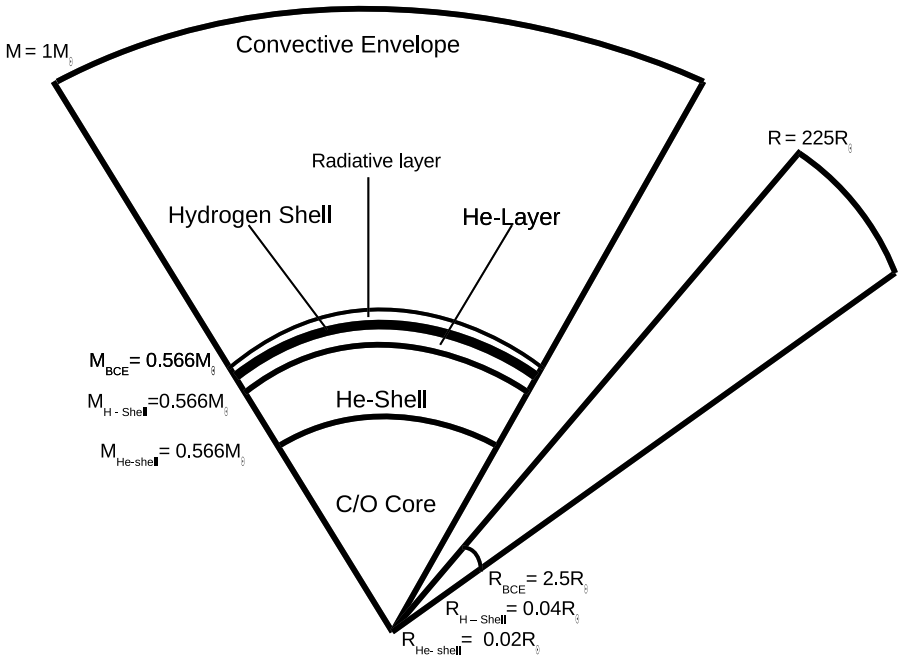


Figure 3.1: A model showing the interior structure of a $1M_{\odot}$ star. The regions of the star are shown on the left with mass variation as function of distance from the center. The extent of the envelope is shown on the right. $M_{bce}$ is indicates the mass at the base of the convective envelope, $M_{He-shell}$ and $M_{H-shell}$ are the masses at the middle of the hydrogen and helium burning shells respectively. Masses and radii adapted from Lattanzio & Woods 2004 [45]

at a radius of $225R_{\odot}$ far away from from the center. Thus a typical AGB star has a very small dense core where energy generation occurs, and a very large convective envelope.

There is also a radiative layer between the envelope's convective zone and the hydrogen shell. The existence of a radiative layer makes it possible for the CO - core mass to evolve independent of the mass of the envelope. This layer is very important in the calculations of stellar evolution of AGB because this radiation buffer zone allows the energy generated by the core to be absorbed within the H-shell. Hence the inner regions below the radiative layer can be modeled independent of the convective envelope. In low mass stars the radiative layer is prominent because of low core

temperatures and small convective zone that allows such separation. However the situation is a bit different when considering high mass stars because they posses very deep convective envelopes and very hot C-O cores. This means that the inner regions below the hydrogen shell and the convective envelope are not clearly separable. Thus in high mass stars the radiative layer can disappear completely because material from the deep envelopes can easily be mixed into the layers below the hydrogen layer causing the convective currents below this layer near the core. More over since the CO-core is very hot for high mass stars the energy it generates during contraction makes it possible for hydrogen layer to be pushed pass the region where radiation layer exist. There are debates about the inclusion of this layer in high mass AGB stars. In those calculations that includes the effects of radiative layer in high mass stars it is a common practice to include some mechanism that causes convective envelope not to penetrate beyond the hydrogen layer. In that scenario the mass loss is one mechanism considered because when the star losses mass on the outside, the convective envelope will decrease making it feasible for the radiative layer to re-appear. Thus theories suggest that an AGB star with high mass star have to lose more mass through the envelope in-order for the radiative layer to exist.

Then if we assume that in all AGB stars the core is the main driver of the evolution of the star and has to evolve independently, the inclusion of mass loss on the outside have critical influence on the internal evolution of the core and maybe the entire star. This is a big challenge facing the models to date because the mass loss formalism is yet to be found. The mass loss mechanism by AGB star is not known, observations suggest that the dust forming on the outside can drive mass loss because of radiation pressure on dust grains. So the presence of dust around AGB stars have influence on their internal evolution. In fact giving a structure like the one in figure 3.1 is very simplified because there is no inclusion of circumstellar dust shell and what at what parts of the convective envelope does the atmosphere develop. So in the next section

atmosphere of an AGB star is presented in-order to show how it re-shapes the entire structure of these stars.

## 3.3 Atmospheres of AGB stars

In general the atmosphere of an AGB star can be defined as a region where most of the electromagnetic emission that is observed in the stellar spectrum originates (Gustafsson and Hö fner, 2004, in Chapter 4 of [45]). The atmosphere of an AGB stars can be defined to be the region above the convective envelope that is warm enough that molecules can form, the rate of molecular condensation should allow for the formation molecules like CO, $H_2O$,SiO, CN, silcates etc. It is the presence of these molecules that determines the spectral appearance of these AGB star. The material in this region is less bound by gravity, as a result pulsations must be originating at layers below the atmosphere. Shock waves may develop and at high altitudes dust grain may form in the post shock gas. The gas velocities appears reach escape speed under the conditions that the radiation pressure on forming grains drives material transport out from the star. The exact limits of the dimensions of the atmosphere depends on the model used, for simplicity lets assume an idea by Th. Le Bertre et al. 1997 [83] shown in figure 3.2. In this diagram the atmosphere is defined to be the region between the hot less dense convective envelope and the cool circumstellar dusty envelope before the ISM. The chemical composition of the atmosphere of an AGB star is largely dependent on how much material was originally present and also how much dredge-up material get mixed by convection currents from the interior of the star. So the atmosphere is dynamic in composition. As the star evolves on the AGB, some elements like carbon are expected to increase in the atmosphere because of dredge up events during thermal pulse.

AGB stars are born from oxygen-rich environments because their early atmospheres

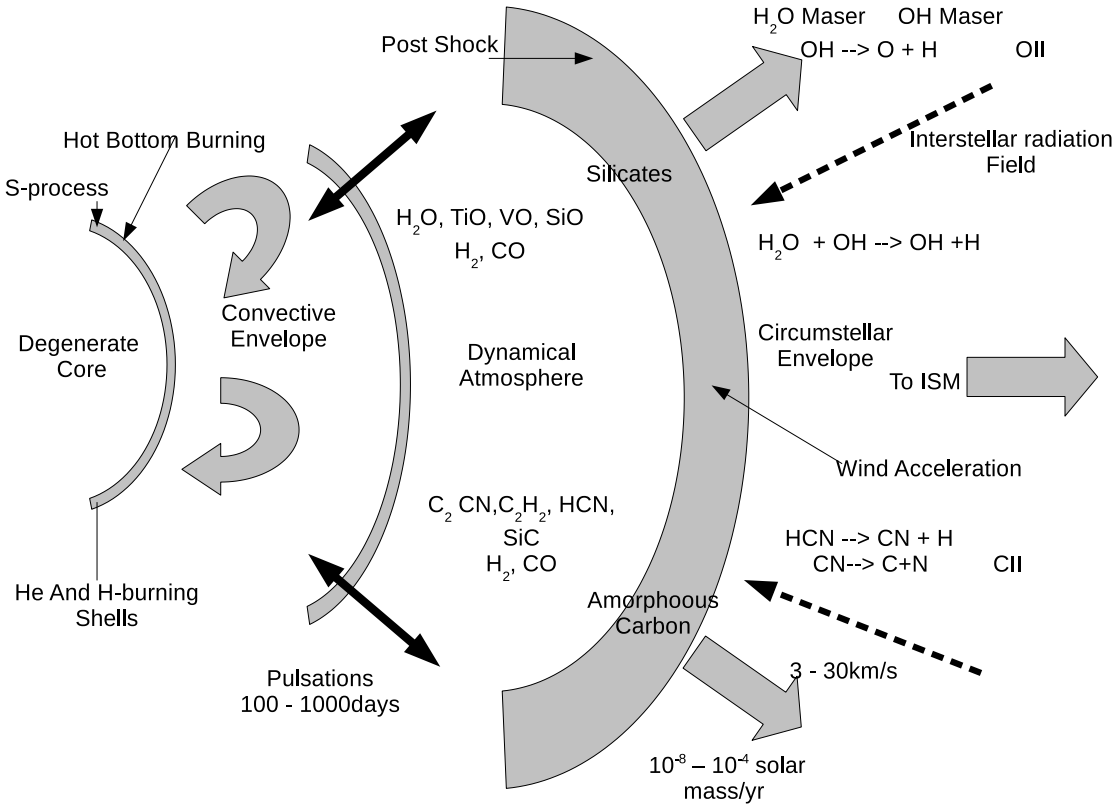


Figure 3.2: The internal structure of an AGB star showing four regions: the degenerate core, the convective envelope, the atmosphere and circumstellar envelope in terms of their expected chemical compositions. Other sub-regions such as s-process site, H-shell, He shell are also indicated.

have more oxygen than carbon. Carbon is locked mostly as CO such that there is more oxygen in the atmosphere. There is more carbon near the core where shell burning occurs than in the outer layers. Therefore the atmospheres of newly born AGB stars are by default oxygen-rich. During the AGB phase the outer layers of the star expand and cool and thus become opaque and convective. Convection extends deep into the nuclear burning shells and therefore carry newly-formed elements up into the star surface which becomes enriched with these nuclear burning products, especially carbon, nitrogen in cases where HBB dominates. In some stars this continues sufficiently long for the carbon abundance to exceed that of oxygen, and their atmospheres change from oxygen-rich to carbon-rich (Iben, 1965 [62]; Sugimoto &

Nomad, 1975). The stars that have more carbon relative to oxygen in their atmospheres are termed Carbon rich stars, and those with more oxygen they are called Oxygen-Rich stars. Carbon monoxide (CO) is the most strongly bound molecule in the atmospheres of cool stars, if C / O $< 1$ there is a surplus of oxygen atoms available to form oxygen-rich molecules such as Rio, on the other hand if C/O $> 1$ all Oxygen is bound up in CO, and surplus carbon atoms are available to form molecules (e.g. $C_2$, and CNN; Lattanzio & Wood, 2004). The observed atmospheric spectra from the atmospheres of two carbon rich AGB stars, (WBP46) and (HIV12179), is shown in figure 3.3. Notice the enhanced bands rich in s-process elements Zr, and Ti for this MS star. If there are an equal amount of molecular carbon and oxygen in the atmosphere, an S star forms. The formation of these lines offers a window of observations in spectroscopy because their presence confirm what theories predict about the synthesis of molecules in atmospheres of AGB stars. Furthermore, their presence gives the identifying signatures in the grouping of AGB, because theories suggest that as the star evolves in the AGB its chemistry changes. Oxygen rich Miras are believed to evolve into carbon rich stars because more carbon gets dredge-up during TP-AGB. The formation of CO molecule is important in the determination of mass loss rates since the CO emission lines can be used to detect the out flow velocities of the gas that is used to estimate the mass loss rates in AGB stars. The presence of emission lines (as well as absorption) is because atoms absorb radiation form the star and they emit light at different wave bands e.g, radio, far infrared, near etc. In oxygen rich stars water ($H_2O$) and hydroxide (OH) are more abundant, as a result some Miras are OH/ IR sources e.g. V 1300 Aql in Chapter 7. As a result the circumstellar OH maser emission lines due to infrared pumping of OH molecules is observed in the circumstellar envelopes of OH/IR rich Mira using OH 1612 MHz line emission e.g. Baud & Habing 1983. The occurrance of these emmision lines is used calculate the mass loss rates that are high enough (higher that those predicted by

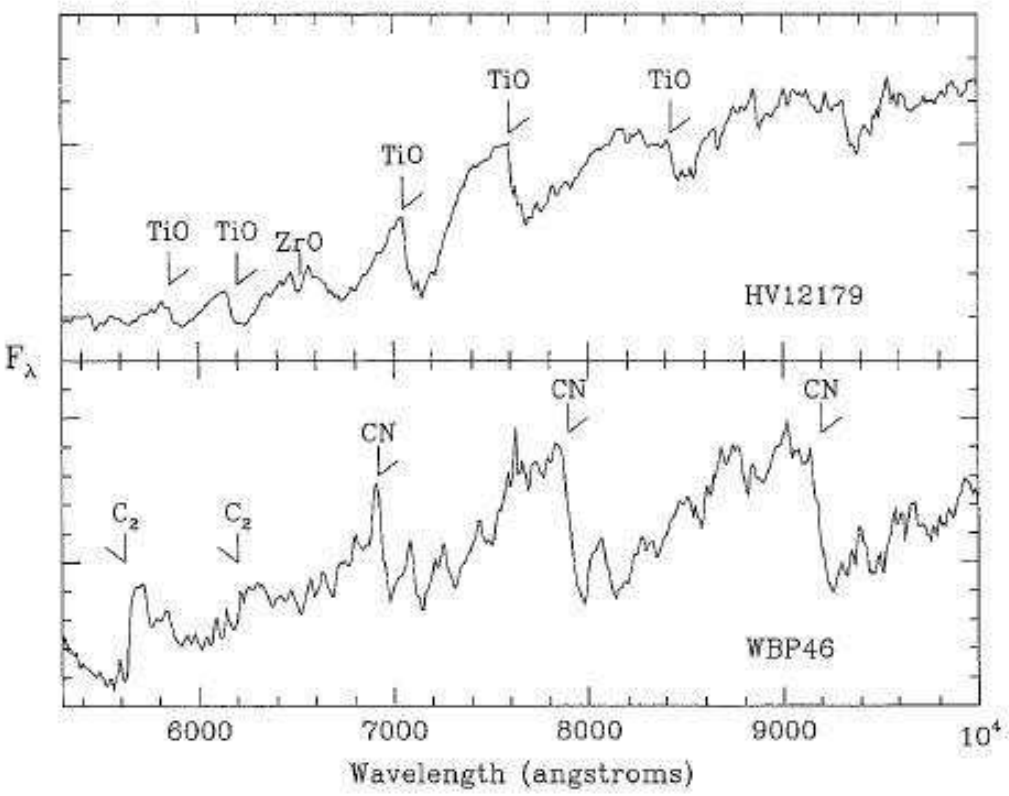


Figure 3.3: Spectra of an MS star (oxygen rich) HV12179 at the top panel and a carbon star WBP46 at the bottom panel. The oxygen rich candidates are dominated by TiO and ZrO while the carbon rich ones are dominated by $C_2$ and CN molecules. These stars are members of the LMC.

Reimers equation 4.14 in Chapter 4) to produce the superwind mass loss that occurs at the end of the AGB phase.

A complete picture of molecule formation and nucleosynthesis is beyond the scope of this project; it is a subject on its own. Lets now focus on pulsations of AGB stars because during AGB phase theories suggests that when the AGB stars lose mass, their envelopes pulsate leading to levitation of mater that can also be esential in driving of mass loss.

## 3.4 Thermally pulsing AGB

Helium burning in the shell of an AGB star does not proceed smoothly, it is subject to thermal instabilities that causes the luminosity to vary periodically. This luminosity variations was first reported by the work of Schwarzschild & Härm in 1965 (Schwarzschild et al. 1965 [120]), a year later, Weight et al. 1966[154] performed calculations of thermal instabilities.

At some point in the AGB star's evolution when the helium burning rates are very low such that the hydrogen burning shell becomes the main source of energy in star, the mass of helium in the layer above He-shell will start to grow (see figure 3.1. As the mass of the He-layer increases it compresses the He-shell such the gas at the base of the dormant He-shell becomes hotter and re-ignites helium burning in the shell. Eventually the He-shell luminosity starts to oscillate with the increase in Helium shell luminosity leading to a near simultaneous decline in H-shell luminosity. The spikes in the overall luminosity as a result of the brief periods of runaway helium shell burning are called Helium Shell flashes often called a Thermal Pulses. The energy released during the He-flash causes the He-layer to expand pushing the H-shell to cool and extinguish the Hydrogen burning, at this point Helium burning dominates. Eventually the He-burning shell cools with reaction rates going down; at the very same time the H-shell compresses back and the whole process repeats. The star has entered a stage of burning Helium in the shell that switches on and off, causing the total luminosity to change and vary over time as shown by the models below of $2.5M_{\odot}$ in figure 3.4.

What is immediately noticed in figure 3.4 is that the time spent by intermediate mass stars at the AGB phase is roughly about $10^6$ years and also that low mass intermediate mass stars have low AGB luminosities than high mass ones. What is also shown is that the core mass of low mass AGB stars increases with an increase average surface luminosity once the thermal pulses have been established (compare

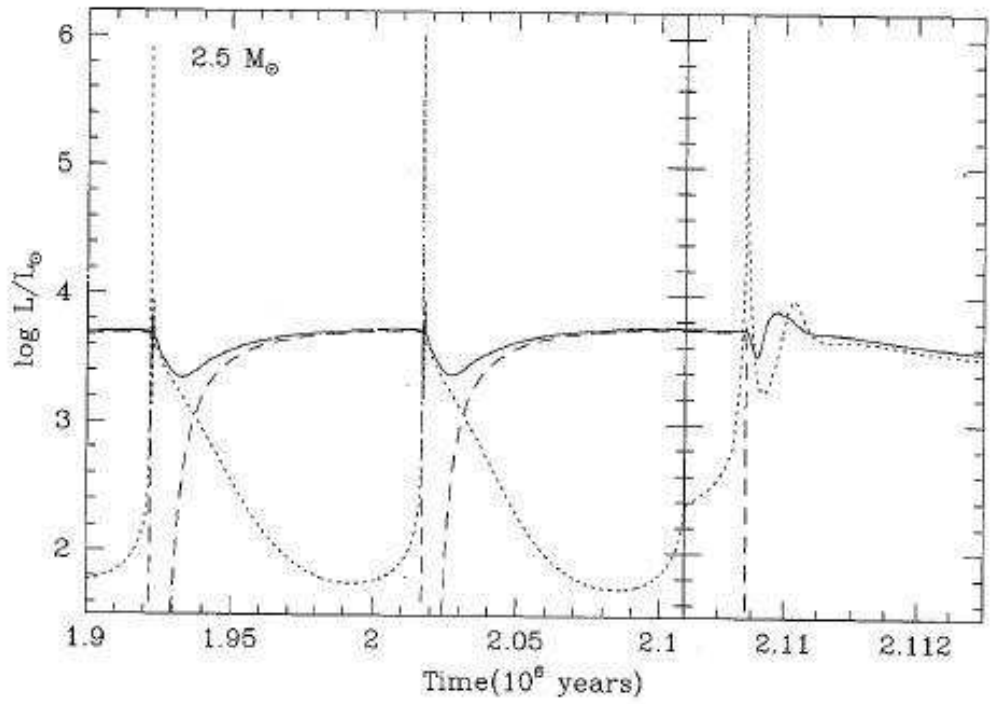


Figure 3.4: The surface luminosity variation of thermally pulsating AGB stars of mass $2.5M_{\odot}$ . Luminosity (solid line), the H-burning shell luminosity (a dash line) are plotted against the time for three consecutive thermal pulses. The right panel shows the thermal pulse in more details.

1 and 2.5 $M_{\odot}$ luminosity increase in figure 3.5).

The plots indicates the early AGB phase in which hydrogen and helium shell luminosities are increasing before the onset of thermal pulsation. At each graph the thermal pulses tend to grow with luminosity as the star evolves on the AGB. When masses of the stars increases the thermal pulses get shorter over time and increases with luminosity, compare $1M_{\odot}$ and 5 $M_{\odot}$ star to see this trend. The evolution start when the luminosities of H-shell and He-shell are equal at early AGB until the luminosity extinguishes at planetary nebula. The initial time (t=0) corresponds to the time when the star enters AGB after Core-He exhaustion when He-luminosity dominates H-shell luminosity. (This model calculation of thermal pulse variations at different masses is from Vassiliadis, and Wood, 1993 [137])

At the pulse, He-luminosity spikes and simultaneously H-shell is extinguished.

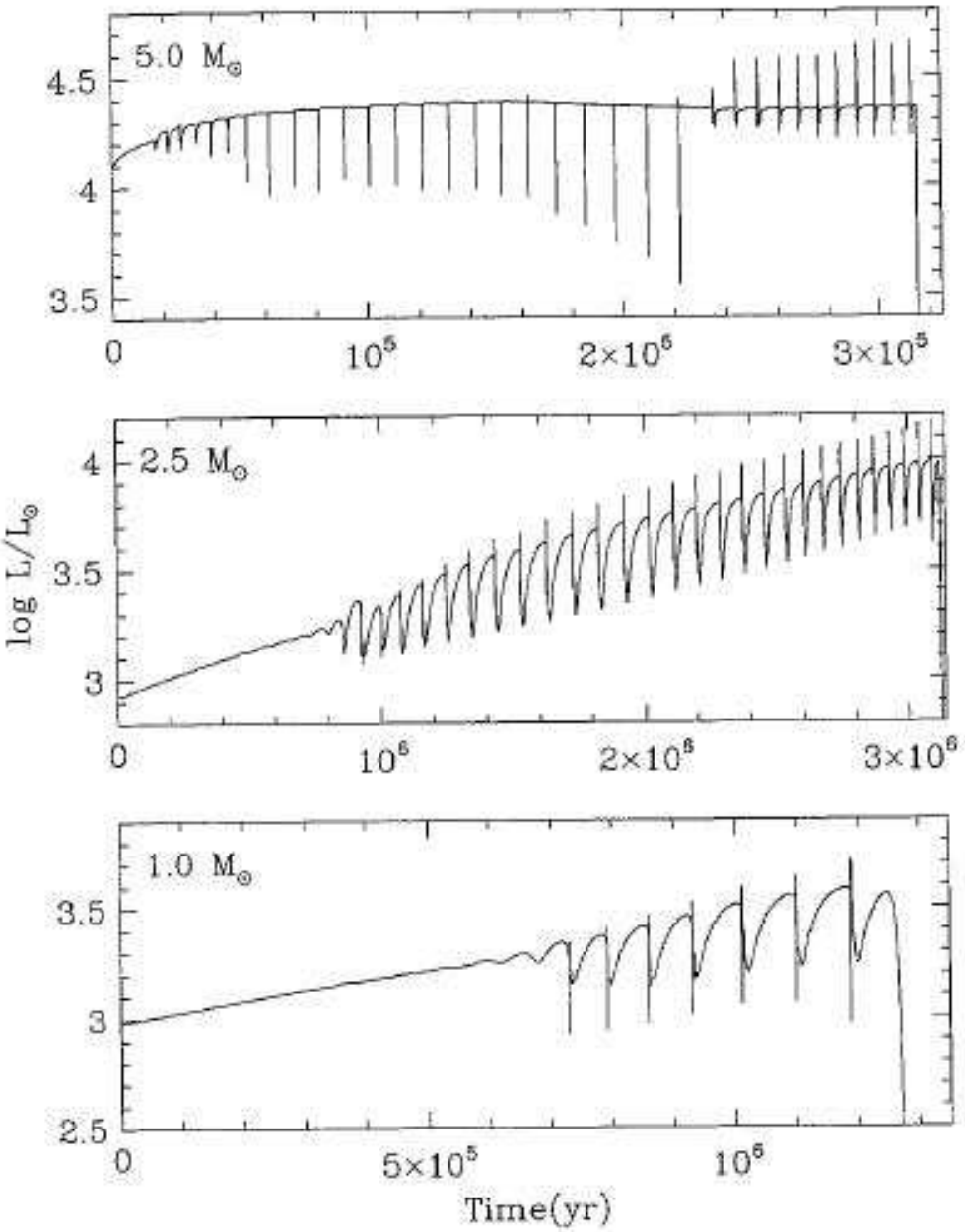


Figure 3.5: The surface luminosity variation of thermally pulsing AGB star of masses 1, 2 and $5M_{\odot}$ modeled by initial composition Y = 0.25 and Z = 0.016, ref [45].

During the decline phase of the luminosity, He-shell dominates the star's luminosity and is decreasing over a gradually increasing H-shell luminosity. At the minimum luminosity both H and He-shell luminosities are equal. During the recovery phase the He-luminosity continues to decrease while H-shell gradually increase until a steady $'$maximum$'$ value is reached. The maximum luminosity reached is called quiescent

maximum luminosity, whereas the region between two thermal pulses is called quiescent evolutionary phase.

The overall behavior of surface luminosity variation when the star is thermally pulsating, is such that, a thermal pulse cycle consist of the spike in luminosity that is followed by a slow decline until a minimum point, and then there is a slow recovery until a maximum luminosity is reached before the next spike occurs. This behavior in luminosity when the star having thermal pulses is shown details in figure 3.4

### 3.4.1 The effect of Core Mass on Thermal Pulses

The evolution of an intermediate mass star at the AGB phase depends on the core mass evolution, therefore in this section we would like to make a connection as to how this correlation occurs.In 1970 Paczynski and Uus [102] showed that there is a linear relationship between the core mass and the luminosity, this correlation can be represented as follows

$$L = 52950(M_c - 0.522) \tag{3.1}$$

where L and $M_c$ are measured in solar units. Equation 3.1 seems to works well to for stars that are less than $3M_\odot$ but it fails to explain the nearly constant luminosity like the one presented by a $5M_\odot$ star (Blöker & Schoenberner, 1991 [11]; Bessel & Wood, 1983 [8]).

At the onset of AGB, the luminosity of the star increases linearly as the star evolves at an early AGB phase (E-AGB) (refer to figure 3.5. In the E-AGB phase, He-shell dominates the luminosity while there is a steady increase in H-shell luminosity. The H-shell luminosity increases until it is the same as the He-shell luminosity. The H-shell stays dormant while the H-shell dominates the luminosity, up until the He-shell re-ignites with a sharp (pulse like) decline in the H-shell luminosity. This

period of luminosity increase varies with mass, it is shorter for high mass stars than for low mass stars, (notice this trend in Figure 3.2). After the star starts to pulsate , the maximum luminosity of each pulse grows rapidly with pulse number until an approximate limiting value is reached. Higher mass stars less than $3M_{\odot}$ have short pulse period than low mass ones,however for those stars between $3 - 8M_{\odot}$ the interpulse period shows a longer time occurs at almost constant luminosity, (compare thermal pulse of $5M_{\odot}$ to the 1and$2.5M_{\odot}$ in figure 3.2 at times less than $2 \times 10^5$ yrs). Therefore the interpulse period also breakdown also for those stars higher than $3M_{\odot}$. The shortening in the interpulse period ($T_{interpulse}$ can be explained by the relationship between the interpuls period and the core mass given by Paczsyski Paczynski in 1975 (Paczynski et al. 1975 [103] as

$$log(T_{interpulse}) = 3.05 - 4.5(M_{core} - 1) \tag{3.2}$$

Such a breakdown on the interpulse period at higher mass is because higher mass stars have deep and larger convective envelopes that makes the whole star to be involve when its thermally pulsating, there is very little variation in surface luminosity over a thermal cycle when convection zone penetrates near the H-shell. Higher mass star do not develop a radiative layer between the H-shell burning and the convective zone; and therefore the simple dependence of AGB's stellar evolution on mass alone breaks. Thus high mass stars shows longer quiescent period and the luminosity is almost constant at the onset of thermal pulses, whereas at later stages when the mass of the envelope have been reduced (maybe by mass loss) the radiative layer re-appears and the behavior becomes similar to the low mass star, notice the reappearance of spikes at times greater than $2 \times 10^5$ years on a $5M_{\odot}$ model in Figure 3.5.

## 3.5 Production of Carbon ($^{12}_{6}$C) during thermal pulsing AGB phase

At the onset of thermal pulses, the sudden increase in energy production by the He-shell creates a new intershell convection zone (ISZ) between the H-shell and the He-shell, this layer is believed to last a few hundred years depending on the mass of the core As the thermal pulse strength grows over time, the convective envelope deepens more onto layers beyond the H-shell (in more massive stars will emerge) and then will extend down onto an area where Carbon ($^{12}_{6}$C) is synthesized. The most possible area above He-shell where temperatures are high enough to make carbon, the region between H-shel and He-shell can have carbon about ten times higher than the abundances found at the atmosphere. The Third dredge-up occurs when this carbon is mixed into the surface of convective envelope by convection currents.

The off phase correspond to a period before thermal pulse begins when H-shell luminosity ($L_H$) dominates He shell luminosity ($L_{He}$). When He-shell switches on, $L_{He}$ dominates over $L_H$, the ICZ appears. As the power goes down (during the decline of $L_{He}$ when $L_H$ is still down not increasing), the ISZ disappears. The dredge-up occurs when the energy released by the core in response to the He-flash hits the envelope base causing it to move inward, and the hot material gets up mixed into the convective layer. Then hydrogen shell will start to heat-up and reignite causing the total luminosity gradually increase until the star enters the quiescent stage, notice that the convective envelope is retreating back during quiescent evolution. The He-shell heats up again and the the off phase of H shell is set and the process repeats.

As more and more carbon is enriching the surface of the convective envelope its abundances in atmosphere of the star gradually increases. More and more carbon is deposited on the surface its surface abundance when the star is undergoing thermal pulses, at the very same time, the mass of the C-O core is growing as well because, every time He shell is set in making more carbon and oxygen, more mass rains down

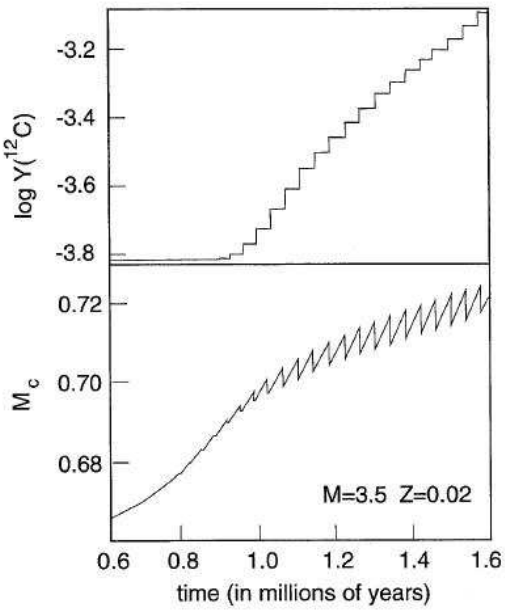


Figure 3.6: *Top panel*: CO core mass and *Bottom panel*:the abundance carbon ($^{12}_{6}$C) during the AGB evolution of a 3.5M$_\odot$ model with Z = 0.002. Y is the mass fraction (X) of carbon divided by the mass number (A = 24). As carbon abundances increases in the atmosphere during dredge-up the mas of the core also increases because the He - burning shell deposits more carbon as well.

to the core. The increase in core mass due to helium burning shell is shown is in a 3.5 M$_\odot$ model(ref: Lattanzio & Wood 2004 [45] in figure 3.6.

When carbon reaches the surface of the convective envelope it changes the chemistry of the atmosphere of the AGB star. If Carbon abundance is more than that of oxygen a carbon AGB star is born, whereas if oxygen dominates carbon an oxygen rich AGB star results. The chemistry of the atmosphere of AGB stars is presented in section 3.6 A lot of work in this area covers modeling the quiescence phase using the following stellar parameters, mettalicities on the basis of CNO, envelope mass, mass loss rates and mixing length e.g Wagenhuber & Groenewegen 1998 [138] who showed that for intermediate mass star in the range $0.8 - 7M_\odot$ the luminosity -core mass is given by

$$
\begin{aligned}
L = 18160 + 3980 log\tfrac{Z}{0.02}(M_c - 0.4468) + \quad (\mathbf{A}) \\
+[10^{2.705+1.649M_c} \quad (\mathbf{B}) \\
\times 10^{0.0237(\alpha-1.447)M_{c,0}^2 \; M_{env}^2(1-e^{\delta M_c/0.01})} \quad (\mathbf{C})] \\
-10^{3.529-(M_{c,0}-0.4468)\delta M_c/0.01} \quad (\mathbf{D})
\end{aligned}
\tag{3.3}
$$

where $\alpha$ is the mixing length parameter, that accounts for the influence of hot bottom burning (see section 3.6.4 below), $\alpha \sim [1.5 - 2, 75]$. This equation encompases most of the relationships of luminosity core mass relations under general considerations in AGB stars based on synthetic calculations. So I will briefly describe each term separately to show its influence at AGB stars: Term (**A**) represents the clasical Paczynski relation given by 3.1, it applies to core masses in the range: $0.6M_{\odot} \leq M_{core} \leq 095M_{\odot}$. Term (**B**) added, is the correction term to (**B**) term (**A**) for core masses $M_{core} \geq 095M_{\odot}$, term (**C**) is the correction term that accounts for hot bottom burning for those stars that are larger than $0.95M_{\odot}$ as a function of the envelope mass. Term (**D**) gives the correction to the luminosity in order to mimic the subluminous deep and steep evolution typical of the first thermal pulse.

## 3.6 Nucleosynthesis at AGB phase

The observations of AGB stars indicates that their atmospheres are rich in chemical elements that are produced within the hot interior regions where nuclear synthesis occurs. The dredge up of elements to the these atmospheres of AGB stars results from the inward penetration of the convective envelope reaching layers of the star where nuclear reactions occur, and elements get dregde up into the surface. The sites of nucleosynthesis in AGB stars is provided by the Hydrogen and Helium burning shells in association with neutron captures around interfaces where nuclear burning can occur. During thermal pulses more material gets dredge-up into the surface. Thus

when dealing with AGB surface enrichment during thermal pulse, we have to consider the effect of subsequent passages that the dredge up material has to go through until it reaches the surface. If the convective zone has penetrated deeper than the He-shell, when it retreats (during the next interpulse) more material coming from both H-shell and He-shell gets dredge-up to the surface.

amongst other elements that reaches the gets dredged-up to the surface, carbon is the abundance is important in determing the chemistry of the star. All stars are born with oxygen rich atmospheres.However, when carbon reaches the surface of the convective envelope it changes the chemistry of the atmosphere of the AGB star. If carbon abundance is more than that of oxygen a carbon AGB star is born, whereas if oxygen dominates carbon an oxygen rich AGB star results. The production of carbon when the star is thermally pulsing is coveered extensively in Appendix A.3 section § A.3.1

Lets look at how each of the nuclear synthesis site contributes to the surface enrichment.

### 3.6.1 Hydrogen - shell burning site

In Hydrogen burning shell, ${}^{4}_{2}\mathrm{He}$ production gets processed through pp chain reactions and CNO cycle as discussed in Chapter 2. Amongst the other products of the H-burning that gets mixed to the surface (discussed on the First Dredge Up (FDU)), there are three most common nuclides observed in high abundances in the atmospheres of AGB stars, namely ${}^{17}\mathrm{O}, {}^{13}\mathrm{C}, {}^{14}\mathrm{N}$. The ${}^{13}_{6}\mathrm{C}$ nuclei is synthesized by CNO cycle by these reactions,

$$ {}^{12}_{6}\mathrm{C} + {}^{1}_{1}\mathrm{H} \rightarrow {}^{13}_{7}\mathrm{N} $$

$$ {}^{13}_{7}\mathrm{N} \rightarrow {}^{13}_{6}\mathrm{C} + e + \nu_e $$

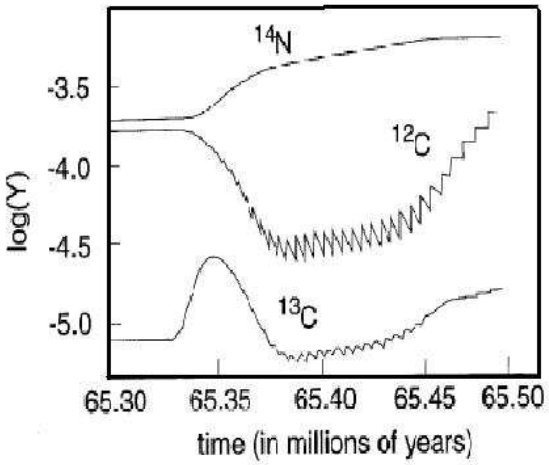


Figure 3.7: The variation of surface ratio of $^{12}C/^{13}C$ during AGB evolution of $6M_{\odot}$ model with metallicity Z = 0.02

From the above reactions $^{4}_{2}$He gets used up and $^{13}_{6}$C is over produced, the ratios of $^{12}_{6}C/^{13}_{6}C$ decreases to typical values around 20 (Dearborn et al. 1992 [22]) in the atmospheres.

As an example lets look at the variation of $^{12}_{6}C/^{13}_{6}C$ ratios that is shown in figure 3.7 for a $6M_{\odot}$ model.

In figure 3.7, it is clear that at early AGB phase the star will have the ratio $^{12}C/^{13}C$ about the same, however as evolution proceeds $^{13}C$ increases the whole ratio declines. The increase in $^{12}C/^{13}C$ at end of AGB indicate more $^{12}C$ content gets added into the surface, maybe as result of Hot bottom burning to be discussed in the next section § 3.6.4.

The synthesis of $^{17}_{8}$O by the CNO cycle occurs when $^{16}_{8}$O gets destroyed in the following reactions,

$$^{16}_{8}O + ^{1}_{1}H \rightarrow ^{17}_{9}F + \gamma$$

$$^{17}_{9}F \rightarrow ^{17}_{8}O + e^{+} + \nu_{e}$$

$$^{17}_{8}O + ^{1}_{1}H \rightarrow ^{14}_{7}N + ^{4}_{2}He.$$

Thefore we can see that the ratio of $^{16}_{8}$O / $^{17}_{8}$C decreases, typical values from observaions are around 20.

$^{14}$N is produced in high abundances by CNO cycle while its isotope $^{15}$N is less synthesized in the CNO cycle. The observational ratios shows $^{14}$N increase by a factor of 4 and $^{15}$N decreases by factor between 2&3(Dearbon, 1992 [22], El Eid & Champain, 1995 [26]).

The composition of the star at this point reflects the initial composition that the star had plus the additional compositions by the first dredge up (Lattanzio & Wood 2004[45]. The changes produced by the FDU again depends on mass of the star (especially masses $< 2.5M_{\odot}$) and the initial composition of the envelope. Thus in the H-shell burning nucleosynthesis of AGB stars, an increase in the abundances of $^{17}$O, $^{13}$C, $^{14}$N and some $^{14}$He is associated with a decrease in abundances of $^{12}$C, $^{16}$O, $^{18}$O (Dearbon, 1992 [22], El Eid and Champain 1995 [26], Lattanzio & Boothroyd, 1997 [80])

### 3.6.2 Helium shell burning site

Another nucleosynthesis site is the Helium burning shell, where the convective envelope can penetrate onto a region that has completely burn all of the hydrogen, resulting into the material rich in Helium to be added to the surface. Earlier in the evolution of an intermediate mass AGB stars of about $4M_{\odot}$ a second dredge can occur, that will cause material processed by triple alpha process to enrich the surface. The added materials by the He-burning shell may include, more

$^{4}$H and $^{14}$N and additional $^{16}$O, $^{19}$F, $^{22}$Ne, $^{23}$Na, $^{26}$Mg, $^{25}$Mg, $^{27}$Al.

All these nuclei are products of Helium burning shell, and for most of them, the observational abundances in their atmospheres of the AGB stars are under a lot of debates, so no formidable trend has been established yet.

### 3.6.3 Helium shell producing s-process elements

We have learned in the previous sections that elements heavier than hydrogen and helium were first created inside the stars, through the nuclear fusion process that takes place initially inside stellar core's and subsequently at the shells (H-shell and He-shell) around the core. Helium and Hydrogen are by far the most abundant elements in the universe, this is reflected by observational data shown in figure 3.8 in which relative solar abundances of atoms in the sun's photosphere are shown (Sauval & Grevasse 1996 [1]). The observational data was first shown by Russel in 1929 [111], and in the 50's more data came from Goldberg, Aller& Muller 1957[43]. The history behind the construction of abundance curves is a subject beyond the scope of this thesis, we can point out pioneering work by Goldschimidt et. al 1937 and later refinements by work of Sue and Urey et al. 1956. The work of Burbidge, Burbidge, Hoyle & Fowler in 1957 [18],(hereafter($B^2HF$)′) in the famous classical paper ′Synthesis of elements inside the stars, showed for the first time how how heavier elements are produced inside the stars. And these authors($B^2HF$) argued that that the neutron capture was responsible for the production of nuclei heavier nuclei than stable $^{56}$Fe in AGB stars. The atmospheres of evolved TP-AGB stars of spectral type MS, S, SC and C types shows the presence of Techtenium isotope $^{99}_{43}$Tc (e.g. Merrill et al. 1956 [96], ) Techtenium has a lifetime of about 4.2 million years that correspond very well with the AGB phase and $^{99}_{43}$Tc and isotope of Tc has a lifetime of about 0.2 million years which strongly suggests that this isotope must have been dredged up from the surface of the AGB star very recently in the star's history.

Figure 3.8 indicates that in the solar neighborhood, helium and hydrogen are by far the abundant nuclei, the elements have been synthesized during the early stages after the Big Bang. All other elements shows low abundances, and they were made inside stars. The nuclei produced before iron (Fe) are processed inside stars during Hydrogen and Helium burning in the core or in the shells, while all elements after Fe

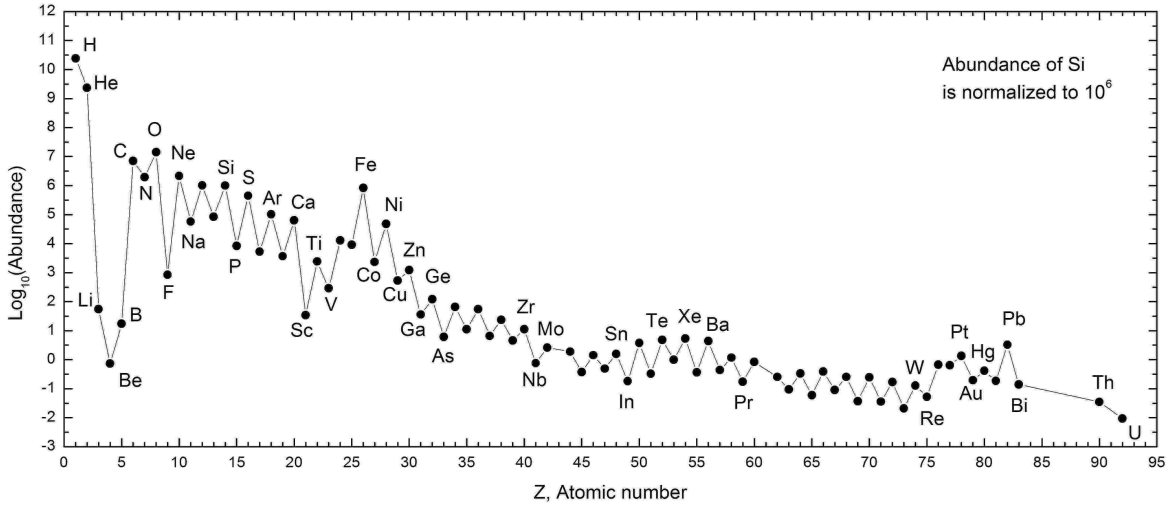


Figure 3.8: Atomic abundances in the Sun's photosphere, all values are normalized to $10^{12}$ hydrogen atoms.

formed through $s$ and $r$-processes presumable in the He-shell. Lithium in the solar spectra poses a problem by being lower than the one observed in the meteorites, this posses disagreement of models with observations.

The neutron capture mechanism is a slow process (hence s-process) in which a neutron can react with nuclei heavier than ${}^{12}_{6}\mathrm{C}$ in order to produce some elements heavier than ${}^{56}_{26}\mathrm{Fe}$. Fusion processes that involves alpha capture (i.e carbon burning or oxygen burning see section § A.3.1) in creating heavier nuclei beyond ${}^{56}\mathrm{Fe}$ are very harder for low mass AGB stars ($< 4M_{\odot}$) because these reactions require a lot of energy for a alpha particle to overcome a high coulomb barrier to interact with iron nucleus. If the interior of a star can generate enough energy like in high mass stars $> 12M_{\odot}$ a rapid neutron capture (r-process) can occur in which a high mass nucleus (like${}^{22}_{10}\mathrm{Ne}$) can quickly absorb a neutron that results in the formation of heavier nuclei. The r-process is thought to be responsible for the formation of the nuclei such as S, Ca, Ti, Ti (e.g. B$^2$HF, 1957), however in intermediate mass stars the conditions for r-process are not met, only the beta decays are more frequent and the s-processes dominate the production of heavy elements.

The s process occurs in stellar environments with low number densities of neutrons ($\sim 10^7 \mathrm{cm}^{-3}$), in which beta decays ($\beta^{\pm}$) rates are very high in producing heavier nuclei. A neutron is slowly injected over a long time (100 years - $10^5$ years) onto a nuclei ${}^{A}_{Z}\mathrm{X}$ via the reactions

$$ {}^{A}_{Z}\mathrm{X} \rightarrow {}^{A+1}_{Z}\mathrm{X} $$

and new nucleus can unstable under $\beta$ decay

$$ {}^{A+1}_{Z}\mathrm{X} \rightarrow {}^{A+1}_{Z+1}\mathrm{X} + e^- + \bar{\nu_e} + \gamma \qquad \beta^- $$

$$ {}^{A+1}_{Z}\mathrm{X} \rightarrow {}^{A+1}_{Z-1}\mathrm{X} + e^+ + \nu_e + \gamma \qquad \beta^+ $$

The s–process requires the sources of neutrons in AGB stars, and pre-existence of nuclei synthesized by He-shell burning until Fe is reached. It was believed that there are were two possible sources of neutrons in the AGB stars, in the first case when

(i)

$$ {}^{22}_{10}\mathrm{Ne} + {}^{4}_{2}\mathrm{He} \rightarrow {}^{25}_{12}\mathrm{Mg} + n $$

$$ shorthand : {}^{22}_{10}\mathrm{Ne}(\alpha, n)\ {}^{25}_{12}\mathrm{Mg} $$

.

This reaction requires the production ${}^{22}_{10}\mathrm{Ne}$ that can be synthesized via high abundances of ${}^{14}_{7}\mathrm{N}$ that was created during the CNO cycle. The intershell region between He-shell and H-shell where s process occurs can be quite rich in CNO elements like ${}^{4}_{2}\mathrm{He}(\alpha), {}^{14}_{7}\mathrm{N}$ and also the products of He-burning. Cycle I of the CNO cycles is the first one to occur and favors high production of ${}^{14}_{7}\mathrm{N}$ shown in section A.1. And during the pulse period when the He-shell is providing more energy at the intershell region such that the temperatures are high such for the ${}^{4}\mathrm{He}$ to interact with ${}^{14}\mathrm{N}$,

$$^{14}_{7}\mathrm{N} + ^{4}_{2}\mathrm{He} \rightarrow ^{18}_{9}\mathrm{F} + \gamma$$

$$^{14}_{7}\mathrm{N}(\alpha,\gamma)\ ^{18}_{9}\mathrm{F}$$

the unstable $^{18}_{9}$F can undergo a $\beta^+$ decay to produce $^{18}_{8}$O,

$$^{18}_{9}\mathrm{F} \rightarrow ^{18}_{8}\mathrm{O} + e^+ + \nu_e + \gamma :$$

$$^{18}_{9}\mathrm{F}(\beta^+,\gamma)\ ^{18}_{8}\mathrm{O}$$

and $^{18}_{8}$O reacts with abundant $^{4}_{2}$He to produce $^{22}_{10}$Ne, $^{18}_{8}\mathrm{O} + ^{4}_{2}\mathrm{He} \rightarrow ^{22}_{10}\mathrm{Ne} + \gamma$.
If the temperature can get high to about 300 million K (maybe at the end of the TP-AGB as models suggests) then a neutron can be synthesized by

$$^{22}_{10}\mathrm{Ne}(\alpha,n)^{25}_{12}\mathrm{Mg}$$

However in 1986 the observation of $^{25}_{12}$Mg in low mass (M$< 2M_{\odot}$) supergiant stars (MS and S-stars) that are known to have s-process elements in there spectra and also are undergoing He burning (correlated by the increase in $^{12}C$ a product of $3\alpha$ process) showed no evidence of expected $^{25}_{12}$Mg (Smith & Lambert 1986 [121]). These results ruled out the $^{22}_{10}\mathrm{Ne}(\alpha,n)\ ^{25}_{12}\mathrm{Mg}$ as the source of the s-process.

(ii) The other possible way of producing neutrons as suggested by work of(Smith & Lambert 1986 [121]) is by the reaction,

$^{13}_{6}\mathrm{C}(\alpha,n)^{16}_{8}\mathrm{O}$,

this reaction occurs at low temperatures of about 100 million K. This work was also able to show that as carbon gets dredge-up during thermal pulse causing an M star to change into becoming an S star, their result agreed very well with a trend (M -MS and S) predicted by models ofIben et al. 1983 [64], herefter Iben 1983. These models(Iben 1983) were able to show that during TP-AGB a star can change from

being an M star (oxygen rich) to being a C stars by slow addition of carbon which can be correlated by an increase of ${}^{12}_{6}\mathrm{C}^{13}_{6}/\mathrm{C}$ as more ${}^{12}_{6}\mathrm{C}$ is added (carbon enrichments) an M-MS-S trend should appear. The observed ${}^{12}_{6}\mathrm{C}$ and s processes abundances (Tc detection) from the work of Smith & Lambert 1986 are in good agreement the models by Iben 1983 for low mass stars about $2M_{\odot}$ up until the the third dredge-up carbon enrichments. This means that ${}^{13}_{6}\mathrm{C}(\alpha, n){}^{16}_{8}\mathrm{O}$ is the possible s-process for low intermediate mass stars ($< 3M_{\odot}$) e.g. (Abia et al. 1999 [2]).

For high mass $> 4.5M_{\odot}$ intermediate mass stars, the models suffer limitations that there are few ${}^{13}_{6}\mathrm{C}$ from CNO cycle present in the intershell to account for the required number of neutrons to produce s-process elements, so if ${}^{13}_{6}\mathrm{C}(\alpha, n){}^{16}_{8}\mathrm{O}$ fails. Then the search for alternative methods of finding ${}^{13}_{6}\mathrm{C}$ for the s-process neutrons was initiated e.g Sackaman et al. 1980[113] and Iben 1982 [64], like injecting protons partially near the region rich in carbon burning.

The mechanism of mixing hydrogen(${}^{1}_{1}\mathrm{H}$) in the convective envelope with with carbon (${}^{12}_{6}\mathrm{C}$) in the hot intershell was initiated by the work of Sakaman 1980 [113] and Iben 1982. These authors proposed that during the interpulse of the third dredge up, when the core contracts, the intershell expands as a result of He-burning. Some parts of the hot intershell can overlap with the convective zone making a low temperature band to appear inside the intershell layer (see Figure 3.9). If the temperature inside this band gets lower to $\sim$ 1million K a slow down proton injection occurs, ${}^{1}_{1}\mathrm{H}$ will interact with ${}^{12}_{6}\mathrm{C}$ making ${}^{13}_{7}\mathrm{N}$ neutron . The unstable ${}^{13}_{7}\mathrm{N}$ can further decay by $\beta^{+}$ decay to produce${}^{13}_{6}\mathrm{C}$. ${}^{13}_{6}\mathrm{C}$ gets encapsulated by intershell convective zone during the next thermal pulse during which it can react with ${}^{4}_{2}\mathrm{He}$ present inside ISCZ releasing s-process neutrons and oxygen (${}^{16}_{6}\mathrm{O}$).

Figure 3.9shows how a ${}^{13}_{6}\mathrm{C}$ pocket is formed from a layer rich in ${}^{12}\mathrm{C}$ (previously formed ISCZ) if this layer overlap with a proton efficient convective envelope during dredge up after a third thermal pulse. The result of this overlap is the partial mixing

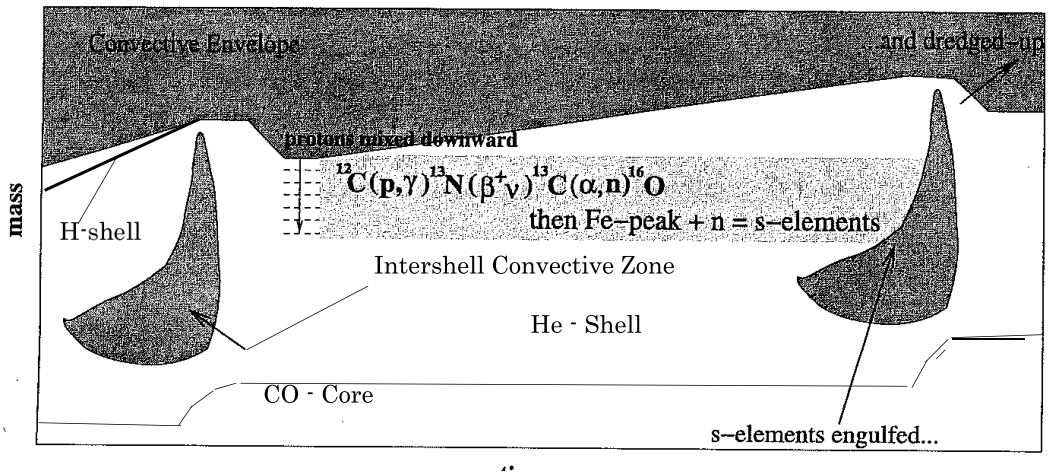


Figure 3.9: An intershell region between the penetrating convective envelope to the CO - core causing during conctaction causes dredge-up of elements synthesized by hydrogen and helium shell. The plot shows the evolution of mass (y- axis) over AGB time (x-axis) during two thermal pulses.

of protons with carbon at low temperatures making $^{13}$C via $\beta^+$ decay of $^{13}$N. $^{13}$C captures an $\alpha$ particle (remnants of previous ISCZ) when the temperatures gets higher to produce an s-process neutron with the production of $^{16}$O.

The $\alpha$ capture process of $^{13}_{6}$C is though to last about 10,000 years. The neutron gets released over this long time can interact with any Fe-peak element to form the 's-process pocket' that gets dredge-up after the pulse. The suggested reaction is

$$^{12}_{6}\mathrm{C}(p,\gamma)^{13}_{7}\mathrm{N}(\beta^{+},\nu_e)^{13}_{6}\mathrm{C}(\alpha,n)^{18}_{6}\mathrm{O}$$

This reaction creates $^{13}_{6}$C pockets that gets engulfed by the appearance of ISCZ between interpulse, and the synthesized s-processes nucleus gets dredge-up in the next thermal pulse during the usual 'dredge-up' after 'the power' down phase before H-shell ignites.

### 3.6.4 Hot Bottom Burning-HBB

Another site of nuclear synthesis in AGB stars can occur if the base of the convective envelope reaches deep hot regions hear the core such that it ignite and burn old nuclear material into new nuclei. This heating of the convective envelope can happen if the envelope reaches the top of the H-shell. VW98 Models predicts that if the base of the convective envelope reaches about 100 million K, HBB will happen. This processes was originally thought to occur in high mass stars between 4.5 and 7 $M_{\odot}$ AGB stars (Iben, 1976 [63]; Boothroyd, Sackmann & Waseerburg 1994 [14]), however the discovery of Li on low mass stars (Lambert & Smith, 1986, Lambert & Smith, 1990 [122]) in the Magellanic Clouds showed that hot bottom burning mostly depends on composition of the star and can extend to AGB stars as low as $2M_{\odot}$ with Z=0.

Lithium is produced in large quantities during HBB (Sackmann, Scalo, Despain & Ulrich, 1975 [115]) and it is a very important in completion of the PPI and PPII productions of He the synthesis. The observations of low mass AGB stars by Smith & Lambert 1986 showed that they have high Li abundances. Li is thought to be produced by hot bottom burning of H into Be as described by Cameron Flower mechanism (Cameron & Flower 1971 [19]; Flower, 1996 [28]). The reaction showing Li production is presented in Appendix A.3 section § A.3.2

All elements ($^3$H and $^4$He) used in the production of new Li by HBB were previously synthesized earlier in the evolution.

The synthesis of new material by HBB can cause the chemistry of the star to change. When temperatures reach $10^8$K in the HBB layer, the first loop of the CNO cycles ($CNO_I$) becomes more efficient in depleting all $^{12}$C into $^{13}$C by $\alpha$ capture methods and a beta decay of unstable $^{13}$N, even though there is always a production of $^4$He by the whole CNO cycle. The high abundances of $^{13}$C can capture another proton making $^{14}$N to further increase. The reduction of carbon is given by the reaction

$$^{12}\mathrm{C}(p,\gamma)^{13}\mathrm{N}(\beta^{+},\nu_e)^{13}\mathrm{C}(p,\alpha)^{14}\mathrm{N}$$

The increase in $^{13}$C content at the onset of HBB has its influence on the surface abundances of the star by altering the ratios of $^{12}\mathrm{C}/^{13}\mathrm{C}$. When the star is thermally pulsating, dredge up of $^{12}$C will cause the surface ratios $^{12}\mathrm{C}/^{13}\mathrm{C}$ to increase until an equilibrium value is reached. As soon as HBB is switched on, more $^{13}$C is produced because C is consumed, as a result the ratio of $^{12}\mathrm{C}/^{13}\mathrm{C}$ decreases. The material in a HBB envelope is transported through the small hot region (Intershell Convective Zone) many times between thermal pulses; while this carbon rich material gets circulated between the inner regions of the star and the the surface by convection. At the end of the AGB the convective envelope decrease in mass (maybe because the star is also losing mass) causing its base to retreat and HBB to extinguish, this result onto an increase in carbon.

Depending on the initial mass and chemical composition of the star, a star may not become a carbon star because of $^{12}$C conversion into $^{13}$C despite the effects of dredge up. The effect of this new nuclear synthesis of high $^{14}$N in AGB stars is that some super-giant stars can develop a nitrogen rich atmospheres. Models indicate that $^{13}$C, $^{12}$C, and $^{14}$N should evolve according to Figure 3.7..

Hot bottom burning can also consume $^{18}$O to produce $^{13}$C e.g. Boothroyd 1993 [13]. The reaction is,

$$^{18}\mathrm{O}(p,\alpha)^{15}\mathrm{N}(p,\alpha)^{12}\mathrm{C}(p,\gamma)^{13}\mathrm{N}(\beta,\nu_e$$

HBB models show luminosities that are usually higher because than the ones predicted by surface luminosity core- mass relation (Pacyznski′s relation) for low mass stars, meaning the Paczynski cannot be applied in those cases where HBB dominates the luminosity of the star especially in high masses ($> 4M_{\odot}$). The reason is that in

higher masses hot bottom burning tend to dominate the energy production of the star because high mass stars do not develop radiative layer that separate the core from the envelope as a result, the convective envelope can penetrate deeper near the H-burning shell and reach higher burning temperatures. In HBB, the whole convective envelope is involve in the material transport and hence the whole star is involved in the evolution than in a situation where the mass is allowed to evolve isolated. The particular case comes when finding the limiting mass of an AGB star which uses the Chandrasekhar limit in conjunction with luminosity- mass relations that is assumes that the core and envelope separation, HBB does not apply. In this thesis we do apply Paczynski relation to estimate the mass of the core from the luminosities calculated from period- luminosity relations. The period - luminosity relations comes as a result of the fact that the atmospheres of AGB stars pulsate, and during that time the luminosity varies. Some models assumes that they are correlated to the thermal pulses that causes the core-luminosity to change.

# Chapter 4

# Mass loss and dust formation

## 4.1 Introduction

Intermediate mass stars are known to lose mass at tremedous rates when they evolve up the AGB. The process by which this evolution occurs is hotly debated. The presence of circumstellar dust shells around AGB and post-AGB stars is strong evidence that they do lose mass. Indeed, since the formation of dust shells is expected to be a result of the mass loss. The main purpose of the work presented in this thesis is to use manifestation of mass loss in the circumstellar shells to study the mass loss from dying stars using far infrared observations. I discuss how the mass loss occurs under what proposed driving mechanisms. Particular focus will be the formation and influence of dust in thse circumstellar shells.

As early as 1600, Bleau discovered the outburst of a star called P Cygni (luminous blue variable star) that showed an increase in brightness to a third in magnitude for about sixty years.Subsequently spectroscopic studies of this object revealed an interesting spectral feature, that would later be known as the P Cygni line profile, an example of which is presented in Figure 4.1.

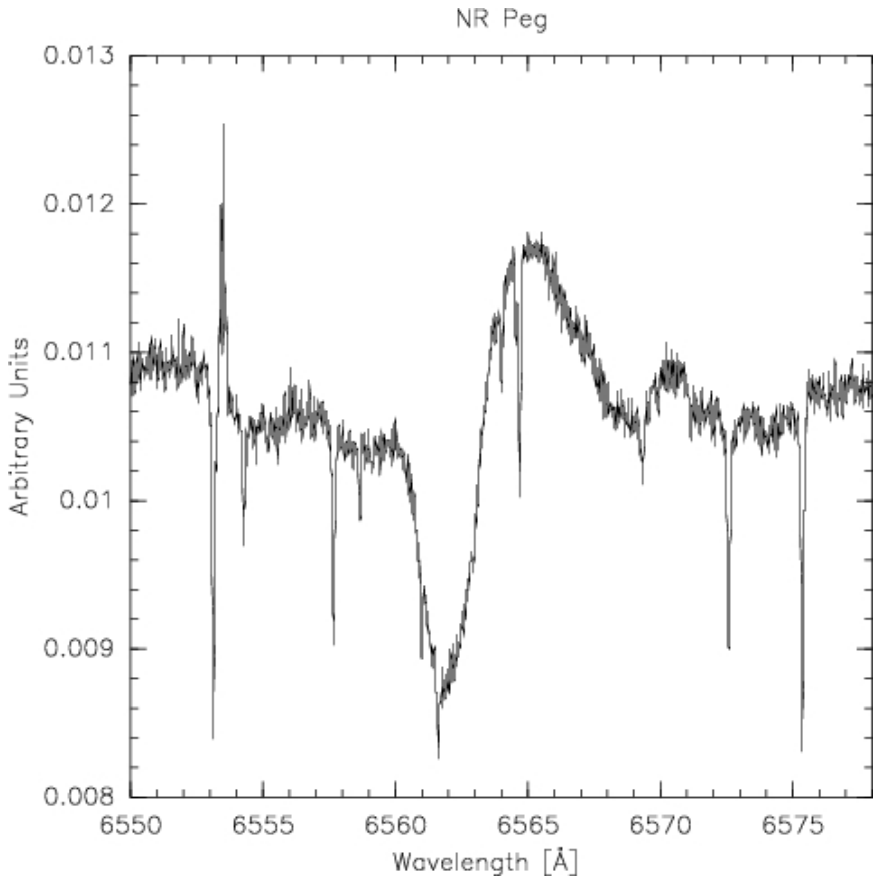


Figure 4.1: The P Cygni profile line is formed from the combination of absorption and amission of light coming from a star whose shells are expanding. From the obsever's perspective who is infront of the star; all photons coming directly to the observer are absorbed by the material in front of the observer, causing a decrease in the flux because they are blue-shifted. In the halo, surrounding the the star are the photots that reaches the observer are red-shifted because the gas in these areas is moving away from the observer, this causes the emmission with central peak around in the continuum.

In this chapter I will first provide a historical overview of mass loss based on early observations of the spectra of novae (cataclysmic variable stars) and luuminous cool super giants. Then I will discuss the theoretical driving mechanisms for the outflow material leaving the star. Finally I will discuss the stellar evolutionary models and their formalism on mass loss tracing the intermediate mass stars, starting with Main sequence, Red giant Branch up until the AGB phase.

## 4.2 Historical review of Mass loss

Observationally, we observe circumstellar material (dust and gas) by its interaction with starlight that passes through discussed in Chapter 5. Absorption and emission features in atomic and molecular gas are particularly important as their narrow spectral line facilitate the observation of the Doppler Effect of material movement of gaseous particles around the star. Thus we can then derive the motion of the outflowing material using the observation of the stellar spectra. The spectral lines observed provide a wealth of information about the structure, dynamics, and the chemical composition of the intervening material. For circumstellar material, spectral observations of the stars with relatively high mass loss show that the widths and /or wavelengths of emission and absorption lines are Doppler-shifted due to outflowing motion of the gas in the stellar wind.

In the early 1600, Bleau discovered the outburst of a star called P Cygni (luminous blue variable star) that showed an increase in brightness to a third in magnitude for about sixty years. Subsequently spectroscopic studies of this object revealed an interesting spectral feature, that would later be known as the P Cygni line profile, an example of which is presented in figure 4.1. Atomic spectral lines are formed when an atom absorb a photon exciting an electron to higher energy level; the same energy (and therefore wavelength) photon is re-emited when an electron returns to the ground state.

In the presence of an expanding shell, the emission and absorption are offset by the Doppler effect; the emission line is typically centered at zero in velocity space while the absorption line is blue-shifted by the material motion towards the observed. The velocity law of the expanding material can be derived from the P Cygni lines, and if the density in the shell is known, the rate at which the star loses mass can be found e.g (Groenewegen et al. 1989[46], Lamers et al. 1995[78]).

Wolf & Rayet (1867) discovered three stars in Cygnus using an optical prism whose

broad spectral lines were very similar to those seen earlier in P Cygni, although the connection was note made for several decades. All these stars are now believed to have been exhibiting nova-like behavior. While the term nova simply means new and comes from the observations of new stars, novae are now known to be stars undergoing a cataclysmic event in which they eject large quantities of material into interstellar space at high speeds. More observations of P-Cygni profiles and other similar Doppler-related spectral line effects in Novae-like objects were used to infer the dynamics of the outflowing circumstellar mass (e.g. Campel 1892,1918).

Milne (1926) studied the velocity distribution of atoms flowing away from the sun and found that atoms were being accelerated. He explained their motions in terms of radiation pressure. Although P Cygni like spectral line behavior had been observed for several decades, Beals (1929) was the first to propose that the similarity between novae P Cygni stars and Wolf & Rayet (WR) stars resulted from a continuous flow of material leaving the star; it was later still that in 1943 Chandrasekhar (1943) gave a theoretical explanation for the formation of P Cygni line profiles

Korisev (1943) was able to use observations to derive the mass- loss rates from the W-R stars $pprox 10^{-5} M_{\odot}$. He also suggested that many stars should go through the Wolf-Rayet phase of evolution. Soon many astronomers believed that stars lose mass. For example Adams & MacCormak (1935) showed that sodium and magnesium lines seen in the spectra of M-super giants ($\alpha$ Her, $\alpha$ Ori) were blue shifted with out flow gas velocities of around $5 kms^{-1}$ indicating that these cool large stars are losing mass in the form of expanding gas envelopes. However, Spitzer (1939) analyzed the same M-star spectral data and proposed that the shift in the absorption features could be explained by a fountain 'flow of material'; through which radiatively driven particles are not sufficiently accelerated by radiation pressure, and thus reach some maximum height above the atmosphere before causing the gas falling back onto the surface of the star; he was not in favor of expanding material. The issue of mass loss was

difficult even to the pioneers and remains so today.

This initial work on stellar mass loss was based upon studies of relatively rare stellar objects like novae and WR stars. We now consider the much more common, regular intermediate mass stars. From the moment an intermediate star joins the main sequence (MS) the particles in the upper layers of the atmosphere are are weakly gravitationally bound, and can leave the leave the surface of the star. As these particles leaves the star they can transfer momentum to the gas in the area around the star. The observational evidence for main-sequence mass came from Biermann (1951) [9],who analyzed the motion of a comet in an elliptical orbit around the Sun. He was able to show that the comet's orbit around the Sun required extra momentum coming from particles leaving the surface of the sun (see also Aslan, 1975 [4]). Bierman used the comet's motion to estimate the velocity of the particles leaving the sun to be $\sim 400 kms^{-1}$. During this replenishment of the interstellar medium by stellar material occurs at high speeds, but at a low rate because for most of the material gravity balance the radiation pressure.

The Sun loses mass at very low rates of about $10^{-14} M_{\odot}$ / yr (e.g. Parker 1958, MacGregor 1998). For the particles to stream out the surface, either the radiation pressure force has to be greater than gravity or some other force must act to counter gravity (e.g. due to the magnetic field). During the main sequence, stars are relatively small and thus gravity tends to win, whereas when a star reaches the RGB phase or at the AGB phase with extended envelopes that are less gravitationally bound; in such cases particles are more likely to escape the surface of a star. Therefore if we assume that the sun can keep loosing mass at this constant rate, only a small fraction of its total mass (less than $0.01 M_{\odot}$) will be lost in the next 5 billion years when it leaves the main sequence. Thus mass loss does not significantly affect the total mass of the sun (or any main sequence star).

During the RGB phase, intermediate mass stars increase in size and luminosity,

but decrease in temperature (see Chapter 2). The outer envelope and atmosphere of such a star is expanding. The outflow velocities of the gas can be used to estimate the mass-loss rates as will be discussed in Chapter 5. Using the outflow velocities from the Deutsch observations, Gehrz & Woolf (1969) [38] derived the mass loss rates of red giants to be between $10^{-7} M_{\odot}$ / yr, - $10^{-6} M_{\odot}$/ yr.

By the late 60's it was already established that the particles leaving the sun's corona causes the coronal wind, these winds are driven by gas pressure due to high temperatures in the corona. However there were debates (e.g. Parker & Chamberlain, 1960) [105],[106] on whether the particles leaving the corona causes a strong solar winds or a slow solar breeze from the sun's photosphere. From such the debates, in 1960, Parker introduces the stellar wind concept as an outflow of particles from stars. Two years later the work of Fred Hoyle & Wickeramasinghe (1962) were the first to suggest that grains are likely to form in atmospheres of carbon rich stars leading to an outflow that is radiation dominated for cool super giant stars. Gilman (1972) [40] develops the idea of momentum coupling in dust driven winds in which dust is driven by radiation pressure, and subsequent collisions drag the gas along. Therefore early the studies of coronal winds in the sun before 1947 as well as the development of solar wind theory between 1947 - 1967, were able to show evidence of outlow of particles from the stars.

Between 1967 - 1980, rockets and satellites were launched, this marked the early observation of stars using on board telescopes in favor of eliminating earth atmospheric aberations. For stellar winds observations, Morton (1967) observed Pcygni profiles of CIV, N V, and Si IV resonance lines in the UV spectra of several O and B super giant stars with a rocket launched spectrometer. He found velocities $> 2000 kms^{-1}$ for super giant stars and estimates their mass loss rates of $\approx 10^{-14} M_{\odot}$ / yr. Lucy and Solomon (1970) develop a radiation driven wind model to explain the high speed outflow from hot stars that Morton observed. Between 1975 - 1977,

(Panagia & Felli 1975 [104]; Wright & Barlow, 1975 [6]) showed that the mass loss rates from hot stars can be measured with radio measurements of free-free emission. Barlow and Cohen, 1977 showed that from Infrared (IR) observations of winds can be used to measure mass loss rates. All these studies (based on super giants), played an important role in the developments of stellar winds in general (Lamers & Cassinelli 1999 [77]).

At the end of the RGB phase, intermediate mass stars enter the Horizontal Branch, during which time they are smaller but hotter than RGB stars. Following the exhaustion of the helium core, intermediate mass stars enter the AGB phase. During this phase the stars are expected to lose the largest fraction of their mass with mass-loss rate ranging from $\sim 10^{-8} M_{\odot}$ / yr in the early AGB to ($> 10^{-4} M_{\odot}$ / yr by the end of AGB). These stars lose their outer envelopes into space leaving little more than the core. Meanwhile, they form circumstellar shells of dust and gas. Finally as the star evolves off the AGB it becomes a proto- or pre-planetary nebula (PPN) for a short time ($\sim$ 1000 years) and then becomes a planetary nebula when the central star remnant become hot enough to ionize the surrounding circumstellar medium. The dust shells eventually merge into the ISM. Dust form around AGB stars believed be one of the driving mechanism for mass loss. Dust grains can absorb all energies of photons, whereas atoms and molecules can only absorb specific wavelengths associated with energy levels. This means that dust can capture the momentum of stellar photons more effective than can gas particles, collisions between dust and gas particles then transfer the captured momentum and the gas can be dragged along in the outflow (Gilman 1972[40]).This process can drag more gaseous material away from the star ausing the star to lose more mass. Therefore mass loss and dust formation should always be coupled when calculating the motion of molecules in the atmosphere and beyond.

## 4.3 The Effect of Dust Formation on Mass Loss

There are currently two hypothetical components that provide the mechanisms for the ejection of stellar material and lead to the formation of stellar winds. AGB stars pulsate and the pulsation of the surface leads to mass loss; and radiation pressure on dust grains leads to further mass loss. Stellar pulsation can transfer momentum to the particles in the star's photosphere which generates both an outward motion and , shock waves generated causing a both a mechanical and thermal wind (e.g Gustafsson and H$\acute{}$ofner Chapter 4 [45]). Thus both stellar pulsation and radiation pressure mechanisms are important for the motion of particles out of the star, because they both provide the source of outward momentum to the particles. However, gas particles must ouflow before dust can be formed, and thus both mechanisms must be in play. Regardless of their origins and formation mechanisms moilecular dust shells around AGB stars are the result of the star losing mass; these dust shell gets dissipated into the interstellar medium. As discuss in Chapter 3, AGB stars create new elements through H- and He-fusion and slow neutron capture. Meanwhile the high opacities that lead to a pulsating star also lead to convection current that can dredge-up newly formed elements to the star's surface. These newly-formed elements are then ejected in the stellar outflow/mass loss. AGB stars therefore enrich the ISM with material manufactured within the star. To summarize the main driving mechanisms for mass loss require a combination of stellar pulsations , that causes a mass movement of the material out of the star, radiation pressure pushing out dust grains. The pulsations come from the convective envelope and are expected to sends out shock waves that can levitate the material out into the upper layers of the atmosphere, where refractory dust particles can condense. Pulsations create shock waves, and dust can form in the aftershock. Radiation pressure the source of momentum for the dust momentum is transfered to the surrounding ambient gas via kinetic collisions. The whole system of gas and dust gets pushed out ofaway from the

star. In the next section we shall consider the motion of particles that leave the star under the effect of radiation pressure and what effect this momentum transfer has on mass loss.

## 4.4 Dynamics of Gas and Dust motion

### 4.4.1 Momentum transfer by photons

Let us consider the total momentum of photons flowing through a wind composed of gas and dust particles. Each photon carries a momentum $h\nu/c$ that can be transfered to the gas particles via absorption. The total energy of the photons is given by of the luminosity ($L_*$) of the star over some time interval $dt$. Thus the total momentum of stellar photons is given by

$$dP_{photons} = \frac{dE_{total}}{c} = \frac{L_*}{c}.dt$$

where $c$ is the speed of light.

For the same interval of time, $dt$, the change in the momentum of the dust and gas particles is given by

$$dP_{particles} = dM_{tot}.V_{final},$$

where $v_{final}$ is the terminal wind speed, which is assumed to be a constant. and it is usually designated by $v_\infty$.

If $\eta_{gd}$ is the efficiency with which both gas and dust particles absorbs radiation in the wind, we can derive an expression for momentum for outflow particles in terms of the $L_*$ and assuming complete transfer of momentum from photons to both gas and dust, i.e.

$$dM_{tot}.V_{final} = \eta_{gd}\frac{L_*}{c}.dt$$

Which implies that

$$\dot{M}_{tot}.v_\infty = \eta_{gd}\frac{L_*}{c} \tag{4.1}$$

where $\dot{M}_{tot}$ is the mass−loss rate.

The importance of equation 4.1 is that the rate at which the star is loses mass ($\dot{M}_{tot}$) can be calculated from its luminosity provided that both the terminal velocity in the wind and the efficiency of how the particles absorb radiation are known. During the AGB phase, intermediate mass stars substantially increase their luminosity without accompanying increases in terminal velocities which leads to the increasing mass loss rate.

To demonstrate, let us assume that photons interact with wind particles once on their way out of the star such that $\eta_{gd}$ is unit (in the so - called single scattering). For a typical AGB star with a luminosity $\sim 10^4\,\mathrm{L}_\odot$ and terminal wind speeds of around $20kms^{-1}$, we can expect a mass loss rate $\sim 10^{-5}M_\odot$ /yr, which is very close to the mass loss rates observed from observations of AGB stars. However the single scattering limit can-not represent a true picture of how radiation propargates through a dusty outflow. For most circumestellar shells stellar photons will be absorbed and re-emitted or get scattered multiple times before this packet of energy finally escapes into the ISM. Concequently reprocessed photons (i.e. those emitted part gas and dust particles, rather than directly from the star) should also interact with wind material and thus transfer more momentum into the wind. This process continues until photons are emitted in the form of thermal radiation that is observed in the infrared part of the spectrum.

If radiation pressure dominates the momentum transfer from the value of $\eta_{gd}$

should depend on both radiative acceleration by the photons as well as the opacities of both gas and dust particles present in the wind.

As discussed above, mass loss-rate is intimately linked with the velocities of the dust particles in the stellar outflow. That is, it is important to understand these particle's motions from the moment the dust forms until all particles escape. In the next section I shall review the motions in a stellar wind by by looking at the density and velocity relations expected when both gas and dust are subjected to radiation pressure using Newton 2nd law. I will also derive their terminal speeds.

### 4.4.2 Motion of gas and dust particles

let us assume that a star is surrounded by spherical shells, such that there is a continuous out-flow of matter from one shell to the next. In this case the mass continuity suggests that the same amount of material flows per second though - out the sphere at any radial distance $r$ from the center of the star. Thus for the material within a star of mass (M) and contained on a volume $V$, this continuous flow of matter means that there are no sinks or sources of matter in the outflow. Changes in mass comes from the volume change, i.e.

$dM = \rho dV$, where $dV = 4\pi r^2 dr$

Then

$$\frac{dM}{dt} = 4\pi r^2 \rho \frac{dr}{dt}$$

which assumes that the density $\rho = \rho(r)$.

For a symmetric outflow, the mass–loss rate is given by

$$\dot{M} = 4\pi r^2 \rho(r) v(r) \tag{4.2}$$

The motion of particles will be consider under stationary conditions, i.e.-the ve-

locity gradient or the acceleration is a function distance, not of time such that:

$$a(r,t) = \frac{dv(r,t)}{dt} = v(r).\frac{dv(r,t)}{dr}$$

The forces per unit mass ($dm \equiv \rho A dr$) that act on particles, are the gravitational force ($F_g$), the gas pressure force ($F_p$) and the forces due to radiation pressure ($F_{rad}$). These forces are are defined as follows,

$$F_g = \frac{dF_{grav}}{dm} = \frac{GM}{r^2}$$

$$f_{gas} = \frac{AdP_{gas}}{A\rho dr} = \frac{1}{\rho}.\frac{dP_{gas}}{dr}$$

Since dust particles absorbs radiation more efficiently than molecules I will assume that radiation pressure is only transfered to the dust particles, and that they transfer their momentum to the gas particles via kinetic collisions. Furthermore, that the distribution of dust particles varies as $\sim r^{-2}$.

The assertion that only dust particles absorb photons maybe valid in dust winds (Lamers and Casinelli, 1999 Ch7) where dust particle opacity dominates the absorption of radiation from the star. With increasing dust fromation. more and more stellar radiation is blocked at all wavelenghts and emitted in the infrared where dust grains are particular efficient absorbers

Thus if the number density of dust particles in the shell is $n_d$ and each has a small absorbing surface area $\sigma$, then we can use momentum transfer to account for the radiative force they encounter, under the asumption that grain size is smaller than the wavelength of photons. Suppose a photon travels an optical path distance $\Delta x$ during their collisions with dust particles inside the shell located at distance $r$ from the star, such that the radiation pressure on the dust grain is given by $\Delta P_{rad}$

$$\Delta P_{rad} = \frac{dE}{dV} = \frac{Ldt}{4\pi r^2 dr} = \frac{L}{4\pi r^2 c}$$

,

optical path distance for photons $\Delta x = \frac{1}{n_d \sigma}$.

Thus we can make a crude estimate of the radiation force as

$$f_{rad} = \frac{\Delta P_{rad}}{\Delta x} = \frac{n_d \sigma L}{4\pi r^2 c}$$

Then we can write the equation of motion of the particles as,

$$v\frac{dv}{dr} + \frac{1}{\rho}\frac{dP}{dr} + \frac{GM}{r^2} = \frac{n_d \sigma L}{4\pi r^2 c} \tag{4.3}$$

Assuming that the gas obeys the ideal gas law, with constant mean atomic weight, the pressure term can be written as

$$\frac{1}{\rho}\frac{dP}{dr} = \frac{R}{\mu}\frac{dT}{dr} + \frac{R_g T}{\mu\rho}\frac{d\rho}{dr} \tag{4.4}$$

where $R_g$ is the gas constant. The change in density with radius in equation in equation 4.3 can be written in-terms of the change in velocity such under the assumption that the mass–loss rate is a constant ( 4.2) result into

$$\frac{1}{\rho}\frac{d\rho}{dr} = -\frac{2}{r} - \frac{1}{v}\frac{dv}{dr} \tag{4.5}$$

The isothermal speed of sound is

$$c_s^2 = \frac{R_g T}{\mu} \tag{4.6}$$

Here $R_g$ is a gas constant, in $JK^{-1}$ Then combining equations 4.3, 4.5 and 4.6 results in

$$v\frac{dv}{dr} + c_s^2\{-\frac{2}{r} - \frac{1}{v}\frac{dv}{dr}\} + \frac{\mathrm{dc}_s^2}{dr} + \frac{GM}{r^2} = \frac{n_d \sigma L}{4\pi r^2 c}$$

which can be rearranged in order to get the momentum equation

$$v\frac{dv}{dr} = \frac{v}{v^2 - c_s^2}\{\frac{2c_s^2}{r} - \frac{dc_s^2}{dr} + \frac{GM}{r^2}(\Gamma_d - 1)\} \tag{4.7}$$

where $\Gamma_d$ is the ratio of the radiation pressure force to the gravitational force which is given by

$$\Gamma = \frac{n_d \sigma L}{4\pi c GM} \tag{4.8}$$

The $\Gamma_d$ affects the momentum of the particles in equation 4.7, so its value is important when looking at motion these particles at different positions in the shell.
Let us consider the solutions of the momentum equation inorder to see the influence $\Gamma_d$. There are several solutions for equation 4.7, there seems but only one that is meaningful for stellar wind.

When the speeds of the particles approaches sound speed $c_s$ the momentum equation suggests that there is a sonic point (X-singular point) where v = $c_s$. Therefore the particles progress from subsonic velocities close to the star, passing through a sonic point to become supersonic at larger distances. This general trend is for a model figure 4.2, in which the influence of different values of $\Gamma_d$ are shown; the velocity is plotted vs. distance for values of $\Gamma < 1$. The sonic point (usually refered to as the Parker point) considered in this model for dust driven winds can be found by solving

$$r_c = \frac{GM}{2c^2}(1 - \Gamma)\mathrm{at}v = c_s. \tag{4.9}$$

As seen in figure 4.2 increase in $\Gamma_d$ shifts the critical point so that the sonic point is reached at lower values of $r$ closer to the star. Furthermore as the critical point

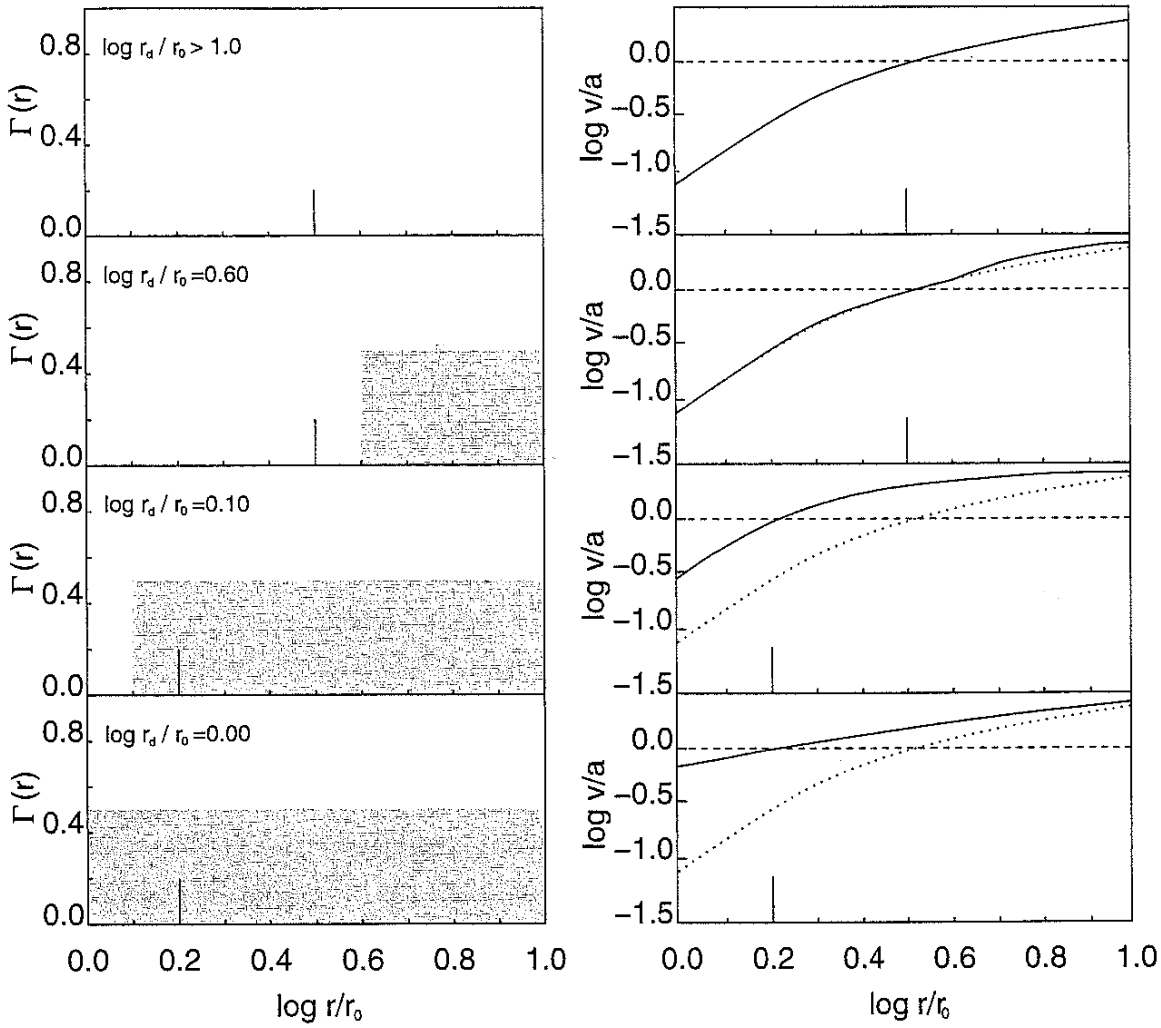


Figure 4.2: *Left Panel*: Radiative pressure force parameter $\Gamma_d$ vs radial distance. *Right panel*: wind velocity vs radial distance. In both panels, a line is shown to indicate a position of the sonic point under the influnce of the changing radiation pressure. The escape velocity curve (indicated by dotted lines) is included for comparison.

shifts closer to the star, the initial velocity positions are shifting to higher values due to an increase in $\Gamma_d$. We can attribute the increase in mass loss in the subsonic region under the influence of higher $\Gamma_d$ that causes an increase in the momentum term on particles such that $\mathrm{v}\frac{dv}{dr}$ becomes more steeper.

This increase in mass-loss rate under the action of $\Gamma_d$ implies that if for a example the sonic point coincide with the poisition where dust particles form, one can expect a rise in the mass loss-rate. The dust condensation does not necessarily coincide with

the sonic point but in dust driven winds observations suggest that it may true.

According to this model the velocity seems flatten out with a change of slope until a supersonic speed is reached, this suggest that even if $\Gamma_d$ is increased its effect does seems not to have any affect on the velocity distribution as long as its values is less than unity. Therefore when modeling the supersonic region when the velocity gradient is increasing the value of $\Gamma_d$ has to be greater than unity for the radiation pressure to affect the momentum of particles.

How $\Gamma_d$ affects mass-loss rate is very important because it tells us that below the sonic point the mass-loss rates are constant and can be determined by hydrodynamic structure at the surface of the star; the application of radiation pressure only shift the sonic point. After this critical point radiation pressure has to increase to drive the momentum of the particles when the velocity gradient is decreasing to keep a constant mass loss-rate. Late super-giant stars and Mira variables (some considered in this thesis) are believed to show this sudden switch -on of radiation pressure causing the formation of bumps in their energy distribution in the infrared. The occurance of bumps is attributed to more dust froming outside the star during the super wind phase when the star if losing more mass at the end of the AGB phase. Thus it is important to know how will the dust opacity and the value of $\Gamma_d$ affects the mass loss, especially since its effect may be noticeable at areas beyond the sonic point up until the outflow velocity of both gas an dust are constant.

The more dust that form in the outer layers of a star the higher the mass-loss rate should be, when the velocity law is about constant. As more dust forms, the dust grains will block more stellar radiation (dust extinction increases). Consequently, the dust extinction must be incorporated into radiation pressure calculations in order to derive the mass loss-rate in the outer regions beyond the super sonic point.

In reality have to consider the opacity of gas molecules and the ratio gas to dust. at well so the value of mass but these are difficult to incorporate into a simple model

and are not considered further here.

By looking at the motion of a small particle, from the moment it is emitted at the surface of the star until it escape, we can approximate the momentum capture from stellar radiation.

Suppose the particle has mass $dm = 4\pi r^2 \rho dr$ , which is acted upon by both gravity and radiation pressure, and is located in a circumstellar shell that extends from, the photosphere until it reaches the ISM (chosen to be at infinity). The momentum equation asserts that

$$\int_{R_{star}}^{\infty} v\frac{dv}{dr}dm + \int_{R_{star}}^{\infty} \frac{1}{\rho}\frac{dP}{dr}dm + \int_{R}^{\infty} \frac{GM}{r^2}dm = \int_{R_{star}}^{\infty} \frac{n_d \sigma L}{4\pi r^2 c}dm$$

which can be simplified using the critical point at $r_d$ and the definition of $\Gamma$ to get
$\int_R^{\infty} \dot{M}dv + \int_R^{r_d}\{\frac{1}{\rho}\frac{dP}{dr} + \frac{GM}{r^2}\}dm + \int_{r_d}^{\infty}(\frac{GM}{r^2})4\pi r^2\rho dr + \int_{r_d}^{\infty}\frac{1}{\rho}\frac{dP}{dr}dm =$
$\int_R^{r_d}(\frac{GM}{r^2}\Gamma_d)dm + \int_{r_d}^{\infty}(\frac{GM}{r^2}\Gamma_d)4\pi r^2\rho dr$

The second integral on the left vanishes because in the subsonic region the gas is in hydrostatic equilbrium and above the sonic point gas pressure is very low because the shells are very big with extended atmospheres making the 4th term to vanish too. The fifth term of the equation above will also disappear because its influence at the subsonic region is to shift the sonic point resulting to a constant mass loss that remains the same until $r_d$ is reached. The first term is the total momentum rate of the star whose value can be found clearly by radiation and gravity terms from $r_d$ until the shell ploughs the ISM.

Then one gets

$$\dot{M}v_{\infty} = (\Gamma_d - 1)\int_{r_d}^{\infty} 4\pi G M_* \rho dr \tag{4.10}$$

Inorder to incorporate the optical properties of the dust into momentum equation 4.10, we need to express the integrand on the left by including extinction as well as the luminosity of the star. That is

$$4\pi GM_* = (\frac{n_d\sigma_d}{\Gamma_d}).\frac{L_*}{c} \tag{4.11}$$

Let us define the optical depth

$$\tau_{dust} = \int_{r_d}^{\infty} n_d\sigma_d\rho dr$$

since $n_d\sigma_d$ has per unit length dimension we can similary express the number density in term of the actual density ($\rho_g$) and the mass of the grain such that

$$n_d\sigma_d = \kappa_d.\rho_g$$

where $\kappa_d$ is absorption surface area per unit mass. The value of $\kappa_d.\rho_g$ is often called the radiation pressure mean opacity, , is wavelength dependent and is denoted by $k_{rp}$ with also per-length units. Thus the optical depth of dust at a particular wavelength in the supersonic region can be expressed interms of $k_{rp}$ i.e.

$$\tau_{dust} = \int_{r_d}^{\infty} k_{rp}\rho dr \tag{4.12}$$

With this definition of $\tau_{dust}$, the mass loss rate in the supersonic region can be expressed interms of the radiative acceleration on the dust $\Gamma$ and the optical depth of $\tau_{dust}$.

$$\dot{M}v_\infty = \frac{(\Gamma_d - 1)}{\Gamma_d}\tau_{dust} \tag{4.13}$$

Consequently, the dust-driven mass-loss rate depends on the radiative pressure on dust as well as the extiction or the optical depth of the dust(which comprises both density distribution and albedo/absorption properties) in the supersonic region.

It is clear that the mass loss beyond the photosphere can be well approximated if

we know both the dust properties and luminosity of the star. The optical properties of dust and its influence on the energy distribution will be covered in Chapter 5. In the next section I will review the current models of stellar evolution that predict what the mass loss rates are in the case of intermediate mass stars.

## 4.5 AGB Mass loss and Stellar Evolution Models

This study is concerned about probing the history of mass loss in AGB stars and post-AGB stars using the infrared photometry; therefore this section focuses on the current models that predict the evolution of intermediate mass stars as they leave the main sequence up until they become planetary nebulae. As the star ages its evolution is tracked through the observable changes in size (R), luminosity (L) and the surface temperature as ($T_{eff}$) outlined by the HR diargram in Chapter 2. Therefore any process that will alter or cause a change in any of these physical quantintitie will cause a significant change on the evolution of the star. In the previous section I showed that when the star is loosing mass, the mass loss rate can change $\Gamma_d$ gets very larger than unity in the outer parts of the star beyond the photosphere. In the outer regions where dust shells form the mass loss rate therefore, can be estimated if the properties of the dust grains ($\Gamma_d$, $\tau_{dust}$) are known in conjunction with the outflow velocity of material; these quantities alter the momentum of the star (L/c) that give rise to the mass loss rate of the star. This implied that the star can loose more mass as a result of dust that forms in the outer layers i.e. if the opacity of the dust gets large the mass loss rate will increase because its occurance drives more radiation pressure out on the particles as a whole. More partcicles leaving the star means that the total mass of the star will decline. What the models suggest is that at the end of AGB, the star can loose more than 80% of its total mass due to the increase in its mass loss rate. At AGB the star suffers high mass loss rates and mabye the main

driving mechanisim of the star's evolution, some authours in this subject believes that it is the mass loss that leads to the termination of the AGB phase in the so called the super wind phase when the mass loss rates get extremely high. The mass that the star looses gets dissipated (or returned) into the ISM in the form of shells containing dust and gas when intermediate mass stars become planetary nebulae. Most theories presented below have been trying to express the mass loss rates in the late stages of stellar evolution using physical quantities (L,M,R, P) depending on the state where the star is at. This section makes a review of mass loss rate predictions and their formalism will be given on how they predict the mass loss on intermediate mass stars. I will start with theoretical models that predict this mass loss rate when the star enters the RGB phase and the core AGB until the mass loss gets very high leading to the so called super wind phase at post - AGB when the intermediate mass stars become pretty planetary nebulae.

In 1975 Reimers [110] used the observations of H$\alpha$ emission lines of the UV spectrum of red giants and super giants to derive the mass loss rates of intermediate stars at red giant phase.

$$\dot{M}_R = 4 \times 10^{-13} \eta_R \frac{LR}{M} \tag{4.14}$$

where $\eta_R$ between $1/3 < \eta_R < 3$ with L,M and R in solar units. The mass loss rates that are derived using Reimers law are between $10^{-9} - 10^{-6} M_\odot$ / year, and works very well onto a small group in modelling intermediate mass stars during their He-burinig at RGB phase. When the intermediate mass star enters the AGB phase the mass loss rates observations show that the rates gets very high, meaning that if Reimers law is used, the value of $\eta_R$ has to be adjusted to higher values. This increase in $\eta_R$ is incontrast with the mass loss rates of low intermediate mass stars $\sim 2M_\odot$ for which $\eta_R$ has to be less or close to unity. Therefore Reimers law can only be used at RGB for all stars and on low mass intermediate mass stars when they enter the AGB phase. The AGB phase has been under a lot of mass loss prescriptions because of

the dificulty in deriving the mass loss rate from the first principles, in the following discussion I will mention a few groups whose mass loss rates have been used to model intermediate mass stars at AGB.

Since it was clear that the mass loss rate by Reimers law does not accomodate the higher mass stars above $2M_{\odot}$ Bryan et al 1990 [16] improved the formula by assuming that $\eta_R$ has to depend on the zero age main sequence mass and its value has to be quadratic in nature (Blöcker 1990 [12]). This group found that the mass loss rate assumes the form

$$\dot{M}_{BR} = 1.15 \times 10^{-13} \eta_{BR} \frac{LR}{M} \tag{4.15}$$

where $\eta_{BR} = M_{zams}^2 - 10.6 M_{zams} + 10.2$

Most AGB stars belong to Mira variables and OH/IR stars that pulsate and these stars are surrounded by circumstellar dust shells. OH/ IR stars are known to exist on stars with very high mass loss rate associated with dust that obscures the star. The dust reprocess the stellar radiation by absorbing and emits it in the infrared and the star becomes an infrared source. The infrared photon inside the dust cocoon can hit the excited OH molecule in the envelope that causes the same photon to be released by stimulated emmision in the same direction the photon was going in the infrared. The excited OH molecules comes from the dissociation of $H_2O$ that forms in cooler dust envelope. Therefore an AGB star with high mass loss can become a strong source of OH masser line, and these molecular lines have been used to derive the mass loss rates e.g. Habing 1996 [47]. When studying the properties of OH/IR stars, Baud & Habing derived the mass loss rate that depends on the mass of the masser envelope relative to the whole envelope mass where masser activity occurs, this mass loss rate is very similar to Reimers law. The mass loss rate by Baud and Habing is given by

$$\dot{M}_{BH} = 4 \times 10^{-13} \frac{M_{e,0}}{M_e} \frac{LR}{M} \tag{4.16}$$

where $M_{e,0}$ is the mass of the envelope at the beginign of massering activity and $M_e$ is the total mass of the envelope.

The models of Vassiliadis and Wood, 1993 (hearafter VW93) are based on the observations of period - luminosity relations of AGB stars ($\leq 5M_{\odot}$) in the Magellanic Clouds. The mass loss rates were computed using equation 1.1 under the conditions that $\eta_{gd} \sim 2$ (Knapp 1986, Whitelock, Feast & Catchpole 1991). These observations indicate that the mass loss increases exponentially with increase in pulsation period before a star reaches periods of about 500 days. The period variations on Mira variable stars in the Galactic Bulge is optically vissible up to 500 days (Lloyd Evans 1976 [**?**]) while at longer periods ($\leq P_0$= 500d) these stars can only be seen in the far infrared as was shown by Whitelock et. at 1991. This indicated that there when low intermediate mass stars become more dust enshrouded they become invissible in the optical wich sgested that they enter a super wind phase according to Vassiliadis and Wood 93. Then VW93 assert that there are possible two parts that a low mass star passes through during its mass loss at AGB, one in which the mass loss rates a show a steady increase with period until it reaches 500d (as a cut off) and then a super wind phase in which a star has very large periods that corresponds to a large momentum transfer of photons by single scatering events. The dependance of mass loss on periods was shown by Vassiliadis & Wood 1993 [137] (ref Figure 1 in this for Mira variables in Galactic Bulge and the LMC. The expansion velocity used by VW93 also varies with period and is given by

$$v_{exp}(kms^{-1}) = -13.5 + 0.056P(days) \tag{4.17}$$

that is constrained for expansion speeds in the range of $3 - 15kms^{-1}$. The mass

loss rates derived by VW93 can be sumarized as follows

$$\dot{M}_{VW} = \begin{cases} \frac{L}{v_{exp}c}, 10^{[11.4+0.0125P_0]} & M \leq 2.5M_{\odot} \\ \frac{L}{v_{exp}c}, 10^{-11.4+0.0125(P_0-100(M-2.5))} & M > 2.5M_{\odot} \end{cases} \tag{4.18}$$

The results from the VW93 models does agree with the momentum equation shown in quation 4.12, however these results seems to suggest that that when the intermediate mass star climbs the AGB phase the mass loss increases is dominated by $\tau_{dust}$ than $\Gamma_d$ to the first oder approximation. On the other hand when there is more dust in case of optically thick OH/IR stars their mass loss rates should be contained inside the envelope in which both $\tau_{dust}$ and radiation pressure are effective drivers of mass loss. Using these result of mass loss rate VW 93 produced models that suggested that during the luminosity at AGB the mass rate of the star should vary with time scales that corresponds to few thermal pulses making the star to loose more mass. The decline in the total mass of the star when the star enters the superwind phase is demonstrated by one of thier models shown by figure A.4.1. In this figure the mass-loss rate and the total stellar mass are plotted against time at AGB phase for a 1 $M_{\odot}$ progenitor AGB star with luminosity, period and the effective temperature indicated. From this model it is clear that the extensive mass loss occurs during the high luminosity part of quiescent evolution stage during the last few thermal pulse cycles. High mass-loss rates are generally confined to the same time intervals with thermal pulses, the period and surface temperature. From the results of this model (VW98) suggest that the signatures of mass loss modulations should be imprinted on the dust shell emission of the AGB stars especially at their late stages of their evolution, likely in the post AGB candidates.

There are other models considered in this thesis are those of Blöcker 1995 [10] (hereafter BB95) that focused on AGB stars with periods less than 100days. Based on mass loss rates of Bowen 1988 [15] who investigated the dynamical structure of

LPVs and calculated shock driven winds of Mira like stars, Blöcker rescaled their mass loss by including the effects of dust inorder for the mass loss rates to agree with initial-mass corelations that are based on Weidermann & Koester 1983 [141]. The mass loss rates derived by BB95 suggested that inorder for the star to have a steep increase of mass loss at AGB, the luminosity and the total mass of the star should be included in Reimers law, leading into

$$\dot{M}_{BB} = 4.83.10^{-9} M^{-2.1}.\dot{M}_R \tag{4.19}$$

where $M$ is the stellar mass and $L$ is the luminosity.

Since the ISM is enriched by stellar winds from mostly intermediate mass star and also supernovae of massive stars, any model that predict their evolution must also agree with the result of stellar birth rates that predict how the ISM changes chemically or in dynamical structure. In general if intermediate mass stars are major contrubutors of mass return to the ISM, then the models presented here also have to agree with masses that are found using star formation rates or initial mass-functions that predict galactic evolution of matter as a whole. In order to show how much mass each of the models duscussed above agree with IMF corelations, a comparative plot of initial mass vs the final mass is shown in Figure 4.3.

All these models shown in figure 4.3 are constrained by Initial-mass function relation of Weidermann & Koester 1983 [141]hereafter WK83; Weidemann, 2000 [140]. The use of IMF WK83 determined the initial masses for the white dwarfs in the Magellanic Cloud clusters and also in other cclusters like Hyades and Pleides. The masses of the white dwarfs were then traced back to their initial mass of formation. The method uses the cooling age of individual stars that is subtracted from the age of the entire cluster, thus they were able to interpolate inital - final mass relations that predicted white dwarf production. The observations showed that a maximum mass of $1.4\,M_\odot$ white dwarf should come from a masses $\sim$8–$9.0\,M_\odot$ in good agreement

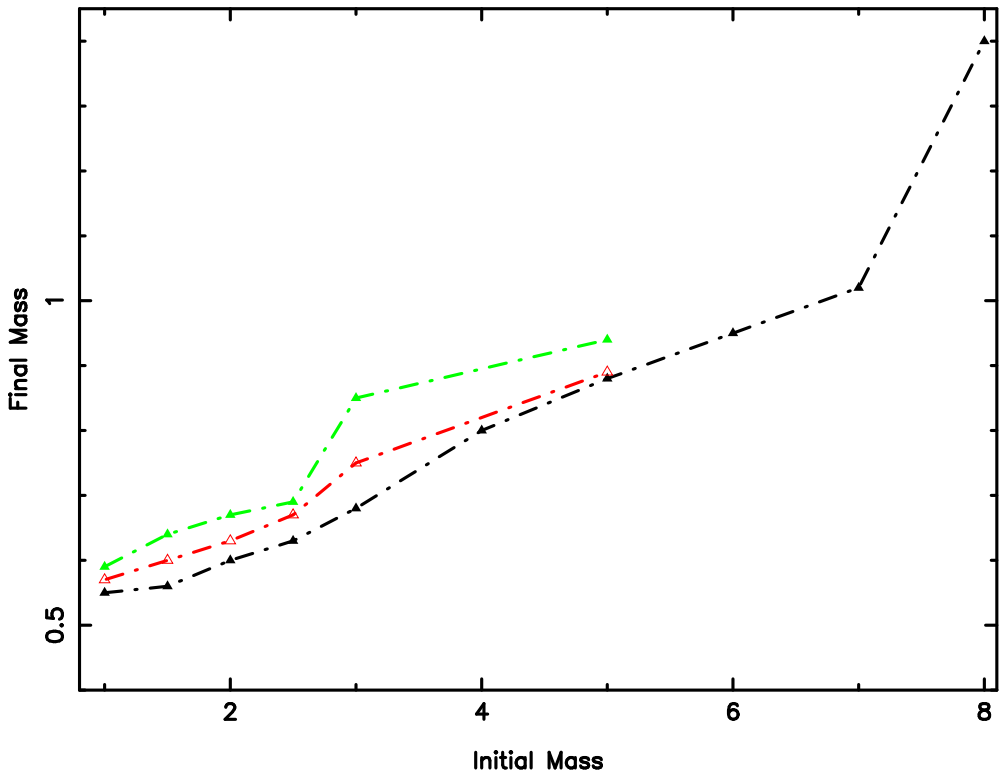


Figure 4.3: Initial mass (solar units) - x axis vs Final mass(solar units) y - axis. The dash - square - dotted lines indicate a curve from Weideman & Koester 2000 [140] data. Triangles are the data points from Vassiliadis and Wood 1993 [137], solid triangle = Z (metallicity) = 0.004, open triangle Z = 0.016

with Chandrasekhar limit that was discussed in Chapter 3, also stars like the sun will endup with final masses about 0.5 $M_{\odot}$ at the end of their lives (cf WK 2000 Fig 1). So the empirical results by WK 83 (reviewed paper Weidemann et al. 2000 [140] has been used widely to constrain model calculations of Blöcker, 1995.

## 4.6 Spectroscopic Observations of Mass loss

We observe light coming from a star that has been reprocessed by a cloud of gas between the observer and the star to derive the specra associated with the star. The spectral lines observed provide a wealth of information about the structure,dynamics, and the chemical composition of the intervening material. In the case of a cloud in motion, as it applies in stellar winds, observations of the stars with relatively high mass loss show that the widths or wavelengths are shifted due to outflowing motion of the gas in the wind. The spectra of a mass-losing star will appear to have emission lines, absorption lines, or the combination of the two cases in the so-called the P Cygni profile. From the historical perspective of observations, the similarity in appearance of the Cygni profiles on the spectra of hot luminous stars to those dying stars with an expanding atmosphere in novae, gave rise to the idea that stars loose mass.

### 4.6.1 P Cygni in hot stars

The most well known P Cygni profiles in the spectra of hot stars are formed by the process of resonace scattering of atom; in this case a line is formed when an atom absorb a photon that excites an electron to higher energy level, the photon with the same frequency is re-emited when an electron returns to the ground state. In the presence of an expanding shell, the emision and part is red shifted makin a bump in the continum spectra towards the observer, while absorption part is blue shifted bcause of scatering of photons out of the line of sight with reference to the observer

making a 'dip' in the continum. A few examples of P Cygni profile lines on the UV spectra of O and early B stars that result from resonace lines of Si IV, C IV, MgII. The velocity law of the expanding material can be derived from the P Cygni lines, and if the density in the shell is known, the rate at which the star looses mass can be found e.g (Groenewegen 1989, Lamers 1995).

### 4.6.2 Atomic Emission lines

Atomic emision lines are good indicators that the star is loosing mass because of their broadness of FWHM (or width) that shows the Doppler shift of atoms that comes from the outflowing motion of the gas in the wind. These lines are formed through recombination process of line formation in stellar wind. Recombination occurs when an ion collides with an electron and produces an ion releases a photon when it return to the ground state. The emissivity of recombination is propotional to the density of a gas, thus atomic line emmision probe the denser regions in stellar winds. Stars with high mass loss rates ($10^{-6}$ / yr) show these emission lines in their spectra, the most well known lines are H$\alpha$, Paschen and Brackett lines of hydrogen atom.

The appearance of these lines in an atmosphere of a mass loosing star offers an insight on the physical conditions under which the ionised atoms in a gas interact with the photons. Figure 4.2 gives a few example of emission lines formed in the stellar winds indicating mass loss in the stars.

### 4.6.3 Molecular Emission lines

Most RGB and early AGB stars have very extended atmospheres with high ubundance of molecules, mass loss in this case occurs over a large

There are five processes associated with the line formation in stellar winds, namely; (a)Line scattering, in which an atom in a gas absorbs a photon causing the electron

to excite into the higher energy level, as the atom cools because of expansion the electron can de-excite by emiting the same photon with same energy in a different direction. (b) Line emission by recombination, here the exited ion present into the stellar wind can recombine with an electron causing the ion to emit a photon as reaches the ground state. (c) Line emission from collision of atoms, a photon can be emitted when an an energetic atom returns to ground state after coliding with another atom, this process can occur in hot plasmas line corona and chromospheres. (d) Pure absorption, an atom absorbs a photo and get excited,the releases the photon(s) into lower levels destroying the initial photon. (e) Masering by stimulated emission, a photon in a stellar wind hits an excited atom or a molecule that causes the atom to release the same photon traveling the the same direction as the original photon.

that were observe to cause the shift on the orbit of a commet accidentally throught the work ofcame whe the suns mass loss Low intermediate mass star like the sun are known to lose mass at rates of $10^{-14} M_{\odot}$ / year, which is very low when compared to the point when the same star reaches AGB phase and start losing mass at rates $10^{-14} M_{\odot}$ at close to $10^{-7} M_{\odot}$ / year till the end when mass loss can get as high as $10^{-4} M_{\odot}$ / year.

# Chapter 5

# Thermal Emission from Dust

## 5.1 Introduction

The main purpose of this chapter is to show how thermal radiation that comes from the presence of dust in the circumstellar dust is used to probe the structure of AGB stars. The dust absorbs radiation from the star, reprocess it through collisions with the gas molecules that drags the gas along leading to the formation of circumstellar dust shells. The emission from circumstellar dust shells that forms can be used to determinde the entire mass of the circumstelar envelope, and also the mass loss rates that the intermediate mass suffers at the AGB can be derived from the dust infrared emission from the shell(s). Therefore the optical properties of the dust in the circumstellar envelope has to be known or estimated since it is the dust presence that effectively causes the extinction of radiation from the star. In the first part of this chapter I will review the opacity of light when there is obscuring material in front of the star, and then use the conditions of dust (e.g. its composition,nature of the extinction) to derive the dust absorption opacities that are used in general when finding the mass of dust present in the circumtellar envelopes.

## 5.2 Dust Grain Opacities

When light from the star with an intensity $I_\lambda$ passes through a small region of thickness dx that causes extinction. The radiation that comes out of the extinguishing region will have an intensity $I_\lambda$ plus the change in intensity $I_\lambda$ associated with extinction. The change in intensity of $dI_\lambda$ is proportional to the original intensity $I_\lambda$ times , the density $\rho$ of the material inside the thickness $dx$. That is

$$dI_\lambda = -\kappa_\lambda . \rho . I_\lambda dx$$

where $\kappa_\lambda$ is the mass absorption coefficient $\kappa_\lambda \equiv (Cross - section/Mass)$ of the extinguishing region in units of $g.cm^{-2}$ in cgs. The change in optical depth $d\tau$ , is defined by

$$d\tau = \frac{dI_\lambda}{I_\lambda} = -\kappa_\lambda \rho . dx \tag{5.1}$$

Equation 5.1 was introduced in Chapter 4, for the dust emission. The values $\kappa_\lambda \rho$ depends on the exact radiative transfer solution[1] that depends of the source and the sink of radiation in circumstellar dust shell under the absorption and scattering by dust and gas molecules that causes extinction. Since this thesis focuses on dust emission, I will only consider the extinction by dust particles. I will also assume that the dust particles are spherical in nature and their extinction efficiencies can be approximated using Mie-theory.

Let us suppose that the number density of particles $n_d(cm^{-3})$ is uniformly distributed over the circumsterllar dust shell around a star. Each dust particle has radius a. The optical depth of photons along the line of sight to the distant star can be expressed in terms of the extinction cross-section and the number density of dust

[1]Equation 5.1 is an approximation, for the most general form see Appendix section C where a complete radiative transfer equation is presented by Eddington approximation that is used when finding the total optical depth of both gas and dust in CSE

properties using equation 5.1. Lets assume that the N dust particles are contained within a column length $L$. The optical depth can be found by integrating equation 5.1 as follow,

$$\tau_{dust} = \int_0^L \kappa_{\lambda,dust}\rho_d dx$$

$$\tau_{dust} = \frac{C_{\lambda,ext}}{m_d}.\frac{Nm_d}{V}.L$$

$$\tau_{dust} = C_{ext}(\lambda).n_d.L \tag{5.2}$$

where $n_d = N/V$, $V$ is the volume containing $N$ dust particles. $C_{\lambda,ext}$ is the total extinction cross-section of particles. The extinction cross-section $C_{\lambda,ext}$ depends on the geometric area of each particle ($\pi a^2$) and the total extinction efficiency ($Q_{ext}(\lambda, a)$) by all particles.

We can define the total extinction cross-section,

$$C_{ext}(\lambda, a) = Q_{ext}(\lambda, a).\pi a^2 \tag{5.3}$$

From equation 5.2, we can define the number of dust particles per unit area ($N_d$) contained within the column L using the number density ($n_d.L$). Then the optical depth can be written in terms $N_d$ and $C_{\lambda,ext}$,

$$\tau_{dust} = C_{ext}(\lambda).N_d \tag{5.4}$$

We can express the intensity reduction in magnitudes, that is the total extinction at some wavelength $\lambda$ is given by

$$A_\lambda = -2.5 \log \frac{I_\lambda}{I_{\lambda,0}}$$

where $I_{\lambda,0}$ is the initial intensity at $L$=0. Since

$$\frac{I_\lambda}{I_{\lambda,0}} = e^{-\tau}$$

then

$$A_\lambda = +1.086\tau_{dust}. \tag{5.5}$$

Equation 5.5 shows that the extinction ($A_\lambda$) is proportional to the optical depth $tau_{dust}$. We can further express the extinction ($A_\lambda$) in equation 5.5 in-terms of the extinction efficiency ($Q_{ext}(\lambda, a)$) using 5.3

$$A_\lambda = +1.086 N_d . \pi a^2 . Q_{ext}(\lambda, a) \tag{5.6}$$

This equation 5.6 represent the extinction in terms of the number density per unit area ($N_d$) and the extinction $Q_{ext}(\lambda, a)$.

If the density distribution of particles changes because the dust particles can have different grain sizes, then we have to replace $N_d$ by $\int n(a)da$ and evaluate the extinction between a to a+da, that is equation 5.6, will change to be

$$A_\lambda = +1.086\pi \int a^2 Q_{ext} n(a) da \tag{5.7}$$

The extinction efficiency (emissivity) $Q_{ext}(\lambda, a)$ was defined in equation 5.3 in terms of $C_{\lambda,ext}$ and the geometric cross section of the dust particles ($\pi a^2$)i.e.

$$Q_{ext}(\lambda, a) = \frac{C_{\lambda,ext}}{\pi a^2} \tag{5.8}$$

When light interacts with particles it get scattered or absorbed such that the extinction cross-section depends on both scattering and absorption cross-sections. That

is

$$C_{ext}(\lambda) = C_{abs}(\lambda) + C_{sca}(\lambda) \tag{5.9}$$

This means that the value of $Q_{ext}(\lambda, a)$ can be written as

$$Q_{ext}(\lambda, a) = \frac{C_{abs}(\lambda)}{\pi a^2} + \frac{C_{sca}(\lambda)}{\pi a^2}$$

that gives the total extinction as,

$$Q_{ext}(\lambda, a) = Q_{abs}(\lambda, a) + Q_{sca}(\lambda, a) \tag{5.10}$$

The extinction emissivities (both absorption and scattering) are functions that depend on the wavelength of light acting on the grains and the dielectric properties of the dust grains (see Borhen and Huffman, 1998). The reflection and the transmission of radiation in dust environment depends on the complex index of refraction (m) of the grains. The When radiation interacts with these particles under the conditions that the particle sizes are smaller than the the wavelength of irradience, these function can take this format,

$$Q_{abs}(\lambda, a) = 4x\mathrm{Im}\left\{\frac{m^2-1}{m^2+2}\right\} \quad \text{and} \quad Q_{sca}(\lambda, a) = \frac{8x}{3}\mathrm{Re}\left\{\frac{m^2-1}{m^2+2}\right\}^2 \tag{5.11}$$

where $x$ is a representative of a wave number defined to be $x = \frac{2\pi \mathrm{a}}{\lambda}$, and m is a dielectric function given by m = n-ik. If the wavelength of light is larger than the radius of the particle (a), the total extinction emissivity depends mainly on $Q_{abs}(\lambda, a)$ because $Q_{abs}(\lambda, a)$ becomes greater than $Q_{sca}(\lambda, a)$, i.e $(\lambda^{-4} \ll \lambda^{-1})$ provided that the dielectric factor on both functions does not depend on the wavelength. This is true for dielectric materials like silicate grains in the infrared whose values of k $\ll 0$,

such that m $\sim$ n (see Whittet & Taylor, 1992). Then in the regime when x $\leq$ 1, i.e when $\lambda \gg$a, the total extinction can be parametrized as

$$Q_{ext}(\lambda, a) \simeq Q_{abs}(\lambda, a) = Q_0(\lambda, a) \left(\frac{\lambda}{\lambda_0}\right)^{-\beta} \tag{5.12}$$

where $Q_0(\lambda, a)$ is emissivity at wavelength $\lambda_0$. If we know the value of $Q_0(\lambda, a)$ at $\lambda_0$, we can make an extrapolation to find the emissivity $Q_{ext}(\lambda, a)$ at wavelength $\lambda$. Scaling the emissivity this way assumes that there is no variation of flux ($F_\lambda$) that may cause the emission to change between the two wavelengths considered. $\beta$ is called the spectral index of emission and it depends on the composition of grains. At short wavelengths $\beta \sim$1 and strongly depends on the grains considered, whereas as the grains become larger than the wavelength of radiation, the value of $\beta$ seems to approach 2 independent of the grain composition. The most possible scenario that will ensure that the value of $x$ is small is, if the wavelength is larger than the of the radius of the particles. To show that when $x$ is very small the emissivity can be parametrized by using equation 5.11, a plot of $Q_{ext}(\lambda, a)$ vs x is shown in figure 5.2.

In this plot dielectric factors are constant of wavelength, with m = 1.6 , for k = 0 that is representative of a dielectric materials and a smaller k= 0.05 that could represent represent refractive index of silicates and ices formed in the CSE's. What is noticed in this diagram is that, for all values of $x \ll 1$ $Q_{ext}(\lambda, a)$ increases steadily with $x$ such that both absorption and scattering emissivities can modeled by $\lambda^\beta$ where $\beta$ can take values from 1-2. When x increases (a$\gg \lambda$) scattering seems to dominate, and a constant radius approach causes resonance variations in $Q_{ext}(\lambda, a)$, this suggests that a size distribution function has to be considered rather than assuming all grains have same size.

Because we are dealing with emission by dust grains in far-infrared with wavelengths between 60$\mu$m - 160$\mu$m; in calculations that requires the usage of the sizes of particles, it was assumed that the oxygen rich stars are dominated by silicate grains

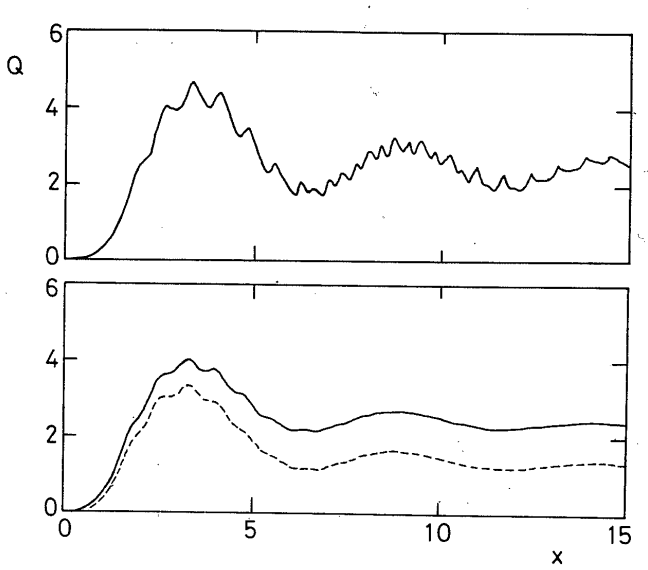


Figure 5.1: Plot of efficiency factors, $Q_{ext}$ and $Q_{sca}$ against $x$ for spherical grains. Upper frame $m = 1.6 - 0.0i$ where $Q_{sca} = Q_{ext}$. Lower frame: $m = 1.6 - 0.05i$, solid curve is $Q_{ext}$, dashed curve is $Q_{sca}$.

whose grain sizes are $\sim 0.1\mu$ m from the lab and meteoritic data, and for carbon rich stars the radii varies and can be estimated between $0.01 - 0.25\mu$ m (e.g. using Annestad, 1975, Draine 1984[25])

Thermal emission observed in the infrared can be used to determine various properties of the envelope containing dust. These properties involve knowing the total mass of the entire envelope, the composition of the dust and the mass loss rates that are coupled to the motion of the particles within the envelope. In order to get the total mass of the envelope, the mass the dust present has to be known. To get the mass of the dust (and mass loss rates inside the envelope), the scattering cross sections per unit mass ($\kappa_{dust}(\lambda, a)$) of the grains present has to be known as well.

In equation 5.2, the optical depth of photons in the the presence of dust grains, was expressed in terms of the scattering cross section of the dust grains and the number density. We can also express the same optical depth in terms of dust density and mass absorption cross section.

$$\frac{\tau_{dust}}{L} = \kappa_{dust}(\lambda, a).\rho_d = C_{ext}(\lambda, a).n_d$$

thus substituting for $C_{ext}(\lambda, a)$ using 5.3 and equation 5.12 we can find $\kappa_{dust}(\lambda, a)$

$$\kappa_{dust}(\lambda, a) = \frac{n_d}{\rho_d \pi r^2} Q_0 \left(\frac{\lambda}{\lambda_0}\right)^{-\beta}$$

since the volume of each spherical grain is $\sim \frac{4\pi a^3}{3}$ then

$$\kappa_{dust}(\lambda) = \left[\frac{3Q_0}{4a\rho_d}\right] \left(\frac{\lambda}{\lambda_0}\right)^{-\beta} \quad \text{in units of } cm^2 g^{-1} \text{ in cgs} \tag{5.13}$$

Lets define $\kappa_{\lambda_0} = \left[\frac{3Q_0}{4a\rho_d}\right]$ to be the mass absorption at $\lambda_0$, that is known such that this value can be used to scale $(\kappa_{dust}(\lambda, a))$ at other wavelengths. Then

$$\kappa_{dust}(\lambda) = \kappa_{\lambda_0} \left(\frac{\lambda}{\lambda_0}\right)^{-\beta} \tag{5.14}$$

Equation 5.14 is only true for fixed the size and the density, under the the conditions that the grains are spherically symmetric. These conditions introduces uncertainties since the densities of the grains are not known with good precision. For example silicate grains are assumed to be spherical with densities around $3gcm^{-3}$, they are assumed to dominate Oxygen rich stars atmospheres, whereas for carbon rich stars, amorphous C ($1.9gcm^{-3}$) Graphite ($2.25gcm^{-3}$) Enstatite($3.1gcm^{-3}$), SiC($3.2gcm^{-3}$) Olivine ($3.2 - 3.4gcm^{-3}$) are the combination of particle in their atmospheres (e.g. Hilderbrand, 1983).

The density of the particles in general vary with particle size, therefore the density distributions has to be known or estimated inside the CSE. The density distribution of the grains can be modeled by assuming the power law distribution in which the density decreases with the particle size, that is

$$\mathrm{n(a)}d(a) = Ka^{-p}da \tag{5.15}$$

where K is a scaling factor that is determined by the composition of gas and dust present as well as their condensation rates of those molecules considered inside the CSE; p is the fitting parameter that depends on the model used. To date, a well known density distribution was given by Mathis, Rump & Nordsieck, 1997 , (termed the MRN distribution) in which the value of p = 3.5.

Knowing the density distribution, the total opacity of the dust ($\chi(\lambda, a)$) can found by integrating the entire optical path length that the photon experiences within the dust envelope before it is emitted.

$$\chi(\lambda, a) = \kappa\rho = \int_{a_{min}}^{a_{max}} Q_{ext}(\lambda, a)\pi a^2 n(a)da \tag{5.16}$$

For the MRN distribution, the size distribution ranges from ($50\mathring{A} - 2500\mathring{A}$). In the case of dust shells, the total extinction emissivity can be estimated from its absorption emissivity, because the scattering emissivity of the dust is smaller than its scattering efficiency as outlined above. The absorption emissivity can be found by using mean Plank emissivity of absorption, under the condition that the star emits radiation as a black body that hits shell envelope that is far from the star. In this case the total extinction can be evaluated from,

$$Q_{ext}(\lambda, a) = \frac{\int_0^\infty Q_{abs}(\lambda, a)B(\lambda, T)d\lambda}{\int_0^\infty B(\lambda, T)d\lambda} \tag{5.17}$$

where $B(\lambda, T)$ is the black body radiation whose functional form has been introduced in Chapter 2 see equation A.2.

## 5.3 Equilibrium temperature of the dust in circumstellar shells

The equilibrium temperature of the dust grains in the CSE, can be approximated by using radiative equilibrium conditions, based on the property that the grains are heated by irradiance from the star and emits the radiation by cooling in the form of thermal emission that is observed in the far infrared. I shall evoke the condition discussed above that the absorbing surface areas of the grains have smaller radii compared to the wavelength heating them. Dust scattering tends to peak along the direction of the incident radiation. Therefore that total emissivity when the dust grains cool is essentially the same as the absorption emissivity at infrared towards submillimeter wavelengths. The whole process of determining the equilibrium condition of the dust grains depends on solving the radiative transfer equation that incorporates the reactions of both gas and dust under heating by the stellar radiation, which is a complex problem and time consuming; therefore I will present here a very simplified analysis in which the dust temperature at equilibrium can be expressed in terms of the surface temperature of the star and the position (r) where dust occurs without solving the radiative transfer. The importance of this temperature in this study, is that we can use the Wien's law to crudely estimate the peak position of the dust emission occurrence corresponding to the wavelengths used in our observations.

In order to derive this equilibrium temperature for an optically thin CSE, we can use the assumption that the star emits as a black body source, then power absorbed by the grains ($P_{abs}(\lambda)$ can be estimated as follows

Lets assume that a photon emitted by the star randomly ant any position has W(r) probability that it leaves the surface of the star and interact with the dust envelope. W(r) can be viewed as the fraction of the solid angle covered by the star

with respect to the observer, and is defined by

$$W(r) = \frac{1}{2}\left[1 - \sqrt{1 - \left(\frac{R}{r}\right)^2}\right] \tag{5.18}$$

This means that photons emitted close to the surface of the star when r $\sim$ R, have about 50% of being intercepted back to the star. And when photons are at larger distances where r larger than R, then W(r)$\sim$ (r/2R)$^2$.

When the diluted radiated reaches the CSE and heats the dust grains, the intensity as function of distance from the star is

$$I_{abs}(r,\lambda) = I_0(\lambda).W(r)$$

where $I_0(\lambda)$ is the original intensity of the star

$$\mathrm{P}_{abs}(r,\lambda) = \int_0^\infty I_0(\lambda).W(r).[C_{abs}(\lambda)]d\lambda$$

Assuming that the star emits as black body source,

$$I_0(\lambda) = B_\lambda(T_*)\text{and also using} \quad C_{abs}(\lambda) = \pi a^2.Q_{abs}(\lambda)$$

Then

$$P_{abs}(r,\lambda) = \int_0^\infty B_\lambda(T_*)W(r)[\pi a^2 Q_{abs}(\lambda)]d\lambda \tag{5.19}$$

$T_*$ is the temperature of the surface of the star with radius R.

The power emitted by dust grains as they cool in the infrared is given by

$$P_{cool}(r,\lambda) = \int_0^\infty B_\lambda(T_{dust})[\pi a^2 Q_{abs}(\lambda)]d\lambda \tag{5.20}$$

under the assumption that dust particles emits as back body sources with tem-

perature $T_{dust}$.

At equilibrium equations 5.19 and 5.20 are equal, and using equation 5.12 gives the final result of the equilibrium temperature as,

$$T_{dust} = T_* \mathrm{W}(r)^{\frac{1}{\beta+4}}. \tag{5.21}$$

If r is larger than R, W(r)$\sim$ (r/2R)$^2$, equation 5.21 takes the useful form of

$$T_{dust}(r) = T_* \left(\frac{\mathrm{R}}{2r}\right)^{\frac{2}{\beta+4}}. \tag{5.22}$$

Equation 5.22 tells the equilibrium dust temperature is expected to decrease with distance from the star, and also, there is a strong dependence of $T_dust$ with the value of $\beta$. Thus the interplay between $\beta$ and $r$ has influence on the position of where dust particles occurs because $\beta$ depend on the composition of the dust particles assumed on the circumstellar shell. Even though this equation 5.22 shows the decrease in dust temperature with distance from a star, we do not expect that any significant change in equilibrium temperature of a shell at a particular location away from the star. This is because if the the shell can be assumed to have the same surface brightness when observed at a single wave band, so the dust temperature can be assumed not to change within a shell. The extended emission around aging stars is done in such a way that there are more than two wave band observations, such that one can assume the same dust temperature inside the shell probed by different filters.

The value of $\beta$ can be determined using the flux coming from a shell containing dust. This is because the dust particles modifies the flux coming from the star, the flux observed will have the spectral index of emission due to the extinguishing particles. In this work, we assumed that a circumstellar shell has the same composition of dust particles, such that the dust contained should have a specific value of beta. The shells reported in this thesis were mapped at more than one wavelength filters in

the infrared, this allowed the value of beta and the dust equilibrium temperature to be calculated from the ratio of the fluxes coming from the shell. We are going to see how this method of determining $\beta$, $T_{dust}$ is performed using far-infrared emission presented in section 5.5.2 below.

## 5.4 Determination of the mass of the dust contained in the circumstellar shell

The mass of the dust in the circumtellar shell can be directly determined from the flux density ($F(\lambda)$) emitted by dust grain if we assume that the shell is optically thin and emits radiation in the far-infrared. Let us first consider what happens when the dust particle is heated by radiation from the star. A grain placed at some distance $r$ from the star, will absorb or scatter radiation, the efficiency with which it does so depends on the wavelength of radiation and also on the nature of the grain. In general we expect that absorption will be most efficient at shorter wavelengths, say from optical to the ultra violet wavelengths. The grains are more likely to absorb radiation that causes the grain to heat up and gain thermal energy, the grain will increase in temperature such that it emits this radiation just like any hot body will do. This occurs until the grain reaches equilibrium when the rate of absorption is equal to the rate of emission.

Let suppose that the star radiates as black body with luminosity ($L_{ast}$) illuminating a grain that has radius $a$, that is located at distance $r$. The star can be assumed to emit radiation isotropically, such that a spherical grain will intercept a fraction $\frac{\pi a^2}{4\pi r^2}$ of the star's radiation. Thus the total power that the grain absorbs is

$$L_{grain}(abs) = L_{ast}.\frac{\pi a^2}{4\pi r^2}$$

at grain site. The grain will attain an equilibrium temperature ($T_d$) when it emits

as much as it absorbs. If the radiation from the the star is very hot for the grain to survive it is destroyed, otherwise if it survives the heat most of the radiation it emits is at lower wavelengths for example at infrared - radio.

An observer on Earth 'sees' the emitted radiation by the grains inside the shell for a star located at distance (D) away. The flux emitted by each grain can be assumed to be

$$F_i = Q_{abs} 4\pi B_\lambda(T_d),$$

that is we assume that grains emits isotropically as black bodies with emission extinction efficiency provided by how much the grains absorbs from star. So for a shell of volume V containing N number of dust particles, the flux ($F(\lambda)$) observed at distance (D) at some wavelength ($\lambda$) in the infrared can be express by summing all individual grain's contribution such that,

$$F_\lambda = N.Q_{abs} 4\pi B_\lambda(T_d).\frac{\pi a^2}{4\pi D^2} \tag{5.23}$$

where $F_\lambda$ could be the flux measured by on board telescope at using a filter at one of the wavelengths e.g. $\lambda - 60\mu m, 90\mu m 160\mu m$etc. for the data considered in this thesis. The total flux density observed at distance D at that particular wavelength is

$$F_\lambda = \frac{N\pi a^2 Q_{abs}(\lambda) B_\lambda(T_d)}{\mathrm{D}^2} \quad \text{in Jy} \tag{5.24}$$

The total mass of the dust contained in CSE

$$M_{dust} = N.v_d.\rho_d \tag{5.25}$$

where $v_d$ and $\rho_d$ are volume and the density of each grain.

We can eliminate N in 5.25 and 5.24 to solve for the dust mass

$$M_{dust} = \frac{v_d \rho_d F_\lambda \mathrm{D}^2}{\pi a^2 Q_{ext}(\lambda) B_\lambda(T_d)} \tag{5.26}$$

since the grains are assumed to be spherical, $\frac{v_d}{\pi a^2} = \frac{4a}{3}$ and we recover $\kappa_{dust}(\lambda, a)$ already defined in equation 5.14. Thus the final result of dust mass is

$$M_{dust} = \frac{F_\lambda \mathrm{D}^2}{\kappa_{dust}(\lambda) B_\lambda(T_d)} \quad \text{units of grams in cgs} \tag{5.27}$$

The mass of the dust determined by this formalism depends on the measured flux ($\mathrm{F}_\lambda$), the distance (D) to the star, and also the mass absorption cross section($\kappa_\lambda$. There are uncertainties associated with each factor that I will discuss later when focus on observations. In the next section I will show how the total mass of the shell can be determined from mapping the stars at far infrared.

## 5.5 Mass of the Circumstelar Dust Shell

In order to calculate the mass of the whole CSE, the ratio of dust mass to the mass of the gas called $\psi$, has to be known. Then assuming that the total mass of the shell comes from the gas component, primary molecular hydrogen and hydrogen gas and other molecular particles like CO molecules. We can estimate the total mass of the shell ($M_{shell}$) as follows,

$$\begin{aligned} &M_{shell} = M_{dust}.\psi \qquad \text{where} \\ &\psi = \tfrac{M_{gas}}{M_{dust}} \end{aligned} \tag{5.28}$$

$M_{dust}$ is calculated from, equation 5.27. The final mass of the whole shell is,

$$M_{shell} = \frac{F_\lambda \mathrm{D}^2}{\kappa_{dust}(\lambda) B_\lambda(T_d)} \left[\frac{M_{gas}}{M_{dust}}\right] \tag{5.29}$$

The value of $\psi$ needs to be known in order to determine the total mass of the shell. There are uncertainties that are related to how $\psi$ is obtained, therefore it is important to discuss a few aspects of how I chose the values of $\psi$ used in this thesis.

### 5.5.1 Mass of gas to Dust

In any astrophysical environment there are few dust particles compared to the molecular counterparts, this includes the composition in the ISM and also in the circumstellar envelopes of intermediate mass stars considered for this work. Interestingly, even if there are a few of them and are small, their effect on radiation can be substantial. Dust storms here on earth can block light from the sun such that even on a clear it gets dark if you are inside the dust cloud. On the stellar sites, constitute a small fraction and are subject to very harsh conditions because the stars are hot they can can get destroyed easily ad their presence depends onto the availability of the atoms they are made of. For example, Silicates or forsterite formation into grain on the CSE's of oxygen rich stars, depends on the over abundance of oxygen atoms available after the molecular CO molecule has formed. Even on carbon rich stars, CO molecule is always more stable such that any carbon dust grains forming will depend on the ratio of carbon to oxygen atoms present in the shell. The value of $\psi$ therefore has been formulated under those conditions (see Olofsson, Chapter 7, Asymptotic Giant branch Stars,editors, H Harbing & Ollofson) to show that

$$\frac{1}{\psi} \leq \left[ X. \left( \frac{C}{O} - 1 \right) . \frac{O}{H} . \frac{v_d}{v_\infty} \right] \tag{5.30}$$

Notice in equation 5.30 that $\frac{1}{\psi}$ is ratio of dust to mass, and X is the ionization fraction of all atoms with respect to Hydrogen, $v_d$ and $v_\infty$ are dust and expansion velocities respectively. There is a good correlation of this formalism with data of carbon rich stars. Observations by Groenewegen 1997, showed $\psi$ seems depend on the

the period of pulsation, i.e. carbon stars with periods that are lower than 500days, have constant dust to gas($\frac{1}{\psi} \approx 0.0025$) suggesting $\psi = 400$. And also these observations showed that once the star enters the super wind phase P$\geq$ 500 the value of $\psi$ decreases (more dust) to a maximum 67. Thus the dust to mass ratio of 400 is used to calculate the shell mass for carbon rich stars because of the limit imposed data and equation 5. And also the observations by Knapp, 1985 gives $\psi$ of 386 $\pm$ 90 in good agreement with Groenwegen, 1997. The oxygen rich stars show a different variations in $\psi$, observations by various groups suggest different values, i.e.Knapp 1985 observations showed that the dust to gas of 170, and Justtanont,1994 reported values between 300-160, Whitelock, 1994 showed through observations a value 200. Therefore for oxygen rich stars a gas to dust ratio of 200 is assumed is is representative of the mean of all the observations cited here.

### 5.5.2 Spectral index ($\beta$) from FIR emission

The flux density shows the emission characteristics of the grains because of the appearance of the spectral index ($\beta$) on the right side of equation 5.24 through $Q_{abs}$. Since the flux density is a function of wavelength at a specific filter at which the observations, then equation 5.24 can be used to determine the spectral index provided that the flux is measured at more than two wave bands. This method requires the knowledge of the dust temperature inside in the circumstellar shell, which is also an unknown.

We can show this method by writing the flux density in the form,

$$\begin{aligned} &F_\lambda = K(T_d, \lambda, \beta)\lambda^{-(\beta+5)} \qquad \text{where} \\ &\mathrm{K}(T_{dust}, \lambda, \beta) = \left[\frac{2hc^2N}{Q_0\lambda_0^\beta\left(\exp\left(\frac{hc}{\lambda k_b T_d}\right)-1\right)D^2}\right] \end{aligned} \tag{5.31}$$

When the observations are done at more that one wavelengths, say at $\lambda_1$ and $\lambda_2$

with the corresponding fluxes, $F_{\lambda_1}$ and $F_{\lambda_2}$ the value of $\beta$ can be found from the ratios of the fluxes assuming that the temperature of the dust is constant in the CSE. The dust spectral index can be found by solving

$$\log\left\{\frac{F_{\lambda_1}[\exp\left(\frac{hc}{\lambda_2 k_b T_d}\right)-1]}{F_{\lambda_2}[\exp\left(\frac{hc}{\lambda_1 k_b T_d}\right)-1]}\right\} = -(\beta+5)\log\left(\frac{\lambda_1}{\lambda_2}\right) \tag{5.32}$$

Equation 5.32 is the solution for finding $\beta$ using 2 wavelength observations, if the temperature of the grains is known. However in general the dust temperature is not known, this means that another third observation is always required in order to get the two unknowns. This is the reason that most projects studying circumstellar dust shells uses multi-imaging photometry (see Speck et al 2000, Ueta 2005, Tuan et al. 2010).

In an event that only two observations are available, equation 5.32 can be solved analytically for $T_d$ and $\beta$. The Infrared Space Observatory (ISO) measured fluxes using infra-red photon mapping to construct at least two surface brightness maps at wave bands 50, 60, 90 and 160$\mu m$) of several oxygen rich and carbon rich stars that will be presented in Chapter 6.

The spectral index of emissivity also influences the shape of Spectral Energy Distribution (F($\lambda$)$vs\lambda$), because adding $\beta$ as seen in equation 5.32 shifts the maximum peak to longer wavelengths of Wiens law .Recalling that the Wien's law at the peak is used to determine the peak temperature. Most AGB stars that are infrared sources often exhibit bumps more than one bump in their SED, and extra component bumps, are associated with dust emission. The bumps in the SED usually occur at longer infrared wavelengths that indicate the presence of dust shells. The modified Wien's law takes the form

$$\lambda_{peak}.T_{dust} = \left[\frac{5}{5+\beta}\right] 2890\mu\, m.K \tag{5.33}$$

In equation 5.33, the flux coming from the the dust shell emission, determined by equation 5.24, will have a peak wavelength at different position than predicted using black body radiation without dust influence. Take $\beta = 0$, the Wien's law is recovered and for $T_{dust} = 20K$,$\lambda_{peak} = 145\mu m$. However for $\beta$ between (1 - 2); $\lambda_{peak}$ shifts to $\sim (120\mu m - 103\mu m)$ for $T_{dust} = 20K$. This difference in peak positions of the dust emission shows that different composition of dust grains will predict different peak positions in the bumps associated with dust emission.

Now let us look at the influence of equation 5.33 on the changes in equilibrium dust temperature at different positions away from the star predicted by equation 5.22. When combining these two equations, we get

$$r = \frac{R_*}{2}\left[\left(\frac{5}{5+\beta}\right)\frac{2890\mu mK}{T_*\lambda_{peak}}\right]^{-(\frac{4+\beta}{2})} \tag{5.34}$$

which shows that as the distance $r$ from the changes star in terms of $\lambda_{peak}$, different different wavelengths will probe different parts of the circumstellar shell.Take an example of an AGB star whose $T_* = 3000K, R_* = 3 \times 10^{13}$ cm and $\beta = 1$, at 50 $\mu$ m, $r_{50} = 3.5 \times 10^{17} cm \equiv 11.3pc$ and at $160\mu m, r_{160} = 8.3 \times 10^{18} \equiv 270pc$. Although, these are not the same radii at which most of the flux at these wavelengths originates, it is clear that different wavelengths probe different parts of the circumstellar shell.

In the next section I will derive the equations for the mass loss rates, associated with the flux measured at far-infrared. the change in density of the particles under expansion and also changing temperature distribution under the influence of dust (equation) .

## 5.6 Dust Mass Loss Rates by FIR emission

The general form of the mass loss rates was introduced in 4 using equation 4.2, that is

$$\dot{M} = 4\pi r^2 \rho(r) v(r)$$

The mass-loss rate defined in this way means that the mass-loss rate and the expansion velocity and the density are related. The changes in one parameter can cause significant changes in the others, for an example; if we assume that the mass loss rate is a constant , then if the velocity is also constant then the density of the particles is expected to assume inverse square law in which the density $\rho(r)$ should vary as $r^{-2}$. If we let the expansion velocity to change with radius at constant mass loss-rate we would get a different solution in density. So even on a simplest case of constant mass loss rate we can realize that the density distribution of particles will change depending on what one chooses for the functional form of velocity or the mass-loss rate. Many models of mass loss assumes a power law dependence in density to model the mass loss rate. The mass loss rates were not modeled in this thesis, the results from observations were compared with what models predict. In this section I am using the power-law to show how the existing mass loss rates are derived. This is because we compare the observations with the theory of mass loss rate that is still debatable since there is no formalized equation of mass loss.

Let us define $n(r)$ to be the number density of grains as a function of distance $(r)$ from the star, using a power law which indicate this change of density with radius.

$$n(r) = n_0 \left(\frac{r}{r_0}\right)^{-\alpha} \tag{5.35}$$

$n_0$ is the number of particles at some point relatively closer to the star $r_0$ whose value has to larger than at later times. The value of $\alpha$ is assumed to be a constant but can essentially take many forms depending on the distribution, for example we

should reproduce spherical symmetry if $\alpha$ is 2 or a very steeper decline if $\alpha$ is 3 etc. Lets apply this distribution on a shell bound by the inner radius at $R_{in}$ and outer radius $R_{out}$, with respect to the star of radius R. In this case the shell is spherically symmetric from the observers point of view, but the distribution of the grains inside are decreasing according to the power law, such that

$dV_{shell} = 4\pi r^2 dr$, the mass loss rates still assumes stationary conditions.

This means that the density distribution of the grains in the shell also assumes the power law dependence provided that, we assume that their masses have constant sizes. To see this,

$\rho(r) = \mathrm{m}_d.n(r)$ where $\mathrm{m}_d = \frac{4\pi\rho_d a^3}{3}$ = constant.

Then $\rho r_{dust}$ that appears in the mass loss rate will have the same power law dependence as the number density. This assertion has the following significance on the mass loss rate of the dust.

$$\dot{M}_{dust} = 4\pi m_d n_0 r_0^{\alpha}(r)^{2-\alpha} v_d \tag{5.36}$$

If $v_d$ is assumed to be constant in a shell; then if $\alpha = 2$, the mass loss rate is a constant with a spherical outflow at $r = r_0$, with a rate of,

$$\dot{M}_{dust} = 4\pi m_d n_0 r_0^2 v_d \tag{5.37}$$

For $\alpha = 3$,$\dot{M}_{dust}$ will have $r^{-1}$ dependence.

If the velocity of the dust depends on the distance and then the mass loss rate can take different forms. The mass loss rates considered here comes from the emission in the extended emission due to dust far from the transonic region, so we can assume that the dust and gas moves at the same velocities determined by the expansion of the gas that is usually assumed to be constant. Such assertion has its short comings, because observations oxygen rich stars and carbon rich stars indicates that the mass

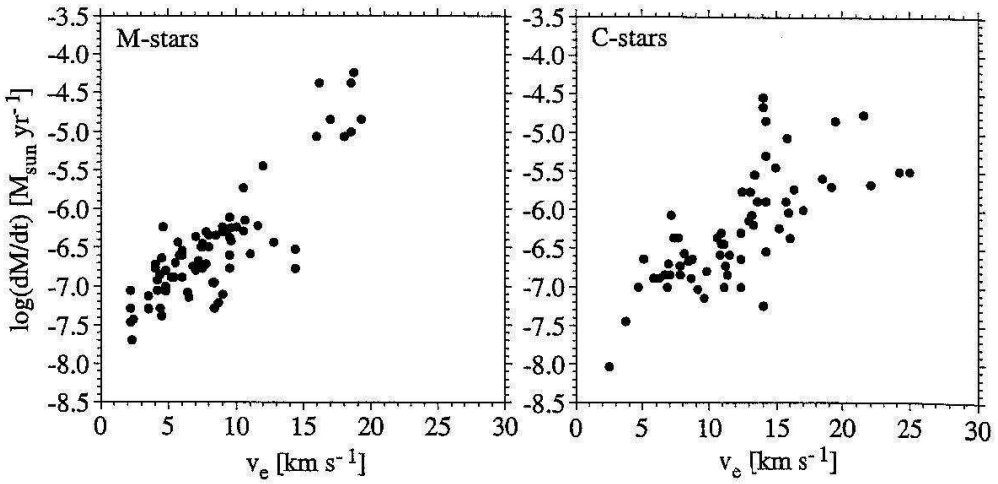


Figure 5.2: The circumstellar gas expansion velocities vs. mass loss rate for M-stars and C-stars(Data from Gonzalez et al. 2003 [44])

loss rates increases with increasing expansion velocities (Habing & Olofsson 2003,). See figure 5.6 below.

From this data the mass loss rates seems to be constant at gas expansion velocities between 15 - 20km/s. Therefore I assumed the a maximum of 20k/ms expansion velocities in determining the mass loss rates. This is because the mass loss rates derived from the far-infrared emissions have functional forms that depends on knowing the expansion velocity of dust grains in CSE.

To determine the mass loss rates from far-infrared emission, the flux density from the mapped CSE has to be known. This is based on the theory presented below, in which the luminosity or the power coming from dust grains in the CSE is used measured the flux density at some distance D from the observer.

The Flux density is related to the luminosity function,

$$F_{dust}(\lambda) = \frac{L_{dust}(\lambda)}{4\pi D^2}$$

where the luminosity is

$$L_{dust}(\lambda) = \int_{R_{in}}^{R_{out}} 4\pi r^2 n(r) 4\pi a^2 Q_{abs}(\lambda, a) B_\lambda(T_d) dr \tag{5.38}$$

If the number density distribution assumes the power law from equation 5.35, the flux density can be written in terms of the constant mass of the grains as well as their mass absorption cross section at distance D. This is achieved by eliminating the radius of the grains in equation 5.38 and using equation 5.35, since the integrand depends on distance ($r$). The temperature of the grains can vary with distance or can be a constant depending on the region of CSE considered. Using these conditions, the flux density that assumes power law distributions can be written as,

$$\mathrm{F}_{dust}(\lambda) = \frac{4\pi \kappa_{dust}(\lambda) m_d n_0 r_0^\alpha}{D^2} \int_{R_{in}}^{R_{out}} B_\lambda(T_d) r^{2-\alpha} dr \tag{5.39}$$

where $m_d$ and $\kappa_{dust}(\lambda)$ are the mass and the mass absorption per cross section of the dust grains. There are various cases to consider here with respect to optical thin CSE's with $\alpha = 2$, 1) if the temperature of dust varies with distance r, and also that at shorter wavelengths the source is unresolved, one can assume the most general case by integrating equation 5.39. It can be shown that if one change variables in equation 5.39,

$$x = \frac{hc}{kT_d} = \frac{hc}{kT_*} \left(\frac{R_0}{r}\right)^{-\frac{2}{4+\beta}} \quad \text{where} \quad R_0 = \frac{R_*}{2}$$

$$F_{dust}(\lambda) = \frac{(4+\beta)h}{c^2} . \frac{\kappa_{dust}(\lambda) . \mathrm{R}_0}{v_d D^2} \left(\frac{kT_*}{h}\right)^{\frac{4+\beta}{2}} (\lambda)^{\frac{\beta-2}{2}} \zeta(x_{in}, out) \tag{5.40}$$

where

$$\zeta(x_{in}, out) = \int_{x_{in}}^{x_{out}} \frac{x^{\frac{\beta+2}{2}}}{e^x - 1} dx$$

2) In a situation in which a star has inner shell and an extended emission. Under

the assumption that these regions can have space density proportional to $(\frac{1}{r^2})$ and constant expansion velocity. We can apply derivation of the surface brightness by Gillett et. al. 1989,i.e.

$$I_\lambda = 2\pi\kappa_{dust}(\lambda)m_d n_0 r_0^\alpha \int_{R_b}^{R_{out}} \frac{B_\lambda(T_d)dr}{r^{\alpha-1}(r^2 - R_b^2)^{\frac{1}{2}}} \tag{5.41}$$

where $R_{in} \leq R_b \leq R_{in}, R_b$ is the projected physical distance from the source in the sky. The Flux densities derived by using equation 5.41 , in terms of mass loss rates, are,

$$F_\lambda(b) = \frac{\dot{M}_{dust}\kappa_{dust}(\lambda)B_\lambda(T_d)}{2\pi v_e R_b} \begin{cases} \cos^{-1}\left(\frac{R_b}{R_{out}}\right) & \text{for} \quad R_{in} \leq R_b \leq R_{in} \\ \cos^{-1}\left(\frac{R_b}{R_{out}}\right) - \cos^{-1}\left(\frac{R_b}{R_{in}}\right) & \text{for} R_b \ll R_{in} \end{cases} \tag{5.42}$$

## 5.7 Other methods of getting the flux density

The flux density derived in in 5.19 can be written in terms of the optical depth and the angular diameter $(\Delta\Omega)$ of the beam measured at distance D from the star

$$F_\lambda = (1 - e^{\tau\lambda}).B_\lambda(T_d).\Delta\Omega \tag{5.43}$$

if the CSE is optically thick at visual wavelengths but optical thin at infrared , ie $\tau_\lambda \leq 1$ at IR we can use expansion series $e^{\tau_\lambda} \approx 1 + \tau_\lambda$ then

$$F_\lambda = \tau B_\lambda(T_d).\Delta\Omega \tag{5.44}$$

To get $\tau$ requires the knowledge of extinction at visual as well as at the IR, this is because $\tau_\lambda$ is related to the extinction $(A_\lambda)$, i.e.

$$A_\lambda = -2.5 \log \tau = 1.087\pi \int a^2 Q_{ext}(\lambda) n(a) da \tag{5.45}$$

To find $A_\lambda$ requires one to know or assume the number density distribution like MRN presented above and also the extinction emissivity from the laboratory data.

## 5.8 Radiative Transfer

In the generalized form of 5.1 there are no sources and the equation of radiative transfer takes the simplified version. Lets look at the most generalized form of radiative transfer that is considered when calculating the optical depth in dusty circumstellar shells. Suppose $J_\lambda$ is the mean intensity heating the dust grains from the star such that when angle averaged over the total surface of the grain,

$J_\lambda = \frac{1}{4\pi} \int_0^\infty I_\lambda d\Omega$

where $d\Omega$ is the differential solid angle and $I_\lambda$ is the mean intensity that is observed coming out of the shell and is associated with cooling effect from the dust shell.

$$\mu \frac{\partial I_\lambda}{\partial r} + \frac{1-\mu^2}{r} \frac{\partial I_\lambda}{\partial \mu} = -\kappa_\lambda \rho (I_\lambda - J_\lambda) \tag{5.46}$$

where $\mu = cos\theta$, $\theta$ is the angle between

The determination of flux in the FIR depends on knowing the area (or the size of the shell ) mapped covered by observation at that particular wavelength used. FIR emissions are generally faint observations that generally suffer from cirrus emission; The stars are normally in the vicinity of a bright areas that raises the background emission in which part of the shell exist, this effect causes the uncertainties measured flux coming from the star. This means that under-estimating the size of the shell and also background subtractions, can cause uncertainties in the measured flux measured that may cause the decrease in the mass of dust calculated.

# Chapter 6

# Observations

## 6.1 Introduction

AGB stars are bright and numerous enough to allow detailed observational exploration of infrared imaging photometry to be performed e.g IRAS (Infra-red Astronomical Satellite; Neugebauer et al. 1984[99]) and KAO (Kuiper Airborn Observatory; Harwit et al. 1990 [52]). The availability of observational data has since increased drastically due to the creation of of additional space-based infrared telescopes ISO(Kessler et al. 1996), Spitzer Space Telescope (Werner et al. 2004 [37]). These observations opened the way for spectra and photometric studies in wavelength regions inaccessible from the ground.

In the following sections we briefly highlight how ISO made these observation before the discussion of data reduction and analysis. This is essential, since ISO data contained many artifacts that were related to detector array's performance, and also there were noise confusion for infrared measurements. Henceforth, the collection of these artifacts caused the data not to be scientifically validated when the project (by SMK00) was initiated, however since then, the reduction procedures improved e.g.

for filters $90\mu m \leq 200\mu m$ have become scientifically validated under corrections / procedures to be discussed below. For more details see Kiss et al. 2005 [71], Juvela et al. 2009 [67].

### 6.1.1 ISO-Imaging photo-polarimeter: ISOPHOT

European Space Agency's (ESA) Infrared Space Observatory (ISO; Kessler et al. 1996) is an astronomical satellite that was operational between November 1995 and May 1998. It operated at wavelengths from 2.5 to 240 microns in the infrared, making it possible to obtain a continuous flux spectra and various imaging surveys extending from visual to FIR for many stars. ISOPHOT was designed and built by a consortium of various science institutes and industrial enterprises in Europe (Lemke et.al 1996). We used ISOPHOT far infrared mapping capability to explore the circumstellar regions around our observed stars. The primary mirror of ISO had a diameter of 60cm. The imaging photo-polarimeter on ISO PHT-C consisted of two gallium-germanium array detectors, C100 and C200. ISOPHOT used the AOT PHT-C 32 two array detector arrays, namely; C100 and C200. The size of the C100 array is 3×3 pixels, with $43.5 \times 43.5 arsec^2$ each; and the C200 array has 2×2 pixels, with$89.5 \times 89.5 arsec^2$ each. All short wavelengths observations were performed using the C100, namely, 60$\mu$ m, 90$\mu$m in our sample and for long wavelengths observations namely, 160 $\mu$m, 120$\mu$m and 180$\mu$m, the C200 was used. The C100 and C200 PHT32 array detector pixels are shown in Figure 6.1, a diagram from online material by Schulz et al. 2002.

The flow of signal from the source star entering the ISO telescope apertures reaching these array detectors is indicated in Figure 6.2.

For each observation, the telescope was pointed towards the source and a scan direction was chosen from which the images of surface brightness were to be constructed. All the images were constructed using the chopper. The chopper was used

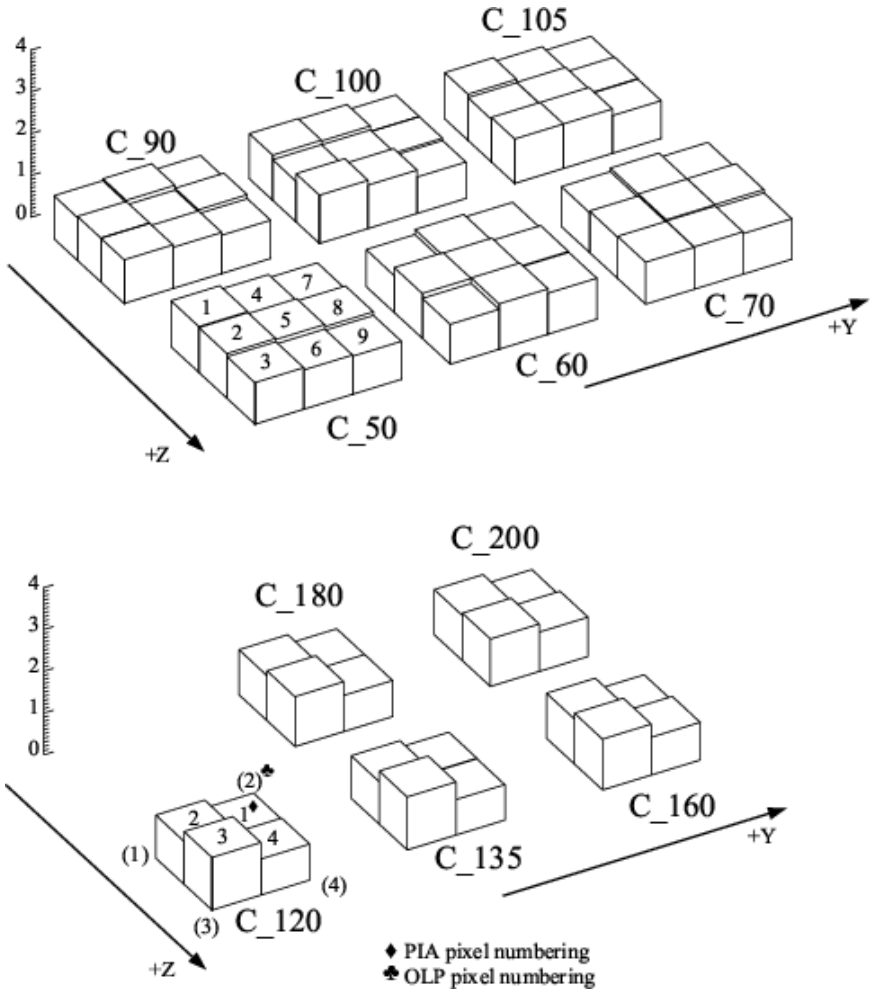


Figure 6.1: Relative illumination of the array detectors C100 and C200. Pixel numbers and ISO coordinate axes are given. Figure from Schulz et al. 2002

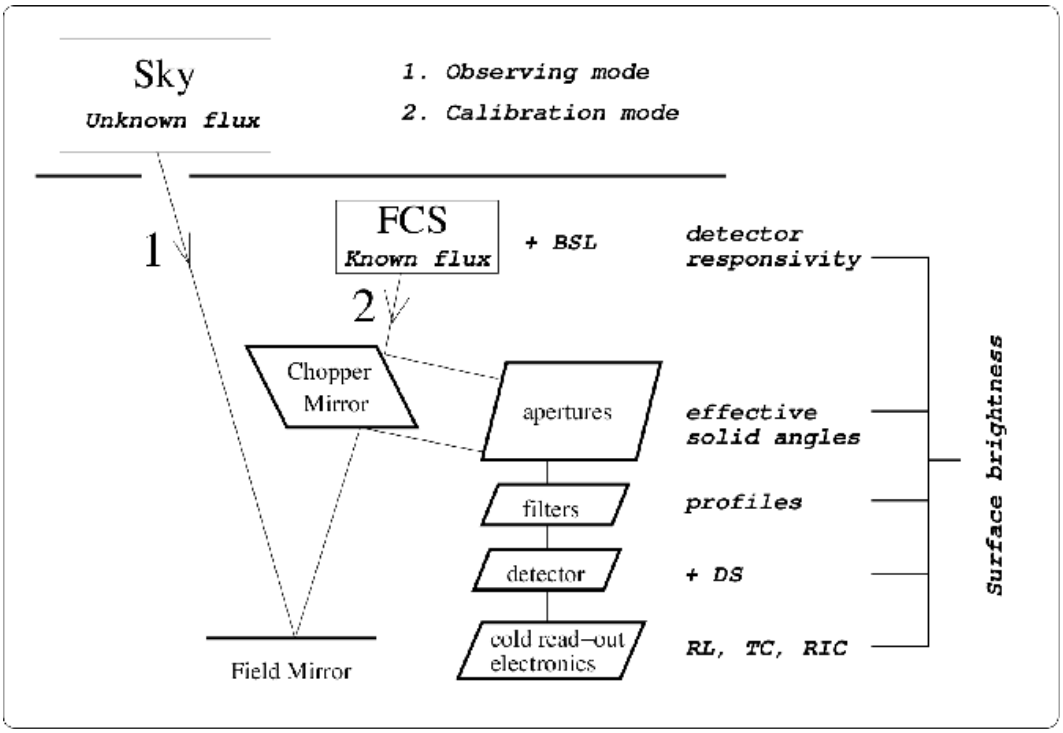


Figure 6.2: Scheme of the ISOPHOT calibration steps associated with the different instrument components. The meaning of the abbreviations is the following: BSL = Bypassing Sky Light correction, DS = detector Dark Signal, RL = Ramp Linearisation, TC = signal Transient Correction, and RIC = Reset Interval Correction. A diagram from Juvela et al. 2009 [67]

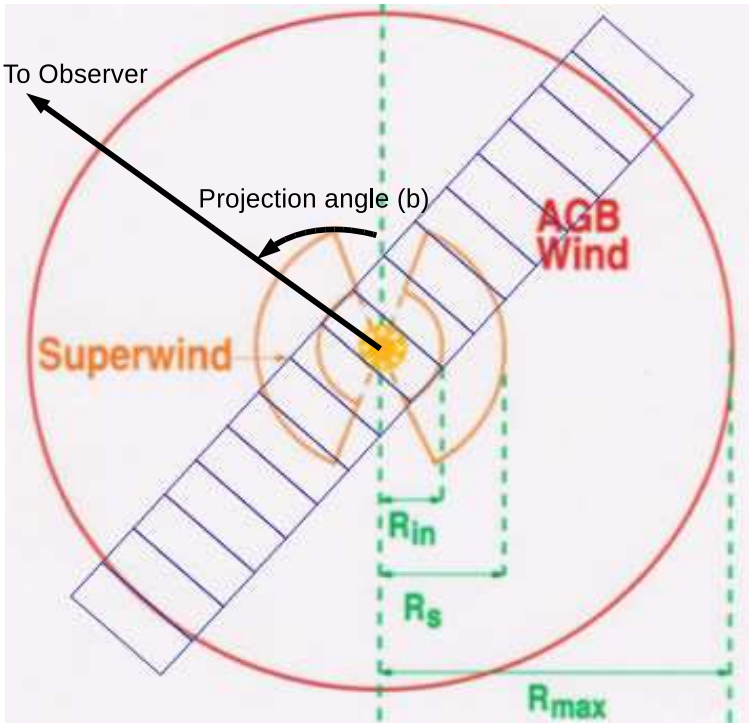


Figure 6.3: A geometric view of the fossil dust shell of a post AGB star showing a super-imposed mode of ISO ′s PHT32 AOT scanning observations. See text for more details.

measure the flux at different spacecraft positions along the scan line as indicated by the overlaid grids in Figure 6.3.

During observations, the same celestial position was observed more than once during several raster pointing's (telescope pointing's), with an aim of elimination of temporal changes in detector response. At several spacecraft positions, the chopper made 3 observations per pixel one times per raster point/ position. This caused the oversampling factor of 1/3 per pixel at a direction orthogonal to the scan line, which resulted in only half of the array to be used. This mode of observation, called PHT32 AOT (Astronomical Observing Template), was chosen for this project because it provided a better oversampling that provides a better spatial resolution for the extended emission to be investigated around our source objects. For the C100 array detector, the chopper was commanded to perform in sawtooth mode with 13 chopper

steps with 15 arcsec separations symmetrical to the center field of view. For C200, the chopper was commanded to perform in sawtooth mode with 7 arcsecs chopper steps with 30 arcsecs separations. For every star, the background at each of the 9 (for C100) or 4 (for C200) pixels was obtained from the off1 and off2 images about $2.5'$ closer to the celestial pole in - order to account for the uniform background on each image. Thus the pixel sizes changed due to the oversampling method e.g. in the C100, using $1/3(43.5)'' \times 1/2(43.5 + 2.5)''$ will result on the pixel scale of $15'' \times 23''$ in the $90\mu m$ filter images. The flux of each pixel was divided by the background flux of the corresponding pixel and multiplied by the average of the total number of pixels.

Calibration measurements were performed at dark and two off sequence positions using Fine Calibration Sources (FCS) on board the satellite. So every signal of light reaching the detector was bracketed by two calibration measurements using the FCS's. The final signals at the the detector were calibrated into flux by using bright point-sources e.g. asteroids such as Vesta and Ceres that were were measured prior ISO mission.

The infrared photons that are collected using the chopper and space craft raster positions are used to construct surface brightness images. The measurement of how much photons fall into the detector in order to construct a signal, is found by using how much voltage increase the the photons cause on the detecting amplifier over the chopper duration[1]. Since the increase in voltage is proportional to the increase in current (I) which in turn is proportional to the number of photons collected, the signal can be constructed. A signal ($S_{signal}$) is defined as the slope of the in crease in voltage increase over duration time.

$$I = \frac{\Delta Q}{\Delta t} = C_{int}\frac{\Delta V}{\Delta t} = C_{int}.S_{sig}$$

where $C_{int}$ is the internal capacitance of the detector and $S_sig$ is the signal in V/s.

[1]in ISO this time is called *chopper dwell time* or the duration of chopper plateau

The current is measured in Ampere′s (A). For the C200 and C100 array detectors, it was assumed that the values of $C_{int}$ remained constant throughout ISO mission. Then many signal collected by the movement of the chopper integration time[2], are used in final image construction per pixel that is considered.

For the observer, the signal is a fundamental concept: once signals from the source is obtained and calibrated using calibration standards (e.g FCS), it is possible to relate the signal to a power from the source at a specific filter band used. When the signal reaches the detector, it get registered using all pixels of an array. This means that the user had a choice of using one of any pixels (or the combination pf pixels) in both detectors to construct the image from the data. The detection of photons on the other hand depends on the detector characteristics of gallium-germanium array detectors (C100 & C200). When recording the signal, a detector is characterized by the detector responsivity $R_{det}$ which is the ratio of the photo-current and the in-band power $P_{source}$ (Watts) for a signal at a particular filter. $R_{det}$ is defined as

$$R_{det} = \frac{I}{P_{source}} \quad (A/W) \tag{6.1}$$

$R_{det}$ is not a constant over time when the signals arrive at the detector, it depended on external parameters such as the *strength of the ionizing radiation* and the *flux history*. The flux history on each of PHT 32 detectors caused detector transients that affected our data. A discussion of the detector transients and their corrections is presented on the data reduction section 6.1.4.

The in band power also called the source signal power, can be derived from signal (slopes of voltage increase) and responsivity, if the capacitance of the integration $C_{int}$ , are known by inverting Equation 6.1.

[2]This time is the total time necessary to perfom a measurement at source position, it excludes the time measured by chopper at background position

$$P_{source} = \frac{C_{int}.S_{sig}}{R_{det}} \quad (W) \tag{6.2}$$

The flux $F_{IR}$ is constructed from signal power i.e.

$$\frac{F_{\nu}}{k_{col}} = \frac{\Sigma P_{source}}{C_{const}.f_{psf}}(Jy) \tag{6.3}$$

where $k_{col}$ is the color corrector for a filter, $C_{const}$ is a constant in $m^2.Hz$ that describes the transmission of the signal, $f_{psf}$ is the dimensionless fraction of the ISO point-spread function entering the field aperture falling into the entire array of the PHT-C. When collecting photons, the voltage increases until a cut-off output voltage set at Cold Read-out Electronics (CRE) of the detector is reached. A reset pulse is then applied to the signal pulse after the number of desired voltages had been sampled. The readout associated with this reset is called the destructive readout; the other sampled voltages are called non-destructive readouts. The time between two reset pulses (in seconds) is called the fundamental integration time, or reset interval. A ramp is a collection of readouts that makes the slopes at different reset intervals. The photometric map is constructed by convolving all the signals (V/s) into surface brightness (MJy sr$^{-1}$)[3] covered by the area scanned by the chopper.

In doing so, a mini map of the surface area vs. brightness at a particular position is formed using raster positions. To construct a photometric map , the raster positions are mossaicked (stiched together) to form a final image. The surface area where brightness is measured is expressed in angular scale e.g. arcsecs or galactic co-ordinates, and the brightness (MJy $sr^{-1}$) covered over the area observed. To get the flux density (Jy) of a particular area in the map, the surface brightness is multiplied by the emitting physical surface area covered within the map. For more information of how ISOPHOT photo-polarimeter produced surface brightness maps from infrared

[3]MJy sr$^{-1}$is the surface brightness unit equivalent to 2.35 $\times 10^{-5}$ Jy.arcsec$^{-2}$

photons, refer to the ISO hand book manual (ESA SP-1262,Volume IV,PHT, version 2.0.1,2003, Laureijis et. al 2003 [81], herafter ISOHABO03).

### 6.1.2 Photometry

The exact nature of signal processing for PHT 32 raster maps can be found on Chapter7 section 7.7 of ISOHABO03, here a brief description of the determination of the source in-band power for chopped observations using all pixels for a given PHT-C array is given, and furthermore the methods applied to derive infrared images is presented. The observations presented, intended to measure extended emission of a point source flux with PHT-C detector arrays. On the basis of ISO, the total power on the array is determined by summing the respective powers over all pixels $P_i(s)$ such that $P_{source}$ given by equation 6.2 is modified to give

$$P(s) = \Sigma_i P_i(s) \tag{6.4}$$

where s $\equiv$ source.

For the source and the background (b) powers,

$$\begin{aligned} P(s+b) &= \Sigma_i P_i(s+b) \\ P(b) &= \Sigma_i P_i(b) \end{aligned} \tag{6.5}$$

To get the final source power, and the power uncertainties the following relations were applied,

$$\begin{aligned} P(s) &= P(s+b) - P(b) \\ \sigma_P &= \sqrt{\Sigma_i \sigma^2 P_i} \end{aligned} \tag{6.6}$$

A 2 dimensional Gausian function was fitted to the intensity pattern on the array. This process was done in addition to the sum of all pixel in band powers. However in

the case of faint sources and noisy data, the derived fluxes suffered high uncertainties, this has caused point source photometry not to be scientifically validated. Instead surface aperture photometry is the best way to account for point source. The point source here refers to a single identifiable localized source of light with negligible extent in distinguishing from other source geometries; and it is modeled mathematically by a point source spread function (PSF) or an impulse response whose distribution is usually Gaussian and extended source emission. The fitting of the 2D Gaussian point source in the C-arrays was performed using NAG mathematical routines library e.g[108]. The fitting functions used under NAG library routines were,

$$\begin{aligned} g(x,y) &= c + de^{\frac{z^2}{2}} \quad \text{where} \\ z^2 &= (x-x_0)^2 + (y-y_0) \end{aligned} \tag{6.7}$$

where (x,y) are pixel positions; c is the constant background; d is the background subtracted height of the peak source centered at $x_0$ and $y_0$; x and y are offsets of the peak from the array center. The accuracy of this method depended on the correctness of assumption of a Gaussian on top of a constant background.

In the case where the pixels were missing, the interpolation[4] was performed for undefined in-band powers for those pixels. See section 8.4.4 of **??**.

To convert the mean in-band power on a PHT-C detector pixel to monochromatic flux density (Jy) a constant $\nu\ F_\nu$ spectral energy distribution was assumed. It follows from Equation 6.3 that the flux $F_\nu(\lambda)$ with its uncertainty can be derived using Equation 6.5 i.e.

$$\begin{aligned} F_\nu(\lambda) &= 10^{26}\frac{P}{C1.f_{PSF}(\lambda,aperture)} \quad \text{Jy} \\ \Delta F_\nu(\lambda) &= 10^{26}\frac{\sigma_P}{C1.f_{PSF}(\lambda,aperture)} \end{aligned} \tag{6.8}$$

where $f_{PSF}(\lambda, aperture)$ is the fraction of the telescope point source spread func-

[4]Interpolation is a method of constructing new data points within the range of a discrete set of known data points or pixels.

Table 6.1: Photometric parameters

| Detector array | Filter ($\lambda_c$) ($\mu$ m) | Aperture [arcsec] | $f_{PSF}$ [arcsec] | $\Omega_{eff}$ ($\times 10^{-7} sr$) | C1 $[10^{11} m^2 Hz]$ | Background (MJy $sr^{-1}$) | Sensitivity (mJy) |
|---|---|---|---|---|---|---|---|
| C100 | 60 | 43.5×43.5 | 0.667 | 0.357 | 0.659 | 10 | 7.5 |
| | 90 | 43.5×43.5 | 0.586 | 0.4577 | 1.51 | 10 | 7.5 |
| C200 | 160 | 89.4×89.4 | 0.620 | 1.94 | 1.01 | 5 | 40 |
| | 120 | 89.4×89.4 | 0.678 | 1.78 | 0.355 | 5 | 40 |
| | 180 | 89.4×89.4 | 0.609 | 1.96 | 0.537 | 5 | 40 |

tion falling onto a FULL aperture array for PHT-C. C1 is a constant related to each filter band and describes the total transmission of the bandpass along the optical path onto the detector; this includes the size of the mirror, reflections filter transmission and the spectral response of the detector. ISO intensity fraction $f_{PSF}$ of a point source response function and the the sensitivity of the detectors are given in Table 2 of Schulz et al. 2002, here we only show those parameters used in our analysis. This is shown in Table 6.1.2

The surface brightness ($I_\nu(\lambda)$ and the uncertainty $\Delta I_\nu(\lambda)$ of the resulting image is derived from the flux density $F_\nu(\lambda)$ from equations 6.8.

$$\begin{aligned} I_\nu(\lambda) &= \frac{F_\nu(\lambda).f_{PSF}}{(1-\epsilon^2).\Omega_\lambda} \\ \Delta I_\nu(\lambda) &= \frac{\Delta F_\nu(\lambda).f_{PSF}}{(1-\epsilon^2).\Omega_\lambda} \end{aligned} \tag{6.9}$$

$\Omega_\lambda$ is the effective solid angle on the sky of the detector pixel or selected aperture; $(1-\epsilon^2)$ is the correction for obscuration by the secondary mirror.

Since ISOPHOT detectors were calibrated against a flux grid of celestial point source standards consisting of stars, asteroids and planets, the flux measured covered a range between $\sim$ 100mJy - 1000Jy. This included the minimum flux sensitive on the C-array detectors given in Table 6.1.2, see Shulz et al.2002 section 5. To estimate the flux of an unknown source, each detector aperture/pixel was *individually* calibrated against these celestial standards. The point source used to calibrate the flux was constructed by convolving the pixel psf with the aperture response.

First the ISOPHOT′s effective solid angles were determined by 2-D scanning of a

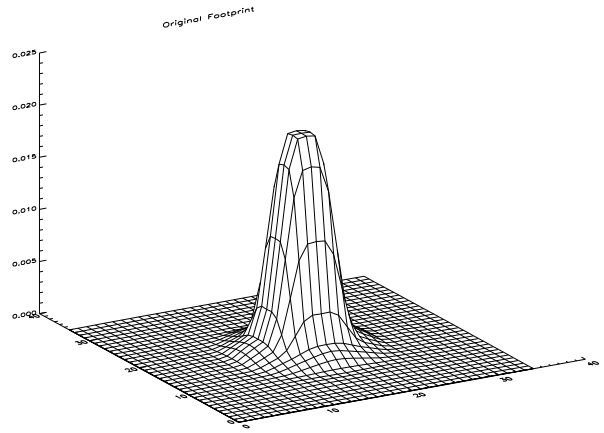


Figure 6.4: 60 $\mu m$ synthetic footprint of the convolved ISO telescope psf with pixel aperture response for the 3×3 ISOPHOT C100 array detector. The solid angles of each pixel are obtained by integrating the footprint area.

point source over the pixel per aperture in fine steps of dx and dy and measuring the resulting intensity at each measurement point ($x_i$,$y_j$), taking into account a non-flat aperture per pixel response to derive what is known as the ISOPHOT footprint. To construct the point source image at a particular wavelength, the effective solid angle ($\Omega_{eff}$) per aperture had to be know and it was determined using the following relation

$$\Omega_{eff} = \Sigma_i \Sigma_j f_{psf}^{aper}(x_i, y_j) dx dy \tag{6.10}$$

Then the proper surface brightness values of the foot print (in MJy$sr^{-1}$), were derived by using the known flux from the celestial source i.e.

$$I_{unknown}(\lambda) = \frac{f_{psf}^{aper}(x_0, y_0)}{\Omega_{eff}} . F_{standard}(\lambda) \tag{6.11}$$

where $I_{unknown}$ is the surface brightness, $f_{psf}^{aper}(x_0, y_0)$ is the fraction of the point source function (psf) contained in the pixel centered at ($x_0$,$y_0$) and $F_{standard}(\lambda)$ is the total flux of a celestial standard. An example of such a synthetic foot print is shown in Figure 6.1.2.

### 6.1.3 ISOPHOT backgrounds

The background accounted for in these observations came from three sources of emission: galactic cirrus emission, galaxies confusion, and Zodiacal light. Con fusion due to diffuse galactic cirrus emission became apparent from the far-infrared maps produced by IRAS. In order to account for galactic cirrus emission, IRAS data was used to estimate the cirrus confusion emission. The diffuse galactic emission component peaks around 170 $\mu$m in the infared and can be approximated by a $\lambda^{-2}$ modified blackbody of 17 K

$$N_{cc} = 1.08 \left(\frac{\lambda}{100}\right)^{2} .5. < B(\lambda) >^{1.5} \tag{6.12}$$

where $N_{cc}$ is the noise background by galactic cirrus emission and$< B(\lambda) >$ is the average galactic cirrus emission around the source at filter band $\lambda$. (see Helou & Beichman 1990,Gautier et al. 1992). To account for emission caused by faint background galaxies which may lie in the beam, which are not d etected individually or by the presence of a identifiable bright source close to the target, corrections were done by counting the number of galaxy infrared sources covered within a beam at a specific wave band. The methods for counting can be found in Oliver 2001, where it is shown that, knowing the resolving angle ($\Omega_{eff}$),

$$\begin{aligned} \Omega_{eff} &= 0.18\pi(\tfrac{1.22\lambda}{D})^2 \quad \text{for ISO} \\ n_q &= \tfrac{1}{3q^2\Omega_{eff}} \end{aligned} \tag{6.13}$$

where q is the detection level above the noise in multiples sigma (a representative OR the signal to noise S/N). This correction was done by using deep ISOPHOT observations at 170$\mu$m in a region with low cirrus emission. Lagache & Puget 2000 derived approximately $\sim$ 0.07 MJy/sr rms fluctuations.

Abraham et al. (1997) searched for arcminute structures in the zodiacal emission at low, intermediate, and high ecliptic latitudes. No structures or fluctuati ons were

found at a level higher than 0.2% of the total brightness. At low ecliptic latitudes ($15^o$), the zodiacal emission includes the dust band and cometary tails (Abr aham et al.1998).

For every object, the background at each of the 9 (for C100) or 4 (for C200) pixels was obtained from the off1 and off2 images. To account for the uniform sky background on each image, the flux of each pixel was divided by the background flux of the corresponding pixel and multiplied by the average of the total number of pixels.

Another important factor about the pixels, is that the background determination / corrections for each signal were performed at pixel level rather than the whole map derived. That means no further background subtraction had to be performed on the images which itself introduces an additional uncertainty e.g (see Juvela et al. 2009) when performing aperture photometry for the extended emission.

The background estimates from pre-flight measurements were 10 MJy $sr^{-1}$ per pixel (45 arcsec) for the C100 detector, and 5 MJy$sr^{-1}$ for the C200 detector array pixels (90 arcsec per pixel). The sensitivity values indicated by Table 6.1.2 are in-flight values that included all possible noise sources. The PHT-C 100 detector was limited by detector transients and cirrus noise confusion, while the the C200 was limited by only cirrus noise. (see Table 2.1 and section 4.9 of ISOHABO03 for more information). The p32 tools were developed to correct for detector transients (Gabriel & Turffs 2001), and cirrus noise corrections for 90 $\mu$m and 160 $\mu$ m were develop under Kiss, Klaas & Lemke 2005, Juvela et al. 2009. For photometric calibration accuracies and the validation of ISOPHOT data pipe - line products see Chapter 9 of ISOHABO03.

### 6.1.4 Data Reduction

The data presented here was reduced using PHOT Interactive Analysis software (PIA) (Gabriel et al. 1997) version 10.0. The are several issues with regard to the ISOPHOT data, here will discuss the most critical cases that affected our analysis.

Detector Transients: A detector transients is a drift effect in response of a PHT detector caused by a change in light levels incident on the detector. When chopper passes through a bright source at the end of a sweep and then swing back away from the source it retains a high flux through a slow response of a detector.

Even though the PHT32 mode was designed to provide high spatial resolution of the extended emission, the chopper suffered a memory effect when passing a very bright regions, especially at source position. The detector transients of bright sourced introduced ghost images in neighboring areas. These ghost images were found when a bright source was observed at the end of a sawtooth sweep. When the chopper mirror was directed back to the starting point of the sweep, the transient caused an increased signal which was recorded at the beginning of the next chopper sweep. The signal (V/s) decays within the relevant time scale, it mimicked a point source detection after a bright source was measured in the forward direction. Consequently, the ghost image was always displaced from its bright source by 180″ (=amplitude of the chopper sweep) in Y-direction (see Figure 6.1 for this direction), allowing it to be identifiable. The result of this effect is that the images became saturated along the scan direction. This effect lead to a ghost image structure as illustrated like one shown in Figure 6.5. Although we have reverse scans on each of our sources, the chopper always chops in the same direction. This makes a ghosts appearance that mimics a point source emission on the image that is often found on the left side of the the scan as shown in Figure 6.5. Another critical issue is that the chopper modulation caused a flux smear in the direction of the scan, this caused some of our images to look elongated on the right side of the scan direction. As a result some

images may look elliptical which is not a true representative of the structure of the emitting region.

There were also long term drifts in responsivity, that is, the condition by which the responsivity could be reset by shining light on the detector. When the chopper passes a bright source in the middle of observations the detector response reset, which caused a dip on the received flux. This issue was very severe for short wavelength observations 50 - 60 $\mu$ m, e.g the images may look like they have holes that caused the reduction in the flux that was measured.

There were also other flux loses due to the fact that the oversampling method by PHT 32 observation did not allow the detector to stay long enough on one area so that the responsivity loss of flux can be accounted for. This issue is very severe for the C100 than the C200 array. About 40 - 70 % of the flux in could be lost when comparing the flux measurements perfomed in the staring mode with those of PHT32 e.g. Speck et al. 2000 [125]. This flux loss seems to vary at pixel by pixel used to make observations.

Due to detector transients discussed above, the data presented was not scientifically validated with respect to previous PIA reduction software volumes used earlier in reducing the image data. The data presented here was reduced using PIA V10 that has since been partial scientifically validated with, see Chapter 9 of ISOHABO03.

Pixel Signal response. The PH32 used different pixel to make maps because the pixels were calibrated individually and each pixels recorded the flux independently on each the detector array. Unfortunately the pixel power responses were not the same, some pixels showed low responses. Thus when doing map construction a careful evaluation / selection of pixels used to derive maps was needed to obtain the final maps. For more details on pixel responses see Schulz et al. 2002[118], Figures 9 & 10.

To address the issues of transients effects on the images, further reduction pro-

cedures were performed using ISO's automated tools that is incorporated with PIA reduction software called the p32 (e.g. Gabriel & Tuffs 2001). The p32 package aims to (a) solve the non-linear optimisation problem for the sky brightness illuminating the detector on the grid of sky sampling response. (b) optionally solve the long term drifts associated with the detector staring state. (c) optionally solves the detector model parameters through self calibration by which default parameters are pre-determined. After running this tool on our images it became evident that the flux emitted in the outer regions were heavily reduced, so it may have removed real structures / or the extent of the emission. The transients were minimized but not completely removed. Therefore, some of the final maps to be presented in Chapters 7 and 8 were further reduced and corrected using the p32 tools.

## 6.2 Mapping Algorithms

PIA also offered different mapping procedures to produce the maps, inside these procedures there are several options to consider. For example, the user can decide to flat field using one pixel or the combination etc. There is by default a Full coverage algorithm in which all pixels are weighed the same to make the map, this mapping procedure tends to smear out the map. Another procedure is weighing the distance between the pixels, while considering the oversampling factors. We used this method in reproducing all our images because it produced better images.

ISO mapping was done using the raster capability of the ISO spacecraft. Distances between raster legs and raster points were not consistent for each observation, leading to different oversampling factors. The observations presented here were oversampled by the chopper moving back and forth along the scan direction at different raster spacecraft positions in order to increase the spatial resolution of the of map. Observing each section more than once created an area of overlap between raster positions.

The spacecraft's jitter during a raster observation also affects the resulting map. The measurements of single sky positions are therefore not regularly gridded, which makes the spatial resolution on each image a complex function of all the elements mentioned above at a specific wavelength filter used.

PIA offers different methods for obtaining a map from an observation, which are included in the general mapping GUI. The distance-weighting method was used to obtain the photometric images presented below. For a given map pixel, every contributing signal is weighted using the distance between beam center and center of the map pixel. The individual weighting factor is given by (1 - D)3, with D being the distance in beam size units (the exponent 3 was empirically found to produce good results). A detailed description of the different ISOPHOT mapping modes can be found in the ISOPHOT Observer's Manual (Klaas et al. 1992 [73]), while the basic mapping capabilities of PIA are described in Gabriel et al. 1997c [33].

Thus when one search for extended emission on the images, it is important to consider all these subtleties in the processed of data.

## 6.3 Extended Emission

These observations have low angular resolution based on the telescope optics and detector; e.g., ISO has a diameter of 60cm, which implies that observations done at 160$\mu$m translates into a point source with angular resolution($\theta_{min}$) $\sim$ 55 arcsec with a full width half maximum (FWHM) of $\sim$ 92 arcsec. The observations were made using ISO PHT32, infrared imaging photo-polarimeter. Both the C100 array detector at 60 $\mu$m, 90$\mu$m and the C200 array detectors at filter wavelength of 160 $\mu$m. The choice of using the PHT32 AOT at these wavelength filters was because this mode of observation was designed to provide a high spatial resolution that is suitable in studying extended emission. And the choice of these long wavelengths far-infrared

observations is suitable for studying cold dust i.e. the dust is very cool to ∼35K; Young et al. 1993a

In ISOPHOT the relationship between angular resolution and the wavelength is

$$\theta_{min} \sim \frac{\lambda}{D}$$

, where $\lambda$ is the wavelength and D is the diameter. The FWHM $\sim \sqrt{ln2}\theta_{min}$. For the observations at far infrared with flux from the star filtered at wavelengths 60$\mu$m, 90 $\mu$m and 160 $\mu$m), the FWHM expected $\sim 34''$, 52 $''$ and 70 $''$. respectively. Therefore, we get a diffraction-limited image, and the precise shape of the diffraction pattern can be determined by calculation or by observing point sources (e.g., asteroids like Vesta or the dwarf planet Ceres). We cannot observe the structures on our images beyond the expected FWHM. Inorder to make an assesment of either the source is extended or not we needed to first compare if the instrumental footprint psfs for all the filters used on ISO detector arrays matched with the point source response function from the objects that were used to calibrate our observations. This was achieved by comparing both the footprint psf used to model the expected fluxes from ISOPHOT observations (e.g called the instrumental foot print) and the observed footprint psf (prior to the observations) with the radial profiles of the observed standard sources (flux calibrators). The reasoning behind this formalism, is that instrumental footprint for all filters were determined by modeling the point spread function of ISO telescope (including the effects by tripod), and was convolved with the pixel size in order to determine the final fluxes that makes our photometric images e.g. refer to section 6.1.2. For more information see Herbstmeier et al. 1998[54] and for point spread function related to ISOPHOT C100 and C200 arrays, see Laureijs et al. 1999 [72]. In Figure 6.6 we present a direct comparison of the footprint psf with the standard source Vesto.

Figure 6.6 proves that the model and and measured footprints psf′s agreed very

well with the radial profile observations of standard sources. There are two implications used for the easement of extended emission from the profiles in Figure 6.6 i.e. first on a resolution limit imposed by the scale of the FWHM's shown in Figure 6.6, any flux that falls within the FWHM observed would implies that the source is a point source as seen by ISOPHOT at far infrared, thus not extended; second, if flux received falls outside the observed FWHM, it may indicate that the source has extended emission. If the observed radial profile matched the footprint psf we classified that the radial profile represented a point source. The analysis of images are the results presented in the form of radial profiles taken along the scan direction. The footprint psf was preferred instead of point sources, because there are high uncertainties in the background surface brightness on ISOPHOT observations in general e.g. Juvela 2009 [67], this also includes the observations of standard sources. For example notice that the wings of the the surface background of the footprint psf do not match precisely with Vesta observations on the bottom panel for 160$\mu$m observations in Figure 6.6, this situation was less severe at 160$\mu$m.

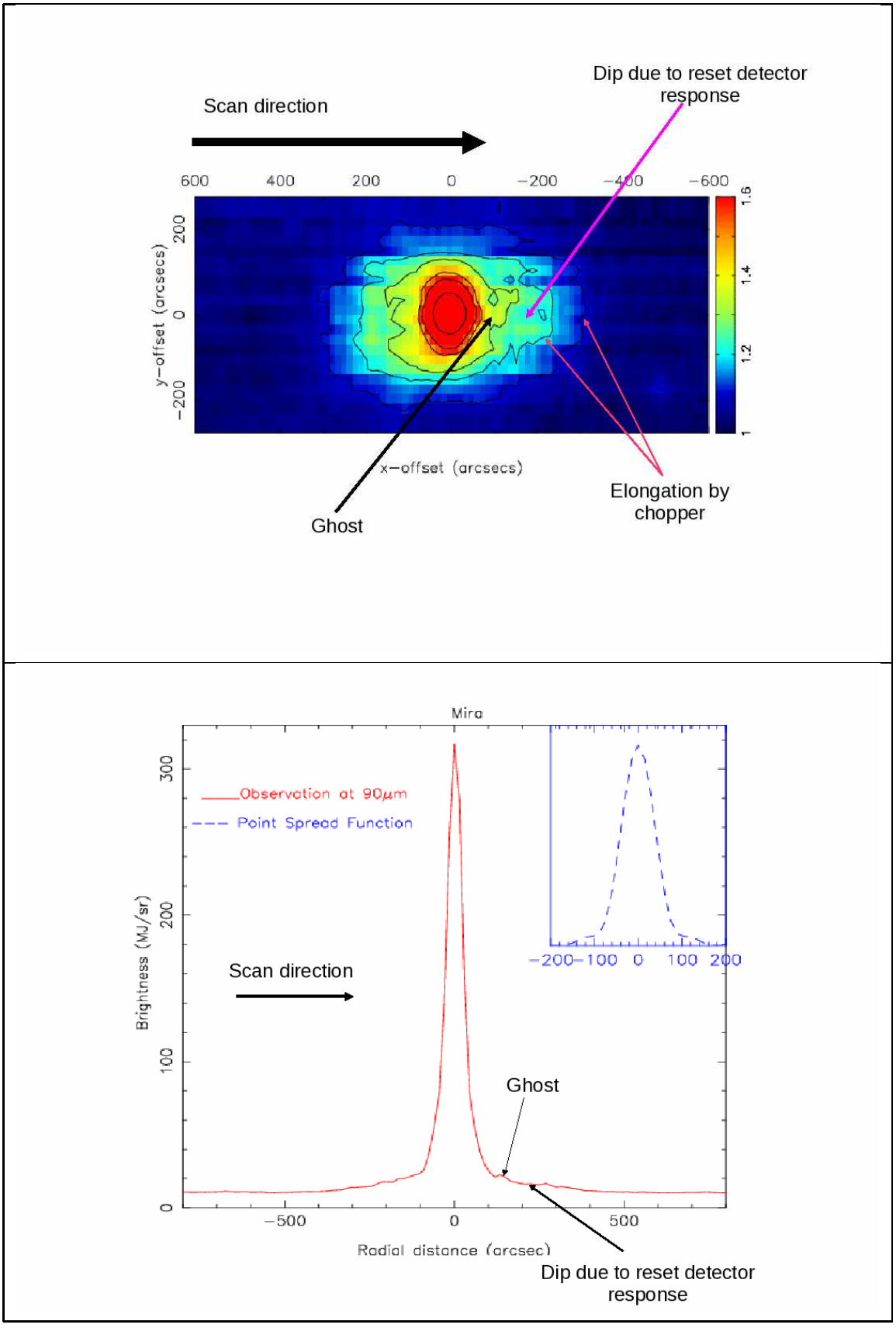


Figure 6.5: 90$\mu$m image (left), and a scan profile showing critical defects by the chopper on ISOPHOT 32 detectors.

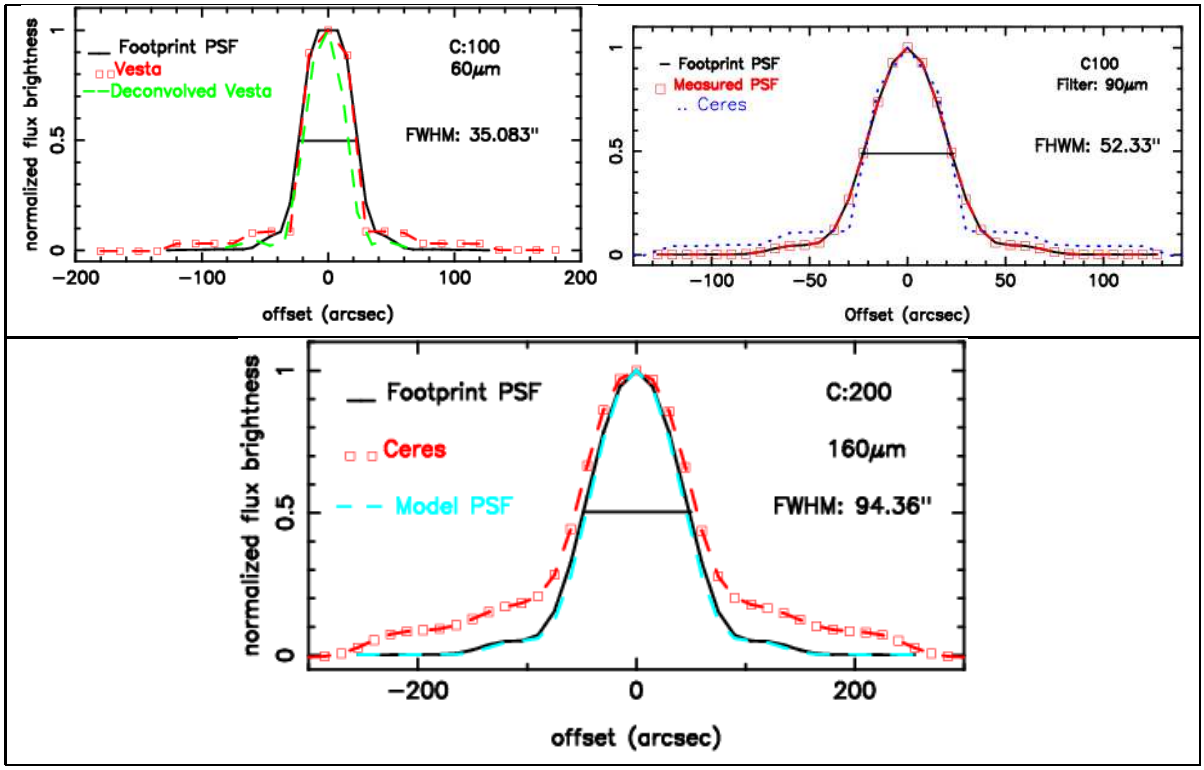


Figure 6.6: *Top Panel*: Comparison of the C100 convolved footprint point spread functions with calibration standard source Vesto at 60 $\mu$m and 90 $\mu$m. *Bottom Panel*: Comparison of the C200 convolved footprint point spread functions with calibration standard source Vesto at 160 $\mu$m.

# Chapter 7

# Probing Dust Around Oxygen-rich Stars

## 7.1 Introduction

In this chapter, we use the results of the photometric images of six evolved oxygen-rich AGB stars that were observed using ISOPHOT as described in Chapter 6. The aim of our analysis of these images is

1. To discern the extended far-infrared emission beyond the central point source.

2. To determine the observed maximum extent of the circumstellar emission, and thus, assuming a constant expansion velocity, estimate the time scale since the oldest observable dust was ejected from the star.

3. To estimate the mass of the progenitor star via determining the mass of the core central star (via Pacysnksi's relation equation 3.1) and the mass of the extended dust from its emission and assuming a canonical dust-to-gas ratio. The mass of the circumstellar dust together with the mass of the core is used to set the lower limit for the progenitor masses of these stars.

In § 7.2 describes the sample of O-rich AGB stars observed using ISO PHT 32 and the basic analysis that gives rise to the linear monchromatic emission profiles. § 7.4 describes how determine size of the extended emission region using two independent methods to ensure reliability of results. § 7.5 describes how the flux densities and thus the total flux from dust shells were determined using surface aperture photometry. This section includes a discussion of the dust temperature. § 7.6 Uses the flux and temperatures for the dust shells to determine the total mass of dust and thus provides a lower limit for the progenitor star mass. The results are discussed in § 7.8.

## 7.2 ISOPHOT PHT C 32 Observations of six O-rich AGB stars

Six oxygen-rich AGB stars were selected for our sample from the ISO data archive based on whether there were high-angular-resolution far-IR images available. We limited ourselves to objects observed using ISO PHT32, infrared imaging photo-polarimeter. Details of the observations and data reduction are described in Chapter 6.

These stars were selected based on the fact that they were previously observed in the infrared by IRAS [99]. Furthermore, the IRAS low-resolution images were processed to give high resolution (HIRES) images which suggests the presence of large dust shells around our source objects. However due to the large IRAS beam and low spatial resolution, IRAS was unable to reliable identify the origin the far infrared emission (circumstellar disk, spherical, or small off-centered dust clumps). ISOPHOT had a mapping capability that provided higher spatial resolution than that of IRAS in the far-infrared. The six oxygen-rich mira variables that were used in this study are listed in Table 7.1, while basic observed parameters collated from the literature which are used in our analysis are listed in Table 7.2. Information such

Table 7.1: Selected target evolved oxygen-rich intermediate-mass stars imaged by Infrared Space Observatory (ISO) using far-infrared PHT32-C camera.

| Name | Right Ascension | Declination | Spectral Type |
|---|---|---|---|
| Omi Cet / Mira | 2h19m20.78s | -2d58m39.5s | M2-M7 III |
| R Hya | 13h29m42.78s | -23d16m52.8s | M6e-M9eS(Tc) |
| ST Her | 15h50m46.62s | +48d28m58.9s | M6-7IIIaS |
| V0833 Her | 17h31m54.98s | +17d45m19.7s | M2 |
| V1943 Sgr | 18h04m16.03s | -30d02m57.9s | M7III |
| V1300 Aql | 20h10m27.87s | -6d16m13.6s | MD |

Hipparcos [107] and VizieR [100] were used to obtain spectral type and sky positions of each source.

Table 7.2: Basic observed parameters of target O-rich evolved stars.

| Name | Distance (pc) | Pulsation Periods (days) | Luminosity $L_\odot$ | $\dot{M}$ ($10^{-7}\,M_\odot\ yr^{-1}$) | $v_{exp}$ $kms^{-1}$ |
|---|---|---|---|---|---|
| Omi Cet | $128^{a,c}$ | $332^a$ | $8900^e$ | $4.4^c$ | $6.7^c$ |
| R Hya | $150^b$ | $388^b$ | $5800^b$ | $3.0^b$ | $7.0^{\ b}$ |
| ST Her | $290^a$ | $148^b$ | $1700^{\ c}$ | $2.0^c$ | $6.0^c$ |
| V0833 Her | $1140^{a,c}$ | — | $5000^c$ | $97^c$ | $17.5^c$ |
| V1943 Sgr | $150^b$ | — | $4000^b$ | $1.3^b$ | $5.4^b$ |
| V1300 Aql | $270^b$ | $680^b$ | $10400^b$ | $25^b$ | $12^b$ |

a = Winters et al. 2003 [144]
b = Gonzalez et al. 2003 [44]
c = Loup et al. 1993 [85]
d = Periman et al. 1997 [107]
e = Woodruff et al. 2004 [153]

as the wavelngth range of the relevant filters and the roll-angle of the ISO PHT C32 observations are listed in Table 7.3. Details of how the observations were taken and how the data was reduced are given in Chapter 6.

The objects in Table 7.1 were reduced using ISO-PHOT Interactive Analysis software (PIA) (Gabriel et al. 1997 [33]) version 10.0.described in Chapter 6. The monochromatic images are presented in Figures 7.1 – 7.6. For each figures, the position of an object in the sky and the orinetation of the imaging observation are shown interms of right ascension and declination on the sky. The color scale denotes the surface brightness in $MJy\,sr^{-1}$. The flux maximum indicates the surface brightness

Table 7.3: ISO PHT C32 observational information for six target evolved oxygen-rich.

| Name | Filters ($\mu$m) | Pixel Size (arcsec$^2$) | Image Size (arcmin$^2$) | Intergration time (s) | Roll Angle ($^\circ$ N of E) |
|---|---|---|---|---|---|
| Omi Cet | 90:160 | 15×23:30×92 | 34.5×9.2 : 34.5×12.3 | 3250:3226 | 254.36 |
| R Hya | 60:90 | 15×23:15×23 | 23.8×9.2 : 23.8×9.2 | 2220:2412 | 65.25 |
| ST Her | 90:160 | 15×46:30×92 | 40.5×8.4 : 41.5×9.2 | 2836:3146 | 343.279 |
| V0833 Her | 160:90 | 15×46:30×92 | 26.8×8.4 : 41.5×9.2 | 2666:1892 | 343.321 |
| V1943 Sgr | 60:90 | 15×23:15×23 | 14.5×11.5 : 41.5×9.2 | 7110:7110 | 285.093 |
| V1300 Aql | 60:90 | 15×23:15×23 | 23.8×9.2 : 23.8×9.2 | | 285.463 |

Table 7.4: Flux brightnesses from Figures 7.1 – 7.6 in MJy sr$^{-1}$.

| Source | Maximum fluxes | | | Sky background | | |
|---|---|---|---|---|---|---|
| Name | 60 $\mu$m | 90 $\mu$m | 160 $\mu$m | 60 $\mu$m | 90 $\mu$m | 160 $\mu$m |
| Mira | — | 317.1 | 40.73 | — | 10 | 6.0 |
| RHya | — | 112 | 250 | — | 16.0 | 25 |
| V1300 Aql | 1070 | 365.3 | — | 20 | 15 | — |
| V1943 Sgr | 141.0 | 66.07 | — | 15.01 | 13.9 | — |
| V0833 Her | — | 89.96 | 22.87 | — | 10.7 | 9.7 |
| ST Her | — | 40.15 | 8.372 | — | 8.5 | 4.77 |

at the location of the star, and flux minimum indicates the sky surface brightness background. The values of the flux maximum and minimum surface brightness values per filter used are sumarized in Table 7.2. Contours on the images delineate different regions of surface brightness and the last contour indicate the minimum surface brightness where the emission assumes a sky background value.

For each image a radial flux profile has been generate. This radial profile is a 1-D plot of surface brightness as a function of angular offset from the central star. These linear scans were produced such that the scan direction is the $x$-direction in image, and shown as the dotted line in Figures 7.1 – 7.6. The radial profiles of our sample of oxygen-rich AGB stars are shown in Figures 7.7, 7.8 and 7.9.

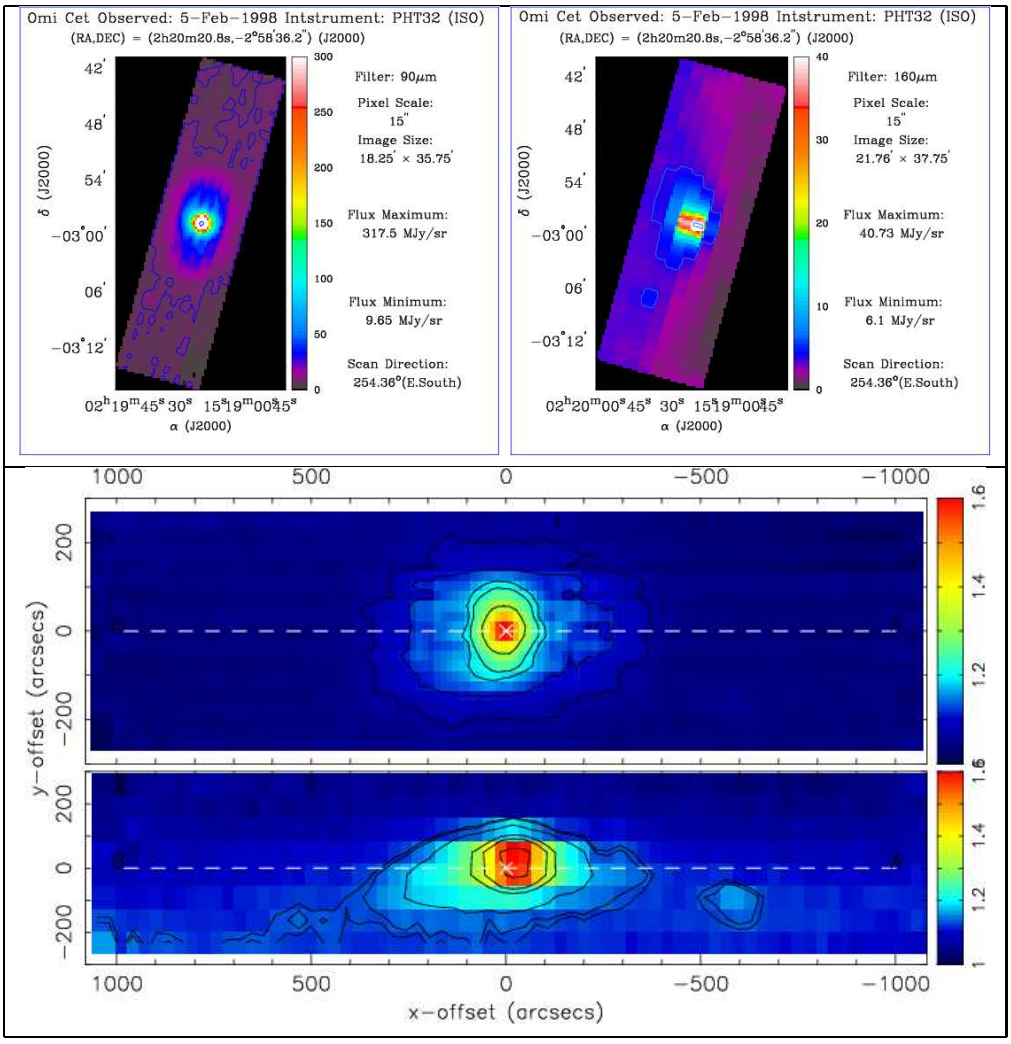


Figure 7.1: Omicron Ceti / Mira; *Top panel*: 90 $\mu$m (left) and 160 $\mu$m (right) images showing the position of the object in the sky in R.A. and Dec. *Bottom panel*: 90 $\mu$m (top) and 160 $\mu$m (bottom) images of Mira rotated such that the $x$-direction is the direction of the image scan. The wedge shows the surface brightness of the image in log scale. The contour levels are set between minimum at 1 and maximum at 1.6 which is the log of the surface brightness measured in MJy sr$^{-1}$. The cross indicates the peak position of the maximum flux.

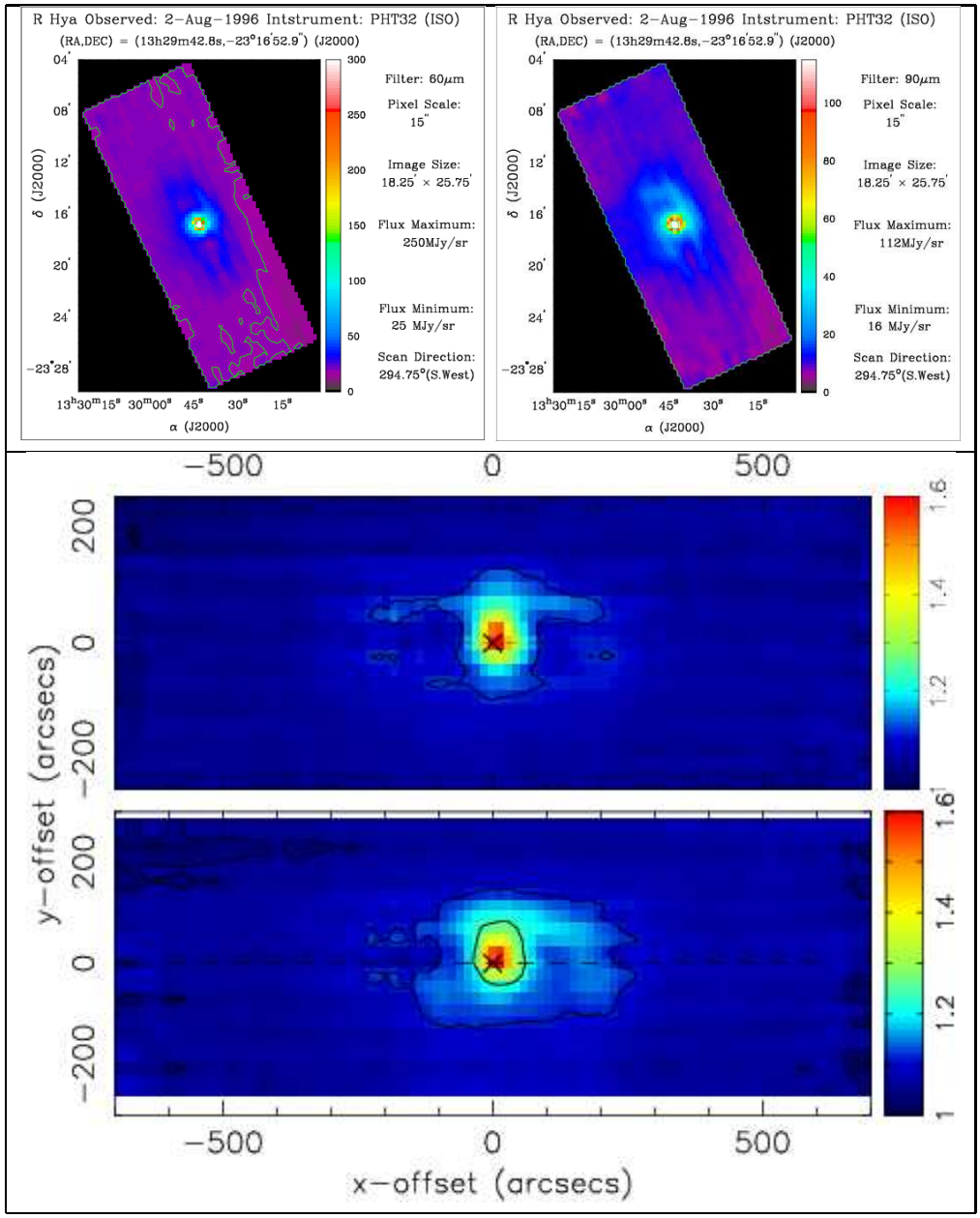


Figure 7.2: R Hya; *Top panel*: 60 $\mu$m (left) and 90$\mu$m (right) images showing the position of the object in the sky in R.A. and Dec. *Bottom panel*: 60 $\mu$m (top) and 90 $\mu$m (bottom) images rotated such that the $x$-direction is the direction of the image scan. The wedge shows the surface brightness of the image in log scale. The contour levels are set between minimum at 1 and maximum at 1.6 which is the log of the surface brightness measured in MJy sr$^{-1}$. The cross indicates the peak position of the maximum flux.

## 7.3 Analysis of radial profiles

In order to assess the extended nature of our observations we need to compare the observed radial profile with that of a point-source. This is achieved by using the

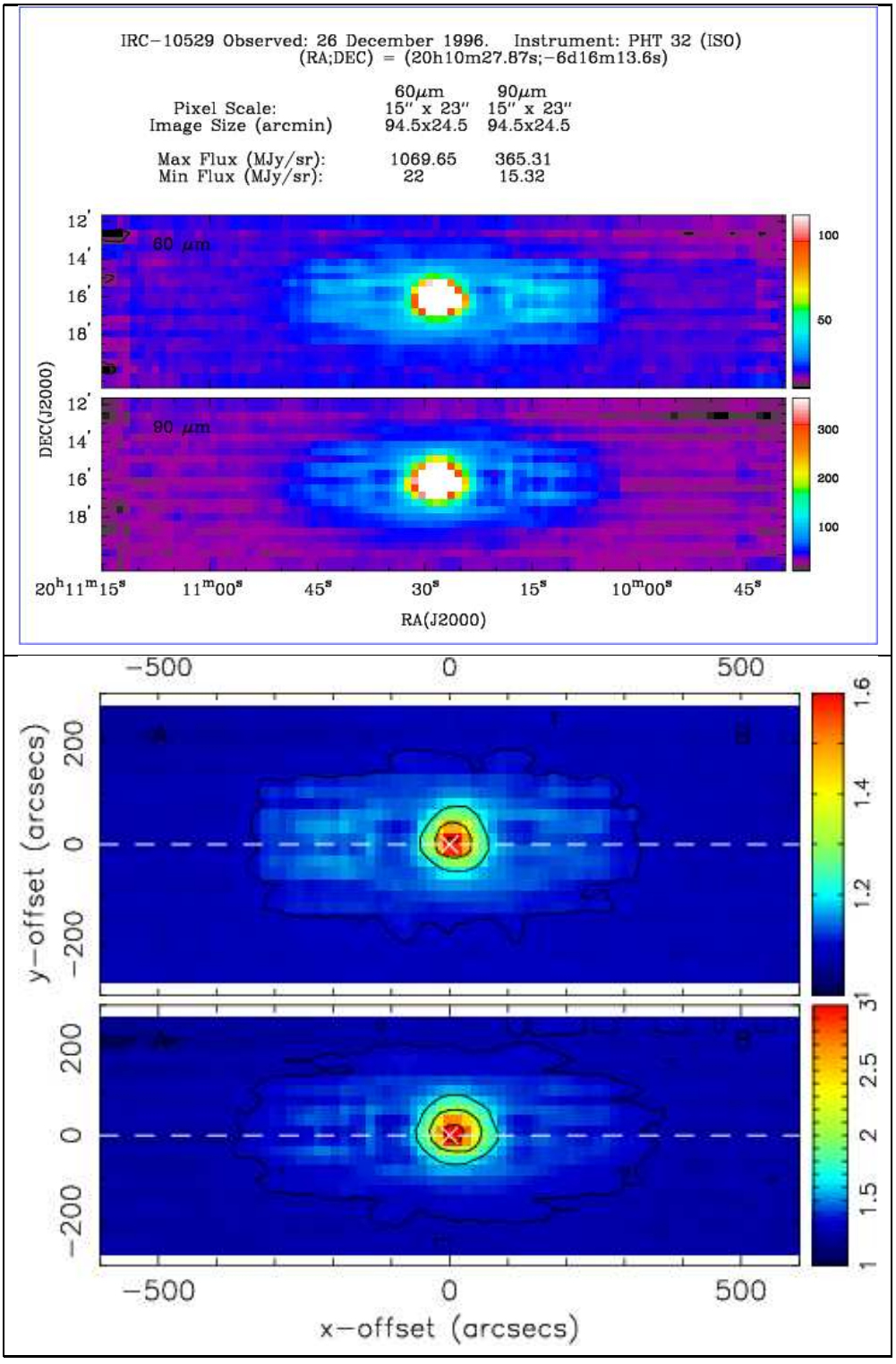


Figure 7.3: V1300 Aql; *Top panel*: 60 $\mu$m (top) and 90 $\mu$m images showing the position of the object in the sky in R.A. and Dec. *Bottom panel*: 60 $\mu$m (top) and 90 $\mu$m (bottom) images rotated such that the $x$-direction is the direction of the image scan. The wedge shows the surface brightness of the image in log scale. The contour levels are set between minimum at 0.5 and maximum at 1.0 which is the log of the surface brightness measured in MJy sr$^{-1}$. The cross indicates the peak position of the maximum flux.

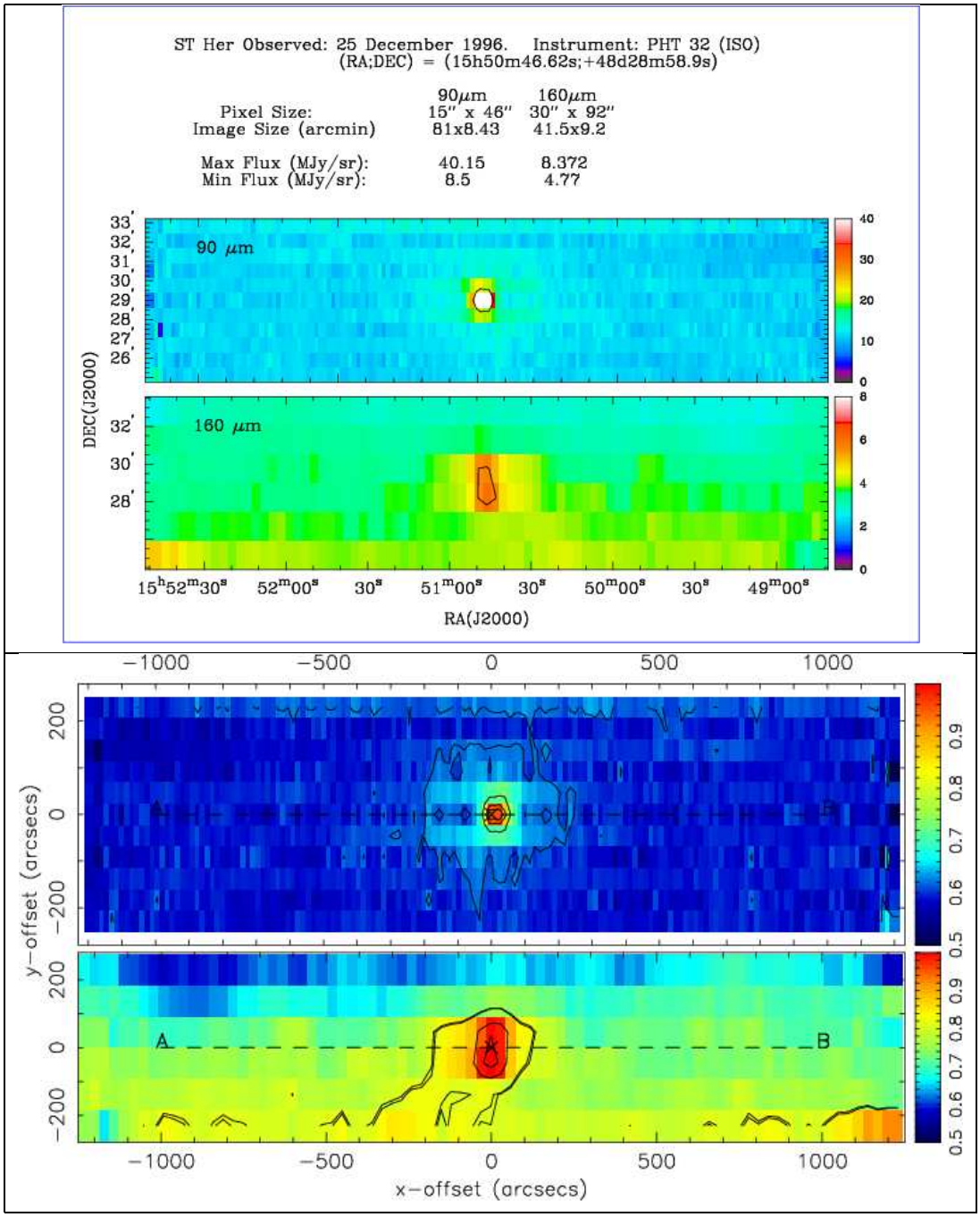


Figure 7.4: ST Her; *Top panels*:90 $\mu$m (top) and 160 $\mu$m images showing the position of the object in the sky in R.A. and Dec. *Bottom panel*: 90 $\mu$m (top) and 160 $\mu$m (bottom) images rotated such that the $x$-direction is the direction of the image scan. The wedge shows the surface brightness of the image in log scale. The contour levels are set between minimum at 0.5 and maximum at 1.0 which is the log of the surface brightness measured in MJy sr$^{-1}$. The cross indicates the peak position of the maximum flux.

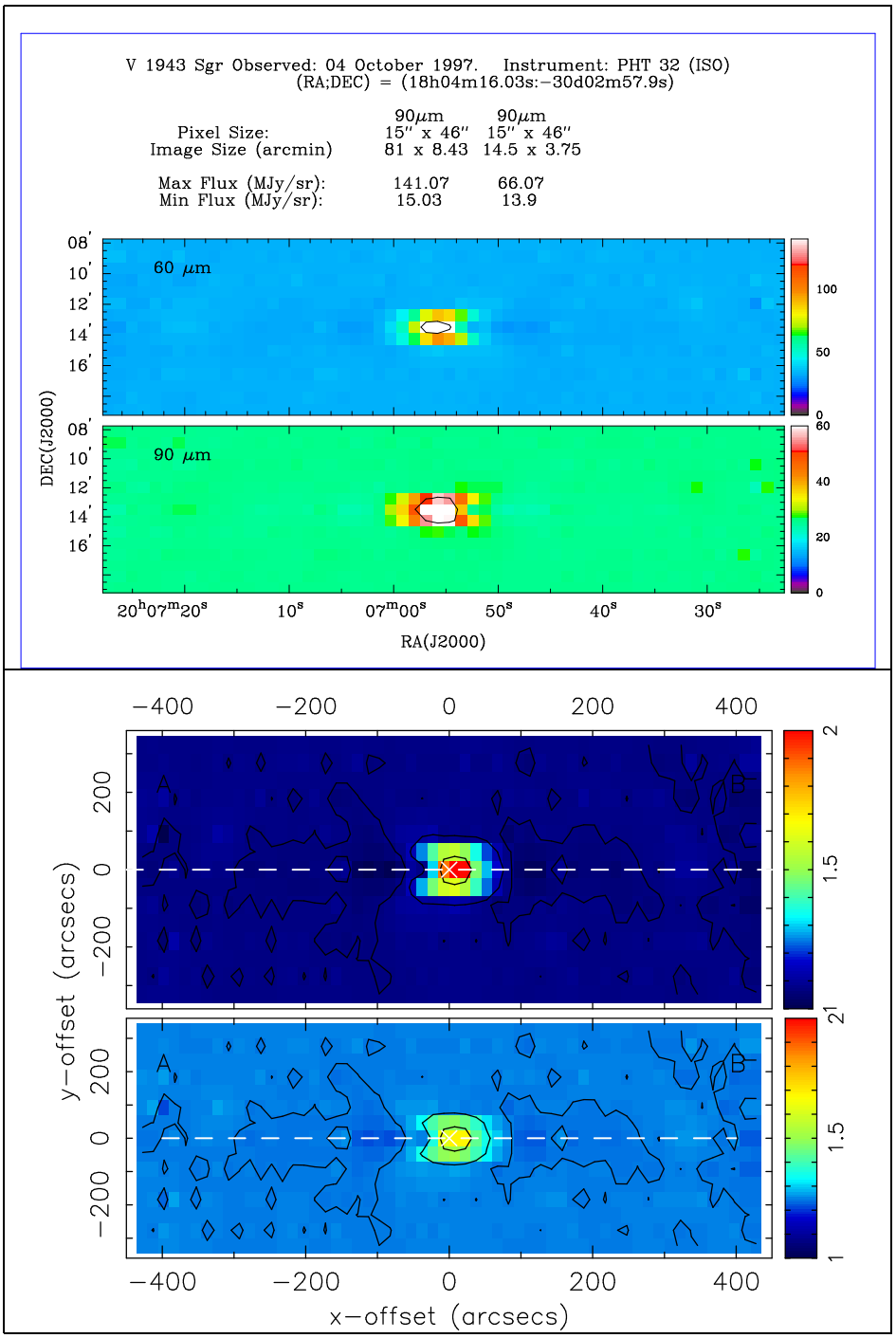


Figure 7.5: V1943 Sgr; *Top panel*: 60 $\mu$m and 90 $\mu$m images showing the position of the object in the sky in R.A. and Dec. *Bottom panel*: 60 $\mu$m (top) and 90 $\mu$m (bottom) images rotated such that the $x$-direction is the direction of the image scan. The wedge shows the surface brightness of the image in log scale. The contour levels are set between minimum at 1 and maximum at 2 which is the log of the surface brightness measured in MJy sr$^{-1}$. The cross indicates the peak position of the maximum flux.

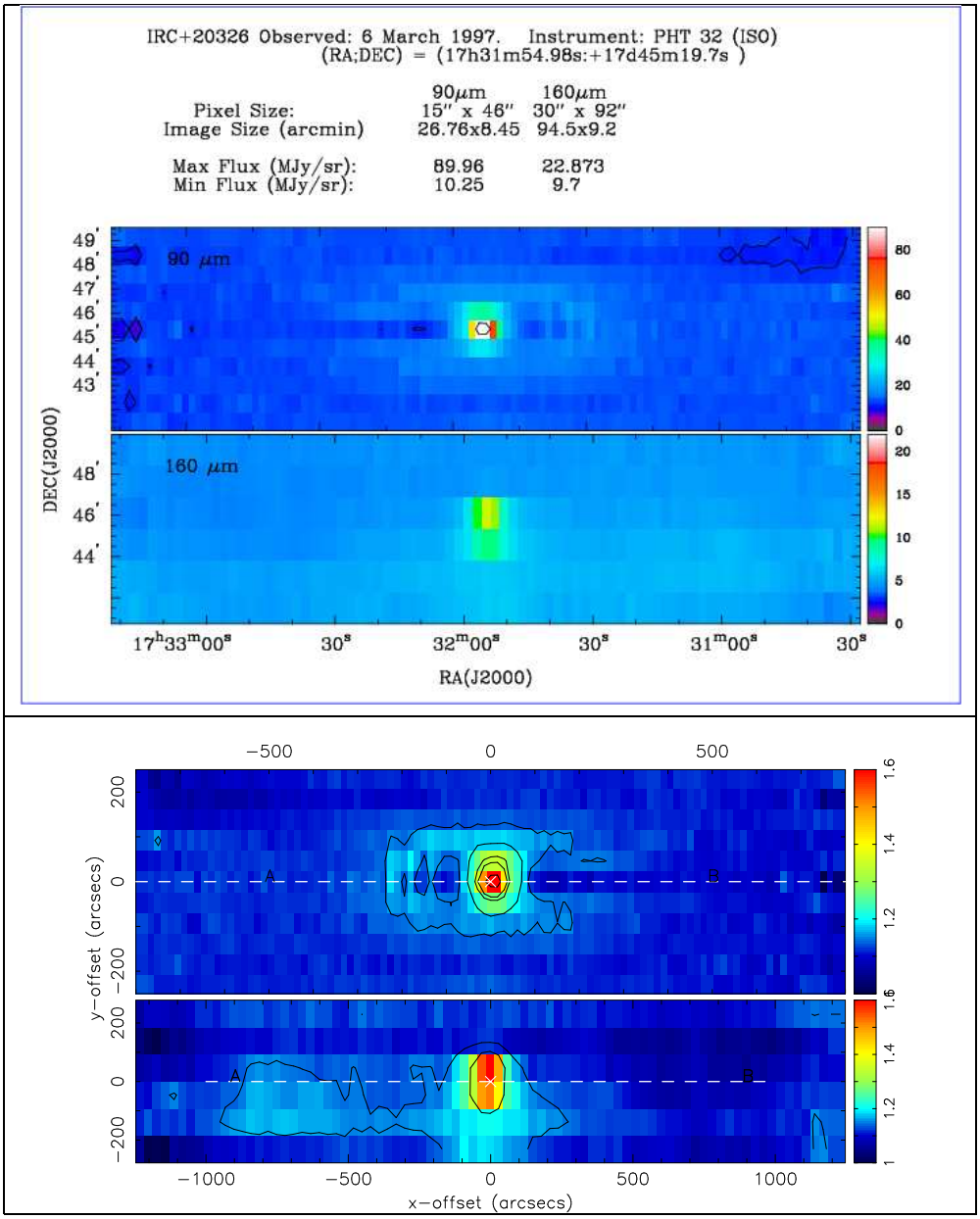


Figure 7.6: V0833 Her; *Top panel*: 90 $\mu$m and 160 $\mu$m images showing the position of the object in the sky in R.A. and Dec. *Bottom panel*: 90 $\mu$m (top) and 160 $\mu$m (bottom) images rotated such that the $x$-direction is the direction of the image scan. The wedge shows the surface brightness of the image in log scale. The contour levels are set between minimum of 1 and maximum at 1.6 which is the log of the surface brightness measured in MJy sr$^{-1}$. The cross indicates the peak position of the maximum flux.

footprint PSF (see also Chapter 6). The PSF was scaled to the observations using the maximum and sky background surface brightnesses given Table 7.2. The scaled PSFs are shown in Figures 7.7, 7.8 and 7.9.

Comparison of the radial profiles with footprint PSFs indicates that there are frequently offsets in the observed peak position with respect to the PSF. These offsets were in the order of 5–10″. In all profiles the off-centered peak is followed by a gradient decrease in surface brightness. As a result the profiles are not symmetric about the center. Since these offsets have not been investigated in detail they set a limitation on the positional accuracy source, and also in finding correct size of the extended emission. This asymmetry effect is probable due to the long term drift in responsivity when chopper passed the bright source at the center, since the offsets occurs along the direction of the scan on the right side of each radial profile. Long-term transient effects in the PHT32 C detectors was discussed in details in Chapter 6.

The measured background surface brightness was used to scale the background level of the PSF in order to determine the size of extended emission. Intrinsic and extrinsic noise provides a major limitation to both sensitivity and photometric accuracy for the measurements performed with FIR detectors of ISOPHOT instrument (e.g. see Kiss, Klass & Lemke 2005 [71]). Consequently there were unavoidable uncertainities is the size estimate owing to observational uncertainties in the measured background level due to noise and cirrus confusion levels around our objects. Furthermore, the background surface brightnesses in these observations vary, as we can see for example in the profile of V0083 Her in Figure 7.8. For observations by C100 camera (e.g. 60 and 90 $\mu$m), the background uncertainities are due to cirrus confusion level, instrumental noise, and the fluctuations of cosmic far infrared background; whereas C200 (160 $\mu$m) camera observations were mostly confusion noise limited, see Chapter 6 and a paper by Juvela et al. 2009 [67].

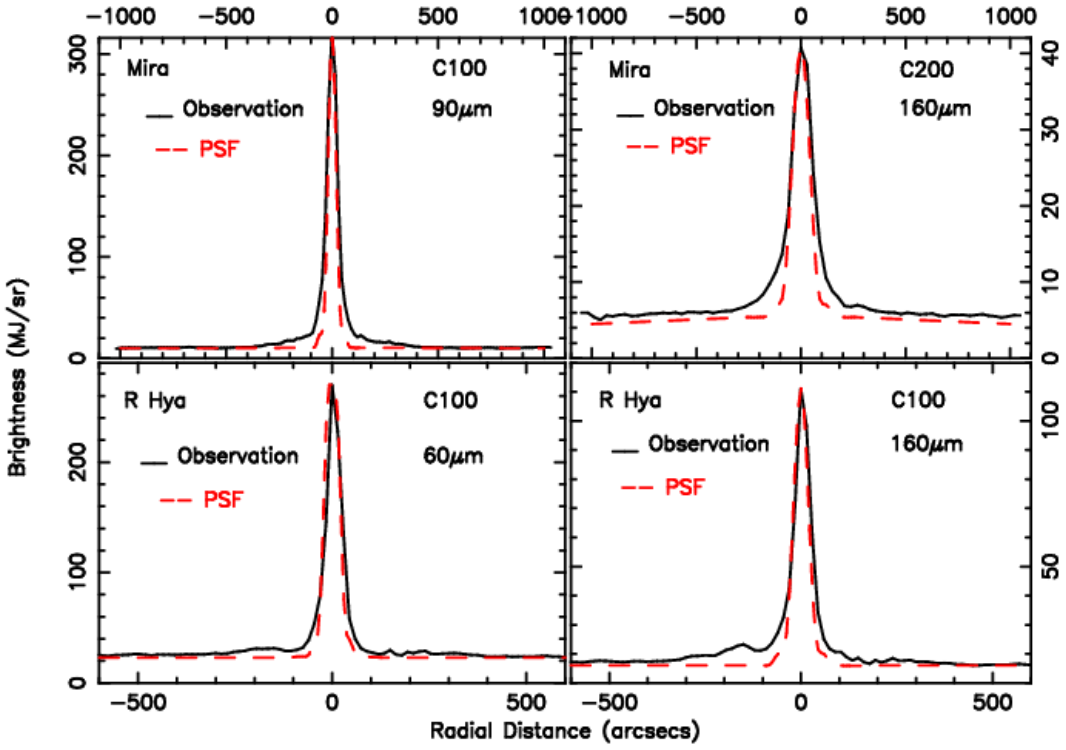


Figure 7.7: Radial surface brightness profiles for Mira (top) and R Hya (bottom). Solid black line = ISO PHT C 32 data from Figures 7.1 and 7.2; dashed red line = footprint PSF scaled using maximum and background fluxes from Table 7.2; $x$-axis is radial offset in arcseconds; $y$-axis is surface brightness in MJy sr$^{-1}$.

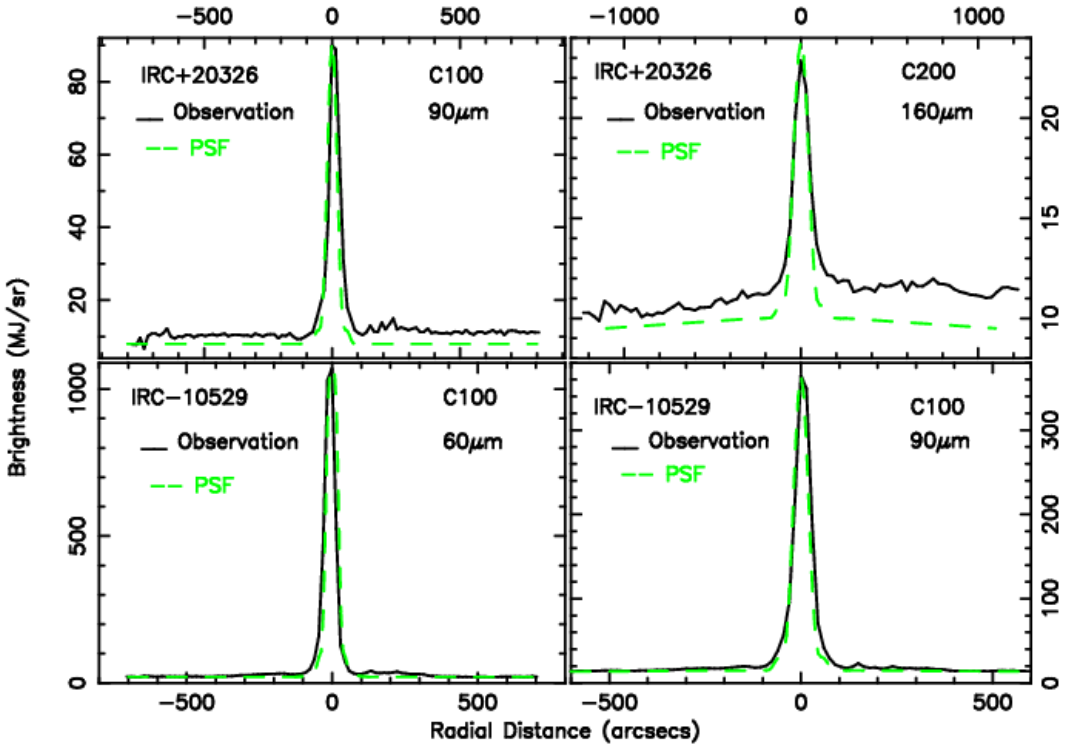


Figure 7.8: Radial surface brightness profiles for V1300 Aql (top) and V0833 Her(bottom). Solid black line = ISO PHT C 32 data from Figures 7.3 and 7.6; dashed green line = footprint PSF scaled using maximum and background fluxes from Table 7.2; $x$-axis is radial offset in arcseconds; $y$-axis is surface brightness in MJy sr$^{-1}$.

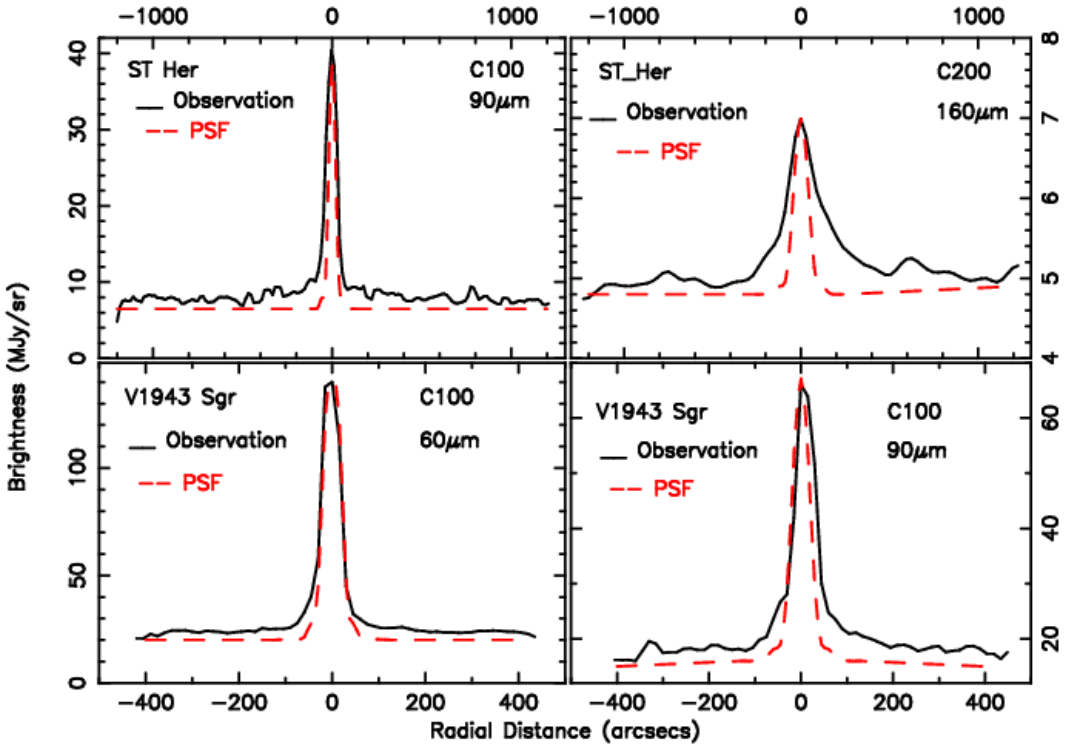


Figure 7.9: Radial surface brightness profiles for ST Her (top) and V Sgr 1943 (bottom). Solid black line = ISO PHT C 32 data from Figures 7.5 and 7.4, respectively; dashed red line = footprint PSF scaled using maximum and background fluxes from Table 7.2; $x$-axis is radial offset in arcseconds; $y$-axis is surface brightness in MJy sr$^{-1}$.

### 7.3.1 1–D PSF Subtraction

We subtracted the psf's from radial profiles in order to eliminate the effects of the point source and show extended emission. The result are shown in Figures, 7.10, 7.11, 7.12, 7.13, 7.14

For Omi Cet, in Figure 7.10, the subtracted profile for this object shows that for observation at 90 $\mu$m, the surface brightness peaks from the central region and smoothly declines until it plateaus at at a radius of about 500″. This gives us a hint of an extended emission from a source whose size is below 500″. At 160 $\mu$m the excess emission goes beyond 500″ up to 800″.

The inner regions of the subtracted profile in Omi Cet observations shows 'kinks' that resulted from the misalignment of the PSF with the radial profile due to positional offsets at peak position. There is a prominent bump in the surface brightness on both subtracted profiles that is located at at about 180″ on the right side. This bump could be a ghost structure since it disappears on the left side on both profiles. The observations does not show any surface brightness variation with distance from the star that could be related to thermal pulses.

For R Hya, the left side of the subtracted profiles at both 90 $\mu$m and 60 $\mu$m observations, shows a bump in surface brightness at about 200″. This bump is due to the bow-shock stucture reported by Ueta et al. 2006 [133]). Our observation also shows the evidence a bow shock nebula around R Hya as shown in the image at 90 $\mu$m observations in Figure 7.2. The 60 $\mu$m observation has high cirrus confusion and suffered detector transients such that the bow structure is not clear defined. In both subtracted profiles, the extended emission levels at about 400″. The right side of the subtracted profiles in both filters suffered flux loss (dip) due to reset detector response, thus it was not useful in our analysis.

The subtracted profiles of V1300 Aql at both 60 $\mu$m and 90 $\mu$m indicate that the surface brightness declines smoothly with distance from the center, until it reaches a

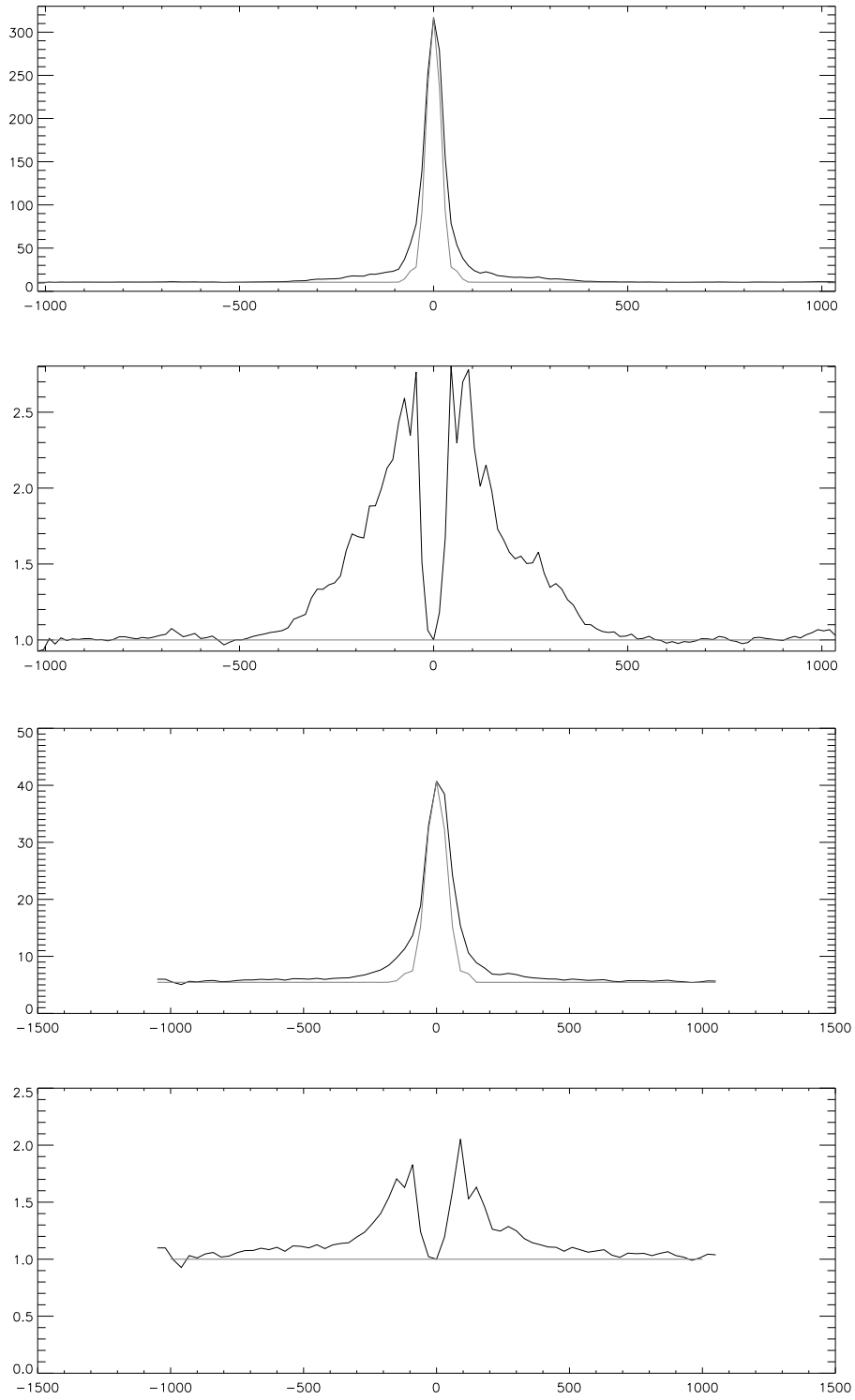


Figure 7.10: Extent of emission from Omi Cet. *Top Panel*: 90 $\mu$m radial surface brightness profiles; *second top panel*: PSF subtracted surface brightness at 90 $\mu$m. *second bottom panel*: 160 $\mu$m radial surface brightness profiles; *Bottom Panel*: PSF subtracted surface brightness at 160 $\mu$m.

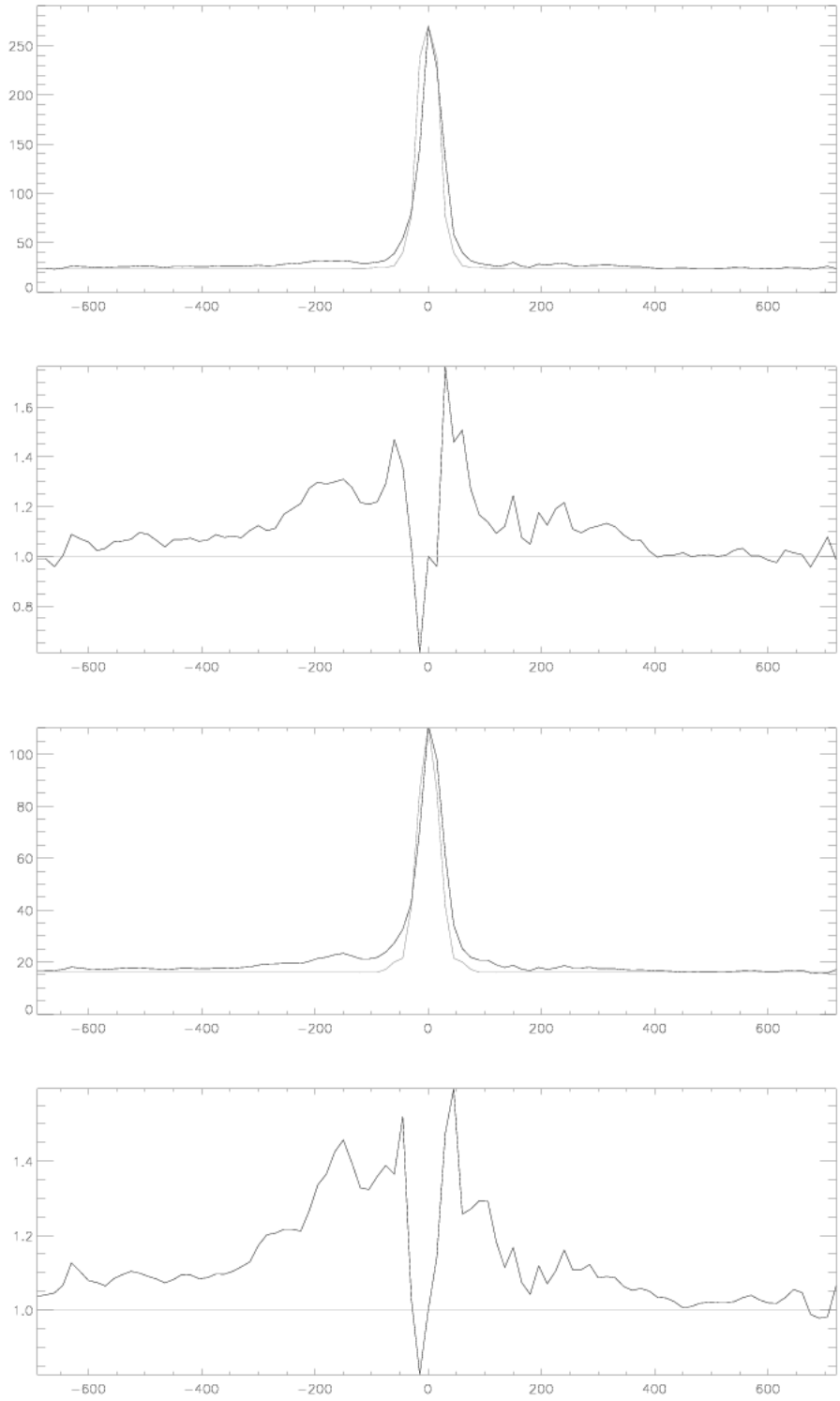


Figure 7.11: Extent of emission from R Hya. *Top Panel*: 60 $\mu$m radial surface brightness profiles; *second top panel*: PSF subtracted surface brightness at 60 $\mu$m. *second bottom panel*: 90 $\mu$m radial surface brightness profiles; *Bottom Panel*: PSF subtracted surface brightness at 90 $\mu$m.

distance of $\sim 160''$. Beyond a radius of $160''$, the surface brightness rises to a peak at a radius of $200''$. The surface brightness then smoothly declines to a radius of $450''$. This trend is noticeable on both radial profiles at 60 and 90 $\mu$m. The drop and rise in surface brightness at $160''$ can be interpreted as circumstellar dust shell or a disk separating from star V1300 Aql. The size of the detached shell is estimated to be $\sim 300''$. There is a positional offsets in peak position at the center of about $20''$, which creates uncertainties in size and position.

The subtracted profile of V0833 Her indicates that this object may be extended to about $800''$ (see the left hand side of Figure 7.13). The right hand side of this profile has higher surface background than the left side, thus the PSF subtraction on the right could not give any reliable results due to high noise confusion level. The overall surface brightness showed a smooth decline with distance from the star up to a radius of $400''$. However there is a surface brightness rise at a radius of $40\ ''$, which is noticeable in both profiles at $60\,\mu$m and $90\,\mu$m. The subtracted profiles of VSgr 1943, shows that this object may be extended up to $350 - 400''$.

## 7.4 Circumstellar dust shell size determination

It was esential to investigate what is the size of the extended source that produces circumstellar emission as discused above in § 7.3. Furthermore it was necessary to find out at what radius does our observations reliable estimate the extent of the emission by other means than using 1 – D psf subtractions presented in 7.3.1.

This was achieved in two ways

(i) Fist by simulating the observations using ISOPHOT mapping Simulator e.g. Gabriel & Hur 2000,2002 [34], [35]. The advantage of this method, is that is was possible to simulate the extended emission by construction of observations using the convolution of point sources or extended point sources at objects position under

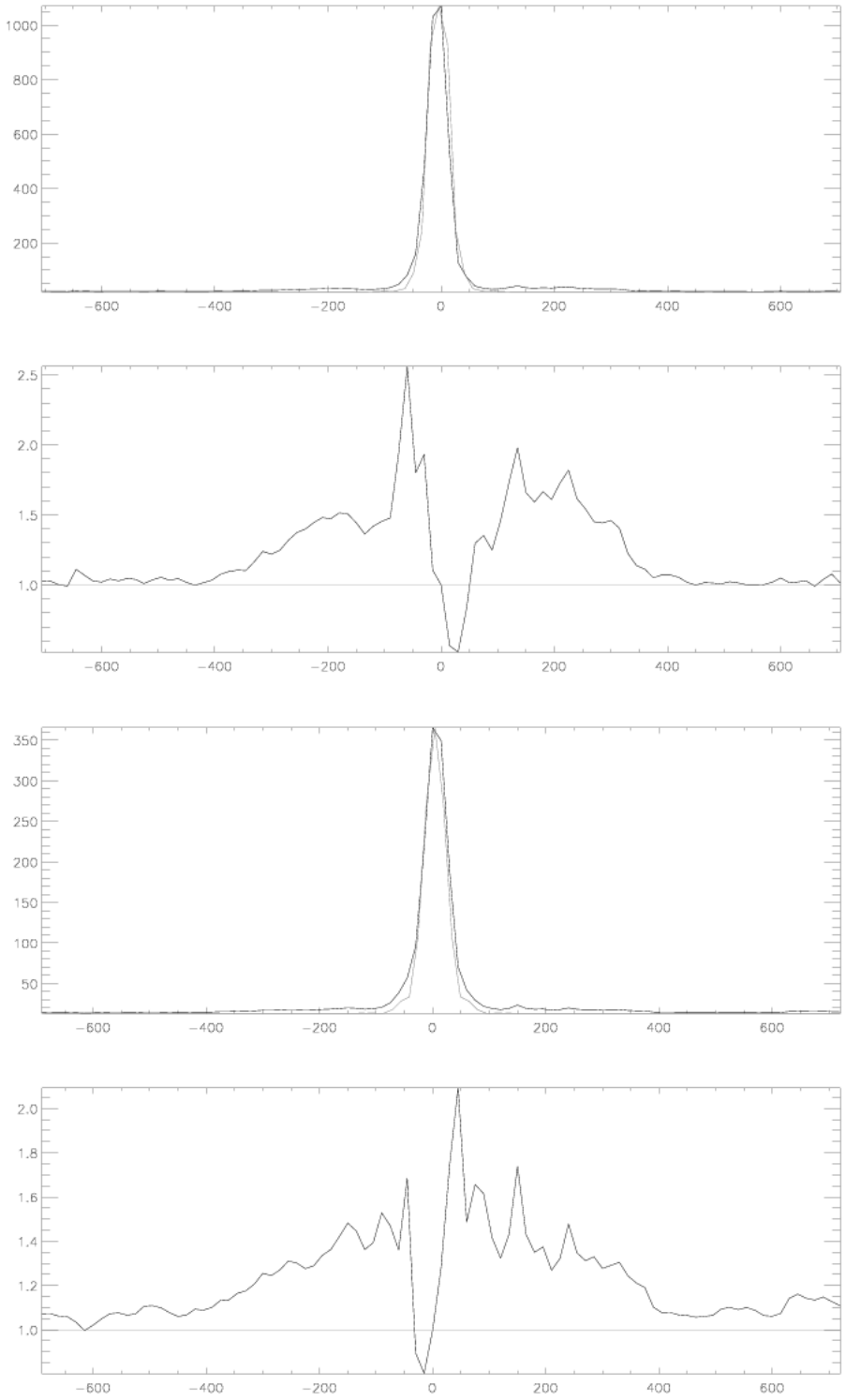


Figure 7.12: Extent of emission from V1300 Aql. *Top Panel*: 60 $\mu$m radial surface brightness profiles; *second top panel*: PSF subtracted surface brightness at 60 $\mu$m. *second bottom panel*: 90 $\mu$m radial surface brightness profiles; *Bottom Panel*: PSF subtracted surface brightness at 90 $\mu$m.

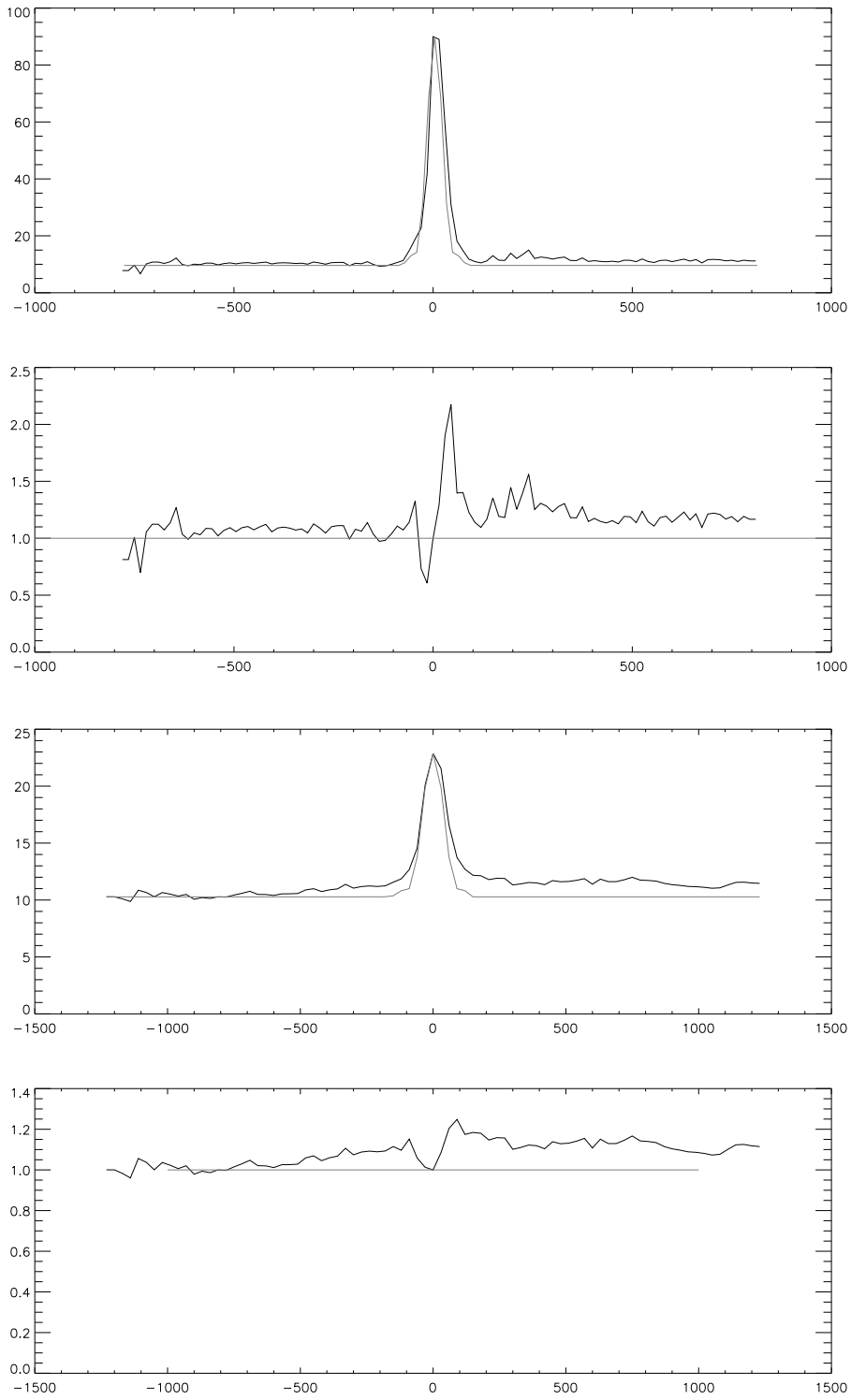


Figure 7.13: Extent of emission from V0833 Her. *Top Panel*: 90 $\mu$m radial surface brightness profiles; *second top panel*: PSF subtracted surface brightness at 60 $\mu$m. *second bottom panel*: 160 $\mu$m radial surface brightness profiles; *Bottom Panel*: PSF subtracted surface brightness at 90 $\mu$m.

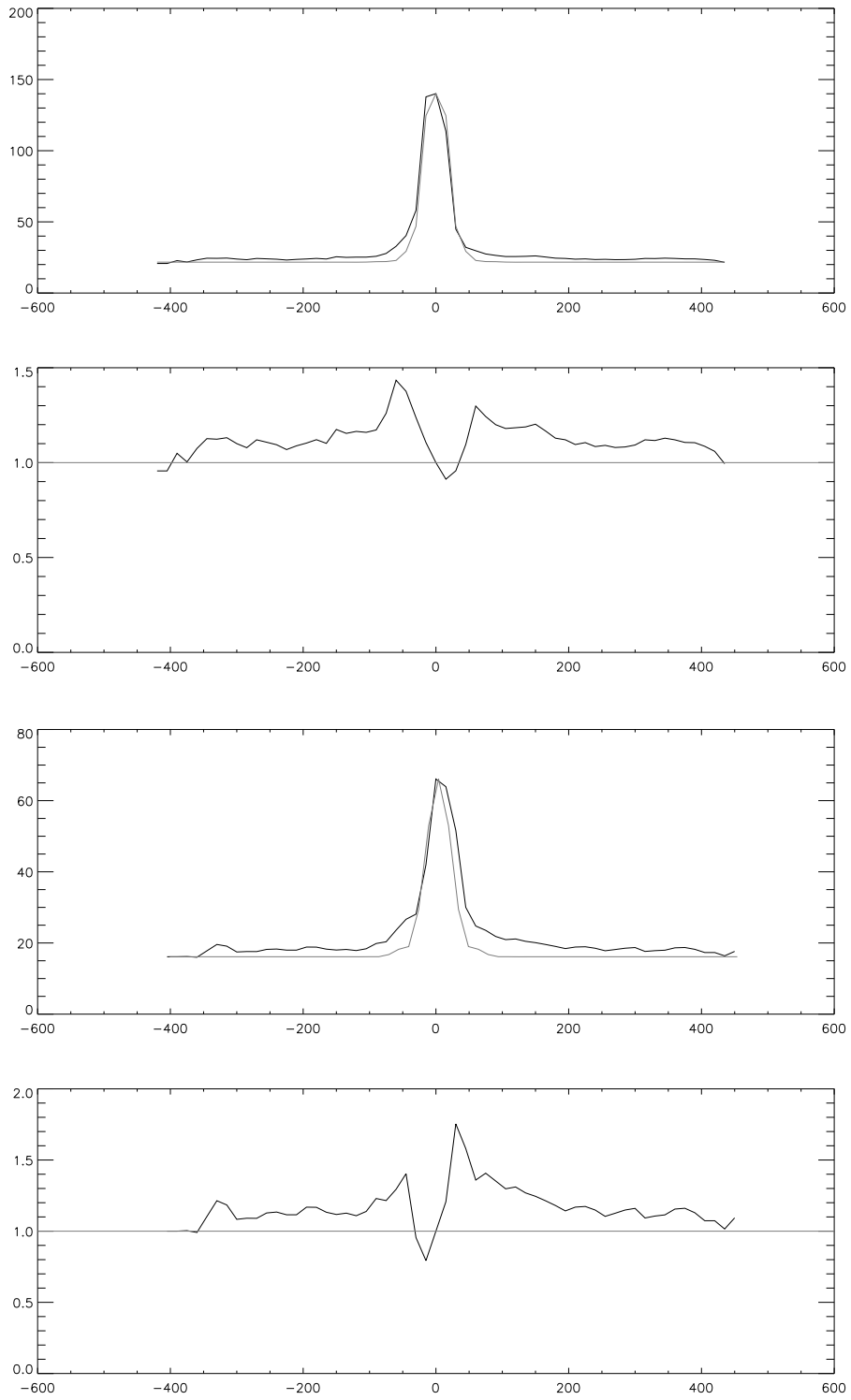


Figure 7.14: *Top Panel*: 60 $\mu$m (top) Radial profiles of V Sgr 1943, and (bottom) profile of the subtracted psf from the radial profile. *Bottom Panel*: 90 $\mu$m Radial profile (top) of V Sgr 1943, (bottom) profile of the subtracted psf from the radial profile.

observation conditions imposed by PHT 32 AOT.

(ii) Second by fitting of two or more Gaussian profiles that reproduces our observed radial profiles. The advantage of this method is that we were able to measure the size of the extended source.

### 7.4.1 Observation Simulations

The ISOPHOT Mapping simulator was used to model PHT 32 AOT observations i.e. to verify what ISOPHOT would observe under PHT 32 oversampling observations. As a result the simulator allowed the user to build point or extended sources, convolves them with a footprint PSF to produce an image of how an object would appear if it was observed with PHT 32. This tool is incoporated within the PIA reduction analysis software. In Table 7.5 we present the flux densities used in the simulations of our observations. The radial profiles that were derived from the simulation are compared with the radial profiles from observations as shown in Figure 7.15 and 7.16.

Table 7.5: Simulations

| Offset Position ($''$) | feature width ($''$) | Flux (Jy) 90 $\mu$m | 160 $\mu$m | Offset Position ($''$) | feature width ($''$) | Flux (Jy) 90 $\mu$m | 160 $\mu$m |
|---|---|---|---|---|---|---|---|
| **Mira** | | | | **V0833 Her** | | | |
| 0 | 5 | 30 | 11.4 | 0 | 3 | 12.7 | 5.05 |
| 0 | 70 | 6 | 4 | 0 | 30–50 | 1.5 | 0.5 |
| 0 | 200 | 0.6 | 0.7 | −230 | 90 | 0.4 | 0.09 |
| 0 | 300 | 0.5 | 0.3 | 250 | 100 | 0.04 | 0.01 |
| 0 | 500 | 0.1 | 0.1 | 0 | 500 | 0.13 | 0.19 |
| **R Hya** | | | | **V1943 Sgr** | | | |
| 0 | 3 | 22 | 10 | 0 | 5 | 10.08 | 4.3 |
| 0 | 60 | 0.7 | 1.5 | 0 | 40–70 | 0.89 | 0.91 |
| 160 | 50 | 0.5 | 0.7 | ±150 | 50 | 0.43 | 0.3 |
| −150 | 60 | 0.4 | 0.25 | −210 | 50 | — | 0.25 |
| 0 | 400 | 0.1 | 0.15 | ±320 | 60 | 0.3 | 0.35 |
| **ST Her** | | | | **V1300 Aql** | | | |
| 0 | 75 | 20.5 | 3.6 | 0 | 30-70 | 0.99 | 1 |
| −240 | 20 | 5 | 0.4 | +200 | 88 | 0.8 | 0.3 |
| +260 | 80 | 0.2 | 0.3 | −200 | 90 | 1 | 0.3 |
| −360 | 20 | 0.7 | 0.2 | 0 | 400 | 0.2 | 0.1 |
| 450 | 30 | 0.1 | 0.28 | | | | |

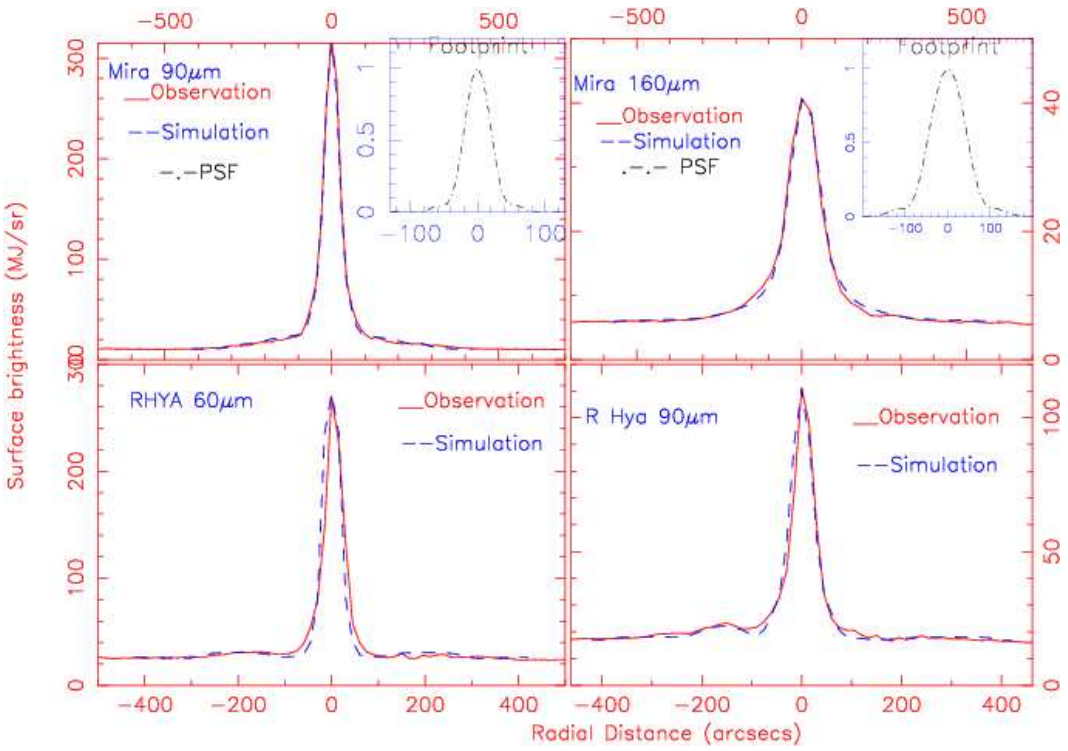


Figure 7.15: Simulation profiles of Mira and R Hya, a point source spread function (PSF) is included for comparison.

### 7.4.2 Gaussians fitted in oxygen – rich radial profiles

I further investigated the size of the extended emission , by developing a code that fits the Gaussian profiles from our image profiles. The program is based on on IDL routines [79] that measures radial features using a profile fitting program called IPIKAIA see on Appendix D.0.4. This program was aimed at fitting multiple gaussian profiles and return the best two Gaussian profiles that reproduces our radial profile from observations. The inner gausian traces the point source emission from object. The outer Gaussian fits the extended emission around the object, hence it is used to estimate the size of the extended source. The size of an extended source is estimated from the measured full width half max (FWHM) of the fitted Gaussian profile.

In Figures 7.17, 7.18, 7.19 7.20, 7.21 and 7.22 the Gaussian profiles that were fitted in our observed profiles are shown. The interpretation behind this code is that it is useful in determining the size of the extended structure from which we can derive

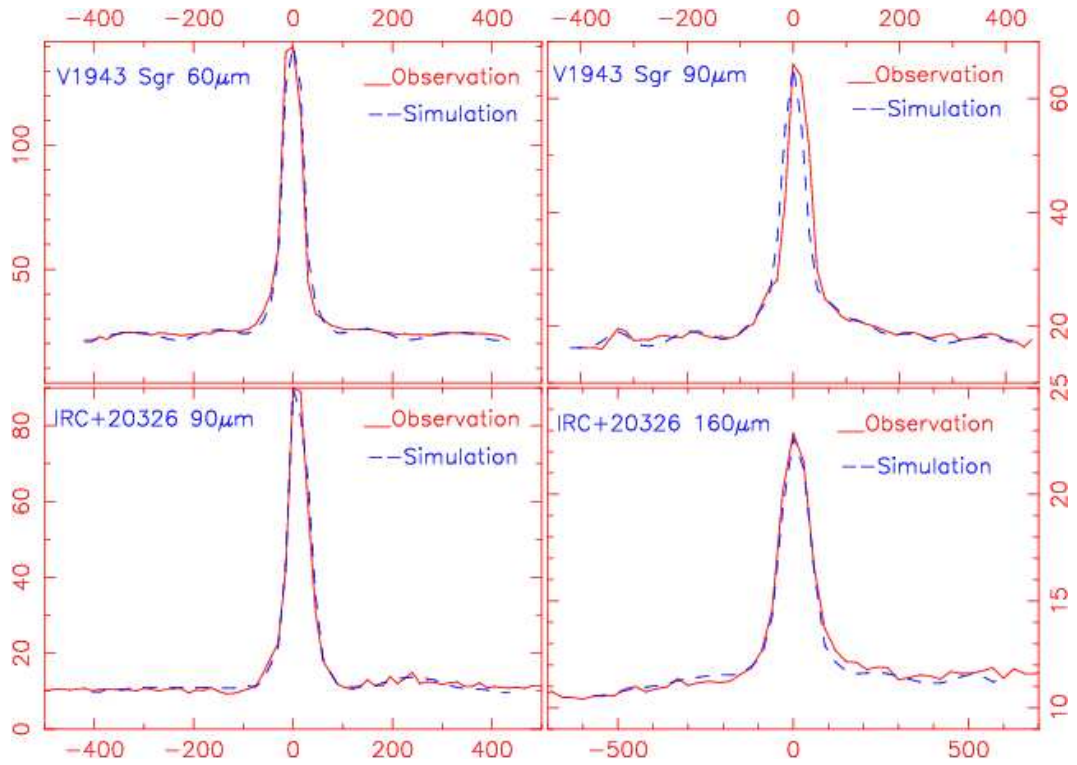


Figure 7.16: Simulation profiles of V1943 Sgr and V0833 Her, a point source spread function (PSF) is included for comparison.

the radius of the extended emission rather that visual interpretation given above in section§ 7.3.1.

For all observations, the radial profiles were first normalized using peak and surface brightness values for better comparison (see Table 7.2). And then the code was run to the the normalized radial profiles inorder to produce the results of the fitted gausians. The normalized footprint psf was also added for comparison, especially in the inner zone where our resolution is limited by FWHM of the observation. The radius of the extended emission was estimated by assuming that $r \sim 1.5\times$FWHM. This choice of finding the radius of the extended emission was chosen because of it offered a better agreement with the results of the radii derived from the simulations and those from 1-D footprint psf subtractions. The FWHM derived from the fitted Gaussian profiles used to estimate the size of the extended source and computed radii of the circumstellar dust shell are presented in Table 7.6.

Table 7.6: Full width half maximum values derived from the fitted gaussian profiles to observed radial profiles

| Source | FWHM (″) | | | Radius (″) | | |
|---|---|---|---|---|---|---|
| Name | 60 $\mu$m | 90 $\mu$m | 160 $\mu$m | 60 $\mu$m | 90 $\mu$m | 160 $\mu$m |
| Mira | — | 303 | 266 | — | 454 | 400 |
| RHya | — | 192 | 270 | — | 288 | 405 |
| V1300 Aql | 114 | 105 | — | 171 | 157 | — |
| V1943 Sgr | 224 | 202 | — | 336 | 303 | — |
| V0833 Her | — | 124 | 206 | — | 186 | 309 |
| ST Her | — | 270 | 242 | — | 405 | 363 |

For example in Mira, in the inner region the fitted Gaussian, at 90 $\mu$m has the FWHM $\sim 57''$ in the which is comparable with the measured FWHM of the footprint psf of $\sim 47.46''$. At 160 $\mu$m, For the halo region, the fitted Gaussian profiles indicates that the size of the extended source has a FWHM of about $300''$ at 90 $\mu$m, which agrees well with a FWHM of $\sim 270''$ at 160 $\mu$m. This indicates that in Mira we might be seeing an extended emission from a circumstellar dust shell with a radius of $450''$ . This radius of the shell is comparable with the radius of $500''$ that was estimated from 1-D psf footprint psf subtraction and also from the simulation photometry of Mira.

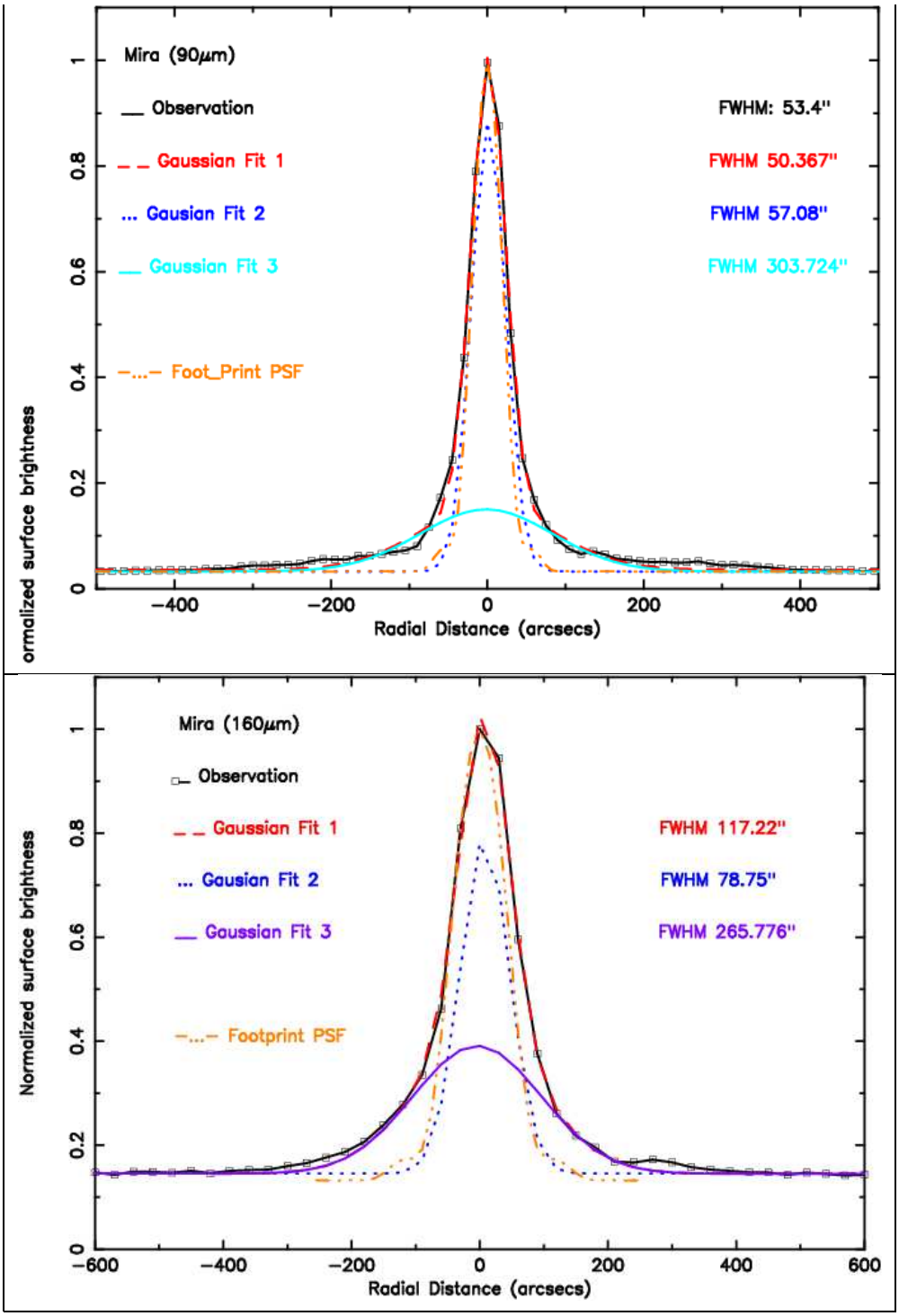


Figure 7.17: 90 $\mu$m (top) and 160 $\mu$m (bottom) fitted Gausian profiles to the observation of Mira profiles

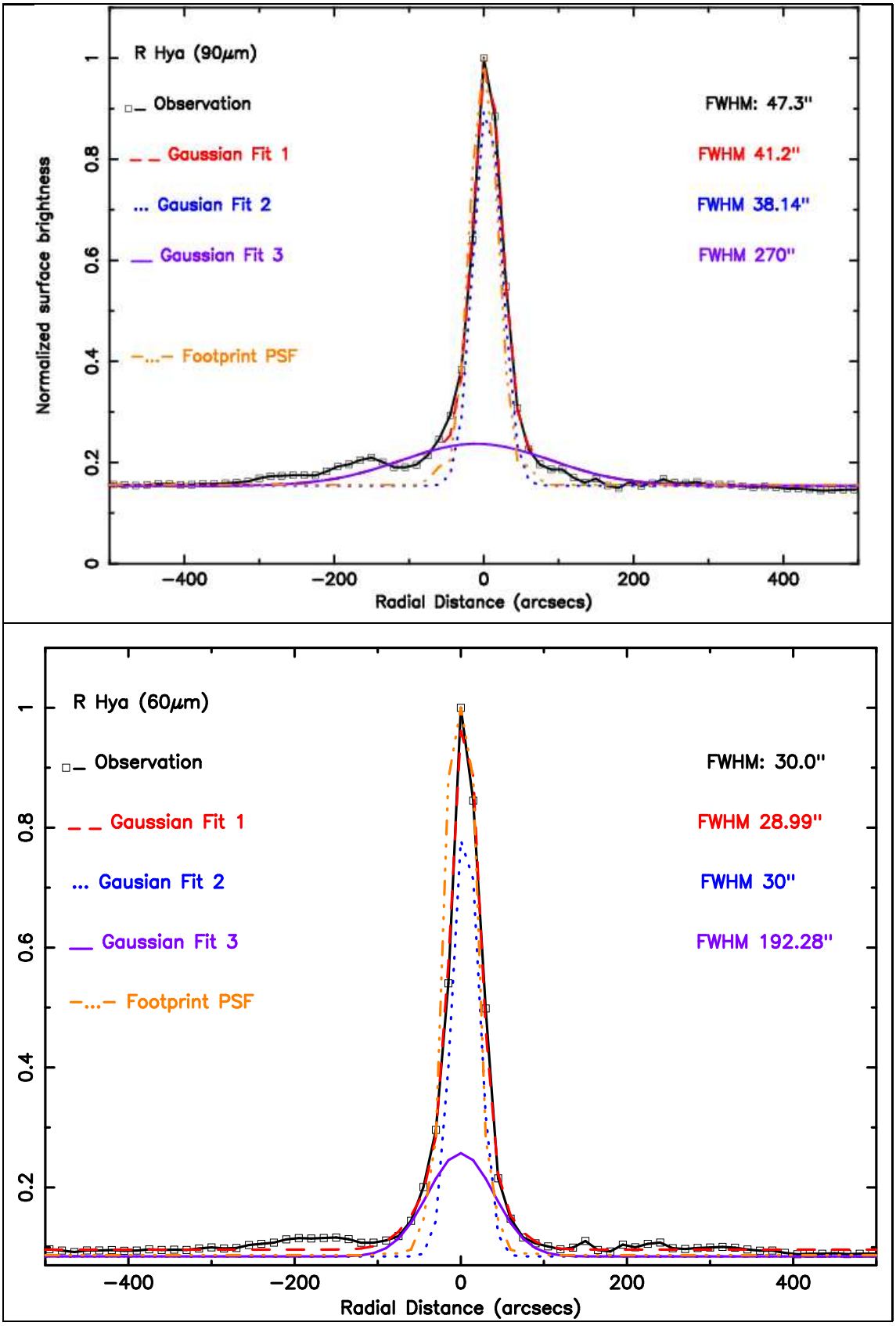


Figure 7.18: 90 $\mu$m (top) and 60 $\mu$m (bottom) fitted Gausian profiles to the observation of R Hya profiles

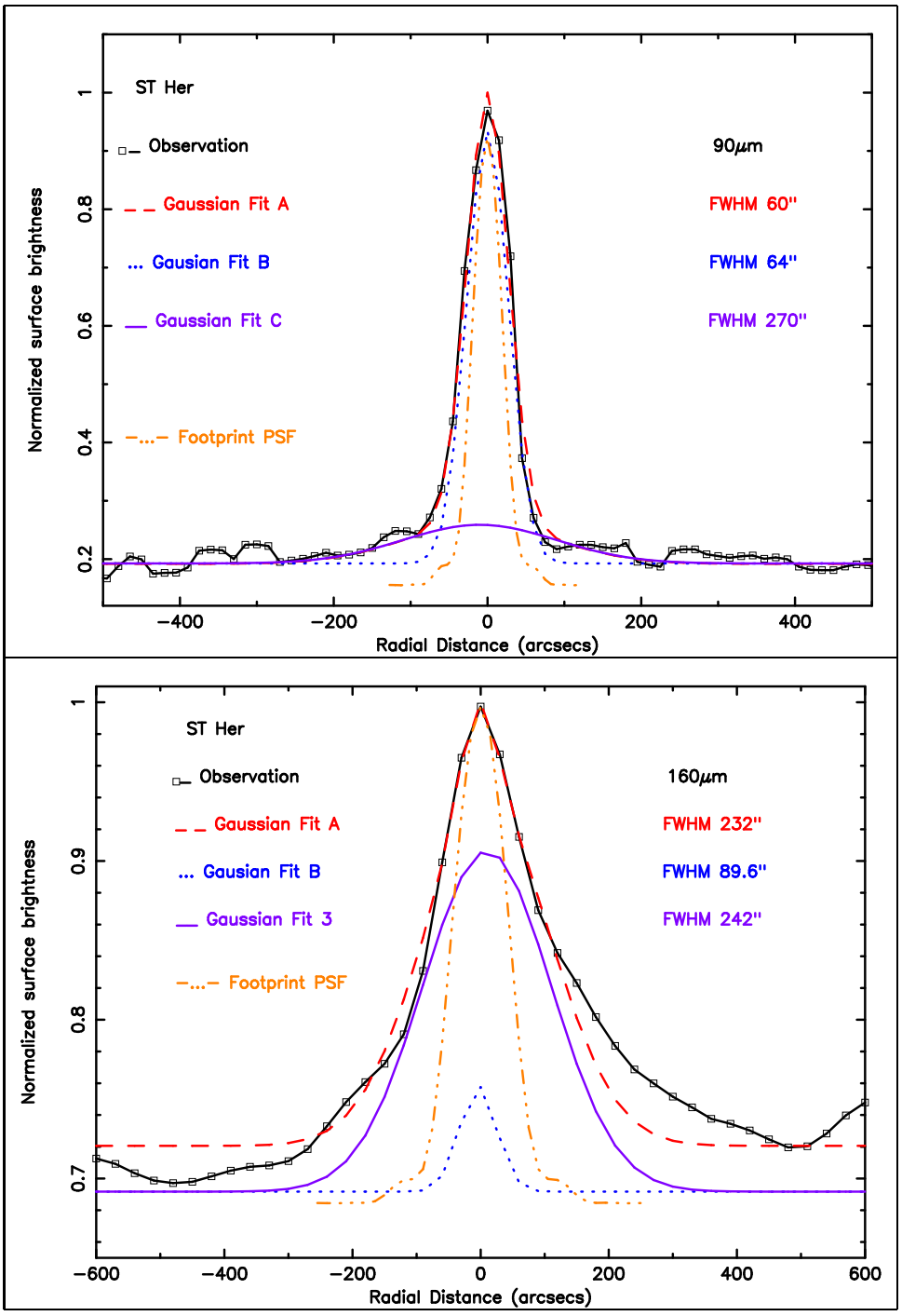


Figure 7.19: 90 $\mu$m (top) and 160 $\mu$m (bottom) fitted Gausian profiles to the observation of ST Her profiles

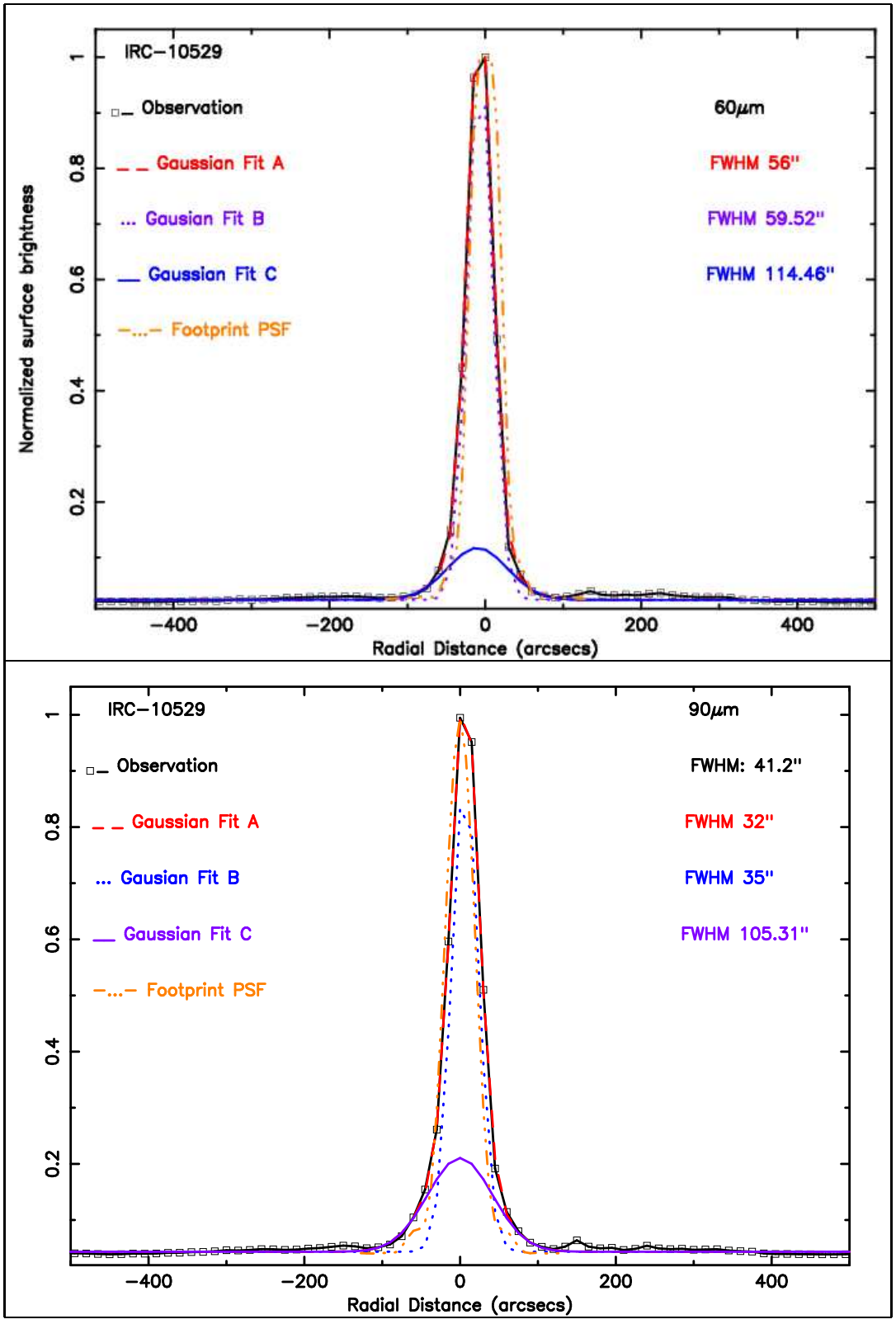


Figure 7.20: 90 $\mu$m (top) and 160 $\mu$m (bottom) fitted Gausian profiles to the observation of V 1300 Aql profiles

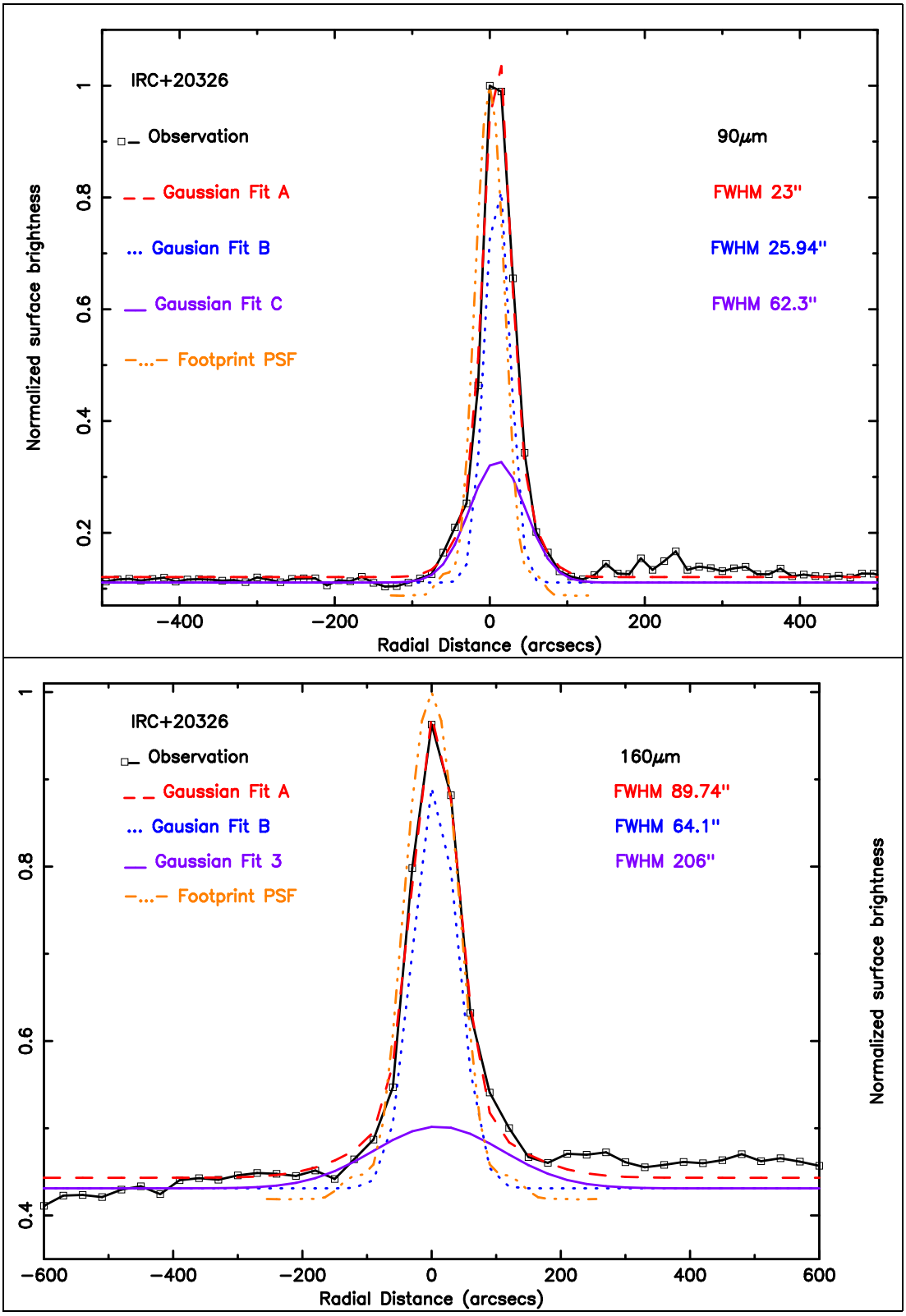


Figure 7.21: 90 $\mu$m (top) and 160 $\mu$m (bottom) fitted Gausian profiles to the observation of V 0833 Her profiles

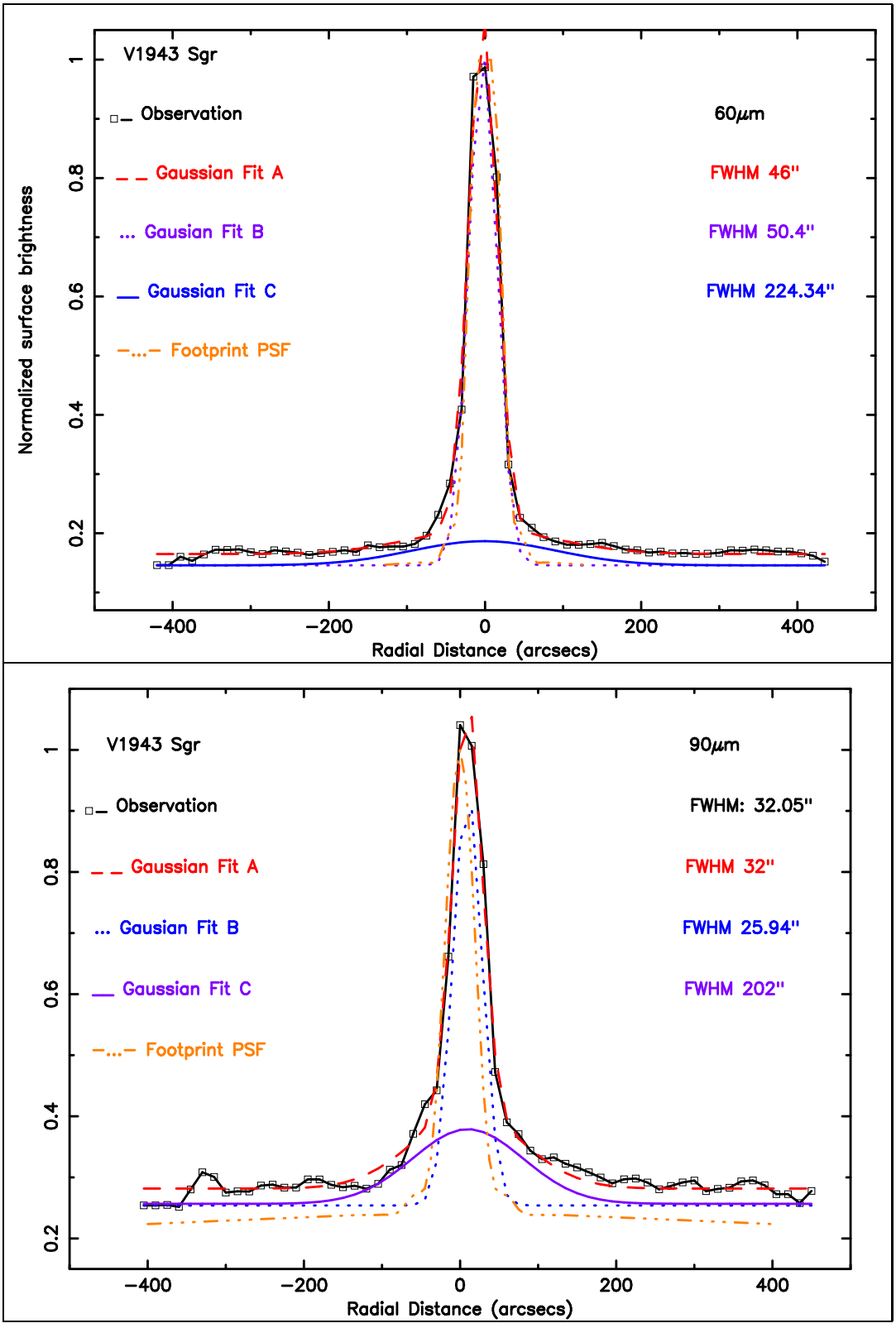


Figure 7.22: 60 $\mu$m (top) and 90 $\mu$m (bottom) fitted Gausian profiles to the observation of V Sgr 1943 profiles

## 7.5 Circumstellar dust flux in the extended emission

The flux (Jy) in the extended emission was measured using Interactive Data Reduction and Analysis Facility (IRAF [135]) surface aperture photometry. Inorder to extract the flux of the extended dust shell, the image was divided into two parts i.e. the region near the core at a minimum radius called $R_{in}$, and at the halo region from $R_{in}$ up to a maximum radius $R_{max}$ for both image at two filters used.

The inner radius was estimated using the minimum radius used to simulate the point source from Table 7.5, and the values for the maximum extent of the circumstellar dust shell was estimated from 1-D footprint psf subtraction aand also using the results from the simulation. The estimated values of the inner radii ($R_{in}$) and $R_{max}$ are shown in table 7.11.

In Table 7.7, the flux measured near the core at $R_{in}$ is labeled $F_1$, and the flux in halo ($R_{in} \leq r \leq R_{max}$) is labeled $F_2$.

Table 7.7: Observed fluxes used to calculate dust masses

| Source | $F_1$ | $F_2$ | $F_1$ | $F_2$ | $F_1$ | $F_2$ |
|---|---|---|---|---|---|---|
| | 60$\mu$m | | 90$\mu$m | | 160$\mu$m | |
| V1300 Aql | 80.34 | 29.89 | 35.72 | 15.38 | | |
| R Hya | 28 | 6.83 | 14.19 | 5 | | |
| V1943 Sgr | 15.65 | 4.39 | 10.71 | 5.19 | | |
| Mira | | 67.86 | 110.23 | 25.15 | 3.21 | |
| V0833 Her | | | 8.39 | 4.79 | 4.83 | 3 |
| ST Her | | | 3.49 | 3.54 | 1.73 | 1.93 |

$F_1$ is flux extracted at $r < R_{in}$. $F_2$ is flux extracted at $R_{in} \leq r \leq R_{max}$.

Table 7.8: Dust temperature and the emissivity derived from observations.

| Name | $T_d$ (K) | $\beta$ |
|---|---|---|
| Omi Cet | 26.5 | 1.5 |
| R Hya | 40.8 | 1.2 |
| ST Her | 34.4 | 1.5 |
| V0833 Her | 47.5 | 1.1 |
| V1943 Sgr | 34.3 | 1.5 |
| V1300 Aql | 23.0 | 1.2 |

### 7.5.1 Emisivity and Dust temperature

The ratios of the flux measured in the halo region ($R_in < r \leq R_{max}$ ) were used to derive the dust temperature and the emissivity index ($\beta$), this method was discussed in Chapter 6 section 5.5.2. The fluxes derived from ISOPHOT PHT32 observations were perfomed at two wavelenghts, in order determine the dust temperature and emisivity we needed another observations. IRAS observation could not be used because of high uncercainities in the beam profiles and uncertainities in the background , thus the values of $\beta$ and $T_d$ were obtained by solving the ratios of the modified blackbodies using the flux ratios of the two filters used. The results found are shown in table 7.8.

## 7.6 Mass of circumstellar dust shell and the mass of the core

The mass of dust in the circumstellar dust shell is estimated by using equation 5.27 in Chapter 5 section § 5.4. The mass of the circumstellar dust in the inner zone ($r \sim R_{in}$) is estimated by assuming that the temperature of the dust is 500K. The reason for this assumption is that, the majority of the emission comes from the inner radius where the dust is more densely packed and the higher temperature leads to high emission levels. The temperature in the inner zone varies from approximately 300 K at the inner dust radius, to the plateau level near 30 K at 50″ radius. e.g. Speck at

al. 2002. However a choice of a dust temperature of 500 K was appropiate for the mass estimates since it is the average dust temperature used to model the inner zone of on oxygen rich Mira - type AGB stars, eg. see Gonzalez et al. 2003 [44], Table 3 on page 7.

$M_1$ in Table 7.7 represents the mass of the dust estimated within our estimated inner zone $R_{in}$.

The dust temperatures in Table 7.8 derived from our observed the flux ratios in the halo region were used to estimate the mass of dust in the outer of the circumstellar shell. $M_2$ in Table 7.9 represents our final results of the mass of the dust estimated within the halo region $R_{in}$ to $R_{max}$.

Table 7.9: Calculated dust masses

| Source | Mass Dust $\times 10^{-4}(M_\odot)$ | | | | | |
|---|---|---|---|---|---|---|
| | 60$\mu$m | | 90$\mu$m | | 160$\mu$m | |
| | $M_1$ | $M_2$ | $M_1$ | $M_2$ | $M_1$ | $M_2$ |
| V1300 Aql | 0.24 | 3.68 | 0.29 | 1.65 | — | — |
| R Hya | 0.14 | 1.69 | 0.14 | 0.7 | — | — |
| V1943 Sgr | 0.09 | 0.61 | 0.1 | 0.41 | — | — |
| Mira | — | — | 1.17 | 6.34 | 2.15 | 0.57 |
| V0833 Her | — | — | 0.078 | 3.22 | 0.026 | 3.83 |
| ST Her | — | — | 0.06 | 3.58 | 0.02 | 1.86 |

$M_1$ is mass of the dust estimated by assuming a dust temperature of 500 K at $R_in$
$M_2$ is mass of the dust estimated by assuming an the dust temperatures given in table 7.8 in the halo at ($R_in < r \leq R_max$ )
$C_{sca}$/vol ($cm^{-1}$): $Q_{60\mu m}$= 329.6: $Q_{90\mu m}$= 141: $Q_{60\mu m}$= 44.6; density: 3 g/$cm^3$
Mass absorption coefficient ($cm^2$/g): $\kappa_{60\mu m}$ = 109.7 : $\kappa_{90\mu m}$ = 141, $\kappa_{160\mu m}$ = 24.8

The dust mass depends on the mass absorption coefficient ($\kappa_\lambda$). For the dust mass calculations, the values of $\kappa_\lambda$ were obtained by assuming that oxygen rich stars are dominated by Silicate grains with density of 3 g $cm^{-3}$ e.g. Hildebrand et al. 1983 [57]. The values of the $\kappa_\lambda$ presented in Table 7.9 were derived by using the scattering cross sections per unit volume for silicate grains from the laboratory data by Draine et al. 1984 [25].

Table 7.10: Dust, Gas and Central Star Masses

| Source | $M_{gas}$ | | | $M_{core}$ | $M_{progenitor}$ |
|---|---|---|---|---|---|
| | 60$\mu$m | 90 $\mu$m | 160 $\mu$m | | |
| Mira | — | 0.15 | 0.055 | 0.66 | 0.76 |
| R Hya | 0.02 | 0.015 | — | 0.55 | 0.58 |
| ST Her | — | 0.07 | 0.04 | 0.52 | 0.58 |
| V1943 Sgr | 0.03 | 0.02 | — | 0.53 | 0.55 |
| V0833 Her | — | 0.065 | 0.077 | 0.63 | 0.7 |
| V1300 Aql | 0.079 | 0.039 | — | 0.65 | 0.73 |

$M_{gas}$ is calculated using a gas-to-dust ratio of 200

The mass of the gas is found by assuming a gas-to-dust ratio of 200, see § 5.5.1 in Chapter 5 for details. We calculated the mass of the core by using Pacysnksi's relation equation 3.1 in Chapter 2, the results are shown in Table 7.6. And also the progenitor mass of these stars were are presented in Table 7.6.

## 7.7 Time Scales

To get the time scales associated with the maximum extent for the circumstellar dust, the physical sizes of the extended emission is determined by using the observed distances to the stars presented in Table7.2. i.e.

$$R_{max}(pc) = D(pc) \times R_{max}(rad) \tag{7.1}$$

1pc = $3.086\times10^{13}$ km, $\pi$ rad = $6.48\times10^{5}$ $''$

The estimated maximum radii of the circumstellar dust is presented in 7.11.

We estimated the time scales using equation 1.3 in Chapter 1, the results are presented in table 7.11. The expansion velocities presented in Table 7.11 were used to estimate the time since the circumstellar dust was ejected at AGB, i.e. $T_{AGB}$. These values come from velocity meassurements of CO emission lines.

Table 7.11: Calculated times scales for oxygen rich stars

| Star | $v_0$ ($\mathrm{km\,s^{-1}}$) | $R_{max}$ (pc) | $T_{AGB} \times 10^4$ yr | ($M_\odot$ /yr) $\times 10^{-7}$ | Extent ($''$) | $R_in$ ($''$) |
|---|---|---|---|---|---|---|
| Mira | 6.7 | 0.28 | 4.07 | 4.4 | 450 | 70 |
| R Hya | 11 | 0.41 | 3.62 | 4.7 | 420 | 30 |
| V1300 Aql | 12 | 0.52 | 4.26 | 25 | 400 | 70 |
| V1943 Sgr | 5.4 | 0.25 | 4.6 | 1.3 | 350 | 70 |
| V0833 Her | 19 | 2.65 | 13.64 | 1000 | 480 | 50 |
| ST Her | 9.5 | 0.7 | 7.23 | 290 | 500 | 50 |

## 7.8 Disscusion

Our results indicate that there is extended emission beyond the point source in all all our objects. The surface brightness distribution for these stars indicate that there is no flux variation or enhancements that are related to the effects of thermal pulses in oxygen rich stars. We were able to measure the size of extended emission at radii beyond $300\ '' - 500''$ from the star. This give usa hint that these stars have large exteded circumtellar dust shell around them. The uncertanities in sizes of the extended emission depends on the uncertainities in the surface backgroud values used. The values in surface background may be higher, due far infrared noise of the instrument and also high galactic cirrus emission around our source stars. Thus the extended emission measured may be lower than the values reported here because the extent of the flux might be lower than that of the surface background used. There is also an additional uncertainity in physical sizes ($R_{max}$) presented in Table 7.11 due to the differences in finding the distances to these stars. The values found in the literature comes from different methods of finding luminosity, e.g. Period - Luminosity relations relations and angular measurements of the star, so they vary, however we do not expect very high erros because all the objects in our sample are not far away. The time scales derived depends on the expansion velocieties used. And these values are within the speeds of 10 - 30 km $s^{-1}$ expected for expansion velocity of both gas and dust in circumtellar dust shell. When we compare the time scale from these results with the time scales calculated by models of stellar evolution,

e.g. those by Vassiliadis & Woods 1993 [137], hearfter VW93. In VW93 models, the expansion velocities used depends on the pulsation period, e.g. equation 3 of VW93 estimates the expansion velocity using equation 4.17 in Chapter 4. For our observed period used, this means the expansion velocities used from CO emission lines are higher than those predicted from VW93. As an example in Omi Cet, at a period of 332 day the expansion velocity by VW93 is about 5.1 km/s instead of 6.73 km/s used in our calculations. Thus is clear that the derived time scales are shorter by the order of magnitude than those predicted by VW93. The differences maybe due to the periods used to model the stars and the assumes metalicity in VW93 models. Also since our time scales are limited by the extent of the circumstellar emission; we may have under – estimated the sizes of the shell due to uncertainities in the measured surface background, this will cause the time scale shorter. The the distances to the objects are a within few hundreds of parcecs away with an exception of V0833 Her; this will also makes our measured times smaller.

The lower limit to the progenitor masses found are masses between 0.53 - and 2.35 $M_{\odot}$, see Table 7.6. These values are limited by, the region selected i.e. $R_{max}$, and the uncertainities in the measured flux densities, the distance used, and the assumed mass of gas to dust ratio. If we assume that the duration of mass loss to be $T_{AGB}$, then the total mass by the star can be estimated using the mass loss rates given in Table7.11. The results indicates that the total mass of the entire dust shell are within 0.1 - 0.02 $M_{\odot}$. Thus if we assume that the remnant stars for our objects are within the 0.6 - 1.4, this would suggest that these stars evolved from progenitors with masses 1.0– 5.0 $M_{\odot}$ with metalicity variation between 0.01 - 0.016 when we compare our results with the initial and final masses from VW93 models (table 2 and figure 21).

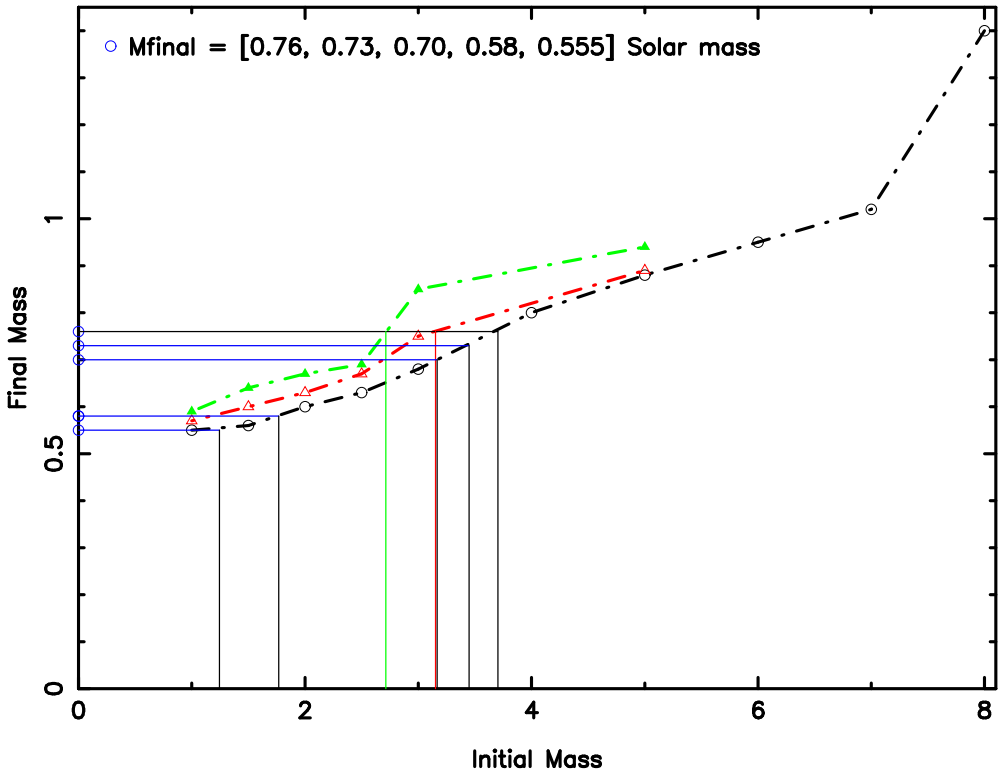


Figure 7.23: Initial mass (solar units) - x axis vs Final mass(solar units) y - axis. The dash - circle - dotted lines indicate a curve from Weideman & Koester 2000 [140] data. Triangles are the data points from Vassiliadis and Wood 1983 [137], solid triangle = Z (metallicity) = 0.004, open triangle Z = 0.016

### 7.8.1 Oxygen rich results comparison with Initial mass relations

The ramnant masses of the stars above are compared with the observations of initial - final mass relations by Weidemann & Koester 2000. Also compared with the data are the model prediction of initial mass relations by VW93 with metalicity Z = 0.016 (solar neighborhood) and Z = 0.004. The results are shown in figure 7.23. Our results indicate that the initial main sequence mass for oxygen rich stars range from 1.2 - 3.5 $M_{\odot}$ for stars with ramnant masses 0.55 – 0.76 $M_{\odot}$ by using Wiedeman & Koester, 2000 [140]. The models by VW98 shows an inital mass range of (1.5 - 3)$M_{\odot}$ for oxygen rich stars with ramant stars in the same region (0.55 - 0.76) $M_{\odot}$).

# Chapter 8

# Probing Dust around C-rich stars

## 8.1 Introduction

In this chapter, we use the results of the photometric images of six evolved oxygen-rich AGB stars that were observed using ISOPHOT as described in Chapter 6. The aim of our analysis of these images is

1. To discern the extended far-infrared emission beyond the central point source.

2. To determine the observed maximum extent of the circumstellar emission, and thus, assuming a constant expansion velocity, estimate the time scale since the oldest observable dust was ejected from the star phase started. By dividing the star's maximum extent of circumstellar emission with the expansion velocity, the AGB time scale is derived.

3. To estimate the mass of the progenitor star via determining the mass of the core central star (via Pazysnksi's relation equation 3.1) and the mass of the extended dust from its emission and assuming a canonical dust-to-gas ratio. The mass of the circumstellar dust together with the mass of the core is used

Table 8.1: Selected target evolved carbon-rich intermediate-mass stars imaged by Infrared Space Observatory (ISO) using far-infrared PHT32-C camera, together with basic observed parameters.

| Name | Right Ascension | Declination | Spectral Type |
|---|---|---|---|
| LP And | 23h34m27.53s | +43d33m01.2s | c8, 35e |
| RY Dra | 12h56m25.91249s | +65d59m39.8086s | C4, 5J(SRb |
| W Hya | 13h49m01.99810s | -28d22m03.4881s | M8e(SRa) |
| R Scl | 01h26m58.09492s | -32d32m35.4374s | C6, 4(SRa) |
| R For | 02h29m15.30831s | -26d05m55.6473s | C4, 3e(M) |
| U Ant | 10h35d12.85153s | -39d33m45.3180s | C, N(SR) |

Hipparcos [107] and VizieR [100] were used to obtain the object's sky position in RA:DEC. Spectral type of comes from Loup et al. 1993 [85].

to set the lower limit of the progenitor mass of these stars.

## 8.2 Carbon Rich stars Observations

In this chapter, we present the linear scan results of six evolved carbon rich AGB stars that were observed using the infrared photo-polarimeter instrument ISOPHOT (Lemke et al. 1996[**?**]) on board the Infrared Space Observatory (ISO; Kessler et al. 1996[70]) using the imaging camera PHT-C.

The periods, luminosities, the distances to the objects and the expansion velocities obtained from the observations in the optical were used in calculations of mass of the core, mass of the progenitor stars and the time scales. The table that showing these parameters is presented in Table 8.2.

Table 8.3 shows the filters ($\mu$m) and the direction of the scan (Roll angle (deg)) used during observations. The roll angle was measured anti-clockwise with respect to the reference star at the center of each image (i.e. East of North at star$'$ location with respect to the positional co-ordinates given in Table 8.1. The chopper was used for oversampling between the spacecraft positions along the scan line. The pixel sizes used in the construction of the images are shown in table 8.3.

Table 8.2: Basic observed parameters (distance, luminosity, pulsation period, mass loss rates and expansion velocities) for six target oxygen-rich intermediate-mass stars found in literature that were used in calculations.

| Name | Distance (pc) | Pulsation Periods (days) | Luminosity $L_\odot$ | $\dot{M}$ ($10^{-7}\,M_\odot\ yr^{-1}$) | $v_{exp}$ $kms^{-1}$ |
|---|---|---|---|---|---|
| LP And | 650[c] | 614[d] | 8000 [c] | 0.80[c] | 20.4 [c] |
| RY Dra | 650[c] | 200[d] | 840[c] | 6.2 [c] | 10 [c] |
| W Hya | 120[c] | 361[d] | 33000[c] | 0.81[c] | 8.2[c] |
| R Scl | 370[c] | 370[d] | 1400[c] | 27[c] | 24.7[c] |
| R For | 254[c] | 388.73[d] | 2000[c] | 22 [c] | 20[c] |
| U Ant | 400[c] | — | 1300[c] | 62[c] | 21.2[c] |

a = Winters et al. 2003 [144], b = Gonzalez et al. 2003 [44] c = Loup et al. 1993 [85]
d = VizieR [100],e = Woodruff et al. 2004 [153]

Table 8.3: Target evolved oxygen-rich intermediate-mass stars imaged by Infrared Space Observatory (ISO) using far-infrared PHT32-C camera - filters and roll angles.

| Name | Filters ($\mu$m) | Pixel Size (arcsec$^2$) | Image Size (arcmin$^2$) | Intergration time (s) | Roll Angle (deg N of E) |
|---|---|---|---|---|---|
| LP And | 90:160 | 15×15 | 43.8×8.5 : 44.5×9.3 | 3046:2876 | 277.3364 |
| RY Dra | 90:160 | 15×23:15×23 | 34.5×9.2 : 35.6×9.2 | 3250:3646 | 212.9746 |
| W Hya | 90:160 | 15×23:30×92 | 49.8×9.2 : 50.5×12.2 | 4720:4766 | 248.705 |
| R Scl | 90:160 | 15×23:30×92 | 34.5×9.2 : 35.3×12.3 | 3250:3226 | 282.893 |
| R For | 90:160 | 15×15 | 34.5×9.3 : 29.3×12.3 | 3250:2946 | 279.5421 |
| U Ant | 60:90 | 15×23:15×23 | 23.8×9.2 : 23.8×9.2 | 2412:2220 | 123.5997 |

Table 8.4: The flux brightness at the center where the star is located, and the minimum flux brightness (forms a background of the image) far from the stars's location, when each object was observed using the filter indicated.

| Source | Maximum fluxes | | | Sky background | | |
|---|---|---|---|---|---|---|
| Name | 60 $\mu$m | 90 $\mu$m | 160 $\mu$m | 60 $\mu$m | 90 $\mu$m | 160 $\mu$m |
| LP And | — | 61.49 | 29.66 | — | 13.68 | 19.6 |
| Ry Dra | — | 29.48 | 5.98 | — | 3.98 | 2.46 |
| W Hya | — | 260.79 | 50.88 | — | 11.2 | 10.38 |
| R Scl | — | 292.92 | 16.38 | — | 7.6 | 6.63 |
| R For | — | 27.42 | 5.25 | — | 5.07 | 4.1 |
| U Ant | 163.04 | 95.55 | — | 11.7 | 8.4 | — |

## 8.3 Images and radial profiles results

The objects in Table 7.1 were reduced using ISO-PHOT Interactive Analysis software (PIA) (Gabriel et al. 1997[33]) version 10.0.described in Chapter 6.

### 8.3.1 PHT32 Images of Carbon – rich stars

The images are presented in Figures 8.1, 8.2, 8.3, 8.4, 8.5, 8.6

The maximum flux at the center and minimum surface brightness values per filter used are sumarized in Table 8.3.1. Contours on the images delineate different regions of surface brightness and the last contour indicate the minimum surface brightness where the emission assumes a sky background value. The orientation of each image is such that the $x$ - direction is chosen to along the scan direction using the roll angle given in Table 8.3.

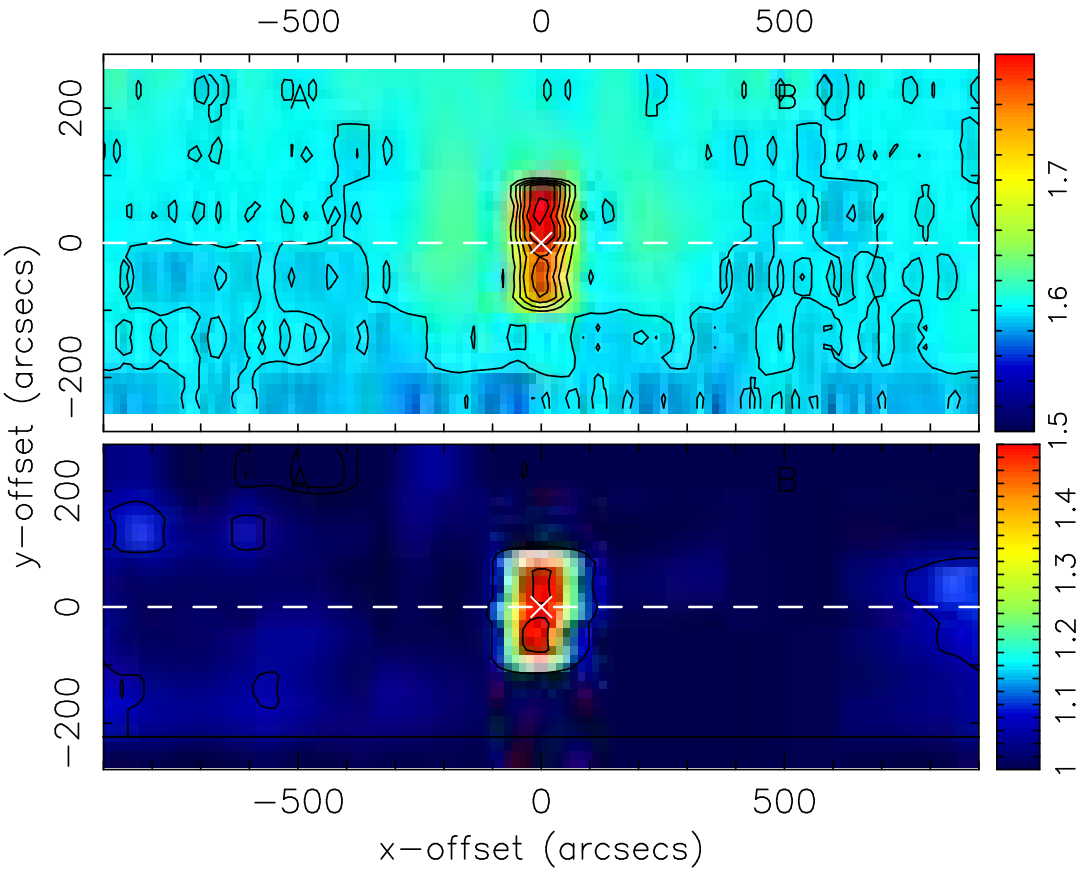


Figure 8.1: : 90 $\mu$m (*Top*) and 160 $\mu$m (*Bottom*) images of a variable Mira Cet typical carbon-rich star LP And. The image orientation is chosen such that the scan direction is chosen to be in the $x$-direction with respect to the positional co-ordinates given in Table 8.3. The dotted lines indicate the scan line used to derive the radial profile shown in Figure 8.7. $x$ and $y$ offsets indicates pixel positions of the area covered in the image. The wedge shows the surface brightness of the image in log scale. The contour levels are set between minimum at 1 and maximum at 1.6. The cross indicates the peak position of the maximum flux.

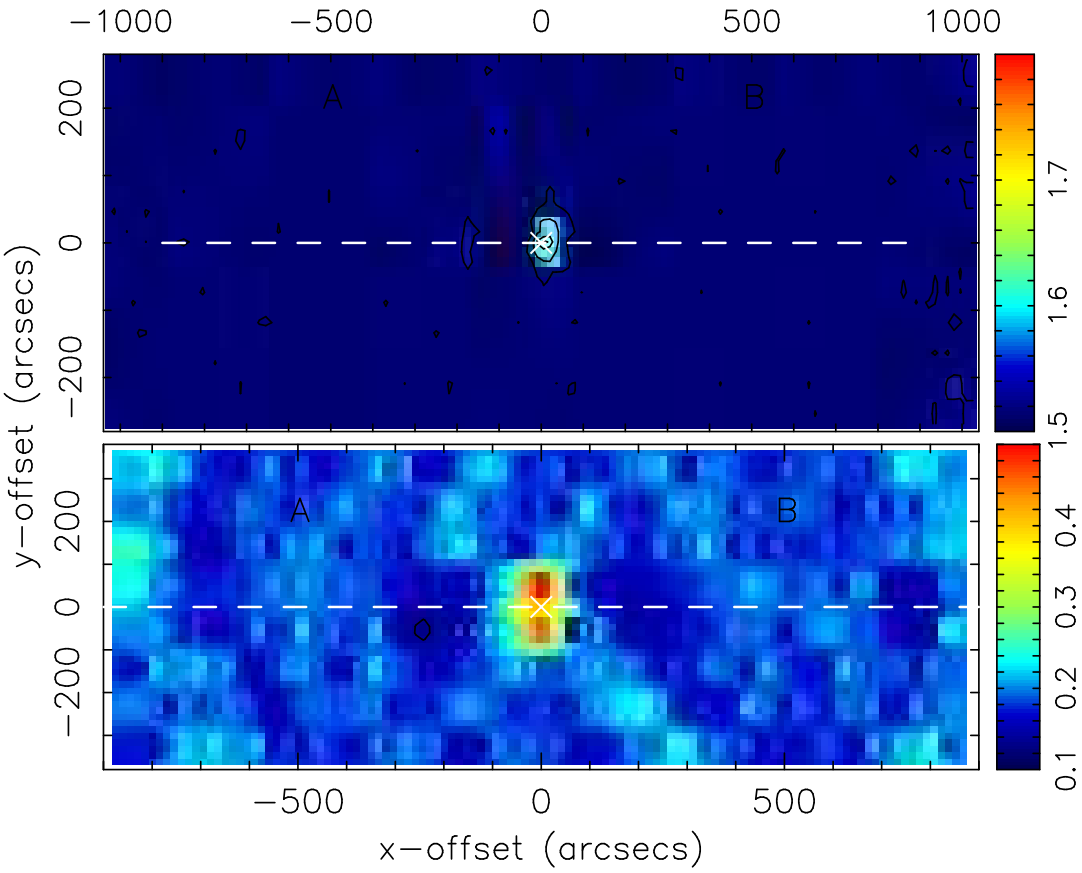


Figure 8.2: *Top panel*: 90 $\mu$m and 160 $\mu$m images of a variable Mira Cet typical carbon-rich star R For. The image orientation is chosen such that the scan direction is chosen to be in the $x$-direction with respect to the positional co-ordinates given in Table 8.3. The dotted lines indicate the scan line used to derive the radial profile shown in Figure 8.7. $x$ and $y$ offsets indicates pixel positions of the area covered in the image. The wedge shows the surface brightness of the image in log scale. The contour levels are set between minimum at 1 and maximum at 1.6. The cross indicates the peak position of the maximum flux.

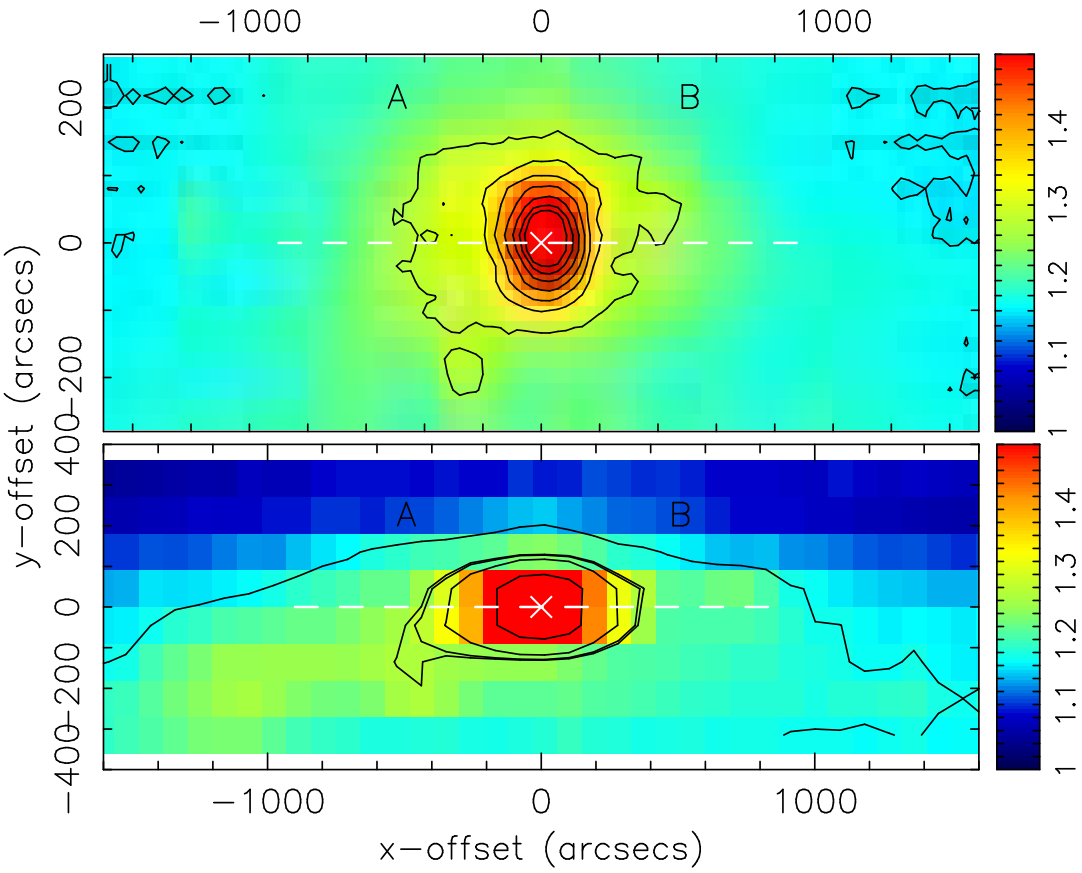


Figure 8.3: *Top panel*: 90 $\mu$m and 160 $\mu$m images of a semi-regular pulsating carbon-rich star W Hya. The image orientation is chosen such that the scan direction is chosen to be in the $x$-direction with respect to the positional co-ordinates given in Table 8.3. The dotted lines indicate the scan line used to derive the radial profile shown in Figure 8.9. $x$ and $y$ offsets indicates pixel positions of the area covered in the image. The wedge shows the surface brightness of the image in log scale. The contour levels are set between minimum at 1 and maximum at 1.5. The cross indicates the peak position of the maximum flux.

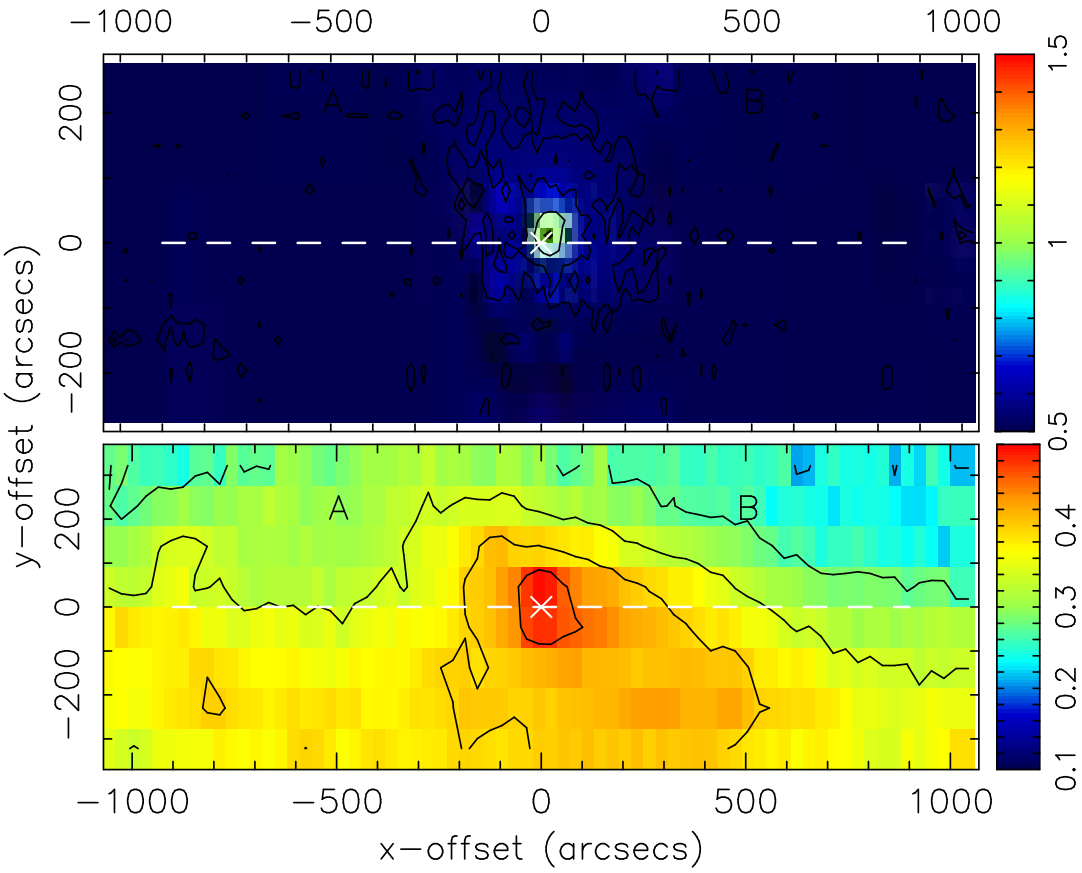


Figure 8.4: *Top panel*: 90 $\mu$m and 160 $\mu$m images of a carbon-rich star Ry Dra. The image orientation is chosen such that the scan direction is chosen to be in the $x$-direction with respect to the positional co-ordinates given in Table 8.3. The dotted lines indicate the scan line used to derive the radial profile shown in Figure 8.9. $x$ and $y$ offsets indicates pixel positions of the area covered in the image. The wedge shows the surface brightness of the image in log scale. The contour levels are set between minimum at 1 and maximum at 1.5. The cross indicates the peak position of the maximum flux.

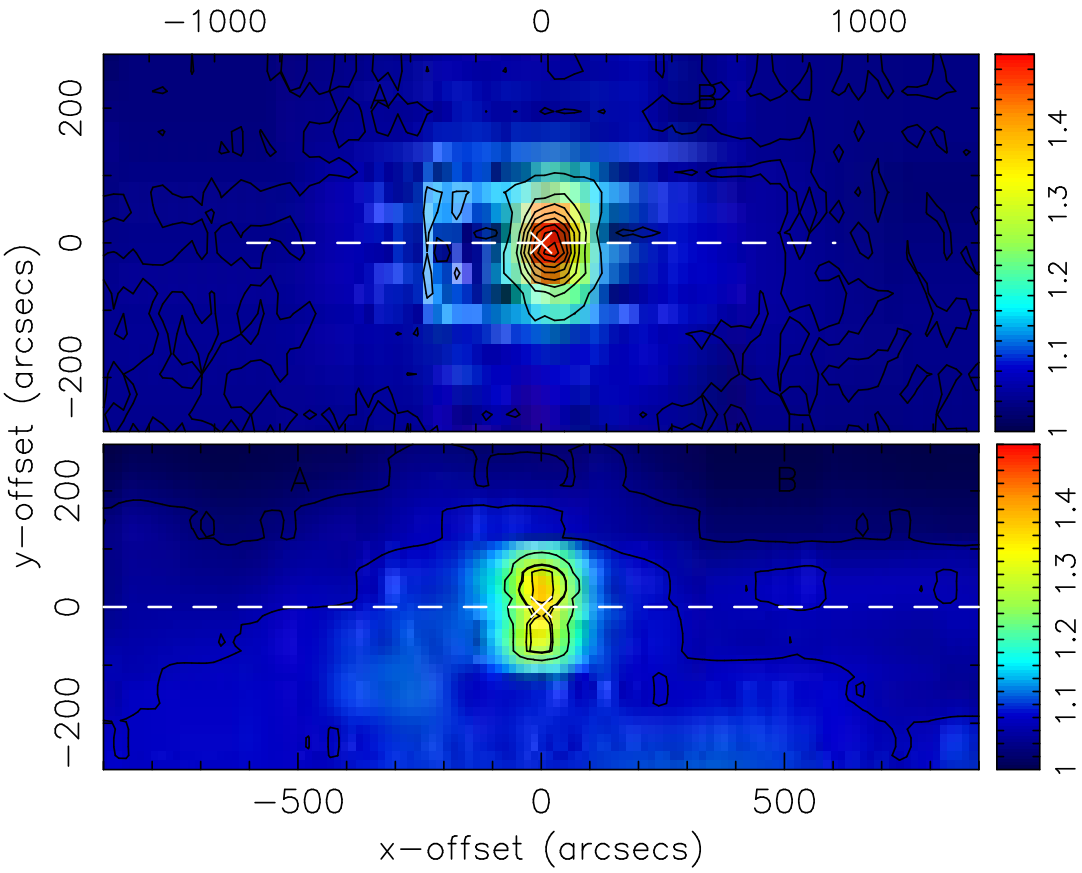


Figure 8.5: *Top panel*: 90 $\mu$m and 160 $\mu$m images of a semi–regular pulsating carbon-rich star R Scl. The image orientation is chosen such that the scan direction is chosen to be in the $x$-direction with respect to the positional co-ordinates given in Table 8.3. The dotted lines indicate the scan line used to derive the radial profile shown in Figure 8.8. $x$ and $y$ offsets indicates pixel positions of the area covered in the image. The wedge shows the surface brightness of the image in log scale. The contour levels are set between minimum at 1 and maximum at 1.5. The cross indicates the peak position of the maximum flux.

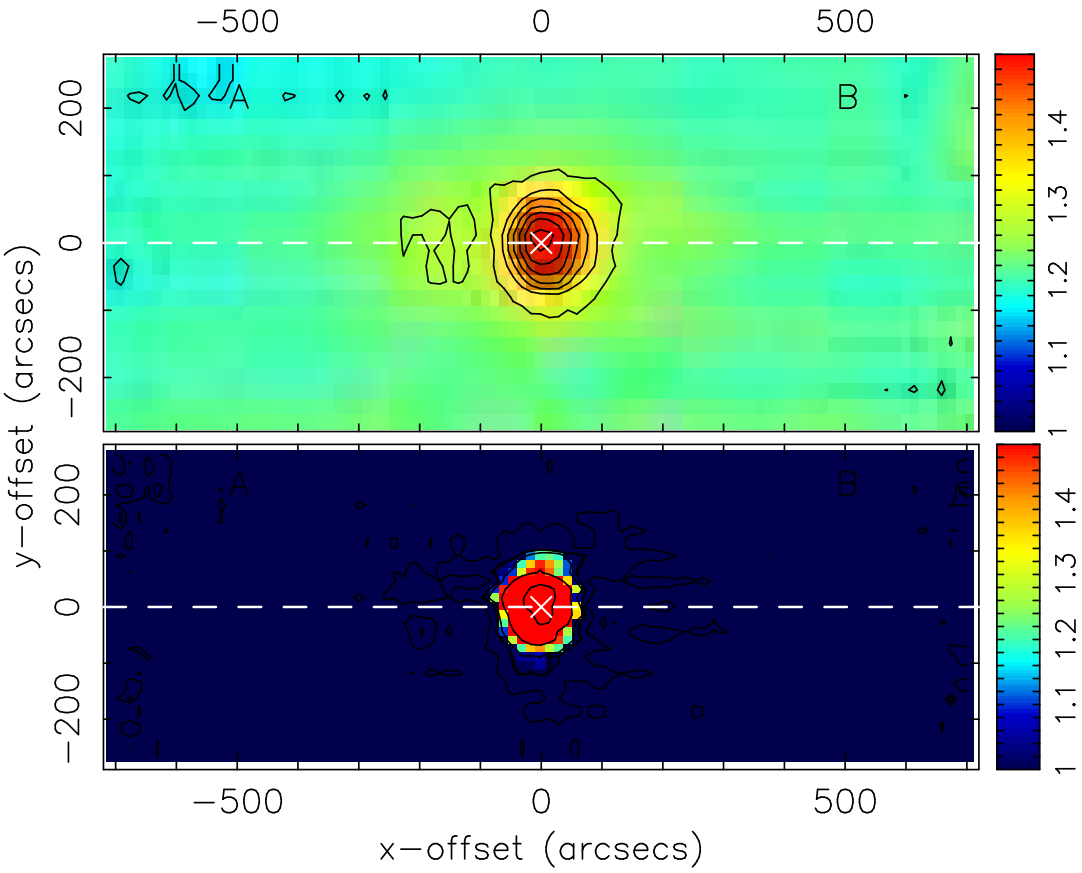


Figure 8.6: *Top panel*: 90 $\mu$m and 160 $\mu$m images of a semi-regular pulsating carbon-rich star U Ant. The image orientation is chosen such that the scan direction is chosen to be in the $x$-direction with respect to the positional co-ordinates given in Table 8.3. The dotted lines indicate the scan line used to derive the radial profile shown in Figure 8.8. $x$ and $y$ offsets indicates pixel positions of the area covered in the image. The wedge shows the surface brightness of the image in log scale. The contour levels are set between minimum at 1 and maximum at 1.5 The cross indicates the peak position of the maximum flux.

### 8.3.2 Linear Scan results: Radial profiles

A radial profile is a 1-D plot of surface brightness of individual pixels vs the pixel positions along the direction of the cut on the image. These scans were taken along the scan direction interpreted as the $x$-direction in image as shown by the dotted line on the images. In this section we present all radial profiles of carbon rich stars in our sample. The resulting profiles are shown in Figures 8.7, 8.8, 8.8 and 8.9.

The foot print psf's were used to make an assessment if object has extended emission. This was achieved by scaling the footprint psf with the the maximum surface brightness and the sky background (see Table 7.2) in in-order to match with radial profiles from observations. As we can see in Figures, 8.7, 8.8, 8.9 and comparison of the psf's with the radial profiles indicates that most of our objects may have extended circumstellar emission since the footprint psf profiles fall inside the area covered by our observed radial profiles. The exception are, the 90 $\mu$m observations of R For and 60 $\mu$m observation of U Ant. However, comparison of radial profiles with footprint psf's indicates that there were offsets in peak position at the center where the source object is supposedly located. These offsets were in the order of 10–20$''$. These offsets appear to shift the center peak of the surface brightness to the right side of all radial profiles scans. A close look at all profiles shows that the off-centered peak is followed by a gradient decrease in surface brightness. As a result the profiles are not essentially symmetric about the center. Since these offsets have not been investigated in details they set a limitation on the positional accuracy source, and also in finding correct size of the extended source. The interpretation of this effect is probable due to the long term drift in responsivity when chopper passed the bright source at the center, since the offsets occurs along the direction of the scan on the right side of each the radial profile. This defect on long transient effect of the PHT32 C detectors was discussed in details in Chapter 6.

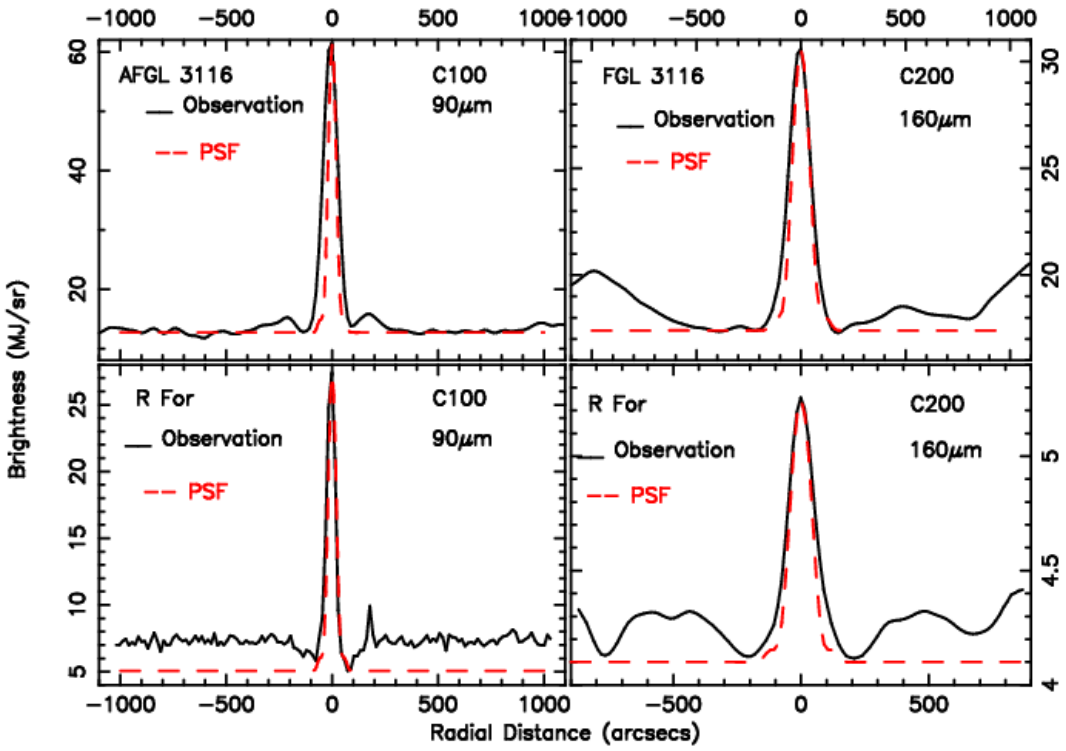


Figure 8.7: Radial profiles of AFG3116 and R For, the PSF is included for comparison.

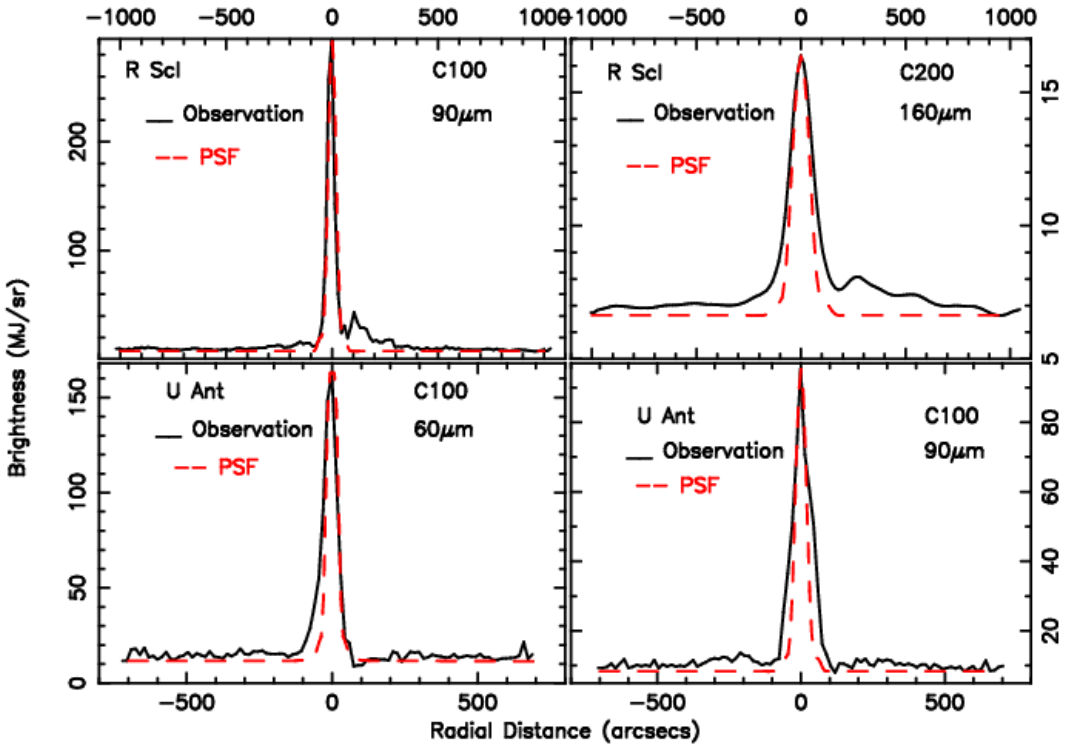


Figure 8.8: Radial profiles of AFG3116 and R For, the PSF is included for comparison.

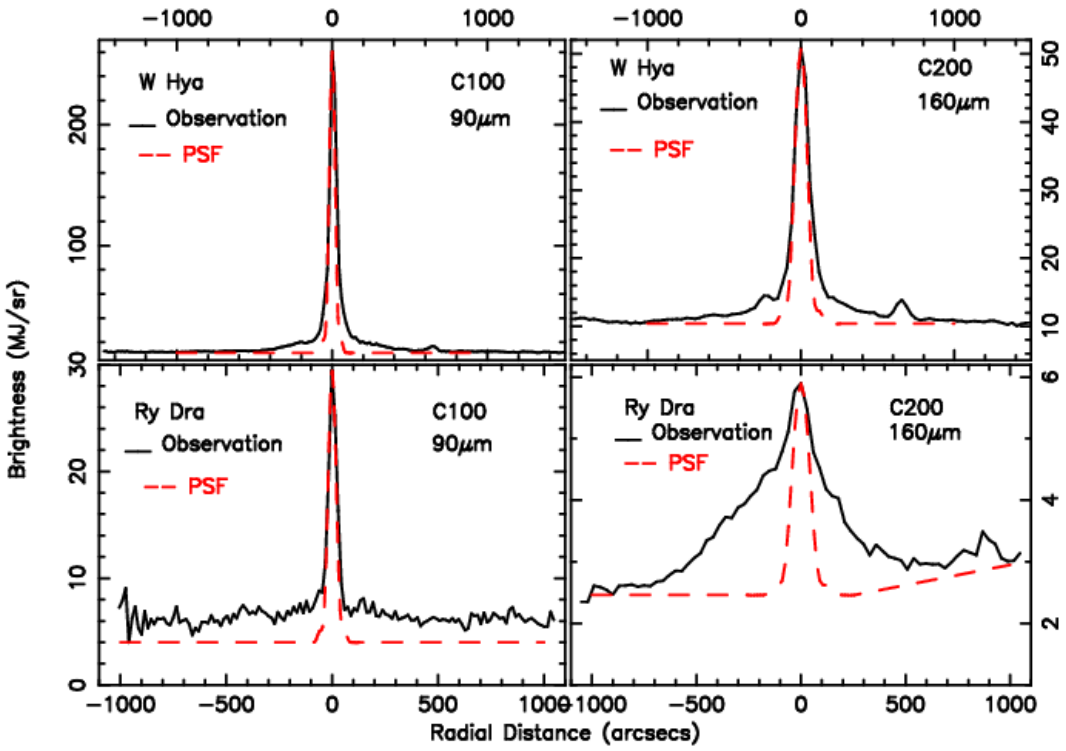


Figure 8.9: Radial profiles of R Scl and U Ant, the PSF is included for comparison.

## 8.4 Analysis of radial profiles for Carbon rich stars

### 8.4.1 Carbon rich stars: 1 – D PSF Subtraction

We subtracted the foot prinf psf's from radial profiles in order to eliminate the effects of the point source and show extended emission. The result are shown in Figures, 8.10, 8.11, 8.12, 8.14, 8.13.

A closer look at the subtracted profile of Mira Cet type star LP And, indicates that at 90 there is a smooth decline in surface brightness with distance until a radius of $\sim 100''$ is reached. This is followed by a flux increase forming a bump at a radius of $200''$. These bumps in surface brightness appear on the same position in radial profile at of 90 $\mu$m, so they maybe showing real structures in this filter. However looking at the 160 $\mu$m these structures are not clearly defined. The peak at $50''$ on right side of the subtracted profile at 90 $\mu$m is due to the footprint psf being higher than the

radial profile due to the positional offset in peak position that caused. For LP And at 90 $\mu$m our observations indicates the presence of a detached circumstellar dust with a radius of $\sim 450''$. When comparing the images of this object, it was noticed that there is a lobe structure in direction perpendicular to the scan direction i.e in y-axis in Figure 8.1. This structure seems real since it is observable at both filters.

The left side of the footprint subtracted profile of R Scl at 90 $\mu$m shows that the surface brightness smoothly declines until it reaches a radius of 85". There are noticeable bumps in the surface brightness at a radii of 150 $''$ and $250''$. This trend is not observed at 160 $\mu$m. At both filters the right sides have high background uncertainties such that the profiles are not able give valuable information, however both profiles indicated that this object is extended a radius of$\sim 700 - 800''$. The two peaks at 90 may indicate that we are observing two detached shells from this object.

The left side of Ry Dra footprint subtracted profile indicates that the surface brightness's have bumps at $\sim 200'', 400'', 850''$. These bumps are clearly visible at filters, even though the 90 observers have high variation in surface brightness due to the noise and cirrus confusion effect around this object. The images of this object indicates clump structures around this object, more noticeable at 90 $\mu$m. At 160 $\mu$m observations, the profile is slanted towards the left due with a lower surface brightness than to right, this effect correspond to image results in Figure 8.4. The reason behind this is at high resolution by PHT 32 oversampling at 160 $\mu$m, this object has a very low peak in the maximum flux close to the surface background brightness (see flux maximum and minimum at 90 $\mu$m in Table8.3.1), such even when we used the p32 tools to eliminate long drift on the detector transients, these transients were not completely eliminated, which caused the image to be very bright on the right side. That is why we notice that the bumps in the surface brightness profile observed at 160 $\mu$m are clearly not well defined, but still visible.

W Hya subtracted profiles indicate that this object is extended up to a radius

of 1000" arcsec. There are no clear bumps in surface brightness distribution. The bump observed at a radius of 90 $\mu$m, seems ghostly since it disappears at 160 $\mu$m. The surface brightness distribution for this object smoothly declines as seen on the profiles of oxygen rich Omi Cet.

The subtracted profile of R For at 90 $\mu$m indicates that this object is a point source at this filter and there is high noise and cirrus confusion at background level. However at 160 $\mu$m we observe a large detached circumstellar disc to a radius of $\sim 700''$ that seem separating from the star from a distance of 200". The size of this disc is $\sim 500''$ as seen in Figure 8.14.

The left hand side of the footprint psf subtracted radial profiles of U Ant, indicates that this object is extended up to a radius of $550''$. The right hand side suffered positional offsets such that it is not giving valuable information as seen in Figure 8.15. What is interesting about this object is that on both filters, the observed radial profiles shows peaks in surface brightness at $300''$ (with a size of 250") and at $450''$ (with a size of $100''$). This regularity in surface brightness may be indicating that we are observing two circumstellar dust shells detaching from this object at a radius of $150''$. imaging polarimetry observations by Gonzalez & Olofsson 2003 [44] indicated multiple four shells at radii, $5''$, $20''$, $40''$ and $60''$ for this star. What we notice from our results is that the 160 $\mu$m psf subtracted profile shows an abrupt shift in surface brightness at a distance of $\sim 55''$ that is followed by a smooth decline to a radius $\sim 150''$ (see bottom panel of Figure8.15. This may indicate that were are observing the last shell reported by Gonzalez & Olofsson 2003.

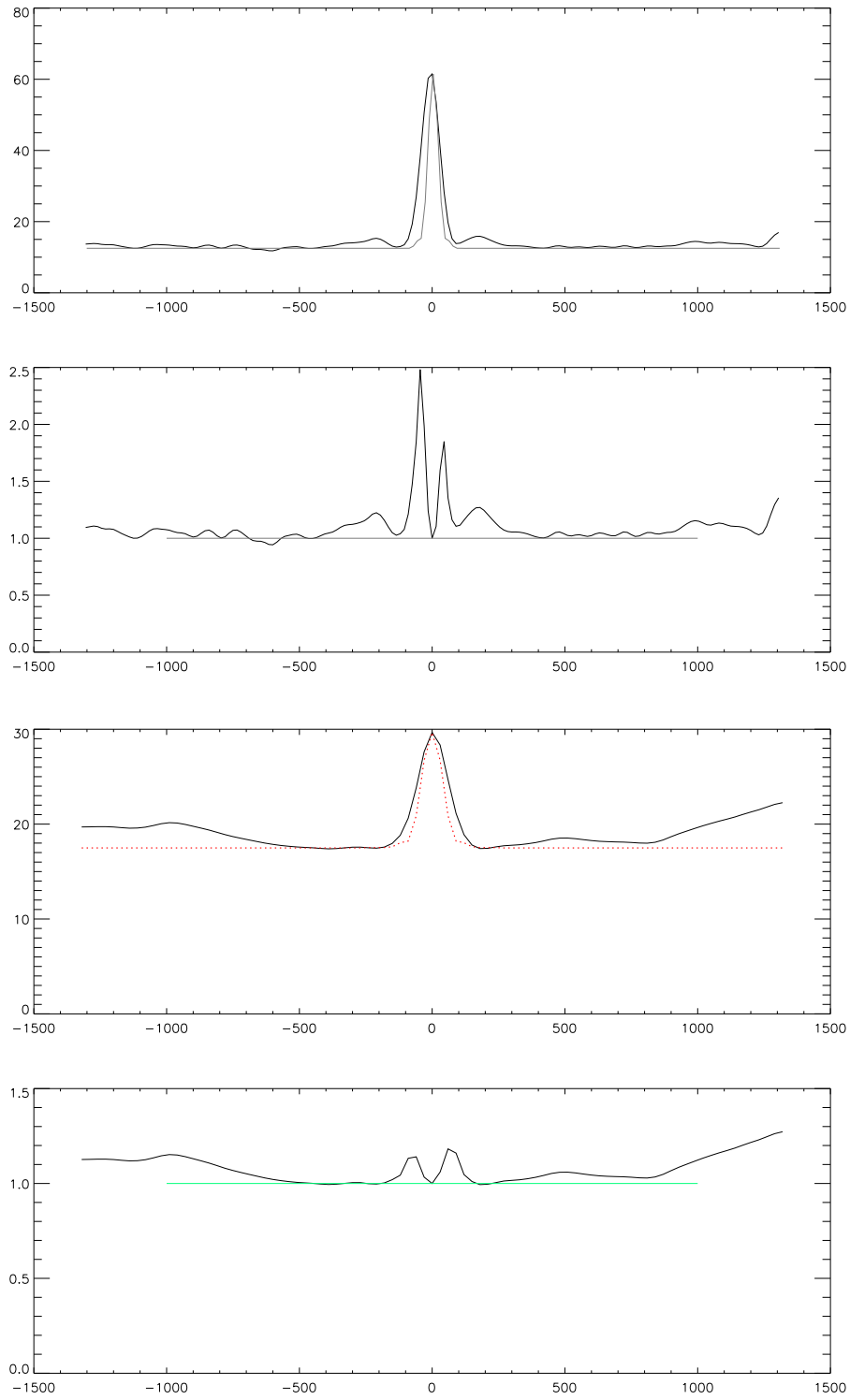


Figure 8.10: *Top Panel*: 90 $\mu$m (top) Radial profiles of carbon rich Mira Cet type star LP And, and (bottom) profile of the subtracted psf from the radial profile. *Bottom Panel*: 160 $\mu$m Radial profile (top) of carbon rich Mira Cet type star LP And, (bottom) profile of the subtracted psf from the radial profile.

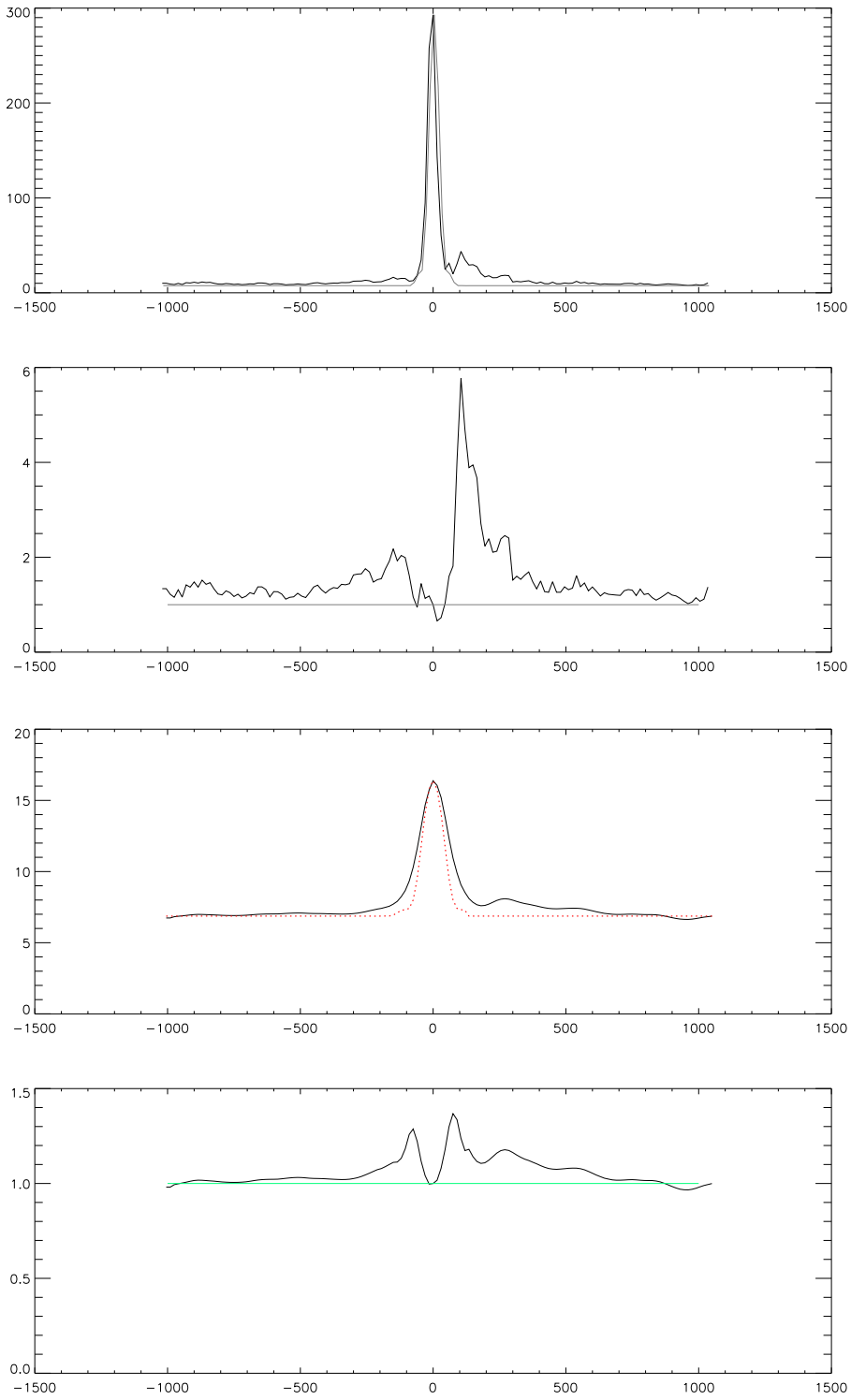


Figure 8.11: *Top Panel*: 90 $\mu$m (top) Radial profiles of a semi–regular pulsating carbon rich R Scl, and (bottom) profile of the subtracted psf from the radial profile. *Bottom Panel*: 160 $\mu$m Radial profile (top) of a semi–regular pulsating carbon rich R Scl, (bottom) profile of the subtracted psf from the radial profile.

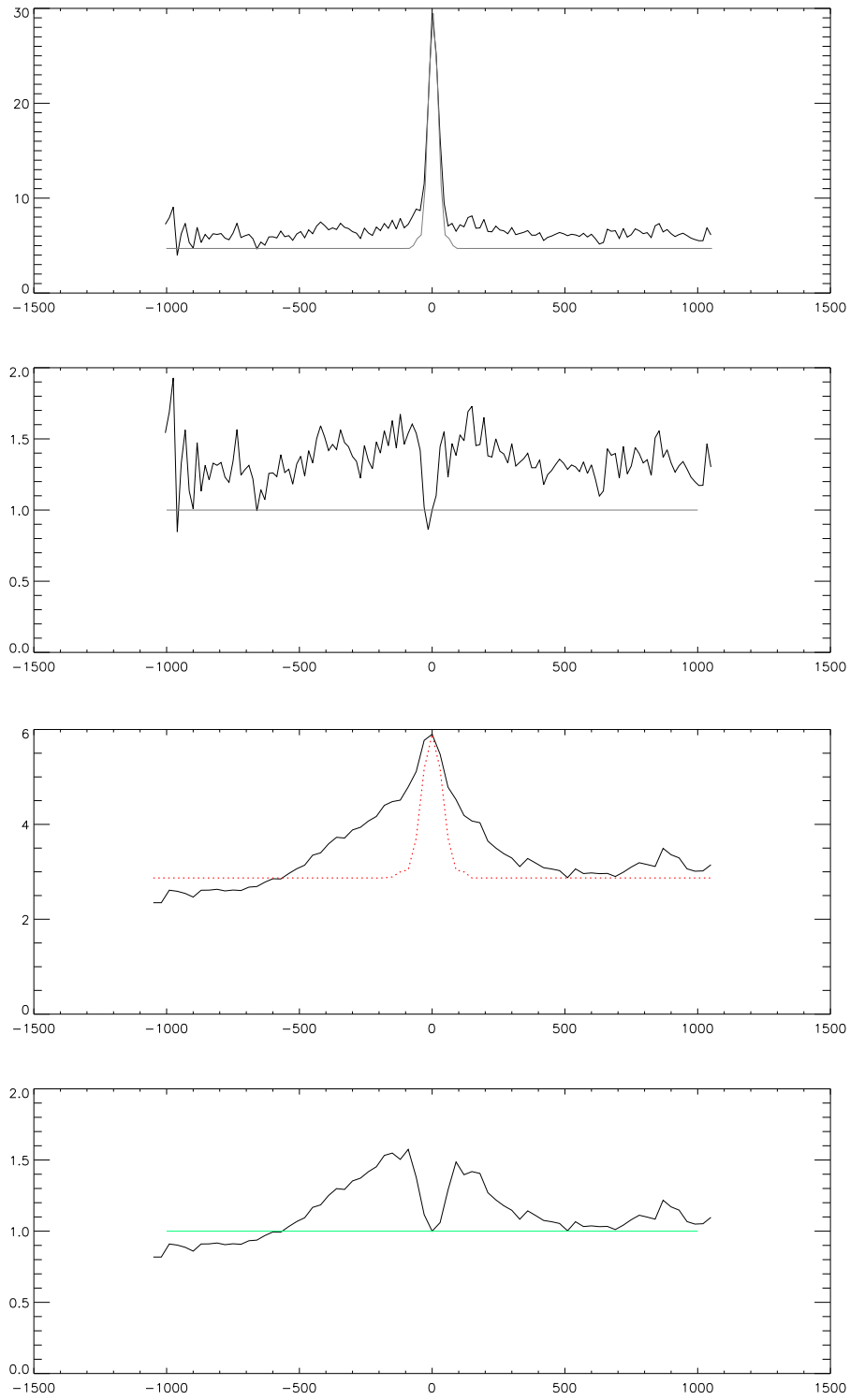


Figure 8.12: *Top Panel*: 90 $\mu$m (top) Radial profiles of a carbon rich Ry Dra, and (bottom) profile of the subtracted psf from the radial profile. *Bottom Panel*: 160 $\mu$m Radial profile (top) of a carbon rich Ry Dra, (bottom) profile of the subtracted psf from the radial profile.

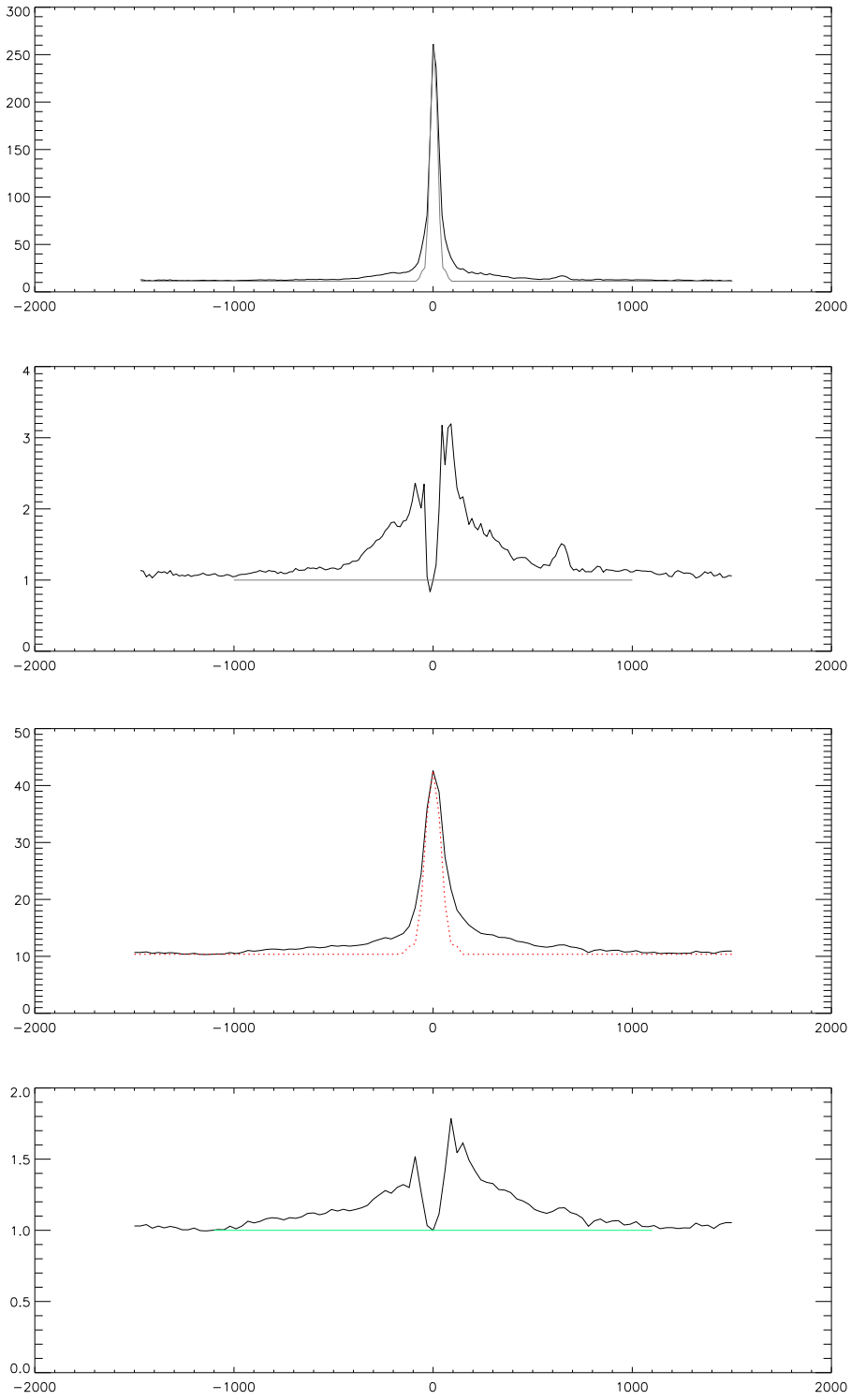


Figure 8.13: *Top Panel*: 90 $\mu$m (top) Radial profiles of a semi–regular pulsating carbon rich star W Hya, and (bottom) profile of the subtracted psf from the radial profile. *Bottom Panel*: 160 $\mu$m Radial profile (top) of a semi–regular pulsating carbon rich star W Hya, (bottom) profile of the subtracted psf from the radial profile.

### 8.4.2 Gaussians fitted on carbon – rich stars radial profiles

In this section we present the results of the Gaussian profiles fitted onto the normalized observed radial profiles. The same procedure described in section § 7.4.2 was followed in deriving the results presented here. However there are subtle differences in profiles of the carbon rich stars, than those of oxygen rich stars. The radial profiles of most carbon rich star's profiles showed variations in surface brightness as was discussed in section § 8.4.2. The observed radial profiles indicated that the surface brightness forms dips at radii beyond 50 - 100 " from the star. This is followed by flux increase that declines smoothly for other objects or (bumps) at different positions from the star. Therefore when fitting the Gaussian profiles in these stars, what was actually measured is the size of the circumstellar emission centered around the object. If the star has multiple shell structures or flux enhancements at different positions, our fitted Gaussian profiles are unable to account for those structures. The structures observed at different positions from the star maybe sitting on top, under or being part of of the circumstellar dust shell from the star. And also due to high uncertainties in surface background the fitted Gaussian profiles did not give reliable results. The results of the fitted Gaussian are shown in Figures 8.16, 8.17, 8.18, 8.19, 8.20 and 8.21.

The FWHM derived from the fitted Gaussian profiles used to estimate the size of the extended source from the star and the estimated radii of the source are presented in Table 8.5.

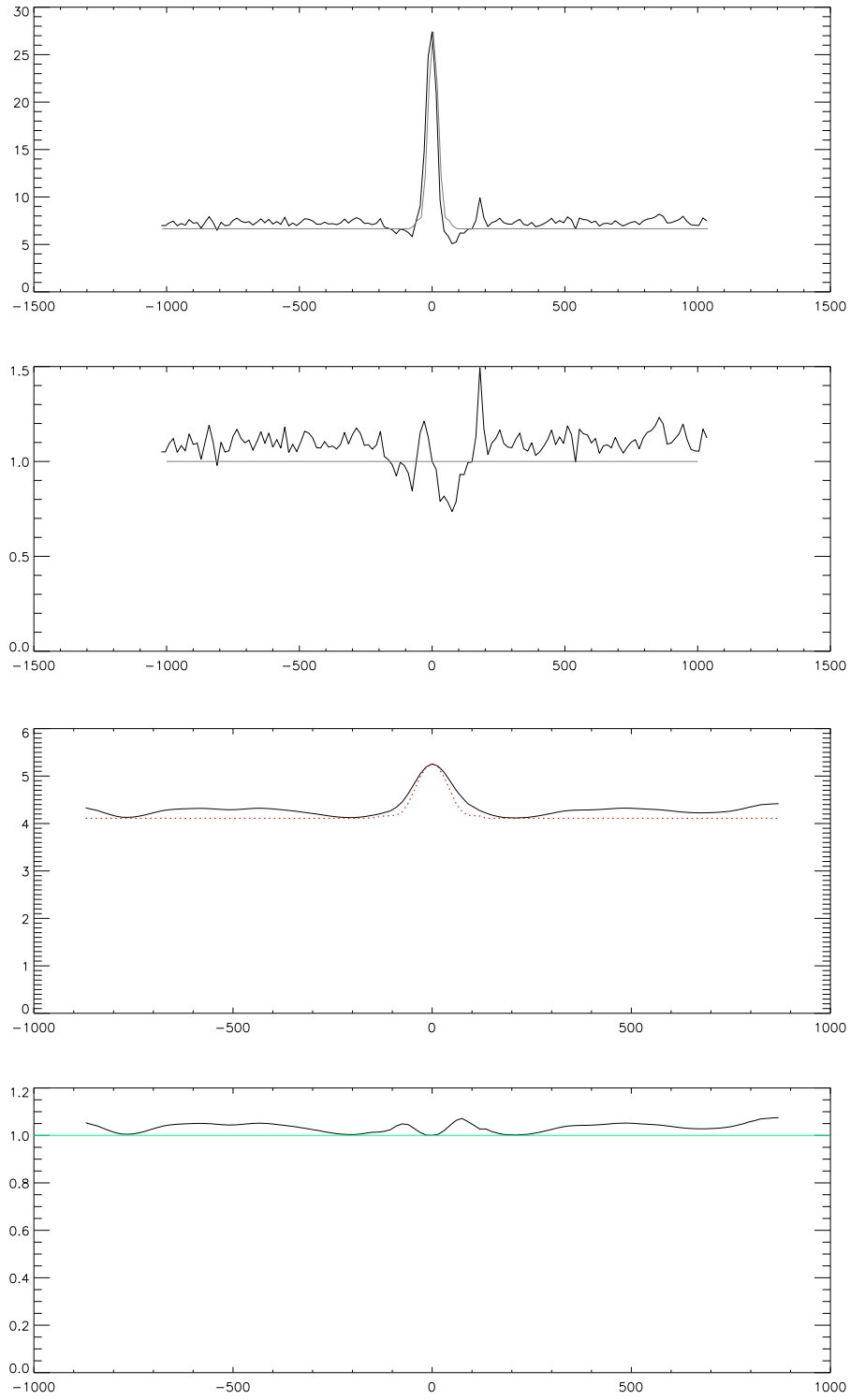


Figure 8.14: *Top Panel*: 90 $\mu$m (top) Radial profiles of a variable star of Mira Cet type carbon rich R For, and (bottom) profile of the subtracted psf from the radial profile. *Bottom Panel*: 160 $\mu$m Radial profile (top) of a variable star of Mira Cet type carbon rich R For, (bottom) profile of the subtracted psf from the radial profile.

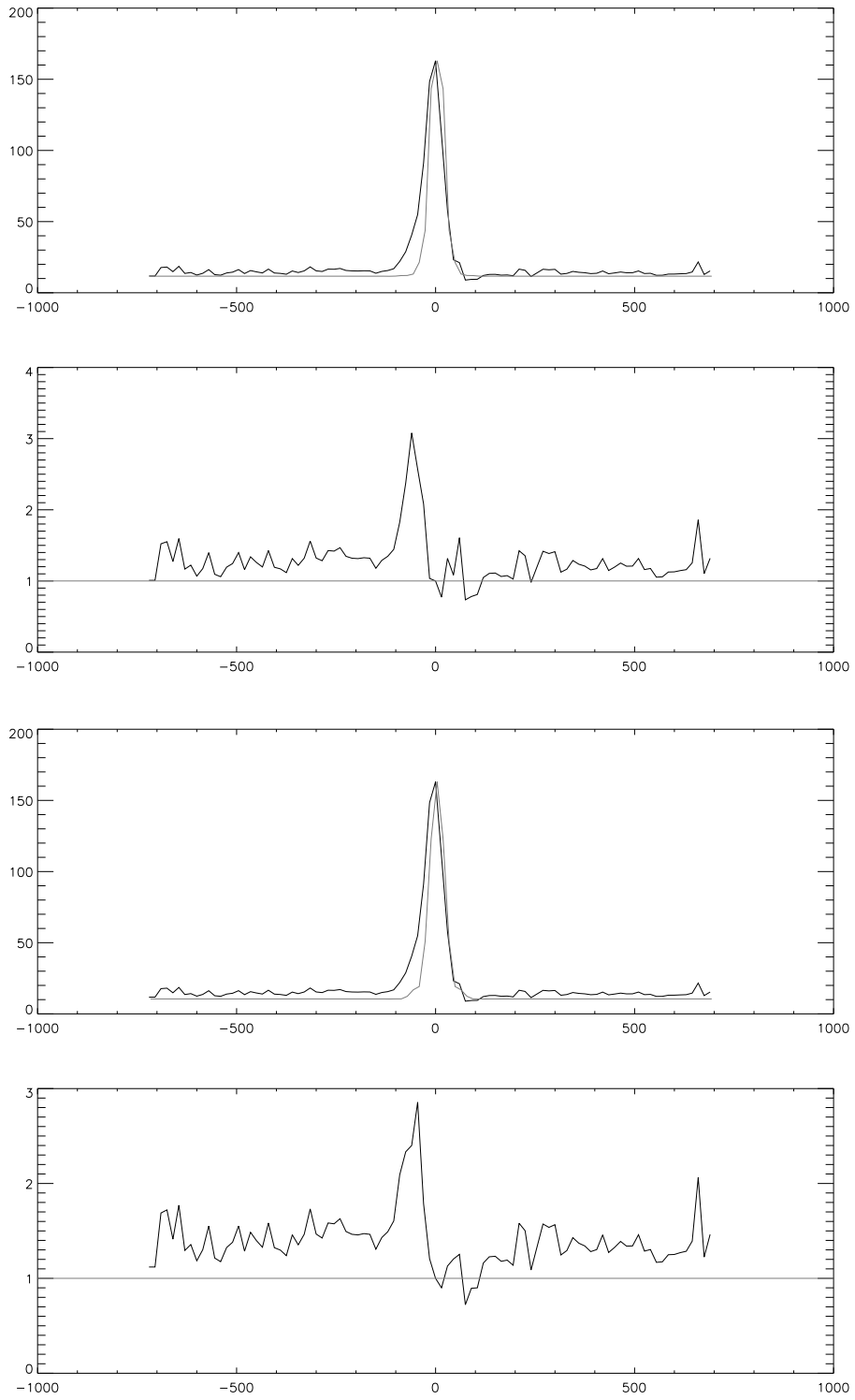


Figure 8.15: *Top Panel*: 90 $\mu$m (top) Radial profiles of a semi–regular pulsating carbon rich star U Ant, and (bottom) profile of the subtracted psf from the radial profile. *Bottom Panel*: 160 $\mu$m Radial profile (top) of a semi–regular pulsating carbon rich U Ant, (bottom) profile of the subtracted psf from the radial profile.

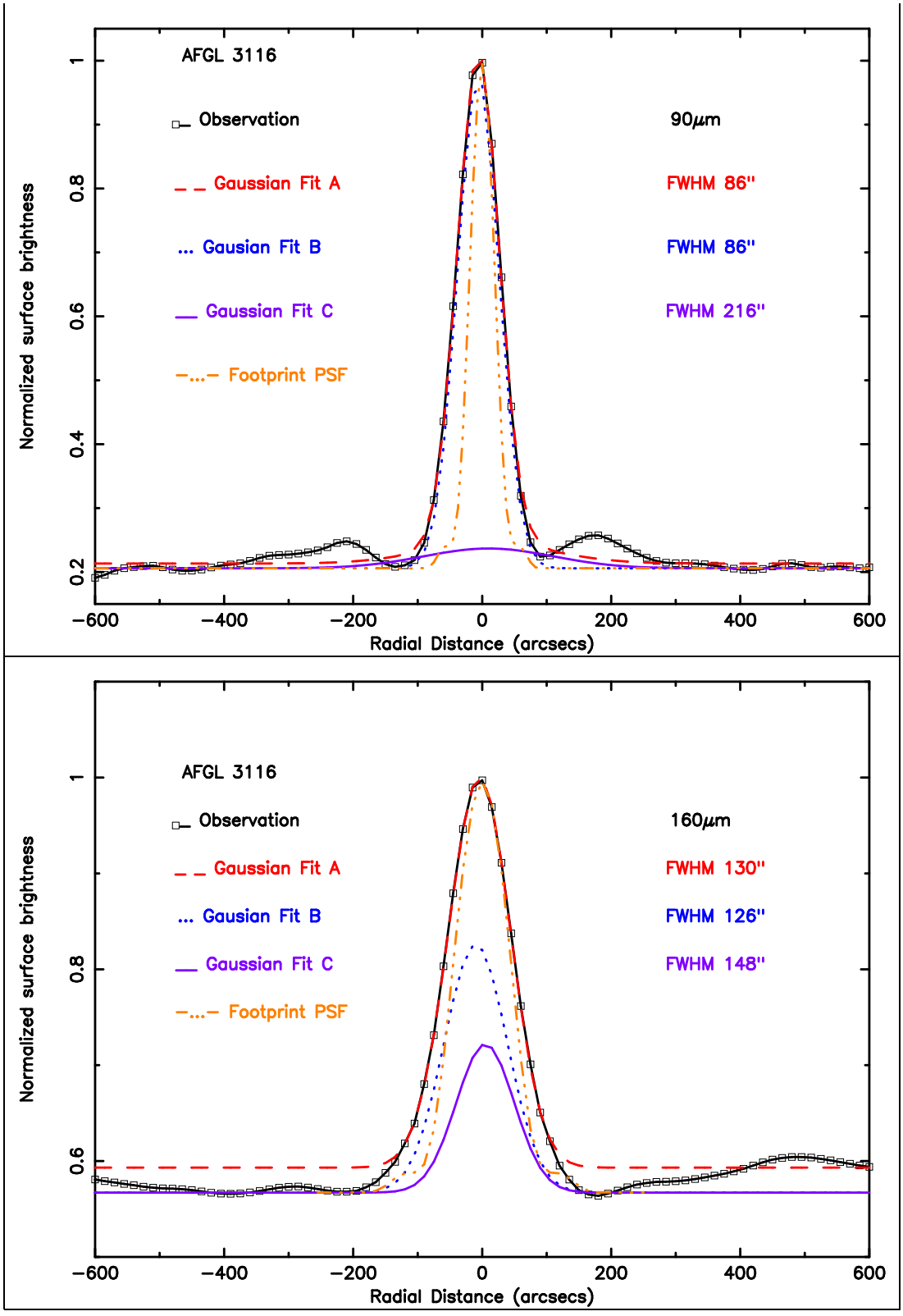


Figure 8.16: 90 $\mu$m (top) and 160 $\mu$m (bottom) fitted Gaussian profiles to the observation of LP And profiles

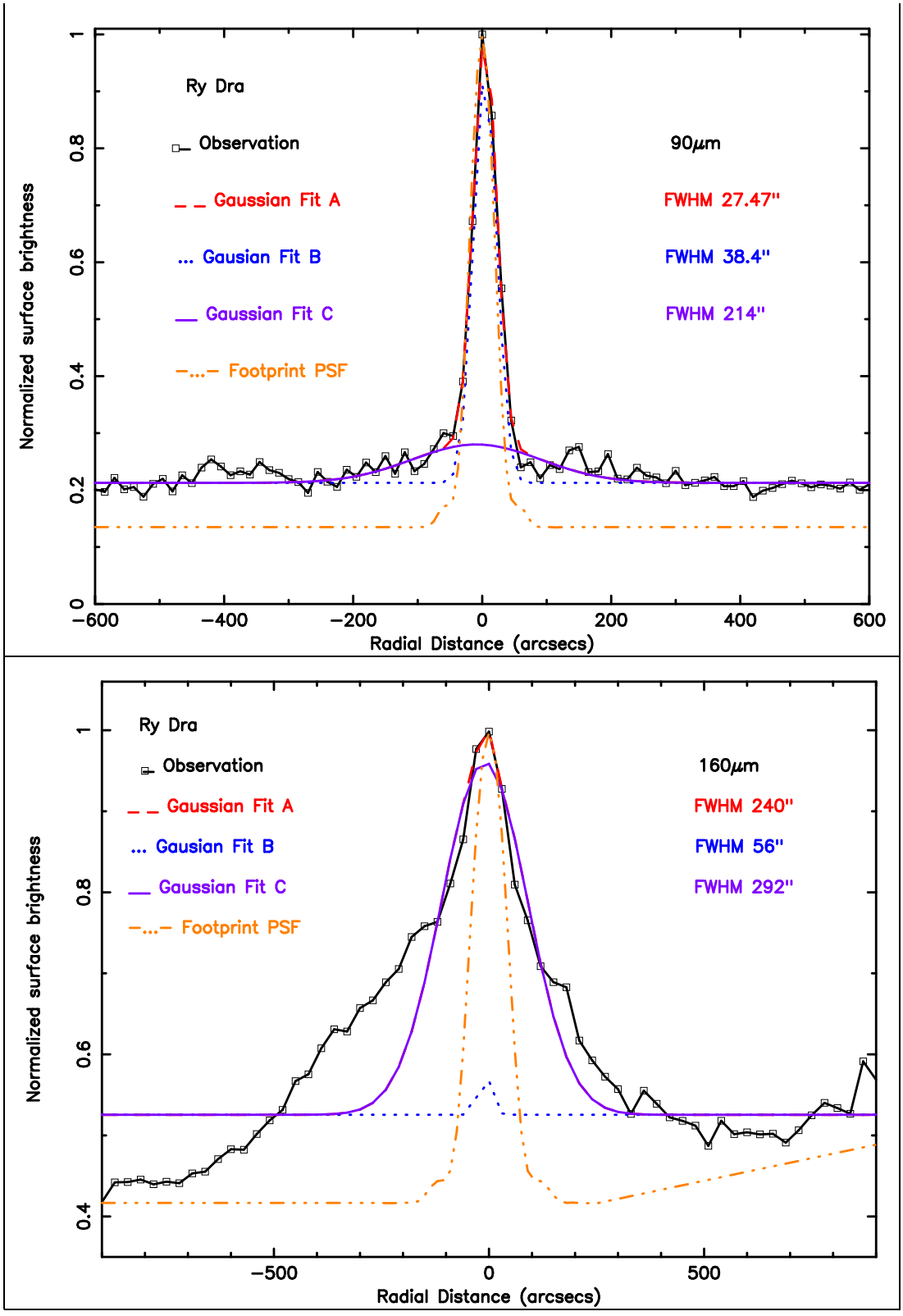


Figure 8.17: 90 $\mu$m (top) and 160 $\mu$m (bottom) fitted Gaussian profiles to the observation of Ry Dra And profiles

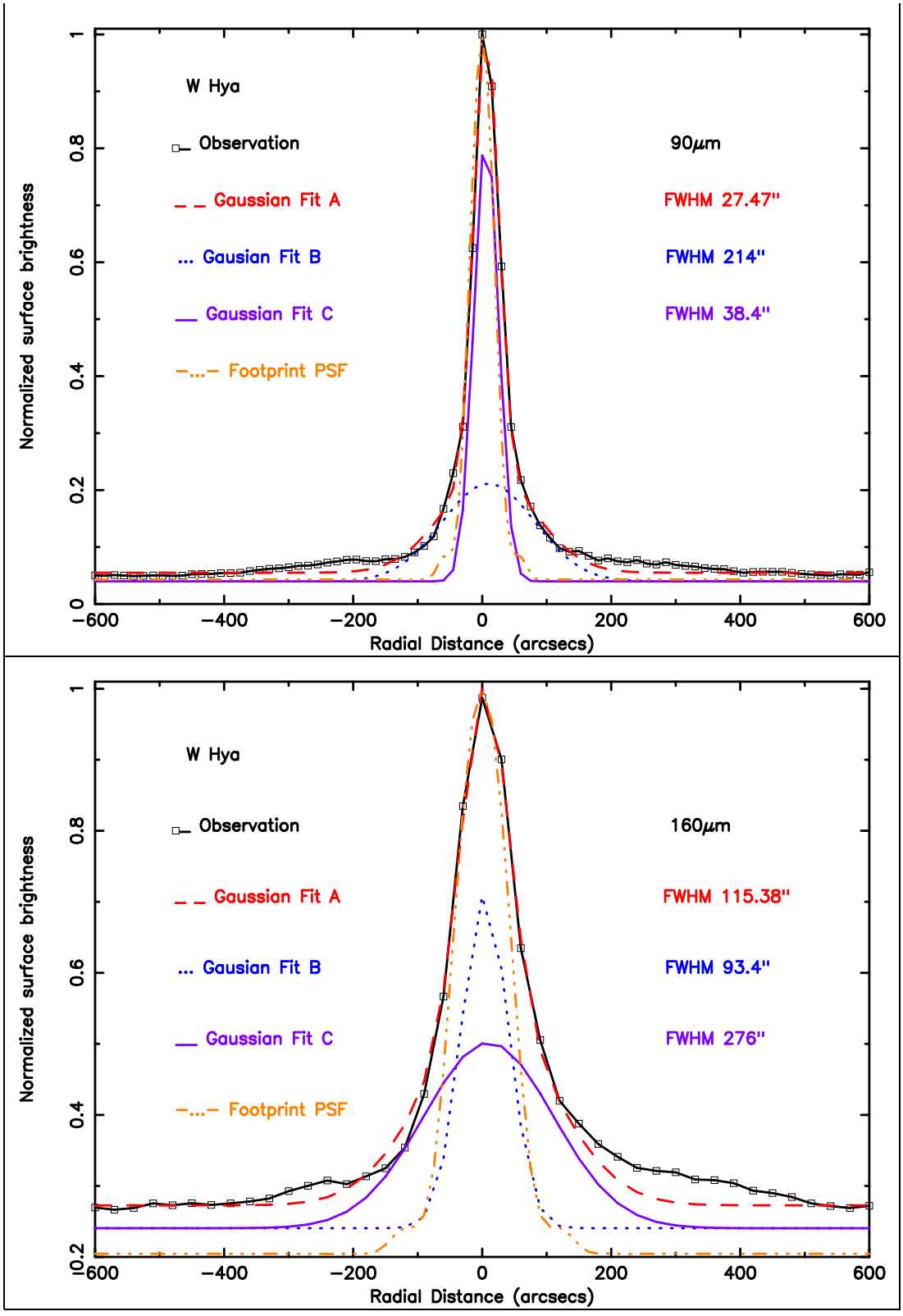


Figure 8.18: 90 $\mu$m (top) and 160 $\mu$m (bottom) fitted Gaussian profiles to the observation of Ry Dra And profiles

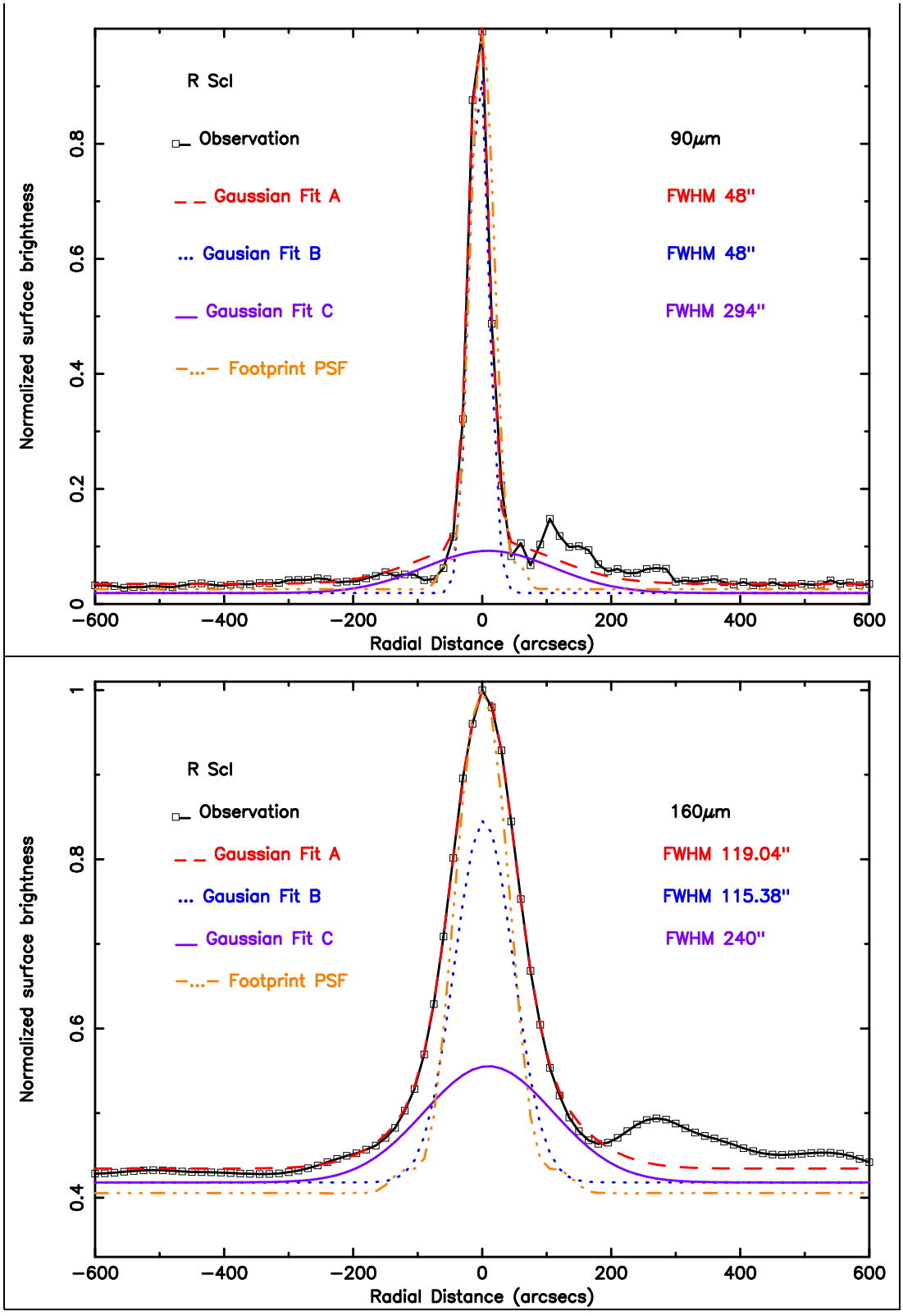


Figure 8.19: 90 $\mu$m (top) and 160 $\mu$m (bottom) fitted Gaussian profiles to the observation of R Scl profiles

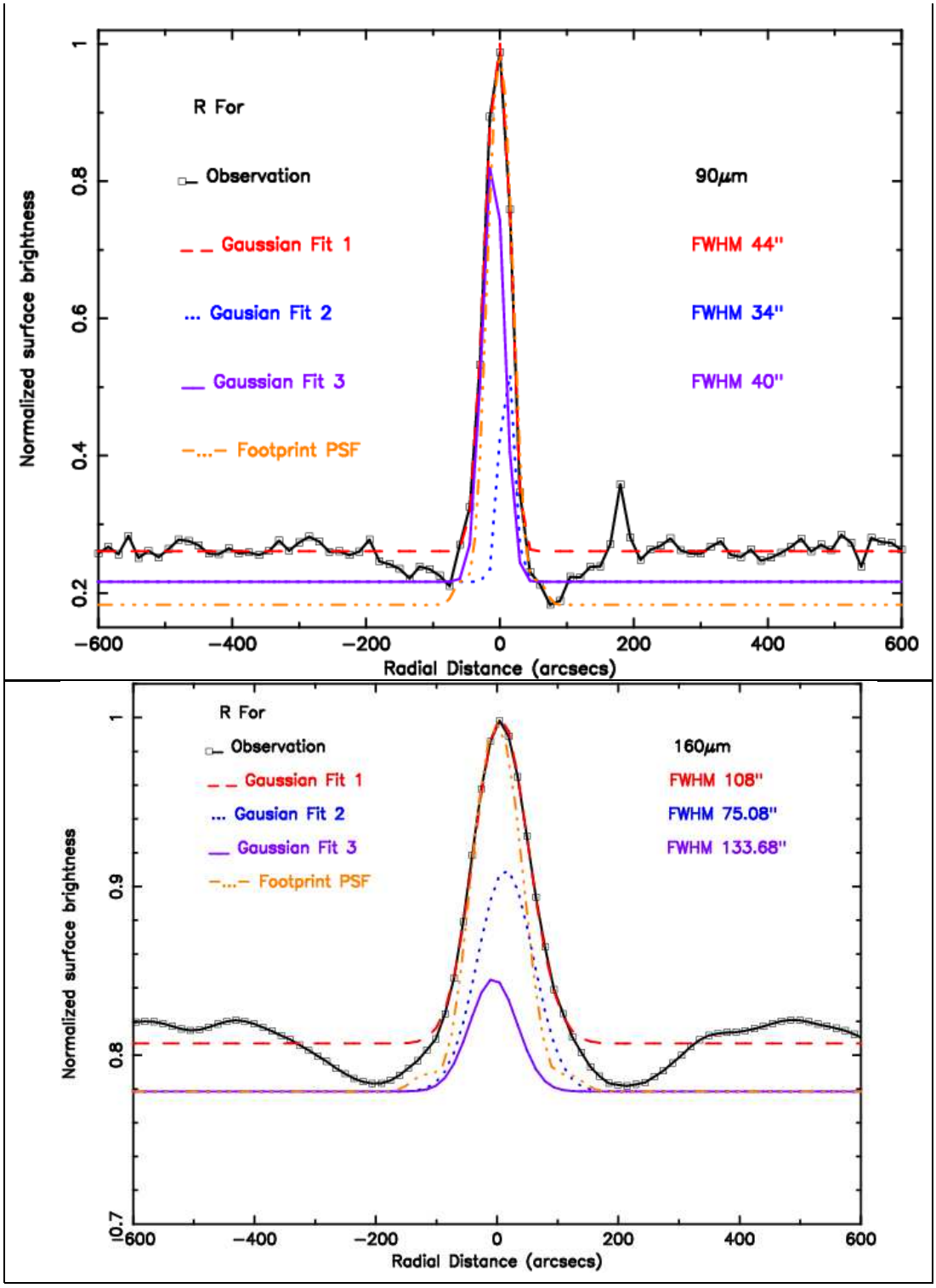


Figure 8.20: 90 $\mu$m (top) and 160 $\mu$m (bottom) fitted Gaussian profiles to the observation of R For profiles

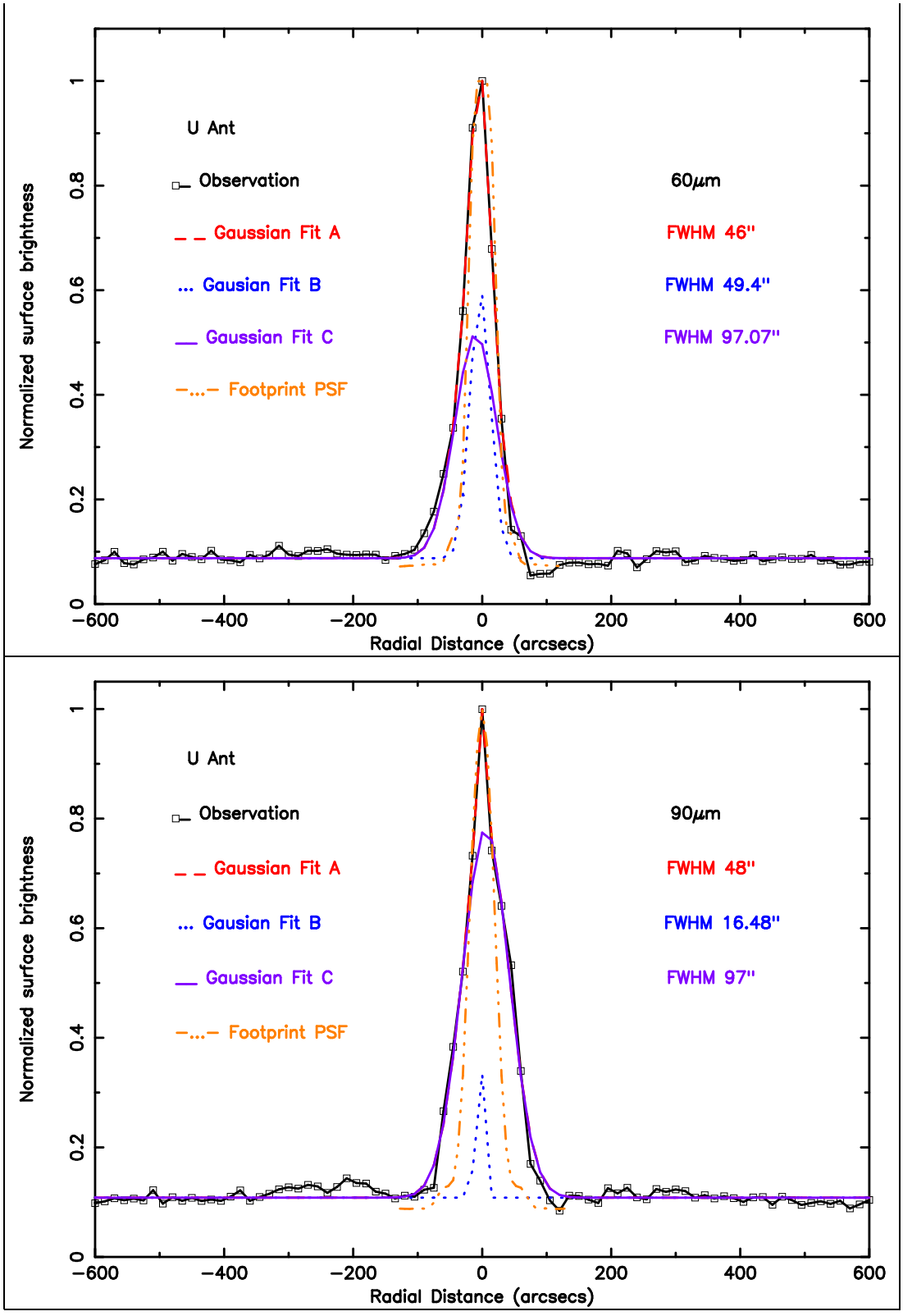


Figure 8.21: 90 $\mu$m (top) and 160 $\mu$m (bottom) fitted Gaussian profiles to the observation of U Ant profiles

Table 8.5: Full width half maximum values derived from the fitted Gaussian profiles to the observed radial profiles of carbon rich stars

| Source | FWHM ($''$) | | | Radius ($''$) | | |
|---|---|---|---|---|---|---|
| Name | 60 $\mu$m | 90 $\mu$m | 160 $\mu$m | 60 $\mu$m | 90 $\mu$m | 160 $\mu$m |
| LP And | — | 216 | 148 | — | 324 | 222 |
| Ry Dra | — | 214 | 292 | — | 321 | 438 |
| W Hya | — | 214 | 276 | — | 321 | 414 |
| R Scl | — | 294 | 240 | — | 441 | 360 |
| R For | — | 40 | 134 | — | 80 | 201 |
| U Ant | 97 | 97 | — | 145 | 145 | — |

## 8.5 Flux measured in the extended emission

The flux densities derived from the images was extracted using Mopex(Makovoz et al. 2004 [87]) software by dividing the images into three regions. The first region is the inner zone near the core at a minimum radius of $50''$, the second region is at a radius $R_1$ where the surface brightness falls near the surface background (i.e. the dip in flux observed using radial profiles), and the third zone is the halo region from $R_1$ up to a maximum radius ($R_{max}$) where the flux assume a constant surface background.

In Table 8.6, the extracted flux densities are shown.

Table 8.6: Measured fluxes from the images used to calculate dust masses

| Source | $F_{50}$ | | | $F_2$ | | | $F_{max}$ | | |
|---|---|---|---|---|---|---|---|---|---|
| Name | 60 $\mu$m | 90 $\mu$m | 160 $\mu$m | 60 $\mu$m | 90 $\mu$m | 160 $\mu$m | 60 $\mu$m | 90 $\mu$m | 160 $\mu$m |
| LP And | — | 8.95 | 5.58 | — | 29.37 | 28.9 | — | 184.36 | 262.2 |
| Ry Dra | — | 2.07 | 0.94 | — | 3.07 | 1.62 | — | 81.92 | 47.88 |
| W Hya | — | 18.4 | 6.42 | — | 21.21 | 8.79 | — | 406.9 | 321 |
| R Scl | — | 4.78 | 3.09 | — | 10.9 | 9.77 | — | 496.95 | 463.35 |
| R For | — | 28.52 | 20.09 | — | 24.11 | 14.04 | — | 270.58 | 155.06 |
| U Ant | 9.61 | 10.42 | — | 28.7 | 23.4 | — | 286 | 203.5 | — |

$F_5 0$ is flux extracted at $r < 50''$ : $F_1$ is flux extracted at $50'' \leq r \leq R_1$.
$F_3$ is flux extracted at $R_1 \leq r \leq R_{max}$

The regions selected for $F_2$ and $F_{max}$ are shown in Table 8.7.

Table 8.7: Regions selected for dust mass calculation

| Source | $R_2$ ($''$) | $R_{max}$ ($''$) |
|---|---|---|
| LP And | 80 | 500 |
| Ry Dra | 100 | 885 |
| W Hya | 100 | 566 |
| R Scl | 150 | 907 |
| R For | 208 | 750 |
| U Ant | 120 | 483 |

## 8.6 Mass of circumstellar dust shell and the mass of the core

The mass of dust in the circumstellar dust shell is estimated by using equation 5.27 in Chapter 5 section § 5.4. For the core we assume a dust temperature of 300 K. The temperature in the inner zone ($r \sim 50''$) varies from approximately 300 K at the inner dust radius, to the plateau level near 30 K at $50''$ radius. Although the average dust temperature is 130 K, the majority of the emission comes from the inner radius where the dust is more densely packed and the higher temperature leads to high emission levels. Therefore 300 K is a more appropriate temperature for the mass estimate. However our observed flux rations indicated that the flux levels at about $100''$ from the star, thus, we estimated the mass of dust using a temperature of 300 K using flux densities computed within the values of the flux within $R_2$.

The mass absorption coefficients were extrapolated from $\kappa_{120\mu m} = 400 cm^2/g$ by using $\lambda^{-1.3}$ emissivity law. This scaling factor was chosen because it has been used to model a well studied carbon rich star IRC+10 216 e.g. Le Bertre et al 1987 [82].This star is already known to have circumtellar dust shells. . The value of $400 cm^2/g$ was chosen because carbon rich stars are expected to have higher opacities than oxygen rich stars e.g Woitke 2006 [145] and also because it has been successfully applied to the other carbon rich stars e.g. by Jura et al. 2000 [66] on the CRL 2688 (Egg Nebula) and by Speck, Meixner & Knapp 2000 [125].

The results of the estimated dust masses are presented in Table 8.8.

Table 8.8: Calculated masses of dust around carbon rich stars

| Source | Mass Dust $\times 10^{-4}(M_\odot)$ | | | | | | |
|---|---|---|---|---|---|---|---|
| | $M_1$ | $M_2$ | $M_1$ | $M_2$ | $M_1$ | $M_2$ | |
| LP And | – | 3.04 | 1.88 | 1.44 | 1.3 | | |
| Ry Dra | – | – | 0.29 | 8.55 | 0.07 | 2.34 | |
| W Hya | – | – | 0.15 | 1.44 | 0.001 | 0.55 | |
| R Scl | – | – | 1.88 | 8.64 | 0.83 | 3.83 | |
| R For | – | – | 0.43 | 4.3 | 0.14 | 1.17 | |
| U Ant | 1.93 | 1.95 | 19.5 | – | 0.087 | 3.7 | – |

Mass absorption coefficient($cm^2/g$): $\kappa_{60\,\mu} = 162.45 : \kappa_{90\,\mu}\text{m} = 275.28\ \kappa_{160\,\mu}\text{m} = 581.41$
$M_1$ is mass of the dust estimated by assuming a dust temperature of 300 K at r < 100 K
$M_2$ is mass of the dust estimated in the halo region.

The mass of the gas is found by assuming a gas-to-dust ratio of 400, see § 5.5.1 in Chapter 5 for details. We calculated the mass of the core by using Pazysnksi's relation equation 3.1 in Chapter 2. The resulting mass of the core and that of the remnant star are presented in Table 7.6.

## 8.7 Time scales derived

Using our observations together with expansion velocities and distances from the literature (see Table 8.2 we can deduce the time scales associated with mass loss

Table 8.9: Dust, Gas and Central Star Masses

| Source | $M_{gas}$ | | | $M_{core}$ | $M_{progenitor}$ |
|---|---|---|---|---|---|
| | 60$\mu$m | 90 $\mu$m | 160 $\mu$m | | |
| LP And | — | 0.197 | 0.109 | 0.66 | 0.813 |
| Ry Dra | — | 0.35 | 0.090 | 0.54 | 0.760 |
| W Hya | — | 0.0636 | 0.030 | 0.55 | 0.597 |
| R Scl | — | 0.35 | 0.44 | 0.56 | 0.950 |
| R For | — | 0.034 | 0.074 | 0.56 | 0.614 |
| U Ant | 0.155 | 0.152 | — | 0.54 | 0.691 |

$M_{gas}$ is calculated using a gas-to-dust ratio of 400

Table 8.10: Calculated times scales for carbon rich stars

| Source | $R_{max}$ (p) | $t_{AGB}$ $\times 10^4$yr | $R_1$ (pc) | $t_1$ $\times 10^3$yr | $R_2$ (pc) | $t_2$ $\times 10^3$yr | $R_3$ (pc) | $t_3$ $\times 10^3$ | $t_{int}$ $\times 10^5$yr | $t_{Swd}$ $\times 10^3$yr |
|---|---|---|---|---|---|---|---|---|---|---|
| LP And | 1.58 | 7.6 | 0.63 | 30.4 | | | | | | 5.32 |
| Ry Dra | 1.75 | 17.24 | 0.32 | 31.01 | 0.79 | 77.53 | 1.42 | 0.36 | | 10.51 |
| W Hya | 0.53 | 6.33 | 0.06 | 7.68 | 0.12 | 13.96 | | | | 28.33 |
| R Scl | 1.59 | 6.33 | 0.18 | 7.15 | 0.27 | 10.72 | 0.45 | 6.21 | 17.42 | 2.47 |
| R For | 0.92 | 4.54 | 0.25 | 12.12 | 0.62 | 30.3 | | | | 2.93 |
| U Ant | 0.94 | 4.35 | 0.19 | 9.0 | 0.58 | 27.01 | 0.87 | 0.18 | 39.3 | 3.00 |

from these objects. If we assume that we are observing the entire dust shell, then $t_{AGB}$ represent these stars were in the mass losing AGB phase. We also observed that some of our objects has enhanced emission, this may be due to a shell separating from the star or enhanced mass loss caused by thermal pulses e.g. a prediction from models by Vassilliadis & Woods 1993 [137]. We define $t_1$ as the time at $R_1$ since outer shell separated from the star (using the first dip in surface brightness from radial profiles). $t_2$ is the time since the inner enhancement was ejected (by looking the first peak in surface brightness after $t_2$). $t_3$ is the time since outer enhancement was ejected. $t_{int}$ is assumed to be the time between $t_2$ and $t_3$. The average of all times is labeled $t_{Swd}$.

Table 8.10 shows the results of the time scales derived by assuming constant expansion velocity.

## 8.8 Discussion on the results on carbon rich stars

Our observations indicate that there is evidence of extended emission around our object. Three objects (Ry Dra, R Scl, U ant) shows surface brightness variation that maybe caused by thermal pulses or the detachment of circumstellar dust shell from a star. The sizes of these dust shells are within 0.1 – 0.7 pc from the star. Assuming constant outflow velocities we estimated the ages of the dust shell to be between 4 –$17 \times 10^4$ years. The estimated $t_{Swind}$ time scale is between 3 – 30 $\times 10^3$ years, when

# VW Model Predictions

| $M_i$ [$M_\odot$] | $M_f$ [$M_\odot$] | $M_{bol}$ | $t_{MS}$ [Gyr] | $t_{EAGB}$ [Myr] | $\frac{t_{EAGB}}{t_{MS}}$ [%] | $t_{TPAGB}$ [Myr] | $\frac{t_{TPAGB}}{t_{MS}}$ [%] |
|---|---|---|---|---|---|---|---|
| | | | | Z=0.016 | | | |
| 1.0 | 0.57 | −4.0 | 11.3 | 12 | 0.16 | 0.50 | 0.004 |
| 1.5 | 0.60 | −4.5 | 2.7 | 9.2 | 0.34 | 0.83 | 0.03 |
| 2.0 | 0.63 | −4.9 | 1.2 | 7.9 | 0.66 | 1.20 | 0.10 |
| 2.5 | 0.67 | −5.1 | 0.62 | 1.1 | 0.18 | 2.20 | 0.35 |
| 3.5 | 0.75 | −5.7 | 0.23 | 2.8 | 1.2 | 0.43 | 0.19 |
| 5.0 | 0.89 | −6.2 | 0.10 | 1.2 | 1.2 | 0.26 | 0.27 |
| | | | | Z=0.004 | | | |
| 1.0 | 0.59 | −4.5 | 6.7 | 8.0 | 0.12 | 0.87 | 0.01 |
| 1.5 | 0.64 | −4.9 | 2.1 | 6.3 | 0.30 | 0.97 | 0.05 |
| 2.0 | 0.67 | −5.2 | 0.89 | 6.7 | 0.75 | 1.60 | 0.18 |
| 2.5 | 0.69 | −5.5 | 0.46 | 5.2 | 1.1 | 1.30 | 0.27 |
| 3.5 | 0.85 | −6.0 | 0.18 | 2.2 | 1.2 | 0.25 | 0.14 |
| 5.0 | 0.94 | −6.5 | 0.08 | 0.6 | 7.3 | 0.31 | 0.39 |

Figure 8.22: Model predictions of initial and final masses from Vassilliadis & Woods 1993 [137]

we compare this time range with $t_{Swnd}$ by models of VW93, there is a reasonable agreement that these stars evolved from the progenitor stars with masses of 2 – 3.5 $M_\odot$. Also taking the mass loss from the literature e.g. Loup et al. 1993 [85], and assuming that $t_{AGB}$ represent the represents the duration of the mass loss rate, we find that total mass loss by these stars are: $0.06M_\odot$ (LP And) , $0.1M_\odot$ (Ry Dra) , $0.6M_\odot$ (W Hya), $0.2M_\odot$ (R Scl) , $0.1M_\odot$ (R For) and $0.27M_\odot$ for U Ant. This suggest that the final masses are within 0.6 - $1.12M_\odot$. When we compare these masses with the final masses from VW93 as shown in Figure 8.22, if we assume a metalicity of Z = 0.006 the results shows that these stars may have evolved from stars with initial masses within a range of 1.5 – $3.5M_\odot$

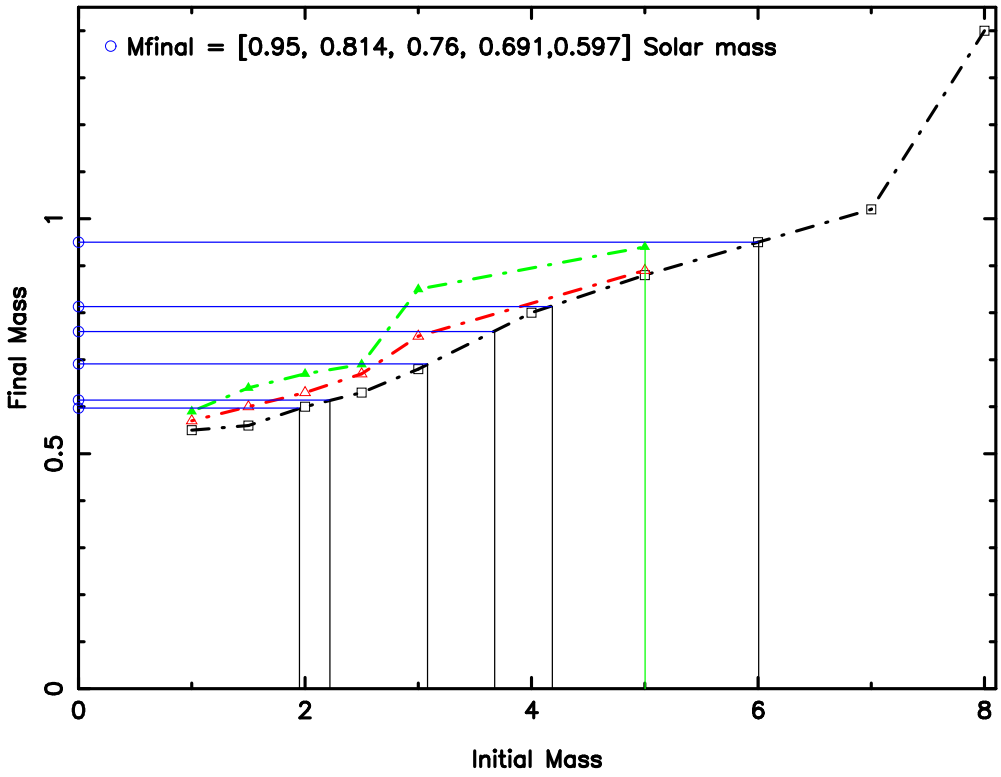


Figure 8.23: Initial mass (solar units) - x axis vs Final mass(solar units) y - axis. The dash - circle - dotted lines indicate a curve from Weideman & Koester 2000 [140] data. Triangles are the data points from Vassiliadis and Wood 1983 [137], solid triangle = Z (metallicity) = 0.004, open triangle Z = 0.016

### 8.8.1 Carbon rich result′s comparison with Initial - final mass relations

The ramnant masses of carbon rich stars above are compared with the observations of initial - final mass relations by Weidemann & Koester 2000[140]. Also compared with the data are the model prediction of initial mass relations by VW93 with metalicity Z = 0.016 (solar neighborhood) and Z = 0.004. The results are shown in figure 8.23. Our results indicate that the initial main sequence mass for oxygen rich stars range from 2 - 6 $M_{\odot}$ for stars with ramnant masses 0.6 – 0.95 $M_{\odot}$ by using Wiedeman & Koester, 2000 [140]. The models by VW98 shows an inital mass range of (1 - 3.7)$M_{\odot}$ for oxygen rich stars with ramant stars in the same region (0.6 - 0.95) $M_{\odot}$).

# Chapter 9

# Summary and concluding remarks

Intermediate mass stars ($0.8 - 8M_{\odot}$) at the asymptotic giant branch phase (AGB) suffer intensive mass loss, which leads to the formation of a circumstellar shell (s) of gas and dust in their circumstellar envelope. At the end of the AGB phase, the mass-loss decreases or stops and the circumstellar envelope begins to drift away from the star. In this study we assumed that the velocity of the AGB phase wind is constant. Based on this assumption then dust or molecular emission furthest from the star represents the oldest mass loss, while material closer to the star represents more recent mass loss. The history of mass loss during the AGB phase is imprinted on the dust shells of the post-AGB envelope. Thus, in studying the distribution of material in the form of dust emission in the circumstellar shells of late evolved stars (i.e. the post AGB phases are pre - planetary nebula (PPN) and the planetary nebula (PN)) we are able to gain a better understanding of the mass-loss processes involved in the evolution of intermediate mass stars. In this thesis a study of evolution of intermediate mass stars stdied by means of observations, using far - infrared (FIR) images based on the observations performed by ISO We observed the physical properties inside the star e.g. the effect of thermal pulses on the material distribution of dust shells of AGB

and post AGB circumstellar envelope. There are issues in using thermal emission in studying structures attributed around these objects. Far infrared emission is very faint such that we are limited by noise and galactic cirrus emission that causes the background emission to be higher close to the source brightness. This issue limits the size circumstellar dust shell and hence the uncertainties becomes higher. As a result the times scales that we derived were shorter the time scale used to model the evolution of these stars.

We also derived the mass of the circumstellar dust present in the dust shells, this gave us clues about how much material intermediate mass stars loses. This mass of dust was very useful in determining setting the lower limit to the progenitor mass of these stars. However, there are high uncertainties in deriving the progenitor masses, the temperature of the dust in the shells are not known and also the emissivity used is not known. These parameters depends on the assumed sizes, the density and nature of the grains used based on the laboratory data. However, the properties of the grains in the interstellar medium maby very different than those used in our calculation. another uncertainty comes from the mass absorption coefficient used. This parameter so essential in the mass of the dust calculated is scaled using different emissivity values, as a result the values fond in the literature differs.

The mass of the progenitor star depends on the the assumed gas to dust ratios, since there is definitely more gas than dust. The values of gas to dust ranges by high three orders of magnitude, and the methods used to obtain these values ranges from the observed gas to dust mass loss rates to the use of period of pulsation and the measured outflow velocities from CO emission lines.

Even though measured masses are challenged by all this uncertainties the values used were carefully selected based on intensive research about the choice and usage of these parameters. The results of the progenitor masses have excellent agreement at both filters used to measure thermal emission.

The dust masses derived from PHT 32 observation of oxygen rich stars are between $1.7 - 4 \times 10^{-4}$ $M_{\odot}$. The mass of the core was estimated using Paczynski relation based on the observed luminosities of the star. The core masses estimates are 0.56 – 0.76 $M_{\odot}$. We assumed a gas to dust ration of 200 to obtain the lower limit of progenitor masses between 0.58 - 0.8$M_{\odot}$ fro oxygen rich stars. These values are consistent with evolutionary models (e.g. Vassiliadis & Woods 1993 [137] for the final masses for the star's with initial masses between 0.9 - 5$M_{\odot}$. The times scales that probe the history of the mass loss since the oldest part of the dust shell was ejected ($t_{AGB}$) is found to lie between

The dust masses around carbon rich star in our sample are between 0.1 - 1.44 $\times 10^{-4}$ $M_{\odot}$. The lower limit to the progenitor masses are between 0.61 – 0.9 $M_{\odot}$ suggesting that these stars evolved from the main sequence masses between 1.5 – 3.5 $M_{\odot}$.

The radial profiles from our observations showed that the carbon rich stars are subject to surface brightness variations. It was not clear enough whether these variations are caused by thermal pulses or the possibility of detached circumstellar dust shells. The oxygen rich stars did not show any brightness variation with distance. PHT 32 observations

The data and results presented in this thesis is based on the European Space Agency's (ESA) Infrared Space Observatory (ISO) an astronomical satellite that was operational between November 1995 and May 1998. The ISOPHOT PHT C 32 observations suffered lots detector transients (e.g. see Chapter 6) such that more time was spent reducing the observations presented in this thesis. Some of the data artifact could not be completely removed, hence additional observations with better resolution than ISO are required for comparison to improve the results presented in this thesis. Since ISO stopped its operational cause, there have been several far - infrared missions launched to observe the existence of dust shells around 'most'

of our objects in our data sample e.g. Spitzer telescope (Werner et al. 2007 [36]), AKARI (Murakami et al. 2007 [98]). The observations from these telescopes indicate when compared with our results does confirm the large extended dust shells that are reported in this thesis. For example Omi Cet, R Hya observations by Spitzer telescope indicated the presence of large dust shells and bow shock nebulae around these objects e.g see Ueta et al. 2008 [130] on Spitzer observation of Omi Cet; Ueta, Speck, Stencel & Meixner 2006 [133] for observations of Mira; Spitzer study of OH 231.8+4.2[24]. Other results e.g. Bunzel et al. 2009 [17] shows that dust shells can exhibit differential chemistry, this offers a new challenging insight towards the evolution of chemistry of the dust shells around AGB and Post AGB stars. Recently new observations by infra - red to submillimiter Herschel Space Observatory [109] with higher resolution is promising to give more valuable data. This will add more knowledge about the existence of dust shells around intermediate mass stars, which will improve our understanding on the mass loss histories and the recycling of material in galactic environments.

# Bibliography


[1] Book Review: Laboratory and astronomical high resolution spectra / Ast. Soc. Pacific, 1995. *The Observatory*, 116:404, December 1996.

[2] C. Abia and J. Isern. Lithium Abundances in AGB Stars: a Probe to Test Convective Theories and Nucleosynthesis. In A. Gimenez, E. F. Guinan, & B. Montesinos, editor, *Stellar Structure: Theory and Test of Connective Energy Transport*, volume 173 of *Astronomical Society of the Pacific Conference Series*, page 285, 1999.

[3] C. Alcock, R. A. Allsman, T. S. Axelrod, D. P. Bennett, K. H. Cook, K. C. Freeman, K. Griest, S. L. Marshall, B. A. Peterson, M. R. Pratt, P. J. Quinn, J. Reimann, A. W. Rodgers, C. W. Stubbs, W. Sutherland, and D. L. Welch. The MACHO project LMC variable star inventory. 1: Beat Cepheids-conclusive evidence for the excitation of the second overtone in classical Cepheids. *Astronomy Journal*, 109:1653, April 1995.

[4] Z. Aslan. On the absolute magnitudes of semi-regular variables in stellar groups. *The Observatory*, 96:149–153, August 1976.

[5] B. Balick. The evolution of planetary nebulae. I - Structures, ionizations, and morphological sequences. *Astronomy Journal*, 94:671–678, September 1987.

[6] M. J. Barlow and M. Cohen. Mass Loss Rates for Wolf-Rayet Stars and OBA Super-giants. In *Bulletin of the American Astronomical Society*, volume 8 of *Bulletin of the American Astronomical Society*, page 302, March 1976.

[7] Bay M. Halpern M. Hinshaw G. Jackson C. Jarosik N. Kogut A. Limon M. Meyer S. S. Page L. Spergel D. N. Tucker G. S. Wilkinson D. T. Wollack E. Wright E. L. Bennett, C. L. The microwave anisotropy probe mission. *The Astrophysical Journal*, 583:1–26, 2003.

[8] M. S. Bessell and P. R. Wood. Deduction of Planetary Properties from Long-Period Variable Precursors. In D. R. Flower, editor, *Planetary Nebulae*, volume 103 of *IAU Symposium*, page 291, 1983.

[9] L. Bierman. *The Solar Wind and the Interplanetary Media*, page 150. 1961.

[10] T. Bloecker. Stellar evolution of low and intermediate-mass stars. I. Mass loss on the AGB and its consequences for stellar evolution. *Astronomy and Astrophysics*, 297:727, May 1995.

[11] T. Bloecker and D. Schoenberner. A 7-solar-mass AGB model sequence not complying with the core mass-luminosity relation. *Astronomy and Astrophysics*.

[12] T. Bloecker and D. Schoenberner. On the fading of massive AGB remnants. *Astronomy and Astrophysics*, 240:L11–L14, December 1990.

[13] A. I. Boothroyd, I.-J. Sackmann, and S. C. Ahern. Prevention of High-Luminosity Carbon Stars by Hot Bottom Burning. *Astrophysical Journal Letters*, 416:762, October 1993.

[14] A. I. Boothroyd, I.-J. Sackmann, and G. J. Wasserburg. Predictions of oxygen isotope ratios in stars and of oxygen-rich interstellar grains in meteorites. *Astrophysical Journal Letters*, 430:L77–L80, July 1994.

[15] G. H. Bowen. Dynamical modeling of long-period variable star atmospheres. *Astrophysical Journal Letters*, 329:299–317, June 1988.

[16] G. L. Bryan, K. Volk, and S. Kwok. On the formation of carbon stars. *Astrophysical Journal Letters*, 365:301–311, December 1990.

[17] F. Bunzel, D. A. García-Hernández, D. Engels, J. V. Perea-Calderón, and P. García-Lario. AKARI/IRC Observations of Heavily Obscured Oxygen-Rich AGB and Post-AGB Stars. In T. Onaka, G. J. White, T. Nakagawa, & I. Yamamura, editor, *AKARI, a Light to Illuminate the Misty Universe*, volume 418 of *Astronomical Society of the Pacific Conference Series*, page 431, December 2009.

[18] E. M. Burbidge, G. R. Burbidge, W. A. Fowler, and F. Hoyle. Synthesis of the Elements in Stars. *Reviews of Modern Physics*, 29:547–650, 1957.

[19] A. G. W. Cameron and W. A. Fowler. Lithium and the s-PROCESS in Red-Giant Stars. *Astrophysical Journal Letters*, 164:111, February 1971.

[20] C. Chiosi, A. Renzini, and J. Dyson. Book-Review - Spectral Evolution of Galaxies. *Astrophysics and Space Science*, 125:421, August 1986.

[21] Y.-H. Chu, A. Manchado, G. H. Jacoby, and K. B. Kwitter. The multiple-shell structure of the planetary nebula NGC 6751. *Astrophysical Journal Letters*, 376:150–160, July 1991.

[22] D. S. P. Dearborn, D. N. Schramm, and L. M. Hobbs. Mass loss and a possible Population II lithium dip. *Astrophysical Journal Letters*, 394:L61–L64, August 1992.

[23] C. Dijkstra and A. K. Speck. Shaping Bipolar Planetary Nebulae: How Mass Loss Leads to Waistline Development. *Astronomy and Astrophysics*, 651:288–293, November 2006.

[24] T. Do, M. Morris, R. Sahai, and K. Stapelfeldt. A Spitzer Study of the Mass-Loss Histories of Three Bipolar Preplanetary Nebulae. *Astronomy Journal*, 134:1419–1431, October 2007.

[25] B. T. Draine and H. M. Lee. Optical properties of interstellar graphite and silicate grains. *Astronomical Physical Journal*, 285:89–108, October 1984.

[26] M. F. El Eid. Sodium Enrichment and the Evolution of A-F Type Supergiants. In M. Busso, C. M. Raiteri, & R. Gallino, editor, *Nuclei in the Cosmos III*, volume 327 of *American Institute of Physics Conference Series*, page 393, 1995.

[27] M. W. Feast and P. A. Whitelock. Red giant variables and the population of the Galactic bulge. In B. J. Jarvis & D. M. Terndrup, editor, *European Southern Observatory Conference and Workshop Proceedings*, volume 35 of *European Southern Observatory Conference and Workshop Proceedings*, pages 3–10, 1990.

[28] P. J. Flower. Transformations from Theoretical Hertzsprung-Russell Diagrams to Color-Magnitude Diagrams: Effective Temperatures, B-V Colors, and Bolometric Corrections. *Astrophysical Journal Letters*, 469:355, September 1996.

[29] D. Fong, M. Meixner, and R. Y. Shah. Discovery of Multiple Molecular Shells in the Outer Envelope of IRC +10216. *Astrophysical Journal Letters*, 582:L39–L42, January 2003.

[30] M. W. Fox, P. R. Wood, and M. A. Dopita. Shock waves in Mira variables. I - Emission-line spectra. *Astrophysical Journal Letters*, 286:337–349, November 1984.

[31] A. Frank and E. G. Blackman. Application of Magnetohydrodynamic Disk Wind Solutions to Planetary and Protoplanetary Nebulae. *Astronomy and Astrophysics*, 614:737–744, October 2004.

[32] J. A. Frogel, J. Mould, and V. M. Blanco. The asymptotic giant branch of Magellanic Cloud clusters. *Astrophysical Journal Letters*, 352:96–122, March 1990.

[33] C. Gabriel, J. Acosta-Pulido, I. Heinrichsen, H. Morris, and W.-M. Tai. The ISOPHOT Interactive Analysis PIA, a Calibration and Scientific Analysis Tool. In G. Hunt & H. Payne, editor, *Astronomical Data Analysis Software and Systems VI*, volume 125 of *Astronomical Society of the Pacific Conference Series*, page 108, 1997.

[34] C. Gabriel and M. Hur. Map Coadding and Simulation Techniques with the Isophot Interactive Analysis (PIA). In R. J. Laureijs, K. Leech, & M. F. Kessler, editor, *ISO Beyond Point Sources: Studies of Extended Infrared Emission*, volume 455 of *ESA Special Publication*, page 11, 2000.

[35] C. Gabriel and M. Hur. The ISOPHOT Mapping Simulation System. In *Photometric Mapping with ISOPHOT using the P32 Astronomical Observation Template*, volume 482 of *ESA Special Publication*, page 51, December 2002.

[36] R. D. Gehrz, T. L. Roellig, M. W. Werner, G. G. Fazio, J. R. Houck, F. J. Low, G. H. Rieke, B. T. Soifer, D. A. Levine, and E. A. Romana. The NASA Spitzer Space Telescope. *Review of Scientific Instruments*, 78(1):011302–+, January 2007.

[37] R. D. Gehrz, T. L. Roellig, M. W. Werner, G. G. Fazio, J. R. Houck, F. J. Low, G. H. Rieke, B. T. Soifer, D. A. Levine, and E. A. Romana. The NASA Spitzer

Space Telescope. *Review of Scientific Instruments*, 78(1):011302–+, January 2007.

[38] R. D. Gehrz and N. J. Woolf. R V Tauri Stars: a New Class of Infrared Object. *Astrophysical Journal Letters*, 161:L213, September 1970.

[39] F. C. Gillett, D. E. Backman, C. Beichman, and G. Neugebauer. IRAS observations of R Coronae Borealis - Detection and study of a fossil shell. *Astrophysical Journal Letters*, 310:842–852, November 1986.

[40] R. C. Gilman. On the Coupling of Grains to the Gas in Circumstellar Envelopes. *Astronomy and Astrophysics*, 178:423–426, December 1972.

[41] O. Gingerich, R. W. Noyes, W. Kalkofen, and Y. Cuny. The Harvard-Smithsonian reference atmosphere. *Solar physics*, 18:347–365, July 1971.

[42] T. M. Gledhill, A. Chrysostomou, J. H. Hough, and J. A. Yates. Axisymmetry in protoplanetary nebulae: using imaging polarimetry to investigate envelope structure. *Monthly Notices of the Royal Astronomical Society*, 322:321–342, April 2001.

[43] L. Goldberg, E. A. Muller, and L. H. Aller. The Abundances of the Elements in the Solar Atmosphere. *Astrophysical Journal Letters*, 5:1, November 1960.

[44] D. González Delgado, H. Olofsson, F. Kerschbaum, F. L. Schöier, M. Lindqvist, and M. A. T. Groenewegen. "Thermal" SiO radio line emission towards M-type AGB stars: A probe of circumstellar dust formation and dynamics. *Astronomy and Asstrophysics*, 411:123–147, November 2003.

[45] E. Griffin. Book Review: ASYMPTOTIC GIANT BRANCH STARS / Springer, 2004. *The Observatory*, 124:393, October 2004.

[46] M. A. T. Groenewegen, H. J. G. L. M. Lamers, and A. W. A. Pauldrach. The winds of O-stars. II - The terminal velocities of stellar winds of O-type stars. *Astronomy and Astrophysics*, 221:78–88, August 1989.

[47] H. J. Habing. Circumstellar envelopes and Asymptotic Giant Branch stars. *Astronomy and Astrophysics*, 7:97–207, 1996.

[48] H. J. Habing and J. A. D. L. Blommaert. Carbon and Oxygen-Rich Progenitors of Planetary Nebulae. In R. Weinberger & A. Acker, editor, *Planetary Nebulae*, volume 155 of *IAU Symposium*, page 243, 1993.

[49] H. J. Habing, P. te Lintel Hekkert, and W. E. C. J. van der Veen. OH/IR stars and other IRAS point sources as progenitors of planetary nebulae. In S. Torres-Peimbert, editor, *Planetary Nebulae*, volume 131 of *IAU Symposium*, pages 359–380, 1989.

[50] H. J. Habing, P. te Lintel Hekkert, and W. E. C. J. van der Veen. OH/IR stars and other IRAS point sources as progenitors of planetary nebulae. In S. Torres-Peimbert, editor, *Planetary Nebulae*, volume 131 of *IAU Symposium*, pages 359–380, 1989.

[51] Olofsson H Habing, H. J. *Asymptotic Giant Branch Stars*, volume 523.

[52] M. Harwit. Submillimeter observations with the Kuiper Airborne Observatory. In B. Kaldeich, editor, *Liege International Astrophysical Colloquia*, volume 29 of *Liege International Astrophysical Colloquia*, pages 21–24, December 1990.

[53] G. W. Hawkins. IRAS observations of a large circumstellar dust shell around W Hydrae. *Astronomy and Astrophysics*, 229:L5–L8, March 1990.

[54] U. Herbstmeier, P. Abraham, D. Lemke, R. J. Laureijs, U. Klaas, K. Mattila, C. Leinert, C. Surace, and M. Kunkel. Small-scale structures in the far-infrared background. *Astronomy and Astrophysics*, 332:739–747, April 1998.

[55] J. Herman and H. J. Habing. Time variations and shell sizes of OH masers in late-type stars. *Astronomy and Astrophysics*, 59:523–555, March 1985.

[56] E. Hertzsprung and H. L. D'Arrest. Bahn des Cometen von 1859, von Herrn Hertzsprung. Mitgetheilt von Herrn Prof. d'Arrest. *Astronomische Nachrichten*, 53:149–+, May 1860.

[57] R. H. Hildebrand. The Determination of Cloud Masses and Dust Characteristics from Submillimetre Thermal Emission. *Quarterly Journal of the Royal Astronomical Society*, 24:267, September 1983.

[58] S. Hoefner. Mass Loss: The Role of Grains. In *IAU Joint Discussion*, volume 11 of *IAU Joint Discussion*, August 2006.

[59] D. Hoffleit. Stellar Spectra. (Scientific Books: An Atlas of Stellar Spectra with an Outline of Spectral Classification). *Science*, 97:536–537, June 1943.

[60] P. J. Huggins, K. Young, P. Cox, T. Forveille, and R. Bachiller. Unwinding the Helix. In *American Astronomical Society Meeting Abstracts*, volume 30 of *Bulletin of the American Astronomical Society*, page 1276, December 1998.

[61] J. D. Hughes, P. Hartigan, J. A. Graham, J. P. Emerson, and F. Marang. The Optical Counterpart of IRAS 12496-7650: A Highly Embedded Herbig Ae Star. In *Bulletin of the American Astronomical Society*, volume 22 of *Bulletin of the American Astronomical Society*, page 1255, September 1990.

[62] I. Iben, Jr. Stellar Evolution. I. The Approach to the Main Sequence. *Astrophysical Journal Letters*, 141:993, April 1965.

[63] I. Iben, Jr. Further adventures of a thermally pulsing star. *Astrophysical Journal Letters*, 208:165–176, August 1976.

[64] I. Iben, Jr., J. B. Kaler, J. W. Truran, and A. Renzini. On the evolution of those nuclei of planetary nebulae that experience a final helium shell flash. *Astrophysical Journal*, 264:605–612, January 1983.

[65] I. Iben, Jr. and G. Laughlin. A study of the white dwarf luminosity function. *Astronomy and Astrophysics Journal*, 341:312–326, June 1989.

[66] M. Jura, J. L. Turner, S. Van Dyk, and G. R. Knapp. What Is Hatching in the Egg? *Astrophysical Journal Letters*, 528:L105–L108, January 2000.

[67] M. Juvela, K. Mattila, D. Lemke, U. Klaas, C. Leinert, and C. Kiss. Determination of the cosmic far-infrared background level with the ISOPHOT instrument. *Astronomy and Astrophysics*, 500:763–768, June 2009.

[68] F. D. Kahn and K. A. West. Shapes of planetary nebulae. *Monthly Notices of the Royal Astronomical Society*, 212:837–850, February 1985.

[69] F. Kerschbaum and J. Hron. Semiregular variables of types SRa and SRb - Basic properties in the visual and the IRAS-range. *Astronomy and Astrophysics*, 263:97–112, September 1992.

[70] M. F. Kessler, J. A. Steinz, M. E. Anderegg, J. Clavel, G. Drechsel, P. Estaria, J. Faelker, J. R. Riedinger, A. Robson, B. G. Taylor, and S. Ximénez de Ferrán. The Infrared Space Observatory (ISO) mission. *Astronomy and Astrophysics*, 315:L27–L31, November 1996.

[71] C. Kiss, U. Klaas, and D. Lemke. Determination of confusion noise for far-infrared measurements. *Astronomy and Astrophysics*, 430:343–353, January 2005.

[72] U. Klaas, R. J. Laureijs, T. G. Müller, E. Kreysa, and W. Krätschmer. Data Reduction, Calibration and Performance of the ISOPHOT Polarisation Modes. In R. J. Laureijs & R. Siebenmorgen, editor, *Workshop on ISO Polarisation Observations*, volume 435 of *ESA Special Publication*, page 19, December 1999.

[73] U. Klaas and F. Sibille. The ISOCAM and ISOPHOT instruments - photopolarimetry, spectrophotometry and imaging capabilities with ISO. In G. Klare, editor, *Astronomische Gesellschaft Abstract Series*, volume 7 of *Astronomische Gesellschaft Abstract Series*, page 10, 1992.

[74] G. R. Knapp. Mass loss from evolved stars. VI - Mass-loss mechanisms and luminosity evolution. *Astronomy and Astrophysics*, 311:731–741, December 1986.

[75] S. Kwok. Test of planetary nebula evolution models by distance-independent parameters. *actaa*, 43:359–370, October 1993.

[76] D. Ladjal, K. Justtanont, M. A. T. Groenewegen, J. A. D. L. Blommaert, C. Waelkens, and M. J. Barlow. 870 $\mu$m observations of evolved stars with LABOCA. *Astronomy and Astrophysics*, 513:A53, April 2010.

[77] H. J. G. L. M. Lamers and J. P. Cassinelli. *Introduction to Stellar Winds*. June 1999.

[78] H. J. G. L. M. Lamers, T. P. Snow, and D. M. Lindholm. Terminal Velocities and the Bistability of Stellar Winds. *Astrophysical Journal Letters*, 455:269, December 1995.

[79] W. B. Landsman. The IDL Astronomy User's Library. In *Bulletin of the American Astronomical Society*, volume 21 of *Bulletin of the American Astronomical Society*, page 784, March 1989.

[80] J. C. Lattanzio and A. I. Boothroyd. Nucleosynthesis of elements in low to intermediate mass stars through the AGB phase. In T. J. Bernatowicz & E. Zinner, editor, *American Institute of Physics Conference Series*, volume 402 of *American Institute of Physics Conference Series*, pages 85–114, March 1997.

[81] R. J. Laureijs, U. Klaas, P. J. Richards, B. Schulz, and P. Abraham. *The ISO Handbook, Volume IV - PHT - The Imaging Photo-Polarimeter*. June 2003.

[82] T. Le Bertre. The opacity of the dust around the carbon star IRC + 10216. *Astronomy and Astrophysics*, 176:107–113, April 1987.

[83] T. Le Bertre. Optical and infrared observations of 23 carbon-rich stars. Modelling of the circumstellar dust shells. *Astronomy and Astrophysics*, 324:1059–1070, August 1997.

[84] D. Lemke, U. Klaas, J. Abolins, P. Abraham, J. Acosta-Pulido, S. Bogun, H. Castaneda, L. Cornwall, L. Drury, C. Gabriel, F. Garzon, H. P. Gemuend, U. Groezinger, E. Gruen, M. Haas, C. Hajduk, G. Hall, I. Heinrichsen, U. Herbstmeier, G. Hirth, R. Joseph, U. Kinkel, S. Kirches, C. Koempe, W. Kraetschmer, E. Kreysa, H. Krueger, M. Kunkel, R. Laureijs, P. Luetzow-Wentzky, K. Mattila, T. Mueller, T. Pacher, G. Pelz, E. Popow, I. Rasmussen, J. Rodriguez Espinosa, P. Richards, S. Russell, H. Schnopper, J. Schubert, B. Schulz, C. Telesco, C. Tilgner, R. Tuffs, H. Voelk, H. Walker, M. Wells, and J. Wolf. ISOPHOT - capabilities and performance. *Astronomy and Astrophysics*, 315:L64–L70, November 1996.

[85] Forveille T. Omont A. Paul J. F. Loup, C. Co and hcn observations of circumstellar envelopes. a catalogue - mass loss rates and distributions. *Astronomy and Astrophysics Supplement Series (ISSN 0365-0138)*, 99:291–377, 1993.

[86] L. B. Lucy. On the mass of the halo population. *Astronomy and Astrophysics Journal*, 203:75–80, January 1976.

[87] D. Makovoz, F. R. Marleau, and D. T. Frayer. Point Source Extraction with MOPEX. In *American Astronomical Society Meeting Abstracts*, volume 36 of *Bulletin of the American Astronomical Society*, pages 153–12, December 2004.

[88] J. R. Marshall, J. T. van Loon, M. Matsuura, P. R. Wood, A. A. Zijlstra, and P. A. Whitelock. Asymptotic giant branch superwind speed at low metallicity. *Monthly Notices of Royal Astronomical Society*, 355:1348–1360, December 2004.

[89] H. Marten, K. Gesicki, and R. Szczerba. Dynamical Structures of Planetary Nebulae - Models Against Observations. In R. Weinberger & A. Acker, editor, *Planetary Nebulae*, volume 155 of *IAU Symposium*, page 315, 1993.

[90] D. C. Martin, M. Seibert, J. D. Neill, D. Schiminovich, K. Forster, R. M. Rich, B. Y. Welsh, B. F. Madore, J. M. Wheatley, P. Morrissey, and T. A. Barlow. A turbulent wake as a tracer of 30,000years of Mira's mass loss history. *Nature*, 448:780–783, August 2007.

[91] N. Mastrodemos and M. Morris. Bipolar Pre-Planetary Nebulae: Hydrodynamics of Dusty Winds in Binary Systems. II. Morphology of the Circumstellar Envelopes. *Astrophysical Journal*, 523:357–380, September 1999.

[92] M. Meixner. The Evolution of Aging Stars and the Return of Matter to the Next Generation. In D. C. Backer, J. M. Moran, & J. L. Turner, editor, *Revealing the Molecular Universe: One Antenna is Never Enough*, volume 356 of *Astronomical Society of the Pacific Conference Series*, page 233, December 2006.

[93] M. Meixner, M. T. Campbell, W. J. Welch, and L Likkel. Mass-Loss Histories of Three Carbon-rich Evolved Stars as Revealed by ˆ12CO Emission. *Astrophysical Journal*, 509:392–414, December 1998.

[94] M. Meixner, T. Ueta, A. Dayal, J. L. Hora, G. Fazio, B. J. Hrivnak, C. J. Skinner, W. F. Hoffmann, and L. K. Deutsch. A Mid-Infrared Imaging Survey of Proto-Planetary Nebulae Candidates. In M. D. Bicay, R. M. Cutri, & B. F. Madore, editor, *Astrophysics with Infrared Surveys: A Prelude to SIRTF*, volume 177 of *Astronomical Society of the Pacific Conference Series*, page 366, 1999.

[95] G. Mellema and A. Frank. Numerical Models and our Understanding of Aspherical Planetary Nebulae. In A. Harpaz & N. Soker, editor, *Asymmetrical Planetary Nebulae*, volume 11 of *Annals of the Israel Physical Society*, page 229, 1995.

[96] P. W. Merrill. Technetium in the N-Type Star 19 PISCIUM. *Astronomical Society of the Pacific*, 68:70, February 1956.

[97] L. Mestel. The influence of stellar radiation on the rate of accretion. *Monthly Notices of the Royal Astronomical Society*, 114:437, 1954.

[98] H. Murakami, H. Baba, P. Barthel, D. L. Clements, M. Cohen, Y. Doi, K. Enya, E. Figueredo, N. Fujishiro, H. Fujiwara, M. Fujiwara, P. Garcia-Lario, T. Goto, S. Hasegawa, Y. Hibi, T. Hirao, N. Hiromoto, S. S. Hong, K. Imai, M. Ishigaki, M. Ishiguro, D. Ishihara, Y. Ita, W.-S. Jeong, K. S. Jeong, H. Kaneda, H. Kataza, M. Kawada, T. Kawai, A. Kawamura, M. F. Kessler, D. Kester, T. Kii, D. C. Kim, W. Kim, H. Kobayashi, B. C. Koo, S. M. Kwon, H. M. Lee, R. Lorente, S. Makiuti, H. Matsuhara, T. Matsumoto, H. Matsuo, S. Matsuura, T. G. Müller, N. Murakami, H. Nagata, T. Nakagawa, T. Naoi,

M. Narita, M. Noda, S. H. Oh, A. Ohnishi, Y. Ohyama, Y. Okada, H. Okuda, S. Oliver, T. Onaka, T. Ootsubo, S. Oyabu, S. Pak, Y.-S. Park, C. P. Pearson, M. Rowan-Robinson, T. Saito, I. Sakon, A. Salama, S. Sato, R. S. Savage, S. Serjeant, H. Shibai, M. Shirahata, J. Sohn, T. Suzuki, T. Takagi, H. Takahashi, T. Tanabé, T. T. Takeuchi, S. Takita, M. Thomson, K. Uemizu, M. Ueno, F. Usui, E. Verdugo, T. Wada, L. Wang, T. Watabe, H. Watarai, G. J. White, I. Yamamura, C. Yamauchi, and A. Yasuda. The Infrared Astronomical Mission AKARI. *Publications of the Astronomical Society of Japan*, 59:369, October 2007.

[99] G. Neugebauer, H. J. Habing, R. van Duinen, H. H. Aumann, B. Baud, C. A. Beichman, D. A. Beintema, N. Boggess, P. E. Clegg, T. de Jong, J. P. Emerson, T. N. Gautier, F. C. Gillett, S. Harris, M. G. Hauser, J. R. Houck, R. E. Jennings, F. J. Low, P. L. Marsden, G. Miley, F. M. Olnon, S. R. Pottasch, E. Raimond, M. Rowan-Robinson, B. T. Soifer, R. G. Walker, P. R. Wesselius, and E. Young. The Infrared Astronomical Satellite (IRAS) mission. *Astronomy and Astrophysics*, 278:L1–L6, March 1984.

[100] Bauer P. Marcout J. Ochsenbein, F. The vizier database of astronomical catalogues. *Astronomy and Astrophysics*, 143:23–32, 2000.

[101] D. A. Ostlie and A. N. Cox. A linear survey of the Mira variable star instability region of the Hertzsprung-Russell diagram. *Astrophysical Journal Letters*, 311:864–872, December 1986.

[102] B. Paczynski. Evolution of single stars iii. stationary shell sources. *Acta Astronomica*, 20:287, 1970.

[103] B. Paczynski. Core mass-interflash period relation for double shell source stars. *Astrophysical Journal Letters*, 202:558–560, December 1975.

[104] N. Panagia and M. Felli. The spectrum of the free-free radiation from extended envelopes. *Astronomy and Astrophysics*, 39:1–5, February 1975.

[105] E. N. Parker. The Hydrodynamic Theory of Solar Corpuscular Radiation and Stellar Winds. *Astrophysical Journal Letters*, 132:821, November 1960.

[106] E. N. Parker. Theory of Solar Wind. In *International Cosmic Ray Conference*, volume 1 of *International Cosmic Ray Conference*, page 175, 1963.

[107] Lindegren L. Kovalevsky J. Hoeg E. Bastian U. Bernacca P. L. Crz M. Donati F. Grenon M. van Leeuwen F. van der Marel H. Mignard F. Murray C. A. Le Poole R. S. Schrijver H. Turon C. Arenou F. Froeschl M. Petersen C. S. Perryman, M. A. C. Hipparcos. *Astrononmy and Astrophysics*, 323:L49–L52, 1997.

[108] J. Phillips. *The NAG library: A beginner's guide*. 1986.

[109] A. Poglitsch, T. de Graauw, M. Griffin, G. Pilbratt, O. H. Bauer, T. Phillips, J. Stutzki, B. Swinyard, L. Vigroux, and C. Waelkens. The Herschel far-infrared and submillimetre space observatory. In *36th COSPAR Scientific Assembly*, volume 36, page 215, 2006.

[110] D. Reimers. Circumstellar absorption lines and mass loss from red giants. *Memoires of the Societe Royale des Sciences de Liege*, 8:369–382, 1975.

[111] H. N. Russel. Sull'idrogeno molecolare delle macchie del sole. *Mem. Societa Astronomica Italiana*, 5:5, May 1930.

[112] H. N. Russell. Relations between the spectra and other characteristics of the stars. *Nature*, 93:pt. I, pp. 227–30; pt. II, pp. 252–58; pt. Ill, pp. 281–86., 1914.

[113] I.-J. Sackmann. Convective penetrations and observable consequences of helium shell flashes in 3 and 6 solar-mass red supergiants. *Astrophysical Journal Letters*, 235:554–564, January 1980.

[114] R. Sahai and C. K. Chronopoulos. The Astrosphere of the Asymptotic Giant Branch Star IRC+10216. *Astrophysical Journal Letters*, 711:L53–L56, March 2010.

[115] J. M. Scalo, K. H. Despain, and R. K. Ulrich. Studies of evolved stars. V - Nucleosynthesis in hot-bottom convective envelopes. *Astrophysical Journal Letters*, 196:805–817, March 1975.

[116] M. Schmidt. The Rate of Star Formation. *Astrophysical Journal Letters*, 129:243, March 1959.

[117] M. Schönberg and S. Chandrasekhar. On the Evolution of the Main-Sequence Stars. *Astrophysical Journal Letters*, 96:161, September 1942.

[118] B. Schulz, S. Huth, R. J. Laureijs, J. A. Acosta-Pulido, M. Braun, H. O. Castañeda, M. Cohen, L. Cornwall, C. Gabriel, P. Hammersley, I. Heinrichsen, U. Klaas, D. Lemke, T. Müller, D. Osip, P. Román-Fernández, and C. Telesco. ISOPHOT - Photometric calibration of point sources. *Astronomy and Astrophysics*, 381:1110–1130, January 2002.

[119] H. E. Schwarz. M 1-16 - Multiple shocked outflows from an evolved object. *Astronomy and Astrophysics*, 264:L1–L4, October 1992.

[120] M. Schwarzschild and R. Härm. Therma Instability in Non-Degenerate Stars. *Astrophysical Journal Letters*, 142:855, October 1965.

[121] V. V. Smith and D. L. Lambert. The chemical composition of red giants. II - Helium burning and the s-process in the MS and S stars. *Astrophysical Journal*, 311:843–863, December 1986.

[122] V. V. Smith and D. L. Lambert. The chemical composition of red giants. III - Further CNO isotopic and s-process abundances in thermally pulsing asymptotic giant branch stars. *Astrophysical Journal Supplement Series*, 72:387–416, February 1990.

[123] N. Soker. Radially Aligned Clumps and Tails in Planetary Nebulae. *Monthly Notices of the Royal Astronomical Society*, 299:562–566, September 1998.

[124] A. K. Speck, M. Meixner, and G. R. Knapp. Circumstellar Dust Around Post-AGB Stars. In R. J. Laureijs, K. Leech, & M. F. Kessler, editor, *ISO Beyond Point Sources: Studies of Extended Infrared Emission*, volume 455 of *ESA Special Publication*, page 83, 2000.

[125] A. K. Speck, M. Meixner, and G. R. Knapp. Discovery of Parsec-sized Dust Shells around AFGL 2688 and AFGL 618. *Astrophysical Journal*, 545:L145–L148, December 2000.

[126] M. Steffen, R. Szczerba, A. Men'shchikov, and D. Schoenberner. Hydrodynamical models and synthetic spectra of circumstellar dust shells around AGB stars. *Astronomy and Astrophysics*, 126:39–65, November 1997.

[127] R. E. Stencel. The Circumstellar-Interstellar Boundary around Evolved Stars - Revealed. In D. G. Luttermoser, B. J. Smith, & R. E. Stencel, editor, *The Biggest, Baddest, Coolest Stars*, volume 412 of *Astronomical Society of the Pacific Conference Series*, page 197, September 2009.

[128] K. Y. L. Su, B. J. Hrivnak, S. Kwok, and R. Sahai. High-Resolution Near-Infrared Imaging and Polarimetry of Four Proto-Planetary Nebulae. *Astronomy Journal*, 126:848–862, August 2003.

[129] Y. Tuchman, A. Glasner, and Z. Barkat. The luminosity-core mass relation - Why and how. *Astrophysical Journal Letters*, 268:356–360, May 1983.

[130] T. Ueta. Cometary Astropause of Mira Revealed in the Far-Infrared. *Astrophysical Journal Letters*, 687:L33–L36, November 2008.

[131] T. Ueta, M. Meixner, and M. Bobrowsky. Dual Axisymmetry in Proto-planetary Nebula Reflection Nebulosities: Results from an HST Snapshot Survey of PPN Candidates. In J. H. Kastner, N. Soker, & S. Rappaport, editor, *Asymmetrical Planetary Nebulae II: From Origins to Microstructures*, volume 199 of *Astronomical Society of the Pacific Conference Series*, page 195, 2000.

[132] T. Ueta, K. Murakawa, and M. Meixner. Imaging Polarimetry of Proto-planetary Nebulae - Probing the History of AGB Mass Loss. In A. Adamson, C. Aspin, C. Davis, & T. Fujiyoshi, editor, *Astronomical Polarimetry: Current Status and Future Directions*, volume 343 of *Astronomical Society of the Pacific Conference Series*, page 260, December 2005.

[133] T. Ueta, A. K. Speck, R. E. Stencel, F. Herwig, R. D. Gehrz, R. Szczerba, H. Izumiura, A. A. Zijlstra, W. B. Latter, M. Matsuura, M. Meixner, M. Steffen, and M. Elitzur. Detection of a Far-Infrared Bow Shock Nebula around R Hya: The First MIRIAD Results. *Astrophysical Journal Leters*, 648:L39–L42, September 2006.

[134] T. Ueta, R. E. Stencel, I. Yamamura, K. M. Geise, A. Karska, H. Izumiura, Y. Nakada, M. Matsuura, Y. Ita, T. Tanabé, H. Fukushi, N. Matsunaga,

H. Mito, and A. K. Speck. The interface between the stellar wind and interstellar medium around R Cassiopeiae revealed by far-infrared imaging. *Astronomy and Astrophysics*, 514:A16, May 2010.

[135] F. Valdes. The Interactive Data Reduction and Analysis Facility (IRAF). In *Bulletin of the American Astronomical Society*, volume 16 of *Bulletin of the American Astronomical Society*, page 497, March 1984.

[136] J. T. van Loon, M. A. T. Groenewegen, A. de Koter, N. R. Trams, L. B. F. M. Waters, A. A. Zijlstra, P. A. Whitelock, and C. Loup. Mass-loss rates and luminosity functions of dust-enshrouded AGB stars and red supergiants in the LMC. *Astronomy and Astrophysics*, 351:559–572, November 1999.

[137] E. Vassiliadis and P. R. Wood. Evolution of low- and intermediate-mass stars to the end of the asymptotic giant branch with mass loss. *Astrophysical Journal*, 413:641–657, August 1993.

[138] J. Wagenhuber and M. A. T. Groenewegen. New input data for synthetic AGB evolution. *Astronomy and Astrophysics*, 340:183–195, December 1998.

[139] C. J. Wareing, A. A. Zijlstra, T. J. O'Brien, and M. Seibert. It's a Wonderful Tail: The Mass-Loss History of Mira. *Astrophysical Journal Letters*, 670:L125–L129, December 2007.

[140] V. Weidemann. Revision of the initial-to-final mass relation. *Astronomy and Astrophysics*, 363:647–656, November 2000.

[141] V. Weidemann and D. Koester. The upper mass limit for white dwarf progenitors and the initial-final mass relation for low and intermediate mass stars. *Astronomy and Astrophysics*, 121:77–84, May 1983.

[142] P. Whitelock and M. Feast. Hipparcos parallaxes for Mira-like long-period variables. *Monthly Notices of the Royal Astronomical Society*, 319:759–770, December 2000.

[143] P. Whitelock, M. Feast, and R. Catchpole. IRAS sources and the nature of the Galactic Bulge. *Monthly Notices of the Royal Astronomical Society*, 248:276–312, January 1991.

[144] J. M. Winters, T. Le Bertre, K. S. Jeong, L.-Å. Nyman, and N. Epchtein. Mass-loss from dusty, low outflow-velocity AGB stars. I. Wind structure and mass-loss rates. *Astronomy and Astrophysics*, 409:715–735, October 2003.

[145] P. Woitke. 2D models for dust-driven AGB star winds. *Astronomy and Astrophysics*, 452:537–549, June 2006.

[146] B. E. Wood. The Solar Wind and the Sun in the Past. *Space Science Reviews*, 126:3–14, October 2006.

[147] M. A. Wood. White dwarf stars and the age of the Galactic disk. *Journal of the Royal Astronomical Society of Canada*, 84:150–165, June 1990.

[148] M. A. Wood. Constraints on the age and evolution of the Galaxy from the white dwarf luminosity function. *Astrophysical Journal Letters*, 386:539–561, February 1992.

[149] P. R. Wood. Variable red giants in the LMC: Pulsating stars and binaries? *Astronomical Society of Australia*, 17:18–21, April 2000.

[150] P. R. Wood. The sequence of mass-losing AGB stars in the Magellanic Clouds - from small amplitude pulsators to post-AGB stars. In Y. Nakada, M. Honma, & M. Seki, editor, *Mass-Losing Pulsating Stars and their Circumstellar Matter*, volume 283 of *Astrophysics and Space Science Library*, pages 3–10, April 2003.

[151] P. R. Wood, A. E. Olivier, and S. D. Kawaler. The long secondary periods in semi-regular variables. In D. W. Kurtz & K. R. Pollard, editor, *IAU Colloq. 193: Variable Stars in the Local Group*, volume 310 of *Astronomical Society of the Pacific Conference Series*, page 322, May 2004.

[152] P. R. Wood, J. B. Whiteoak, S. M. G. Hughes, M. S. Bessell, F. F. Gardner, and A. R. Hyland. OH/IR stars in the Magellanic Clouds. *Astrophysical Journal Letters*, 397:552–569, October 1992.

[153] H. C. Woodruff, M. Eberhardt, T. Driebe, K.-H. Hofmann, K. Ohnaka, A. Richichi, D. Schertl, M. Schöller, M. Scholz, G. Weigelt, M. Wittkowski, and P. R. Wood. Interferometric observations of the Mira star o Ceti with the VLTI/VINCI instrument in the near-infrared. *Astronomy and Astrophysics*, 421:703–714, July 2004.

[154] Weight A. Zeitschrift. Calculation of thermal instability in non-degenerate stars. *Astrophysics*, 64:395, 1966.

[155] A. A. Zijlstra and R. Weinberger. A Wall of Dust around a Proto-Mira? *Astrophysical Journal letters*, 572:1006–1011, June 2002.

[156] B. Zuckerman and L. H. Aller. Origin of planetary nebulae - Morphology, carbon-to-oxygen abundance ratios, and central star multiplicity. *Astrophysical Journal Letters*, 301:772–789, February 1986.

# Appendix A

# Primer on stellar properties and related physics

The brightness of a star can be described by as its apparent magnitude (m), which is a measure of how bright it appears to the naked eye. This scale was introduced by the Greek astronomer Hipparchus who assigned $m = 1$ to the brightest stars he saw whereas dimmest stars were assigned $m = 6$. In modern terms we have made this scale more precise and quantitative. It has been shown that there is a factor of 100 in brightness (i.e. energy flux $F$, usually in visible light[1]) between stars of $m = 1$ and those of $m = 6$, but that the intervening scale is logarithmic. Obviously in this magnitude scale the lower or more negative the number, the brighter the object. Thus, the apparent magnitude is defined by

$$m = \frac{5}{2} log_{10}(F) \tag{A.1}$$

The quantification of the magnitude scale changed the precise numbers associated with certain stars. For instance the brightest star, Sirius was considered by

[1]It is usually assumed that the term apparent magnitude is actually apparent *visual* magnitude - which measures brightness in a well-defined wavelength range known as the V-band

Hipparchus to be 1st magnitude, but its precise visual magnitude is -1.4. Betelgeuse, the brightest star in Orion, was also considered 1st magnitude and is now known to have m=+0.5. Meanwhile, this magnitude scaling can be applied to non-stellar objects such as Venus (-4.4), the Moon (-12.6) and the Sun (-26.7). Apparent magnitude, $m$, is simply a measure of how bright stars appear from earth and does not distinguish between intrinsic brightness and the effect of distance. Consequently, astronomers use the apparent magnitude scale in conjunction with the effect of distance to scale how bright the stars would be if a star were placed at a distance of 10 parsecs[2] from the observer to define Absolute Magnitude ($M$).

In order to determine the absolute magnitude (or intrinsic brightness) of stars we need to know their distances from us. Measuring distances in space is non-trivial and can only be done directly (using parallax) for the closest stars (within $\sim$200 pc). However, enough stars exist within a distance of 200 pc that we have been able to calibrate so-called 'standard candles' which utilize a link between some observable property and intrinsic brightness, allowing distance to be determined from the measured brightness. Amongst the most famous examples of a standard candles are the Cepheid Variables, which pulsate in such a way that the pulsation period is proportional to the absolute brightness of the star. Furthermore, other methods, such as spectroscopic parallax or the use of color measurements have been developed.
The color that we see from the star depends on the star′s effective surface temperature. Stars have different colors which indicates that their surface temperatures vary. In fact stars are almost blackbodies: bluer stars are hotter than yellow or red stars. Figure A.1 show the relationship between the temperature of a blackbody and the wavelength at which it emits most energy.

The energy distribution for each curve shown in Figure A.1 is defined by Planck

[2]A parsec is defined as the distance from which the radius of the Earth′ orbit around the Sun subtends an angle of one arcsecond relative to distant stars. 1 pc = $3.086 \times 10^{16}$meters.

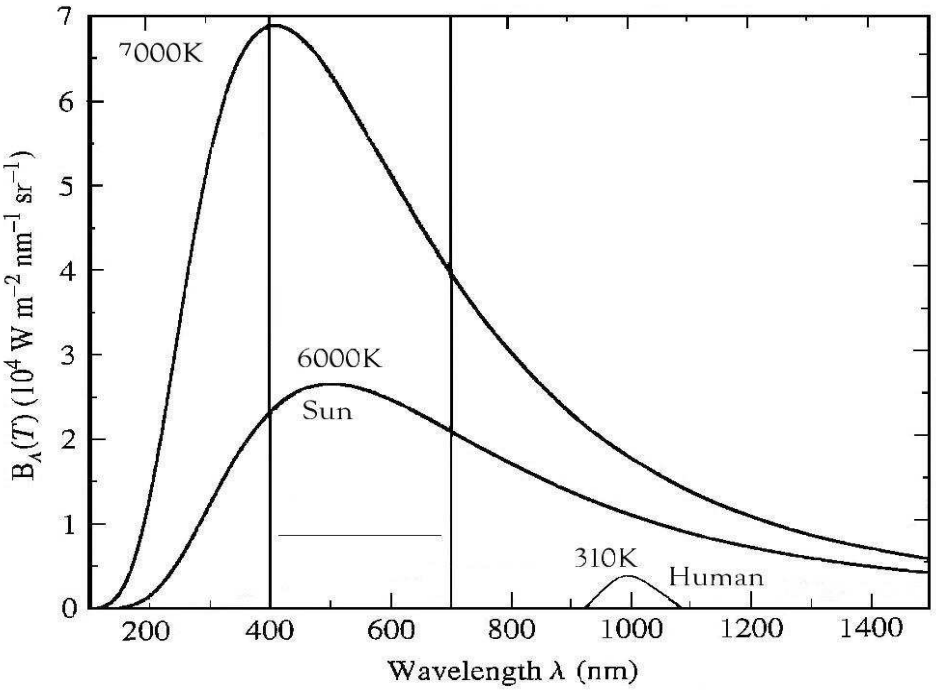


Figure A.1: Blackbody Radiation as described by the Planck equation (equation A.2). The vertical axis is the intensity $B_\lambda(T)$ in units of $\mathrm{W\,m^{-2}\,nm^{-1}\,sr^{-1}}$., The horizontal axis is wavelength ($\lambda$) in nm. The visible light region is indicated by two solid vertical lines.

function:

$$B_\lambda(T) = \frac{2hc^2}{\lambda^5 \left(e^{\frac{hc}{\lambda k_b T}} - 1\right)} \tag{A.2}$$

where $\lambda$ is the wavelength, $T$ is the temperature, $h$ is the Planck constant, and $k_b$ is the Boltzmann constant. Figure A.1 shows that the peak wavelength decreases with increasing temperatures. This relationship between the peak wavelength of each energy distribution ($\lambda_{max}$) with the effective surface temperature($T_{surface}$) can be approximated using Wien's law.

$$\lambda_{max}.T_{surface} = 2890\mu\mathrm{m}.K \tag{A.3}$$

Figure A.1 also demonstrates that the energy emitted per unit surface area is higher

at higher temperatures; the area under the 7000 K curve is larger than that of the 6000 K. Therefore, the total luminosity of an emitting region or a source depends on both temperature ($T$) and surface area ($A$).

The total luminosity can be obtained by summing all monochromatic luminosities ($L_\lambda d\lambda$) and assuming a star that is spherical with radius R, we can use spherical co-ordinates to obtain

$$L_{total} = 4\pi R^2 \int_0^\infty L_\lambda d\lambda = 4\pi R^2 \left(\frac{\sigma.T_{eff}^4}{\pi}\right)$$

where $\sigma = [2\pi^5 k_b^4]/[15c^2h^3]$ is called the Stefan - Boltzmann constant.

$$L_{total} = 4\pi\sigma R^2 T_{eff}^4 \tag{A.4}$$

Equation A.4 is a version of the Stefan-Boltzmann law. Stefan-Boltzmann law in general is given in terms of the flux from the star i.e.

$$F = \frac{L_{total}}{4\pi\sigma R^2}$$

such that equation A.4 becomes,

$$F = \frac{\sigma T_{eff}^4}{\pi} \tag{A.5}$$

where F is the flux in Jy and it does not depend on surface area.

Equation A.4 is used to define the effective surface temperature. The effective temperature is intrinsic to the star's surface, so it can be used to estimate the sizes of the stars from their measured luminosities and surface temperatures. The effective temperature ($T_{\rm eff}$ is different from the color temperatures ($T_{\rm col}$); is the temperature of a black body that would emit the same total amount of electromagnetic radiation and thus is based on the Stefan-Boltzmann law seen in Equation A.5. The color

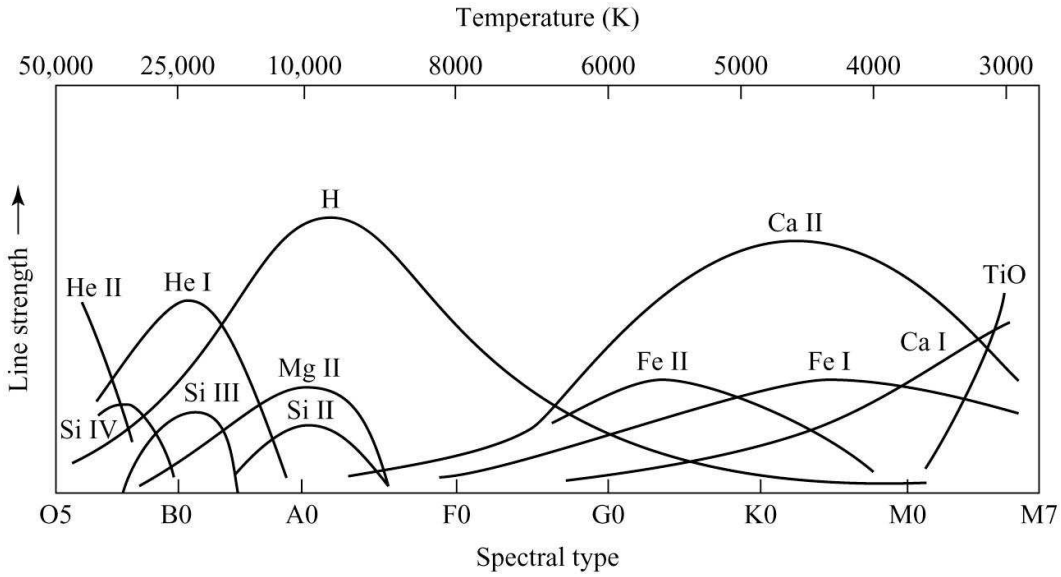


Figure A.2: The dependence on spectral lines strengths on effective temperature

temperature is based on the relative strengths of emission at different wavelengths and is effectively defined by Wien's Laws seen in Equation A.3.

From Figure A.2 and Equation A.3 we can see how multiwavelength observations can be used to determine the colors/temperatures of stars. In fact, stars are classified according to their visible spectra using the strengths of atomic, ionized and molecular lines within the visible waveband. The energetics involved in determining the relative line strengths provide a fairly sensitive probe of stellar surface temperature. The distinctions between the spectra of stars with different temperatures are due to electron occupying different orbital in the atmospheres of the star. The atoms can be found in any degree of ionization and thus will have a unique set of orbitals at each stage e.g. H I (represents neutral hydrogen) ,HeII (single ionized Helium), SiIV (means triple ionized Silicone). Thus we often use 'spectral type' as a proxy for star temperature. To show this classification lets refer to Figure A.2.

In this figure, the grouping of stars is classified according to the so called Harvard classification scheme (OBAFGKM), left to right sequence on the spectral type (bottom axis). The sequence starts with letter O representing the spectral type group

of hottest stars having high effective surface temperatures ($\sim$ 50,000K), up to the coolest M stars with effective temperatures around 3000 K. The numbers (0-9) between each letter group designate the spectral sub-division per group as the effective temperatures also differs within the group giving rise to different ionized atoms. Thus there is a correlation at the beginning of each group a letter and the number (at the bottom axis) and the effective temperature (on the top axis). Because the degree of excitation per atom in the atmosphere of the star depends sensitively on the effective temperature, the strength of spectra lines (vertical axis) peaks at different effective temperatures e.g. H I peaks around 10,000 K whereas Ca II peaks around 5000 K. Therefore the appearance an ion or atom (traced by a spectral line) reflects the sensitive dependence of the atomic state of excitation and ionization of an atom rather than its abundance. As an example, the Sun photosphere[3] shows that there are about 50,000 H I atoms than Ca atoms (e.g. Gingerich et al. 1971 [41]), however about 400 Ca II ions for every H I are in the excited state, making Ca II H and K lines to peak much stronger than H I (because of higher effective temperature ($T_{eff}$ for the sun $\sim$5777K) in favor of Ca II H and K lines).

When we compare Figure A.2 and Figure 2.1, we notice that stars of different groups (e.g. main sequence stars and giant stars) does share same effective temperature (or same spectral type), but they have different luminosities. Hertzsprung wondered whether there might be some differences in strength of spectral lines of giants and main sequence stars that have the same spectral type. As a result, astronomers began a careful comparison of their spectra, discovering that are indeed subtle differences in the relative strenghts of spectral lines. This led to the publication of the Atlas of Stellar Spectra by Morgan & Keenan in 1943 (MK) of Yerkes observatory (e.g [59]) that includes the luminosity classes in spectral classification.

[3]the photosphere is defined as the region of the atmosphere where visible photons originate i.e. where the star becomes opaque to visible light. The value of the optical depth, $\tau$ is approximately unity but depends on the distance a photon can travel, which is wavelength dependent. This is discussed in Chapter 5

Table A.1: Morgan Keenan Luminosity classes

| Class | Type of star |
|---|---|
| Ia - O | Extreme super Giant |
| Ia | Luminous supergiants |
| Ib | Less luminous supergiants |
| II | Bright giants |
| III | Normal giants |
| IV | Subgiants |
| V | Main sequence (dwarf stars) |
| VI | Subdwarfs |
| D | White Dwarfs |

The lumnosisty classisfication by [59] is shown in table A.1.

The classification scheme provided by the luminosity class like that in table A.1 allows for position of a star to be identified on the HR diagram, in conjunction with spectral signatures in their atmospheres such as the one given in Figure A.2. In general, for for stars of the same spectral type, the narrower lines are usually produced by more luminous stars, because the atmosphere of more luminous stars are less dense, there are fewer collisions between atoms to distort the energy of thier orbitals that will broaden the spectral lines. The luminosity classification enables astronomers to locate a star's position on the HR-diagram based on spectral appearance. For example, the sun is star of spectral type G2 V star, Mira is an oxygen-rich variable star with spectral type M2-7III+, and CRL 618 is a carbon rich post AGB star with spectral type B0 D, the latter two stars are amongst the stars researched in this thesis.

## A.1 Main-sequence: Nucleosynthesis at the Hydrogen burning Core

A protostar becomes a Main Sequence star when steady hydrogen burning begins in its core with temperatures reaching about 10 million K and it achieves hydrostatic

equilibrium, which is a balance between the inward force of gravity by surface layers and the outward pressure produced by hydrogen burning at the core. In the core four hydrogen nuclei are converted into a single helium nucleus by either Proton Proton Chain reactions or through Carbon-Nitrogen-Oxygen cycle (CNO cycle).

The base reaction is

$$4\ {}^{1}_{1}\mathrm{H} \rightarrow {}^{4}_{2}\mathrm{He} + 2e^{+} + 2\nu_e + 2\gamma$$

where $e^{+}$ is the positron an anti-particle to an electron with only $+1/2$ spin, $\gamma$ and $\nu$ represents gamma rays and neutrinos emitted.

**Proton - Proton Chains**:

The burning of Hydrogen in these chain of reaction first involve the collision of two hydrogen atoms that involves the $\beta$ - the decay of one proton into a neutron by.

$$p^{+} \rightarrow n + e^{+} + \nu_e$$

A neutron combines with a H - atom to form deuterium $({}^{2}_{1}\mathrm{H})$ , and ${}^{2}_{1}\mathrm{H}$ can react with another proton as there are many of them around for the second reaction to occur leading to the formation of Helium-3 $({}^{3}_{2}\mathrm{He})$ i.e.

${}^{1}_{1}\mathrm{H} + {}^{1}_{1}\mathrm{H} \rightarrow {}^{2}_{1}\mathrm{H} + e^{+} + \nu_e$

${}^{2}_{1}\mathrm{H} + {}^{1}_{1}\mathrm{H} \rightarrow {}^{3}_{2}\mathrm{He} + \gamma$

after which three processes that produces Helium can occur.

About 70% of the time two Helium-3 can fuse together forming stable Helium 4 in the so called PPI as follows

**Proton - Proton One (PPI)**

${}^{3}_{2}\mathrm{He} + {}^{3}_{2}\mathrm{He} \rightarrow {}^{4}_{2}\mathrm{He} + {}^{1}_{1}\mathrm{H}.$

For the remaining 30%, He-3 can react with He-4 $({}^{4}_{2}\mathrm{He})$ already present producing Berylium $({}^{7}_{4}\mathrm{Be})$. After this stage there are two branches that can create Helium - 4. That is, about 99% of the time Berylium can react with electrons creating Lithium

($^{7}_{3}$Li), and Lithium in the presence of protons will produce an extra Helium, this is PPII chain reaction. However about 1% of the time Berylium can also react with a proton producing Boron ($^{8}_{5}$B). Boron decays into isotope of Be ($^{8}_{4}$Be) that decays into two $^{4}_{2}$He , this sequence is called PPIII.

**Proton - Proton Two (PPII)**:

$^{3}_{2}\mathrm{He} + {}^{4}_{2}\mathrm{He} \rightarrow {}^{7}_{4}\mathrm{Be} + \gamma$

${}^{7}_{4}\mathrm{Be} + e^{-} \rightarrow {}^{7}_{3}\mathrm{Li} + \nu_e$

${}^{7}_{3}\mathrm{Li} + {}^{1}_{1}\mathrm{H} \rightarrow 2{}^{4}_{2}\mathrm{He}.$

**Proton - Proton Three (PPIII)**

${}^{7}_{4}\mathrm{Be} + {}^{1}_{1}\mathrm{H} \rightarrow {}^{8}_{5}\mathrm{B} + \gamma$

${}^{8}_{5}\mathrm{B} \rightarrow {}^{8}_{4}\mathrm{Be} + e^{+} + \nu_e$

${}^{8}_{4}\mathrm{Be} \rightarrow 2{}^{4}_{2}\mathrm{He}.$

The energy generation rate in producing ${}^{4}_{2}\mathrm{He}$ depends on internal temperature, it has the form

$$\epsilon_{pp} \approx \epsilon'_{0,pp} \rho X^2 f_{pp} \psi_{pp} T_6^4 \tag{A.6}$$

where $T_6^4$ is a dimensionless expression of the temperature in units of $10^6$K, $f_{pp}$ is the pp chain screening factor that depends mass fraction (X) of particles and gas density, $\psi_{pp}$ is the correction factor that accounts for the simultaneous appearance of PPI PPII PPIII, and $\epsilon'_{0,pp} = 1.08 \times 10^{-12} W m^3 kg^{-2}$ is a constant. In 1938 Hans Bethe proposed the CNO Cycle as another alternate form of hydrogen burning that produces helium. In this cycle of reactions, carbon, oxygen and nitrogen are used as catalyst in the making of Helium nuclei.

About 99.94% stars that have initial mass $0.5 M_{\odot} \leq 8 M\odot$ can produce ${}^{4}_{2}\mathrm{H}$ in the following:

${}^{4}_{2}\mathrm{He} + {}^{1}_{1}\mathrm{H} \rightarrow {}^{13}_{7}\mathrm{N}$

${}^{13}_{7}\mathrm{N} \rightarrow {}^{13}_{6}\mathrm{C} + e+ + \nu_e$

${}^{13}_{6}\mathrm{C} + {}^{1}_{1}\mathrm{H} \rightarrow {}^{14}_{7}\mathrm{N} + \gamma$

${}^{14}_{7}\mathrm{N} + {}^{1}_{1}\mathrm{H} \rightarrow {}^{15}_{8}\mathrm{O} + \gamma$

${}^{15}_{8}\mathrm{O} \rightarrow {}^{15}_{7}\mathrm{N} + e^+ + \nu_e$

${}^{15}_{7}\mathrm{N} + {}^{1}_{1}\mathrm{H} \rightarrow {}^{12}_{6}\mathrm{C} + {}^{4}_{2}\mathrm{He}$

If nitrogen (${}^{15}_{7}\mathrm{N}$) in the last reaction produces oxygen rather than carbon, another branch of CNO cycle occurs.

${}^{15}_{7}\mathrm{N} + {}^{1}_{1}\mathrm{H} \rightarrow {}^{16}_{8}\mathrm{O} + \gamma$

${}^{16}_{8}\mathrm{O} + {}^{1}_{1}\mathrm{H} \rightarrow {}^{17}_{9}\mathrm{F} + \gamma$

${}^{17}_{9}\mathrm{F} \rightarrow {}^{17}_{8}\mathrm{O} + e^+ + \nu_e$

${}^{17}_{8}\mathrm{O} + {}^{1}_{1}\mathrm{H} \rightarrow {}^{14}_{7}\mathrm{N} + {}^{4}_{2}\mathrm{He}$

The energy generation rate depends on temperature has the form

$$\epsilon_{CNO} \approx \epsilon'_{CNO} \rho X X_{CNO} T_6^{19.9} \tag{A.7}$$

where $'_{CNO} = 8.24 \times 10^{-31} Wm^3 kg^{-3}$ is a constant.

When the energy generation rate of the PP Chain reactions ($\epsilon_{pp} \approx \epsilon$) is compared to that of a CNO cycle ($\epsilon_{CNO} \approx \epsilon$), it becomes clear that the CNO strongly depends on temperature i.e $\epsilon_{pp} \propto T^4$ and $\epsilon_{CNO} \propto T^{20}$; this property implies that low intermediate mass stars, that have lower internal temperature are dominated by PP chain reactions, whereas more massive stars with higher surface temperatures convert more hydrogen to helium by CNO cycle than pp chains. Models of stellar evolution theories suggests that, stars with initial mass less than $0.08M_\odot$ never reach central temperatures high enough to ignite hydrogen burning thus they become Brown dwarf stars at the end of their evolution. However for the stars with initial masses above $0.08M_\odot$ but below $0.5M_\odot$ will ignite and burn hydrogen eventually ends as Helium - White Dwarfs. And for stars with initial masses between $0.5M_\odot \leq 8.0M_\odot$ will experience both pp-chains and CNO cycles, these stars do develop the degenerate Carbon-Oxygen (CO) core and end their lives as CO white dwarfs. More massive stars greater than $8M_\odot$ do not even have time to develop CO core, they essentially explode as supernova and these are not stars considered in work. Thus we can make a conclusion that the pressure generated by nuclear processes in the core when the star is in hydrostatic equilibrium, is directly proportional to the internal temperatures but inversely proportional to the initial mass. We are going to investigate this effect by looking at the maximum pressure ($P_{core}$) that an isothermal core must have in-order to support the star in terms of total mass of the core mass ($M_{core}$) and its internal temperature ($T_i$) ;and compare this with the envelope pressure ($P_{env}$) near the core must have ($P_{ic,env}$)

Lets look at what happens when a star is in hydrostatic equilibrium:

As the star starts burning hydrogen, there are few particles bouncing around to provide core's internal pressure ($T_{ic}$); so the core collapses slightly under the weight ($F_g$) of the of the star underlying layers. This compression makes the core denser,therefore an increases its internal temperature as the gravitational potential energy is converted

into kinetic energy. As a result the core's internal pressure ($P_{ic}$) is actually higher than before and pushes the stars outer layers making the radius of the star to slightly increases as well. As the expansion of the outer layers causes the temperature of the star to decrease, gravity takes over again and the whole process is repeated, and the star is in hydrostatic equilibrium. Since this is a slow process stars spend most of their life time on the main sequence burning hydrogen into helium in their cores which provides the outward pressure that is balanced by gravity's inward pull. One can therefore define a main sequence as a core hydrogen burning phase, e.g. the Sun is a main sequence star and has been burning hydrogen for the past 4.5 billion years. In Figure A.3 the motion of a small spherical shell of mass ($dM_r$) is shown for the star that is in hydrostatic equilibrium. If we assume that this layer is located at a distance r from the center, then its motion will depends on the gravitational force ($F_{grav}$) pulling into the central part of the star and the outward force ($dF_{pres}$) that is due change in pressure in side and outside of the star's shell layer of some thickness dr.

We can therefore use Newtons 2nd law to describe the motion of the shell as follows:

$$\sum F_{external\ forces} = dM_r.a = F_{grav} + F_{pres} \tag{A.8}$$

where $dM_r = \rho.A.dr$, A is the surface area of the shell, $\rho$ is the local density that depends on the number density of particles and their masses. For any slab considered here we can safely assume spherical symmetric shells whose area is $4\pi r^2$, this makes

$$\frac{dM_r}{dr} = 4\pi r^2 \rho \tag{A.9}$$

Equation A.9 is called the Mass Conservation Equation since it shows how mass changes with distance if the mass density is known. [4].

[4]This relationship is very important as we shall see under the theory of mass-loss that the intermediate mass star experience at AGB phase covered in Chapter 5

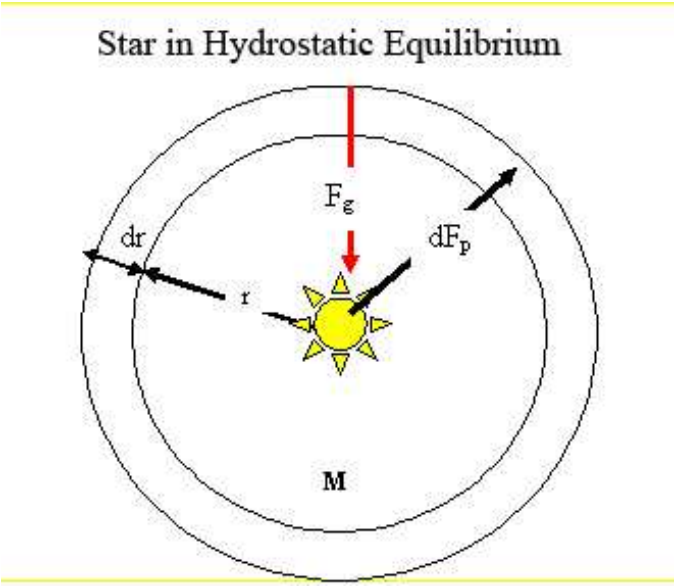


Figure A.3: A star in hydrostatic equilibrium, the gravitational force ($F_{grav}$) (directed towards the center) balances the radiation pressure force ($F_{pres}$) (directed out from the hydrogen burning core). The forces shown apply on a spherically symmetric mass ($dM_r$) with thickness of a star at a distance r from the center.

The gravitational force exerted by the whole star to this layer is

$$F_{grav} = -\frac{GM_r dM_r}{r^2}$$

with $G$ the gravitational constant and $dF_{pres} = AdP$ . At main sequence the star is in static equilibrium so that the acceleration of a shell is zero, thus equation A.8 becomes,

$$\frac{dP}{dr} = -\frac{\mathrm{GM}_r \rho}{r^2} \tag{A.10}$$

break where $'_{CNO} = 8.24 \times 10^{-31} W m^3 kg^{-3}$ is a constant.

Equation A.10 clearly shows that for the star to be in hydrostatic equilibrium, a pressure gradient have to exist to counter balance the gravitational force of collapse. This means that the pressure must decrease with increasing radius; the pressure is higher at the center than it is near the surface. At this stage, the origin of the

pressure comes from two sources, mostly by the gas particles (Hydrogen and Helium molecules) and also by photons generated during the onset of nuclear burning. For any system of either gas particles or photons the pressure can be derived from the momentum that these particles exerts on onto the underlying layers keeping the star in equilibrium. It can be shows that the pressure (P) exerted by particles having momenta between p and p+dp is given by

$$P = \frac{1}{3}\int_0^\infty pvn_p dp \tag{A.11}$$

where $n_p dp$ is some distribution function that represents the number of particles considered in momentum space.

The pressure by gas ($P_g as$) exist as a result the collision amongst gas molecules that get heated up during the collapse gaining more kinetic energy and pressing on the outer layers. Near the core when temperatures are around $10^7 K$ the gas particles are non - relativistic and the momentum of a particle of mass m moving at speed v is $p = mv$.

Therefore we can write the pressure of a gas as

$$P = \frac{1}{3}\int_0^\infty (mv)vn_v dv$$

where $n_v dv$ is the number of particles per unit volume for particles having speed between v and v+dv.

However such gas in also in thermal equilibrium therefore we can use the Maxwell - Boltzmann velocity distribution function to estimate the number of particles per unit volume to get the pressure of a gas. The Maxwell - Boltzmann distribution function depends on the the particle number density (n), the temperature (T) ans well as the mass of each particle, and is given by,

$$\mathrm{n}_v\mathrm{dv} = n\left(\frac{m}{2\pi \mathrm{k}_b T}\right)^{\frac{3}{2}} e^{-\frac{mv^2}{2k_bT}}\ 4\pi v^2 dv \tag{A.12}$$

where $n = \int_0^\infty n_v dv$, and $k_b$ is the Boltzmann constant.

The resulting pressure of a gas after evaluating the integral (see Appendix A) gives the Ideal gas law in terms of the number density and the temperature of a gas as follows

$$P_{gas} = \mathrm{nk}_b T \tag{A.13}$$

It becomes more convenient to represent the the number density in terms of the mass density and the average mass of a gas particle, that is $n = \frac{\rho}{\bar{m}}$. Since stars at this point are mainly made of more hydrogen than any other element, we can express the average mass in terms of the mean molecular weight ($\mu$). That is we seek to express every particle's contribution to the number density that affects the pressure of the gas. That is, $\bar{m} = \mu m_H$ where $m_H$ is the mass of hydrogen.

Thus the ideal gas law in terms of the mean molecular weight and the mass density for an isothermal gas is,

$$P_{gas} = \frac{\rho k_b T}{\mu m_H} \tag{A.14}$$

During Hydrogen burning the gas maybe highly ionized, then the mean molecular weight for a gas containing both nuclei and electrons including hydrogen and helium can be expressed as

$$\frac{1}{\mu_i} \simeq 2X + \frac{3}{4}Y + < \frac{1+z}{A} >_i Z \tag{A.15}$$

here X, Y, and Z are mass fraction of hydrogen, helium and metals respectively. And 1+z represent the number of protons or electrons in a particular type of atom. As a G2 star the sun is a main sequence star with surface composition of X=0.74, Y=0.24 and Z=0.02 meaning $\mu_i$ is 0.62.

The radiation pressure comes from the momentum of photons,

$$p_\gamma = \frac{h\nu}{c}$$

where $\nu$ and c are the frequency and the speed of light. Then equation A.11 becomes

$$P_{rad} = \frac{1}{3}\int_0^\infty h\nu n_\nu d\nu$$

where $n_\nu d\nu$ is the number density of photons having the energy between $\nu$ ans $\nu + d\nu, h\nu$ is the energy of a photon. The energy density distribution function if found by assuming that stars emits as blackbody whose wavelength distribution is given by equation A.2. Solving for the radiation pressure results into

$$P_{rad} = \frac{1}{3}aT^4 \tag{A.16}$$

where $a = 4\frac{\sigma}{c}$, $\sigma$ being the Stefan-Boltzmann constant.
The total pressure of the system can be approximated by combining pressure by gas and by radiation as an

$$P = \frac{\rho k_b T}{\mu m_H} + \frac{1}{3}aT^4 \tag{A.17}$$

For the stars to maintain their luminosities at main sequence, that is 'keep shining' they must get energy supplies from either nuclear burning reactions that produces nuclear energy or from the gravitational potential energy ($U_g$) that occurs during the collapse. The gravitational potential energy for our model star shown in figure A.18 is given by,

$$\mathrm{U}_g = -\int \frac{GM_r dM_r}{r}. \tag{A.18}$$

The gravitational potential energy increases with decreasing distance from the center of the star, meaning that during the collapse some it must be converted to kinetic energy or or other forms like radiation energy. If a star can convert some of this potential energy into heat and radiate some away, then the star will be able to sustain itself and shine for a long time. When a star is in static equilibrium for any gravitationally bound system, the energy the mechanical energy transport mechanism can be described by using the Viral theorem. This theorem tells us how the potential energy gets converted into kinetic energy. The viral theorem states that half of the gravitational potential energy must go to kinetic energy in such a way that the total mechanical energy is always half the potential energy i.e.

$$2K + U = 0 \tag{A.19}$$

where $K$ and $U$ represent the kinetic as well as the potential of a system in equilibrium. This means that for a star in the main sequence one half of the star's potential energy goes into thermal energy that heats the star and the other half gets radiated away. Using the viral we can see that if twice the kinetic energy exceeds the value of the the gravitational potential energy the star must expand because the force due to the gas pressure ($dF_{pres}$) will dominate the force of gravity ($F_{grav}$); otherwise if the internal thermal energy is low the star must collapse. The thermal energy can found be from the ideal gas condition $\mathrm{K} = \frac{3}{2}P_{gas}V$ where V is the volume of gas. The number density (n) can be written in terms of the total number particles(N) and the volume i.e. $\mathrm{n} = \frac{\mathrm{N}}{V}$ with $N = \frac{M}{\mu m_H}$, then the thermal energy is

$$\mathrm{K} = \frac{3Mk_bT}{2\mu m_H} \tag{A.20}$$

Having developed the condition for a star to be at static equilibrium eq. and the energy transport mechanism through the viral theorem, we are now in a position

to use these conditions to find out how the stars supports themselves while burning hydrogen into helium in the core (near) at main sequence. In this case we would like to investigate how the core supports the star,by looking at the pressure that the core exerts at the surface of the star inorder to balance the pressure that the envelope suppresses it.

From our model star in Figure A.3, lets define the mass and the radius of the star to be $M_{star} = M$ and $R_{star} = R$. We are going to assume that the core is burning hydrogen at constant temperature, $T_{iso}$ with the mass of the core given by $M_{ic}$ and the core has radius $R_c$. The mass of the whole envelope surrounding the core is $M_{env}$ at radius R of the star.

$$M_{star} = M_{ic} + M_{env} = M$$

but since

$$M_{env} >> M_{core}$$

then

$$M_{star} \approx M_{env}$$

this is because $M_{ic} << M_{env}$. (the the core mass is smaller than the envelope mass). See Figure A.4 below. We can now find the pressure at the surface of the core that supports the star from the underlying crush of the force of gravity by the envelope. When we combine the hydrostatic equilibrium equation with mass conservation equation we get,

$$4\pi r^3 \frac{dP}{dM_r} = -\frac{GM_r}{r}$$

Since

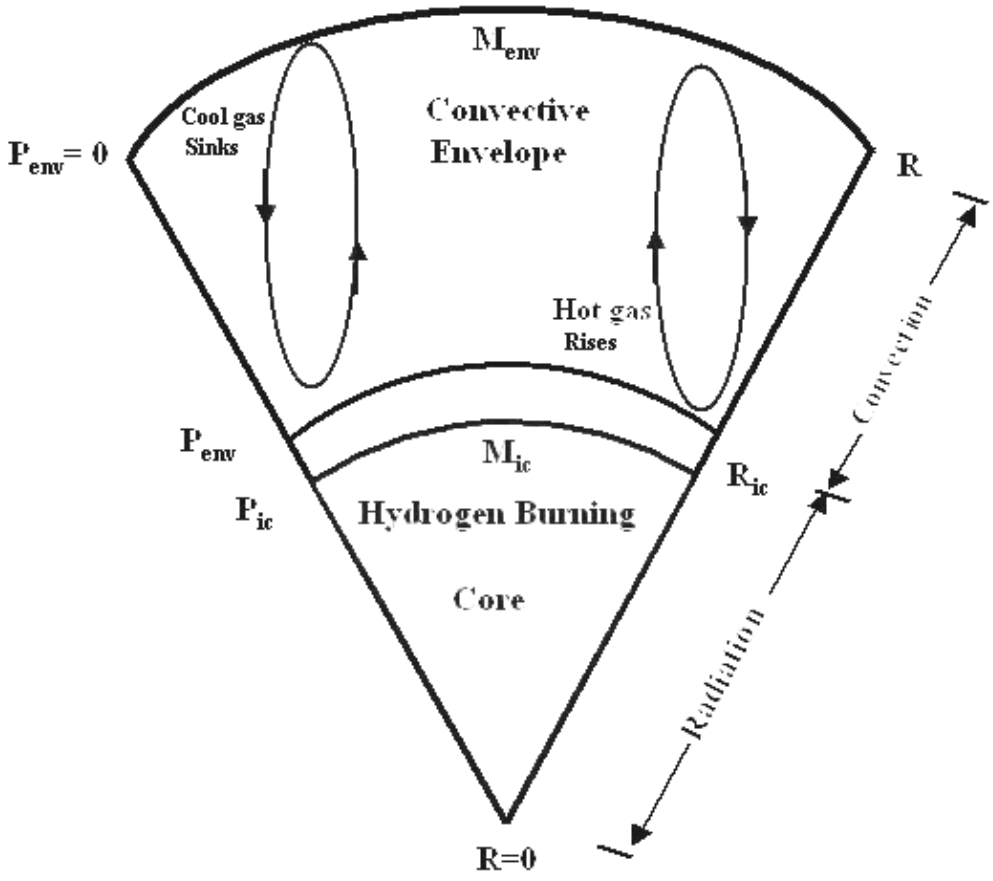


Figure A.4: A star in hydrostatic equilibrium, showing the pressure($P_c$) supporting the core ($P_c$) and the envelope pressure compressing the core ($P_{env}$) are shown. The core is burning hydrogen at a constant temperature $T_{iso}$, such that any changes in the pressure as a function of radius is compensated by changes in gravity and the density of the core.

$$4\pi r^3 \frac{dP}{dM_r} = \frac{d(4\pi r^3 P)}{dM_r} - 3\frac{P}{\rho}$$

we can integrate over mass, from the center where r = 0, $M_r = 0$, to the envelope's surface where $r = R_c$, $M_r = M_{core}$ to get

$$\int_0^{M_{ic}} \frac{d(4\pi r^3 P)}{dM_r} dM_r - \int_0^{Mc} 3\frac{P}{\rho} dM_r = -\int_0^{Mc} \frac{GM_r}{r}$$

the result of the integrands is

$$4\pi R_c^3 P_{ic} - 2K_{ic} = U_{ic} \tag{A.21}$$

where $P_{ic}$ is the pressure of a gas at the surface of the isothermal core. $K_{ic}$ and $U_{ic}$ are thermal kinetic and potential energy of the isothermal core respectively.

The kinetic energy is given by equation A.20,

$$K_{ic} = \frac{3Mk_bT_{iso}}{2\mu_c m_H}$$

where $T_{iso}$ is the isothermal temperature and $\mu_c$ is the mean molecular weight of the core.

To estimate the gravitational potential energy we shall assume that inside the core where r = $R_c$ the density is a constant at

$$\rho_c \approx \frac{3M_{ic}}{4\pi R_{ic}^3},$$

meaning

$$M_r \approx \frac{4}{3}\pi r^3 \rho = M_{ic}\left(\frac{r}{R_{ic}}\right)^3,$$

Therefore gravitational potential energy is $U_c \approx -\frac{3}{5}\frac{GM_c^2}{R_c}$ assuming the mass density is a constant inside the star. Now we can solve for the pressure at the surface of the isothermal core that supports the star, using the estimated $U_{ic}$ and $K_{ic}$ onto equation A.21

$$P_c = \frac{3}{4\pi R_c^3}\left(\frac{M_{ic}k_bT_{iso}}{\mu_c m_H} - \frac{1}{5}\frac{GM_c^2}{R_c}\right) \tag{A.22}$$

Equation A.22 tell us that there is a competition between the thermal energy (first term) and the gravitational potential energy (second term). The interpretation is that at the surface of the isothermal core at temperature $T_{iso}$ and a core of radius

($R_c$), the thermal energy trying to increases the surface pressure, whereas at the same time the gravitational potential energy tends to decreases the surface pressure as the mass of the core increases. So this means that for any change in $\mu$ or T in the kinetic energy it must be compensated by the change in the core mass $M_{ic}$ and $R_c$ such that $P_c$ stays positive (or rather greater than zero). Therefore one can project that there exist a maximum pressure ($P_{c,max}$) that the isothermal core can support the overlying envelope as the mass grows, if the pressure of the core falls below this maximum pressure then the core will collapse. So we maximize $P_c$ with respect to $M_{ic}$ keeping $T_{iso}$ and $\mu_c$ constants, to arrive at the maximum pressure ($P_{c,max}$) that the core can support at an isothermal temperature ($T_{iso}$)

$$P_{c,max} = \frac{375}{64\pi G^3 M_{ic}^2} \left( \frac{k_b}{T_{iso}} \mu_c m_H \right)^4 \tag{A.23}$$

This means that as the mass of the core grows the maximum pressure at the surface decreases as hydrogen burning occurs at constant temperature, this implies that at some point the core will grow to a certain mass at which the thermal pressure can no longer support the overlying envelope, at that point the core will collapse or the star must either find a way to support it self. Another important feature of $P_{core,max}$ is that for those stars that have larger core mass at the onset of their hydrogen burning, their maximum surface pressures are very low so they collapse faster.

We also need to know what is the envelope pressure ($P_{env}$) exerted by the star's envelope near the surface of the core that causes the collapse, and what physical parameters does this pressure depends on. One can expect that this pressure must depend to the total mass of the star because the whole envelope compresses the core and also on the composition of the envelope.

To evaluate the envelope pressure, we assert that at the pressure at the surface of the star must have decreased to almost zero ($P_{surface} \approx 0$) when the mass is $M_{star}$ and the radius is $R_{star}$. At the region near the core where the mass and the radius of the

star is $R_{core}$ and $M_{ic}$ , the pressure is $P_{env}$ (this pressure is higher than the surface because the pressure must increases as the radius decreases $R_{core} << R_{star}$). Then we can find the envelope pressure at the interface by using the condition of static equilibrium A.10,

$$\mathrm{dP} = -\frac{GM_r dM_r}{4\pi r^4}$$

Thus

$$P_{env} = \int_{P_{surf}}^{P_{env}} dP = -\int_{M}^{M_{core}} \frac{GM_r dM_r}{4\pi r^4}$$

$$P_{env} \approx \frac{GM_{star}^2 - M_{core}^2}{4\pi R_{star}^4}$$

we can assume that the density of a gas is constant

$$\rho_{env} \approx \frac{3M_{star}}{4\pi R_{star}^3}$$

and by using the fact that the envelope contains gas, therefore the pressure by the gas is given by equation A.23 in this form,

$$P_{gas} = \frac{\rho_{env} k_b T_{iso}}{\mu_{env} m_H},$$

where $\mu_{env}$ is the mean molecular weight of the hydrogen rich envelope.

$$P_{gas} = \frac{3M_{star} k_b T_{iso}}{4\pi R_{star}^3 \mu_{env} m_H}$$

Then we can eliminate the radius of a star from the two pressure equations and then express the pressure exerted by the envelope to the isothermal core in terms of isothermal temperature ($T_{iso}$), the mass of the star as well as the mean molecular weight of the envelope.

$$P_{env} = \frac{81}{4\pi G^3 M_{star}^2} \Big( \frac{k_b T_{iso}}{\mu_{env} m_H} \Big)^4 \tag{A.24}$$

One can immediately notice the similarities of pressure equations A.22 and A.24 both in terms of mass, temperature and chemical composition(the mean molecular weight in that region). Then difference between these pressure equations rely on the masses and composition; i.e. the core mass is dominated by helium that result from hydrogen burning, while the envelope represent essentially the total mass of the star that is dominated by more hydrogen than helium. These results agrees very well with the Voigt - Russell theorem that asserts that mass and composition dictates the evolution of the star since any changes in the pressures from mass and composition will influence the overall behavior of the star.

### A.1.1 Evolution on the main sequence of intermediate mass stars

How the stars evolve at main sequence depends on the balance between gravitational collapse of the material onto the core changing its composition (hydrogen gets converted into helium), increasing its mass and the pressure out that results from the chemical reactions. What models predict is that as hydrogen is convected into helium, the mean molecular weight ($\mu$) of the core increases (refer to equation A.15). At a constant density and temperature , the gas pressure must decrease as predicted by ideal gas law (see A.14. This means the core must be compressed as can be seen on equation A.23 for the core's surface pressure that supports the star. The gravitational potential energy increases in favor of value of $P_c$ to decrease. Compression makes the core density to increase as the mass of the core grow, which triggers the release of gravitational energy. By viral, half of the gravitational energy released goes into heating the core raising its temperature from the increase in thermal energy of

the core. And the other half of the potential energy is radiated away, so the core is radiative. This means that once hydrogen burning is established or initiated on those regions hot enough to undergo nuclear reactions; the increase in temperature and the density will also cause the mass fraction of hydrogen to decreased. And the process starts over again as the star is in static equilibrium under pressure and gravity.

To elaborate more, lets assume that at main sequence the energy generation rates by the core are constant and given by chemical reactions discussed in section A.1. The energy generation rates of pp-chain and CNO cycle are : $\rho \mathrm{X}^2 T^4$ for pp chain and $\rho$X $\mathrm{X}_{CNO} T^{20}$ for CNO; for both cases any increase in $\rho$ and T makes in the core more that offset the decrease in mass hydrogen mass fraction (X). The decrease in X is more effective for the CNO cycle because T is high core temperature dependence. So as the core contracts the half to the gravitational energy radiated is absorbed by outer layers making the surface temperature and the luminosity increases as energy is radiated out and the total radius of the star slowly increases as well; the star is expanding as the core is subsequently expanding while the core is compressed. Therefore over time, the surface values are increasing, temperature, the luminosity and the the radius increases are the star is evolving off the zero age main sequence. This is shown in figure A.5 for a model of our sun.

In this model the composition of a gas is given by the mass fraction of hydrogen (X = 0.74), helium (Y=0.24) and metals (Z=0.02) based on the observations of the Sun. The sun has become larger and brighter with surface temperature increase 5777K from 5600K it had as zero age main sequence, and the luminosity and radius increasing to about 48% and 15% respectively. What this model also predict is that in the next 4. billion years the sun's surface temperature will increase by about 3K with the radius swelling to about 15% from its present day value with the luminosity increasing by about 35%.

As the star evolves at main sequence, hydrogen burning continues to deposit

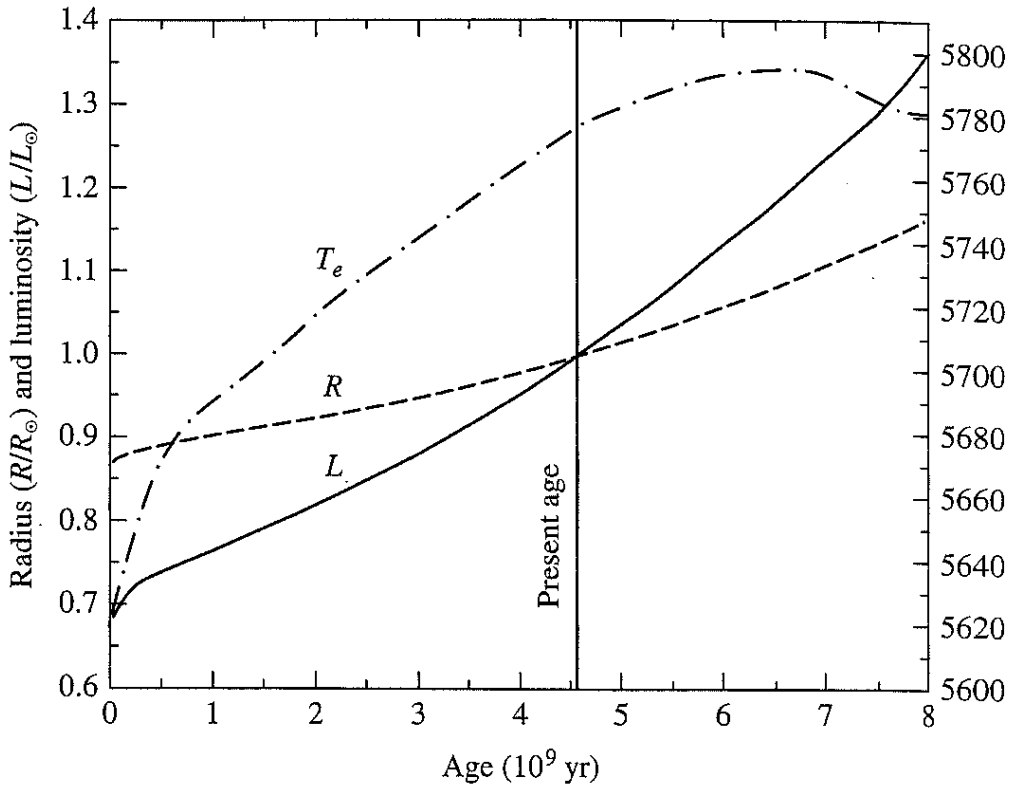


Figure A.5: The evolution of the sun as from its birth to the present, age (4.5 billion years). The sun is an intermediate mass star that has since changed its luminosity (L), surface temperature ($T_e$) and radius(R) because of changes in its internal composition. As a result, this star has become larger, brighter and more luminous than before as it evolves as a main sequence star. The radius and luminosity are scaled to the present values.

He onto the non burning helium core, so the mass of the core grows. There is a maximum mass that the isothermal core can grow to while it can support the star from ultimate collapses. This mass can be found by considering the point when the maximum pressure of the core that supports the star equals the maximum pressure of the envelope that compresses the star. We can infer that this mass should depend on the mass of the star and also on the composition of the core and that of the envelope.

### A.1.2 Shönberg - Chandrasekhar limit

Shönberg and Chandrasekhar in 1942 [117] made a detail calculation on what is the critical mass that is required by the core in order to support the envelope before the star can collapse at main sequence based on relations (equations A.23 and A.24). Their calculations showed that, for the star to maintain its equilibrium status at main sequence, that is inorder for the maximum pressure by the isothermal core ($P_{c,max}$) to balance the maximum pressure of the envelope ($P_{env,max}$, the mass of the core has to be related to the mass of the star by,

$$\frac{M_{ic}}{M} = 0.37 \left( \frac{\mu_{env}}{\mu_c} \right)^2 \tag{A.25}$$

What is noticeable about equation A.25 is that it is the mass and composition (both at envelope and core) that dictates the evolution of the star, instead of the energies and pressure relations that give rise to this limit. This means the pressure and the energy generation inside the star will change because the star is evolving, as a result the mass and the composition changes as well. If the core grows beyond the Sh$\acute{}$onberg - Chandrasekhar limit, the star will collapse ending the core hydrogen burning, and as a result the star will begin its short journey off the main sequence onto the subgiant branch as continued in section A.2.1. The collapsing core causes energy to be radiated out as the star tries to maintain its balance. The energy transport out of the star may also be dominated by another transport mechanism called convection, so basically it depends which process dominates the transport mechanism. Convection is more efficient than radiation on the outer layers of the star because its mechanism requires the motion of hot material from core and the in-fall of cold material on the outer layers constituting convection currents. So we need to understand what are the conditions in a star that makes convection to dominate over radiation as photons stream out of the core.

### A.1.3 Convective Envelope of Intermediate mass stars at main sequence

At main sequence the star can develop a convective core, this is because, as the core is hot from burning hydrogen into helium, the hot photons that result from H-burning carry energy away by radiation from the core to the outer layers beneath the core. As hot material rises the colder material will sink reaching inside the core. The process of convection is very similar to the cooking a soup, where heat generated by the fire causes food particles near the fire to rise and cool while top food sinks to gain heat, resulting in a convective transport of energy out as steam. For intermediate mass stars the core is surrounded by a radiative layer because energy is carried out by radiation at the core, and what follows is a convective envelope that contains hydrogen and helium gas. These processes are shown in Figure A.24, for a model of an intermediate mass star's interior structure in which nuclear reactions occurs at the core, and radiation with convective layers are indicated.

The conditions that radiation energy transport mechanism dominate over convection to transport energy out depends on how the temperature gradients of these two processes compares. The temperature gradients depends on what are the interior conditions (like density, pressure etc.) that the expanding material is subjected as the star changes in composition and mass. For radiation to dominate the temperature gradient is given by (the derivation is done in appendix B),

$$\frac{\mathrm{dT}}{dr}_{rad} = -\frac{3}{4ac}\frac{\kappa\rho}{T^3}\frac{L_r}{4\pi r^2} \tag{A.26}$$

where $\kappa$ is the opacity, that is the cross section per unit mass ($m^2 g^{-1}$) of the absorbing material,$\kappa\rho$ is extinction coefficient per unit length. To make this radiation gradient higher (less negative), the opacity must decrease or the temperature must increase, or the luminosity decrease. For convection to dominate the transport, the gas reaching the surface must be adiabatic, the adiabatic temperature gradient is given by,

$$\left(\frac{dT}{dr}\right)_{conv} = -\left(1 - \frac{1}{\gamma}\right)\frac{\mu m_H}{k_b}\frac{GM_r}{r^2} \tag{A.27}$$

where $\gamma = \frac{C_v}{C_p}$ is the ratio of the specific heats for adiabatic expansion. Clearly $\gamma$ have to be small meaning low $C_p$ and the gravitational mass ($M_r$) must be large for the convective gradient to be steeper (more negative).

For the development of the convective shell making convection to dominate the energy transport,

$$\frac{\mathrm{dT}}{dr}_{conv} < \left(\frac{\mathrm{dT}}{dr}\right)_{rad} \tag{A.28}$$

have to be met.

This means that 1) the stellar opacity must be large to make radiation gradient term to be low, 2) the region of ionization has to exist where the specific heat $C_p$ is large and the surface temperature must be low to make radiation term low, and 3) the temperature of the nuclear generation rate must be high to make the radiative flux to increase the luminosity and a steeper temperature dependence e.g.

$$\frac{d\epsilon_{pp}}{dr} \approx T^3\frac{dT}{dr}\text{and}\frac{d\epsilon_{pp}}{dr} \approx T^{19}\frac{dT}{dr}$$

Higher mass stars are strongly dominated by CNO cycle in burning hydrogen so they are more likely to develop convective cores because their core temperatures are high. The convective zone in high mass star may extend far near the convective zone making whole star star envelope to be nearly homogeneous in composition. Basically both convective and radiative layers shown in Figure A.2 are mixed more efficiently in high mass stars than in lower mass ones, because of high burning internal temperatures of the core and also their larger convective envelopes they have[5]. The

[5]The whole convective envelope in larger mass stars is involved in compressing the core than in the case of low mass stars, therefore the radiative zone is not well established in higher mass stars because of the extension of the convective envelop

time scale for convection processes to occur in high mass stars is smaller than the nuclear time scale.

Once the star has reached steady core hydrogen burning, the mass of the core will still be growing because more helium is added to the core, hence its density increases. The effect of density increase causes the gravitational collapse of the underlying layers near the core. The gravitational potential energy is released, half of it goes into heating the core as energy supply for nuclear burning and the other half is radiated away at or near the core where radiation dominates convection. The energy that leaves the core is absorbed by the envelope with causes it to expand. The expansion of the envelope to makes the luminosity to increase because of the areal increase (star is slowly getting bigger) while the surface temperature drops slightly as the hot gas as reaches outer cooler areas where convection dominates energy transport. Then over time the star will evolve on the main sequence with subsequently increasing luminosity and a decrease in the star's overall effective temperature. Over a long time the star will run out of hydrogen in the core causing it to leave main sequence towards the red giant branch.

### A.1.4 Electron degeneracy of CO core of an intermediate mass star

When the temperature is low and the density is high in the core such that both radiation pressure and gas pressure become insufficient to provide the pressure necessary to prevent the CO core from collapsing, the core electrons can order themselves to provide support. The electrons must first fill the lowest unoccupied states and then successively occupy all higher energy states such that no two electron occupy the same state. Electrons, neutrons and protons belong onto a group of particles called Fermions that obeys Pauli's exclusion principle. Pauli's exclusion principle asserts that no two fermions can have the same set of quantum numbers. A fermion gas

is considered degenerate if all of the lowest possible states are filled and non of the highest state is occupied, as the temperature is lowered to zero Kelvin. The maximum lowest energy that the electron can occupy while in complete degenerate state is called Fermi energy level. Therefore the electrons will pack themselves such some of them can occupy states that are higher than the Fermi level and provide pressure that prevents collapse.

The Fermi energy depends on the number density ($n_e$) of electrons present in the core;. To see this lets look at the Fermi energy and the electron degenerate pressure as a function of the number density.

The total kinetic energy for electron can be written as $E = \frac{1}{2}mv^2 = \frac{p^2}{2m}$, where p = mv is the momentum of the electron of mass (m) with velocity v.

According to the Heisenberg uncertainty principle any change in position $\delta x$ and the change in momentum ($\delta p$) should satisfy $\delta x.\delta p \simeq \hbar$ then the energy is $E_{Fermi} \simeq \frac{p^2}{2m\delta x^2}$.

lets assume that the electron is in a box of length L contains N electrons, such that the number density in a box is given by $n_e \equiv \frac{N}{L}$ and suppose $\delta x^3 \simeq n_e^{\frac{1}{3}}$ is a limiting case for complete degeneracy. Assuming that in 3-D momentum space all momenta are the same, then

$p^2 = 3p_i^2, i = (x, y, z)$ and $p_i \simeq \frac{\hbar}{\delta x}$

$E_{Fermi} \simeq \frac{3\hbar^2}{2m}(n_e)^{\frac{2}{3}}$

Clearly the Fermi energy depends on the number density on electrons, and for a fully ionized gas the electron density depends on the number nucleons (**A**), the number of protons (**Z**) and the total density ($\rho$) of the CO core.

$n_e \equiv \frac{N}{L} = \left(\frac{\mathbf{Z}}{\mathbf{A}}\right)\frac{\rho}{m_H}$

$$\mathrm{E}_{Fermi} \simeq \frac{3\hbar^2}{2m}\left(\frac{\mathbf{Z}}{\mathbf{A}}\frac{\rho}{m_H}\right)^{\frac{2}{3}} \tag{A.29}$$

The condition for degeneracy is that the kinetic energy of electrons at some core

temperature T be less than the Fermi energy $\frac{3k_b}{2} < E_{Fermi}$; this will happen when

$$\frac{T}{\rho}^{\frac{2}{3}} < D \tag{A.30}$$

where D is some constant that depends on the composition (**Z**, **A**) of the gas.

The electron degenerate pressure also depends on the number density of electrons. We can use equation 2.. for the pressure of a fermion gas as follows,

$P_{gas} = \frac{1}{n}_e pv$ $v = \frac{p}{m} = \frac{\sqrt{3}\hbar n_e^{\frac{1}{3}}}{m_e}$ thus $P_{degen} \simeq \frac{\hbar^2}{m_e} n_e^{\frac{5}{3}}$

The electron degeneracy pressure in terms of composition and density becomes,

$$P_{degen} \simeq \frac{\hbar^2}{m_e}\left(\frac{\mathbf{Z}}{\mathbf{A}}\frac{\rho}{m_H}\right)^{\frac{5}{3}} \tag{A.31}$$

## A.2 Evolution off main sequence

The main sequence evolution ends when the core runs out of hydrogen, core hydrogen burning get exhausted. The star must rearrange its structure inorder to accommodate new changes. The star layers may look like the one shown on Figure A.2 for a typical $5M_\odot$ star.

What remains after the core hydrogen burning is a non - burning Helium core (He-core) ash and a hydrogen shell. The He-core may remain isothermal for sometime, however hydrogen burning continues to deposits more helium into the core, increasing its mass. Since the mass of the He - core is increasing, the density of the core also increases. The density is the only means of support to the star since there is no energy generated by non-burning He-core. The temperature inside the core is still very low to ignite helium - fusion. A star finds itself to be at position 4 on the H-R diagram, as shown for both $1M_\odot$ mass star (solar model) and 5 $M_\odot$ star Figure 2.2. The sun in this model is at position 2 in the top panel.

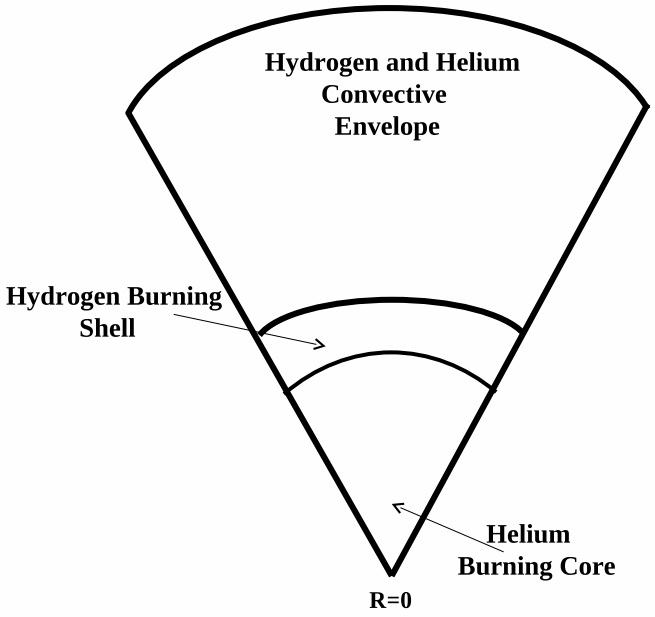


Figure A.6: A subgiant branch star after hydrogen core exhaustion. The prominent features of this subgiant star are: the He-core is surrounded by a hydrogen burning shell, all under a (He and H - rich) convective envelope

As the core grows in mass it also begins to contract because the pressure at the surface of the core gets low. Contraction causes the core to release gravitational energy that heats the shell to higher temperatures. In the case of low intermediate mass stars like the sun, core contraction increases the temperature in the shell such that hydrogen burning occurs at even higher rates so the shell produces more energy than what it actually produced during core hydrogen burning. The effect of the energy released by the shell is that it slows expansion of the envelope, this causes the surface temperature to decrease slightly while the luminosity continues to increase. The result of this is a steeper increase of the evolutionary track between stages 4 and 5 as the star moves toward the subgiant phase. In the case of high mass stars when the core begin to contract, the whole star is involved in contraction. Even though there is a hydrogen burning shell its effect of depositing energy is minimal in decreasing expansion. Since the whole star is involved in the contraction the

whole star to decrease in size. When the radius decreases the luminosity and the temperature increases. Thus the evolutionary track of a higher mass star move to the left towards the bluer region as the star approached the sub giant phase at position 5, (see figure 2.2 panel B stages 4 to 5).

In side the star the chemical composition has changed, hydrogen gets depleted near the core. The abundances of hydrogen as the mass of the core grows is shown in Figure 2.2. The inserts (a) shown in figure 2.2., indicates that as the mass of the core grows, hydrogen abundances gets lower as the star leaves the main sequence at position 4.

### A.2.1 Subgiant phase

As the stars enters the the subgiant phase steady hydrogen shell burning has been established, and the core is still nearly isothermal. Shell hydrogen burning continues to deposit more helium to the core. The mass of the core grows until the Shönberg - Chandrasekhar limit is reached (point 5 on 2.2). The core shrinks more and become more dense and this releases the gravitational potential energy. The gravitational energy produced by the collapsing core causes the star to expand and cools, hence evolution at subgiant phase is goes towards the red on the HR. The hydrogen burning shell heats the star internal towards the core and also external in which case the outer convective envelope receive energy as well. The energy generated by the hydrogen burning shell that heats the surrounding envelope causes the surface luminosity to increase at almost constant temperature as the star approaches the the tip of the red giant phase at stage 8.

### A.2.2 Red Giant phase

As the star enters the red giant phase, the core continues to shrink while hydrogen burning occurs at a thinner shell called hydrogen shell layer. The hydrogen shell deposits more energy to the envelope and also into the core raising the core's internal temperature. As a result the core heats up which causes the surface layers to expand and cool as the envelope absorbs energy coming from the core. The cooling of the expanding envelope with the surface temperature decreasing makes the outer layers to be optically thin, the hot gas reaching the outer zones is ionized mostly with hydrogen ions ($H^-$) that get deposited near the surface making the photospheric opacity to increase. The gas in the outer zone become adiabatic with the temperature gradient of the gas exceeding the radiation gradients as imposed by equation A.28. This makes the star to develop a convective envelope near the surface. The surface luminosity starts to increase because more more energy is deposited to the envelope by the hydrogen burning shell and the star is expanding, the star climbs up the red giant phase increasing surface luminosity. As the star climbs up the red giant phase the convective zone also deepens until it penetrates deep into the hydrogen burning layer where nuclear reactions (s-process element production) occurs. When the convection zone meets the this hot region the processed material from nuclear reactions get dredged up into the surface.

The material that is rich in $^4$He and the products of CNO cycle like $^{14}$N, $^{13}$C, $^{17}$O eventually mixed into the surface by convection currents because of the First Dredge-up. Therefore the surface abundances of the dredged up elements show an increase, while the ratios of stable atmospheric elements like $^{12}$C and $^{14}$N shows a decline. The first dredge-up occurs at stage 8 in Figure 2.2, and the insert (c) shows the development of the convective envelope. The diagram showing the dredge up zone is shown below in Figure A.2.2

The changes in surface composition as a result of the first dredge up depends on

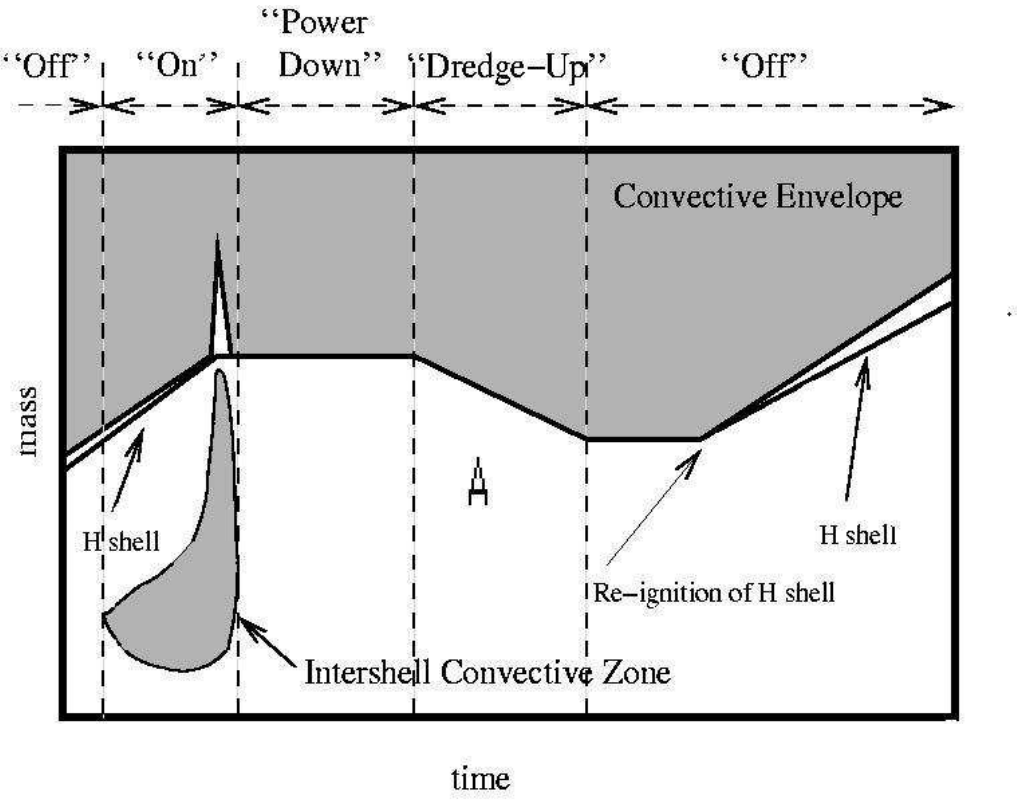


Figure A.7: Convective zone boundary showing the intershell during dredge-up. The Convective currents (by the convective envelop) pass the H-shell reaching the He-burning shell and forms the intershell convective zone (ISZ); this occurs during the maximum He-luminosity peak of a thermal pulse ('power on'). Dredge-up occurs at (**at A**), where a deeper convective envelop engulfs the ISCZ that is rich in He-shell products (e.g. $^{12}$C, $^{4}$He ).

the mass and the composition of the star. Observations of surface abundance changes for stars of about 2.5 $M_{\odot}$ have been reported in these papers Their result shows that the ratios of $^{12}$C/$^{13}$C decreases from 90 to 20, $^{12}$C/$^{14}$N decrease by 2.5, $^{16}$O / $^{18}$O increase by 600.

As the star ascends up the red giant phase, the luminosity is increasing. The star's luminosity mainly comes from the hydrogen burning shell. Because hydrogen burning still deposits helium into the core, the core continues to contract and heat. However since the temperature of the core is isothermal, the only way that the core

can cool itself from contraction is by releasing neutrinos. The cooling from neutrino emission leaves the core 's outer regions cooler than the central regions. As a result of the temperature difference, the core develops a negative temperature gradient near the core called temperature inversion. (as shown in the insert (d) in Figure 2.2).

So the neutrino emission helps in the cooling of the growing core that is increasing in density. The increase in density of the core forces the temperatures around the core to increase irrespective of the neutrino cooling. As a result, when the temperatures around the core reaches about $10^8$ the hot shell around the core ignites the core lifting its temperature inversion and the areas surrounding the core settle onto a steady burning Helium.

Low intermediate mass stars can develop the electron degenerate core first during the RGB phase, this means that in these stars, the core is supported by electron degenerate pressure from collapsing because of its increase in density that causes contraction. When the surface layers of the core reaches He-burning temperatures, more energy goes into lifting electron degeneracy before it gets added to the core. When this happens the core ignites and begin to burn helium in the core. The ignition is called Helium Core Flash, with luminosity increasing to as high as $10^{11}L_{\odot}$ in a few secs. Immediately after ignition, the now helium burning core expands and pushes the hydrogen burning shell out. This expansion of the H-shell makes the total surface luminosity of the star to decrease sharply because the stars luminosity is still coming from the hydrogen burning in the shell.

As a result, when the hydrogen shell is cooling with a decreasing luminosity, the total luminosity of the star also decreases. Even though the core is expanding, the envelope is contracting after the onset of of helium burning, so whole star is actually shrinking making surface radius to decrease. The decrease in surface radius makes the surface temperature to increase , so the evolution of the luminosity and temperature declines from stage 9 until the star enters the Horizontal branch at stage 10. Notice

that the decline in temperature means it is increasing, while the luminosity is actually deceasing.

### A.2.3 Horizontal Branch Stars and Helium burning

The star now is burning Helium at the core, the core has stops expanding and start to grow in mass because of helium burning. When the star burns helium, three helium nuclei are fused to form carbon by a process known as Triple Alpha process (3-$\alpha$). If the temperature is high, the existing carbon can further react with helium to form oxygen. Therefore as the star enters the Horizontal branch burning helium, the resulting core is rich in carbon and oxygen (C-O core).

The triple alpha process occurs when the temperature of the core reaches about 10 million K, and the core begins to burn helium into carbon as shown by the following nuclear reactions.

$^4_2\mathrm{He} + {}^4_2\mathrm{He} \rightarrow {}^8_4\mathrm{Be}$

$^8_4\mathrm{Be} + {}^4_2\mathrm{He} \rightarrow {}^{12}_6\mathrm{C} + \gamma,$

The energy production rate for the triple alpha process is

$$\epsilon_{3\alpha} = \epsilon'_{0,3\alpha}\rho^2 \mathrm{Y}^3 f_{3\alpha} T_8^{41} W k g_1,$$

where $T_8 = T/10^8$, and $\mathrm{f}_{3\alpha}$ is the screening factor for the triple alpha process. The $T^{41}$ in the energy generation rates indicates that the triple alpha process requires high temperatures to occur. For those massive that can develop higher He - burning temperatures (to about 600 million K), carbon atoms can react to produce high elements like sodium(Na), Neon (Ne) in the core.

$$
{}^{12}_{6}\mathrm{C} + {}^{12}_{6}\mathrm{C} \rightarrow \begin{cases} {}^{16}_{8}\mathrm{O} + 2{}^{4}_{2}\mathrm{He} \\ {}^{20}_{10}\mathrm{Ne} + {}^{4}_{2}\mathrm{He} \\ {}^{23}_{11}\mathrm{Na} + p^{+} \\ {}^{23}_{12}\mathrm{Mg} + n \\ {}^{24}_{12}\mathrm{Mg} + \gamma \end{cases}
$$

If the temperature of the core is higher to about $10^{9}K$ the, oxygen can also burn to form Mg, Si, P and S by these reaction.

$$
{}^{16}_{8}\mathrm{O} + {}^{16}_{8}\mathrm{O} \rightarrow \begin{cases} {}^{24}_{12}\mathrm{Mg} + 2{}^{4}_{2}\mathrm{He} \\ {}^{28}_{14}\mathrm{Si} + {}^{4}_{2}\mathrm{He} \\ {}^{31}_{15}P + \mathrm{P} + p^{+} \\ {}^{31}_{16}\mathrm{S} + n \\ {}^{32}_{16}\mathrm{S} + \gamma \end{cases}
$$

For intermediate stars helium burning occurs in a convective core that is surrounded by a thin dormant hydrogen shell. The core becomes convective because of the high temperature dependence of the triple alpha processes. This is because when the star evolves down to the horizontal branch, the hot expanding core meets convective requirements imposed by equation A.26. The density and the temperature of the core are increasing as Helium burning continues. Just like as it was in the main sequence, the stars at Horizontal branch are in hydrostatic equilibrium by burning helium. Helium burning is dominating the luminosity of the star ant horizontal branch, the surface temperature continues to increase because of the whole star still contracting while getting very hot and dense at the center. The star quickly transcends to stage 8.

When the star gets to stage 8 leaving the horizontal branch the density and temperatures has risen so high that the core begins to contract again. Contracting core

releases more gravitational potential energy that makes the whole envelope to expand an cool which in-turn makes the surface temperature to decreases. The luminosity is still gradually increasing because most of the stars luminosity comes from helium burning layer around the CO core. Contraction has made the core so hot such that it is possible for He- burning to occur around the core in shell. The core gets hotter and denser and burns more helium at higher until all of its helium runs out. This occurs at stage 14 on the HR diagram. In the horizontal branch, helium burning is very shorter than main sequence hydrogen burning, it can last up to 100 million years.

Following helium exhaustion and core contraction, the surface luminosity continues to increase while the surface temperature is decreasing. As a result the star begins to climb again the red giant phase for the second time. The luminosity comes from the helium burning shell and the hydrogen burning shells, the CO-core in of an intermediate mass star is becoming degenerate once more as a means of support towards gravitational collapse as it occurred at the tip of RGB. Now the star is approaching the new stage called Early Asymptotic Giant branch.

The consequence of stopping helium burning is that the core can no longer support itself by burning helium, the temperature is becoming constant while the density of the core is growing. At constant temperature and increasing density, the pressure at the surface of the core that supports the star gets weaker under gravity ($P_{ic}$ decrease in equation A.22 at constant T with $\rho$ increasing). The core contracts again because shell helium burning in the helium shell is still continuing to deposit more carbon and oxygen. At this stage (8) any increase in the core's temperature because of contraction makes the core cool itself by emitting neutrinos, this is because the core cannot expand and cool. Therefore the temperature of the core decreases as neutrinos are emitted. The increase in density and the decrease in the temperature makes the CO core to become electron degenerate. The pressure of the core that support the star

now comes from the piling of electrons on the core. Neither the change in temperature or density can help support core from the crush of gravity by the envelope. The CO core has become dormant from burning helium and is the packing of electrons that is supporting the star from collapse.

Such a breakdown on the interpulse period at higher mass is because higher mass stars have deep and larger convective envelopes that makes the whole star to be involve when its thermally pulsing, there is very little variation in surface luminosity over a thermal cycle when convection zone penetrates near the H-shell. Higher mass star do not develop a radiative layer between the H-shell burning and the convective zone; and therefore the simple dependence of AGB's stellar evolution on mass alone breaks. Thus high mass stars shows longer quiescent period and the luminosity is almost constant at the onset of thermal pulses, whereas at later stages when the mass of the envelope have been reduced (maybe by mass loss) the radiative layer re-appears and the behavior becomes similar to the low mass star, (notice the re-appearance of spikes at times greater than $2 \times 10^5$ on a $5M_{\odot}$ model in Figure 3.5).

## A.3 Nucleosynthesis at AGB phase

### A.3.1 Production of Carbon ($^{12}_{6}$C) during thermal pulse

At the onset of thermal pulses, the sudden increase in energy production by the He-shell creates a new intershell convection zone (ISZ) between the H-shell and the He-shell, this layer is believed to last a few hundred years depending on the mass of the core As the thermal pulse strength grows over time, the convective envelope deepens more onto layers beyond the H-shell (in more massive stars will emerge) and then will extend down onto an area where Carbon ($^{12}_{6}$C) is synthesized. The most possible area above He-shell where temperatures are high enough to make carbon,

the region between H-shell and He-shell can have carbon about ten times higher than the abundances found at the atmosphere. The Third dredge-up occurs when this carbon is mixed into the surface of convective envelope by convection currents.

The off phase correspond to a period before thermal pulse begins when H-shell luminosity ($L_H$) dominates He shell luminosity ($L_{He}$). When He-shell switches on, $L_{He}$ dominates over $L_H$, the ISCZ appears. As the power goes down (during the decline of $L_{He}$ when $L_H$ is still down not increasing), the ISZ disappears. The dredge-up occurs when the energy released by the core in response to the He-flash hits the envelope base causing it to move inward, and the hot material gets up mixed into the convective layer. Then hydrogen shell will start to heat-up and re-ignite causing the total luminosity gradually increase until the star enters the quiescent stage, notice that the convective envelope is retreating back during quiescent evolution. The He-shell heats up again and the the off phase of H shell is set and the process repeats.

As more and more carbon is enriching the surface of the convective envelope its abundances in atmosphere of the star gradually increases. More and more carbon is deposited on the surface its surface abundance when the star is undergoing thermal pulses, at the very same time, the mass of the C-O core is growing as well because every time He shell (C&O synthesis) is set in more mass rains down to the core. This is shown in Figure A.3.1 below.

### A.3.2 Lithium production during Hot bottom burning

Lithium is produced in large quantities during HBB (Sackman, Scalo, Despain and Ulrich, 1975) and it is a very important in completion of the PPI and PPII productions of He the synthesis. The observations of low mass AGB stars by Smith & Lambert 1986 showed that they have high Li abundances. Li is thought to be produced by hot bottom burning of H into Be as described by Cameron Flower mechanism (Cameron, 1955; Cameron & Flower 1971)

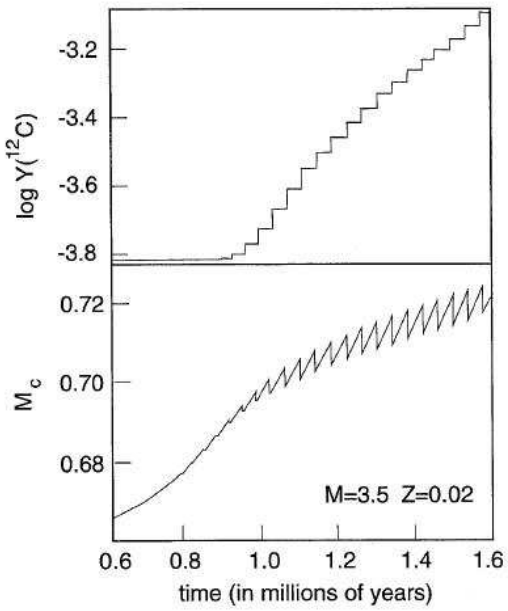


Figure A.8: *Top panel*: CO core mass and *Bottom panel*:the abundance carbon ($^{12}_{6}$C) during the AGB evolution of a 3.5$M_\odot$ model with Z = 0.002. Y is the mass fraction (X) of carbon divided by the mass number (A = 24). As carbon abundances increases in the atmosphere during dredge-up the mas of the core also increases because the He - burning shell deposits more carbon as well.

$$^3\mathrm{He}(\alpha,\gamma)^7\mathrm{Be}(\beta^-,\nu)^7\mathrm{Li} -> {}^7\mathrm{Li}(p,\alpha) = PPII$$

$$^3\mathrm{He}(\alpha,\gamma)^7\mathrm{Be} -> {}^7\mathrm{Be}(\alpha,\gamma)^8\mathrm{Be}(\beta^+,\nu)^8\mathrm{Be}(\alpha)^4\mathrm{He} = PPIII$$

All elements ($^3$H and $^4$He) used in the production of new Li by HBB were previously synthesized earlier in the evolution.

The synthesis of new material by HBB can cause the chemistry of the star to change. When temperatures reach $10^8$K in the HBB layer, the first loop of the CNO cycles ($CNO_I$) becomes more efficient in depleting all $^{12}$C into $^{13}$C by $\alpha$ capture methods and a beta decay of unstable $^{13}$N, even though there is always a production of $^4$He by the whole CNO cycle. The high abundances of $^{13}$C can capture another proton making $^{14}$N to further increase. The reduction of carbon reaction is

$$^{12}\mathrm{C}(p,\gamma)^{13}\mathrm{N}(\beta^{+},\nu_e)^{13}\mathrm{C}(p,\alpha)^{14}\mathrm{N}$$

The increase in $^{13}$C content at the onset of HBB has its influence on the surface abundances of the star by altering the ratios of $^{12}\mathrm{C}/^{13}\mathrm{C}$. When the star is thermally pulsing, dredge up of $^{12}$C will cause the surface ratios $^{12}\mathrm{C}/^{13}\mathrm{C}$ to increase until an equilibrium value is reached. As soon as HBB is switched on, more $^{13}$C is produced because C is consumed, as a result the ratio of $^{12}\mathrm{C}/^{13}\mathrm{C}$ decreases. The material in a HBB envelope is transported through the small hot region (Intershell Convective Zone) many times between thermal pulses; while this carbon rich material gets circulated between the inner regions of the star and the the surface by convection. At the end of the AGB the convective envelope decrease in mass (maybe because the star is also losing mass) causing its base to retreat and HBB to extinguish, this result onto an increase in carbon

Depending on the initial mass and chemical composition of the star, a star may not become a carbon star because of $^{12}$C conversion into $^{13}$C despite the effects of dredge up. The effect of this new nuclear synthesis of high $^{14}$N in AGB stars is that some supergiant stars can develop a nitrogen rich atmospheres. Models indicate that $^{13}$C, $^{12}$C, and $^{14}$N should evolve according to Figure 3.7..

Hot bottom burning can also consume $^{18}$O to produce $^{13}$C (Boothroyd 1993)

$$^{18}\mathrm{O}(p,\alpha)^{15}\mathrm{N}(p,\alpha)^{12}\mathrm{C}(p,\gamma)^{13}\mathrm{N}(\beta,\nu_e$$

HBB models show luminosities that are usually higher because than the ones predicted by surface luminosity core- mass relation (Pacyznski;section 3.4.1) for low mass stars, meaning the Paczynski cannot be applied in those cases where HBB dominates the luminosity of the star especially in high masses ($> 4M_{\odot}$). The reason is that in higher masses hot bottom burning tend to dominate the energy production

of the star because high mass stars do not develop radiative layer that separate the core from the envelope as a result, the convective envelope can penetrate deeper near the H-burning shell and reach higher burning temperatures. In HBB, the whole convective envelope is involve in the material transport and hence the whole star is involved in the evolution than in a situation where the mass is allowed to evolve isolated. The particular case comes when finding the limiting mass of an AGB star which uses the Chandrasekhar limit in conjunction with luminosity- mass relations that is assumes that the core and envelope separation, HBB does not apply. In this thesis we do apply Paczynski relation to estimate the mass of the core from the luminosities calculated from period- luminosity relations. The period - luminosity relations comes as a result of the fact that the atmospheres of AGB stars pulsate, and during that time the luminosity varies. Some models assumes that they are correlated to the thermal pulses that causes the core-luminosity to change.

## A.4 The interplay of Luminosity and Pulsation of AGB stars

### A.4.1 Period - Luminosity relations

Helium and hydrogen burning shells generates the energy that can also cause the star to pulsate. As they burn, part of the energy they generate by will provides a force (maybe radiatively) that pushes the overlying convective envelope causing it to expands. The convective envelope cools so that it compresses back the core. Therefore the convective envelope changes its volume with respect to a fixed location (the core). Under hydrodynamics, an object that is changing in volume while embeded in a compressible fluid, will generate sound waves. In stars, the sound waves generated by periodic expansion and compression of the convective envelope causes the atmosphere

to pulsate. In AGB stars the situation is a little different because the gas surrounding a pulsating source is not homogeneous but characterized by a strong radial density and temperature gradient. The waves travelling outwards will encounter less and less mass per unit volume because of a steep decline in density. The hot region of the convective envelope near the core can can be regarded as a fluid high in density that generates sounds waves; when this region is compresed, the shock wave are created. These shock wave created inside the convective envelope propagates out onto the atmosphere causing it to pulsate. The velocity of the shock increases as they propagate out because the density and the temperature are strongly decreasing. When reaching the higher altitudes in the atmosphere they lose energy by changing from adiabatic into radiative shocks; as they transfer their energy to the molecules in the atmosphere. Furthermore, the energy transport which determines the stability and growth rates of pulsation is dominated by convection.

Radial modes of oscillations that are used to model pulsation in stellar structures are essentially stading wave with a node at the core and anti-node at the surface, thereforethere exist a fundamental mode, the first overtone, second overtone etc (similar to the modes in a pipe).

The period (T) is known to the to be related to the mass and the radius of the star,

$$T \propto \frac{R^{\alpha}}{M^{\beta}} \tag{A.32}$$

where $\alpha$ is $\sim$ 1.5–2.5 and $\beta \sim$ 0.5–1.0 as given by Fox & Woods, (1985) [30], Frogel Mould and Blancho (1990) [32] for AGB models.

So any changes in mass and radius as the star is evolves on the AGB will affect the period. These changes are related to thermal pulses at which helium and hydrogen shell burning dominates the lumnosity of the star.

From the models of Vassiliadis & Wood 1993 [137], the variation with time of

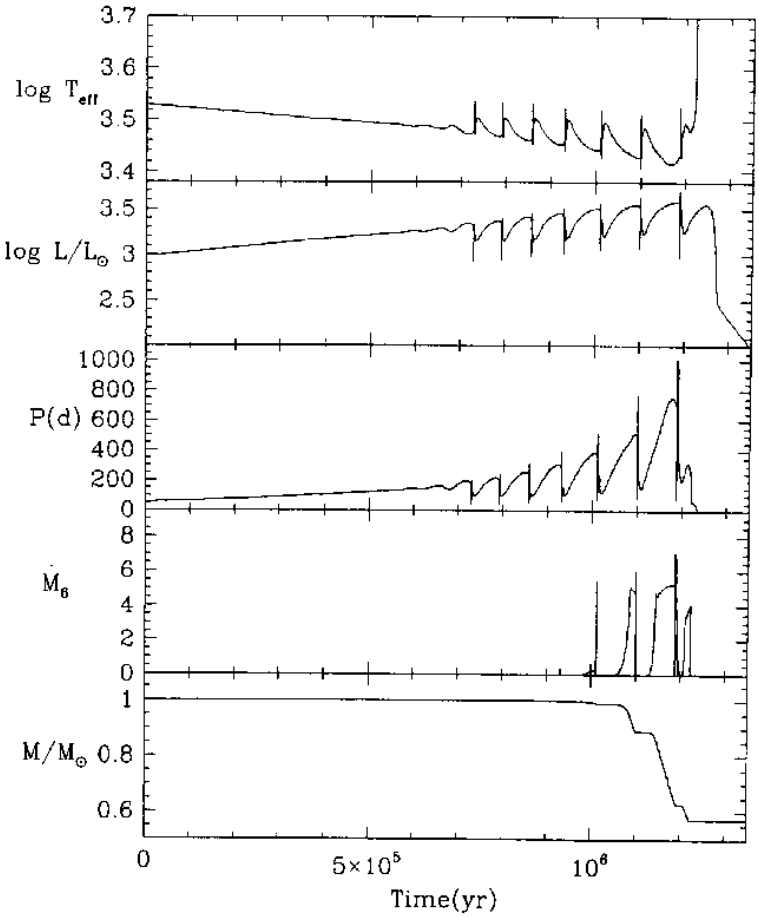


Figure A.9: Variation of fundamental mode period of a $1M_\odot$ star during thermally pulsing AGB phase.

the fundamental mode period for a sun-like star is shown in Figure A.4.1. From this figure, its is clear that the period varies on regular intervals with the changes in effective temperature and thermal pulse. When the superwind phase start (when the mass loss rates goes high) there fundamental mode period increases due to the decrease in mass of the star, and also due the fact that effective temperature of an AGB star decreases as the mass increase. For AGB stars with larger initial mass, they larger portion of their mass than low mass star during the superwind phase e.g. Wood, 1992 [148] & Herman, 1985 [55].

Because of the change luminosiy cause the change in radius, when the AGB star is radial pulsating the surface brightness changes; the star gets bright and dim over

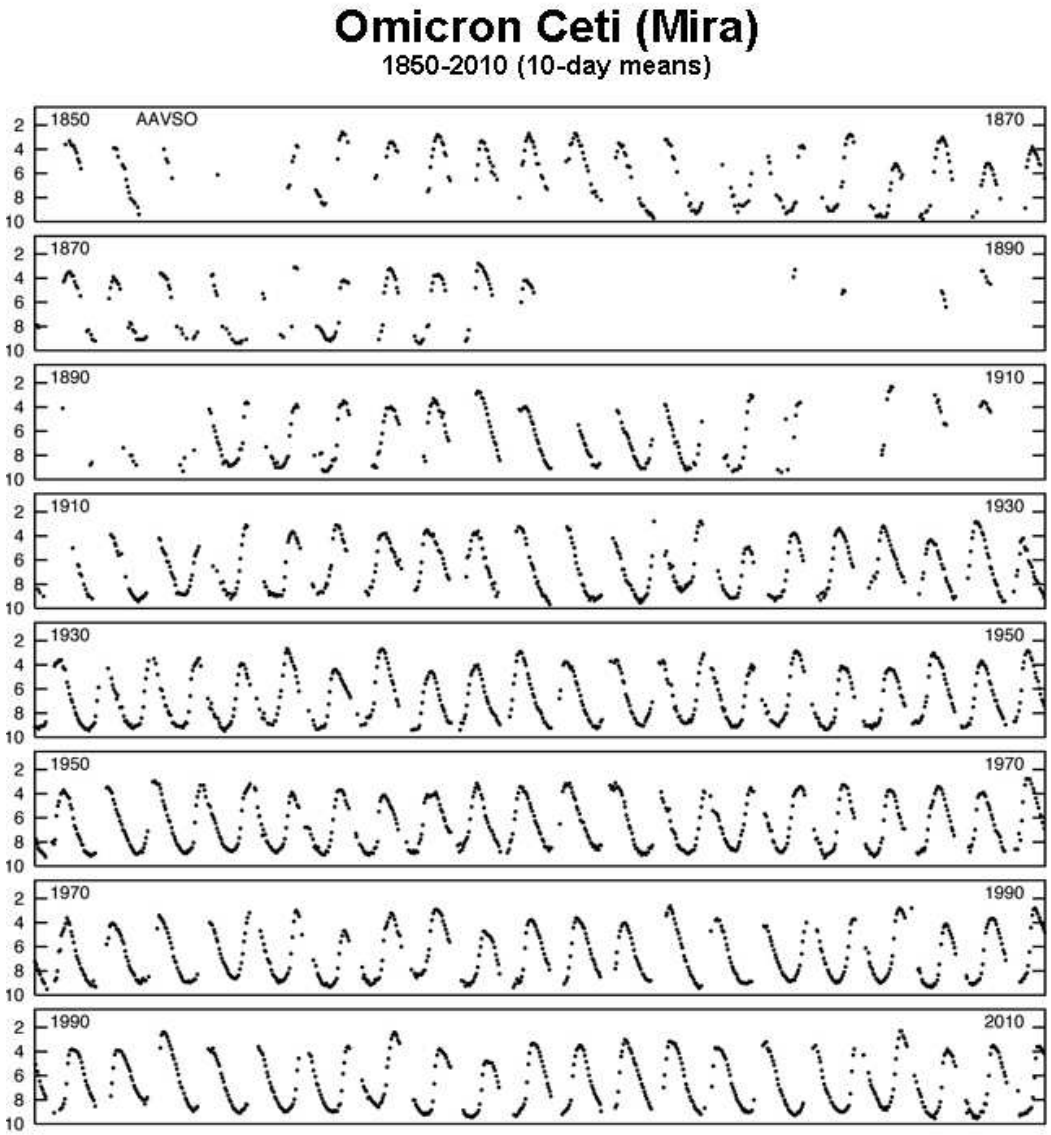


Figure A.10: Mira visual magnitude variations with time (Julian days).

period of days e.g. Figure A.10. AGB stars are known to be variable stars that shows visual brightness variation over a range of periods.

There are three groups of pulsating stars that we can identify based on luminosity variability in the V-band ($\delta$V) namely. There are (I) Mira - like variables: their magnitudes $\delta V > 2.5$ with regular and larger periods; The second (II) catagory is Semi-regular variable, they have ($\delta V < 2.5$) with regular but smaller periods, they are further subdivided into four groups SRa - SRd; and thirdly (III) we have Irregular

Table A.2: Seven types of pulsating stars are shown indicating the range of their periods; information data from General catalog of Variable Stars, Kholopov, 1985. d implies days and hr means hours

| Variable Stars | |
|---|---|
| Type | Period Range |
| Long Period Variables (LPV's) | 80 – 1000 d |
| Cepheids | 1 – 50 d |
| W Virgin Stars | 2 – 45 d |
| RR Lyrae Stars | 1.5 – 24 hr |
| $\delta$ Scuti | 1 – 3 hr |
| $\beta$ Cephei Stars | 3 – 7 hr |
| ZZ Ceti Stars | 1.7 – 17hr |

variables with small irregular periods due to poorly studied light curves. If we look at the distribution of these stars in the HR diagram, it becomes evident that their locations are related to the evolution of the stars e.g. LPV's occupy the AGB phase, while Cepheids are found common along at horizontal branch along the instability strip. The groups of stars making up these three major categories in AGB stars are presented in Table A.2

Intermediate mass stars cover the whole mass range occupied by AGB star, from globular clusters where turnoff mass ($0.8M_{\odot}$) is used set the lower limit of AGB, to stars in Large Magellanic Clouds where their high mass is used to set higher mass limit ($\sim 8M_{\odot}$) at AGB. In the Galactic plane which contains most populations of Mira and semiregular variable, Feast & Whitelock 2000 [142], Kerschbaum & Hron 1992 [69] showed that for Mira' variables in the old disk, the average progenitor mass of star increases slightly with period i.e.$\leq 1.1M_{\odot} > 300$d and $\geq 1.1M_{\odot}$. More Mira variables with periods $\sim 200$ days, are found in metal rich globular clusters (young), their turn-off mass is $0.85\odot$. For semiregulars, their mass distribution is as broad as that of Miras and also may have periods $\geq 200d$ days.

Most observed Miras belong to the Large Megellanic Cloud (e.g. Wood 2000[149], 2003 [150]) as shown in Figure A.11. The data comes from different research groups e.g. (Feast, 1989 [27], Hughes, 1990 [61]) and which also incorporates new infrared

observations by MACHO, Alcock 1995 [3]. The letters A-E are used to label the five sequences visible in the diagram: Wood, 2004 [151] shows that the B sequence splits into two sequences $B_1$ and $B_2$. The positions of the tip of the first red giant branch (RGB)and the minimum luminosity for thermally pulsing AGB (TP-AGB)stars with $M = 1M_{\odot}$ are indicated by arrows. The solid and dashed lines are the K-logP relations from Feast, 1990 [27] and from Hughes, 1990 [61], respectively. Solid circles correspond to stars with J - K $>$ 1.4; spectra show such stars to be mostly carbon stars, although the few longer-period, fainter stars are dust-enshrouded Mira variables that could be oxygen-rich. Open circles correspond to stars with J - K $<$ 1.4, and they are assumed to be oxygen-rich M or K stars. The $x$ indicates MS stars observed in the far infrared on 3$\times$ 3 degree arc of the LMC. The periods of these stars came from the MACHO database.

The P-L distribution shown in Figure A.11, shows that there is a minimum luminosity $K_0 = 12.9$ called T-ABG minimum (this point corresponds to the minimum luminosity when the star enters AGB). The sequences A and B corresponds to the semiregular stars with visual amplitudes $<$ 25 mags, while in C is occupied by Mira-like LPV's. The general consensus thus far is that these groups represents pulsations of AGB stars at different modes e.g. Latanzio & Wood 2004 [45]. The models interpreting this data suggest that semiregular variable (in A or B) can pulsate in a number of modes while Miras(in C) are confined onto one single mode. The theoretical treatment of of the formation of mode requires heavy computer calculations that involves thermal coupling between the pulsation, the effects of convection, mixing length theory, radiation pressure etc., all of which are subject to model used, an interested reader is referred to these papers Fox, 1982; Wood 1990 [147], Ostlie and Cox 1983 [101]; Wood, 2006 [146])

When we look at the distribution of stars in this diagram , we also notice that as the period grows there appears to be more Carbon-stars (dots) than Oxygen rich

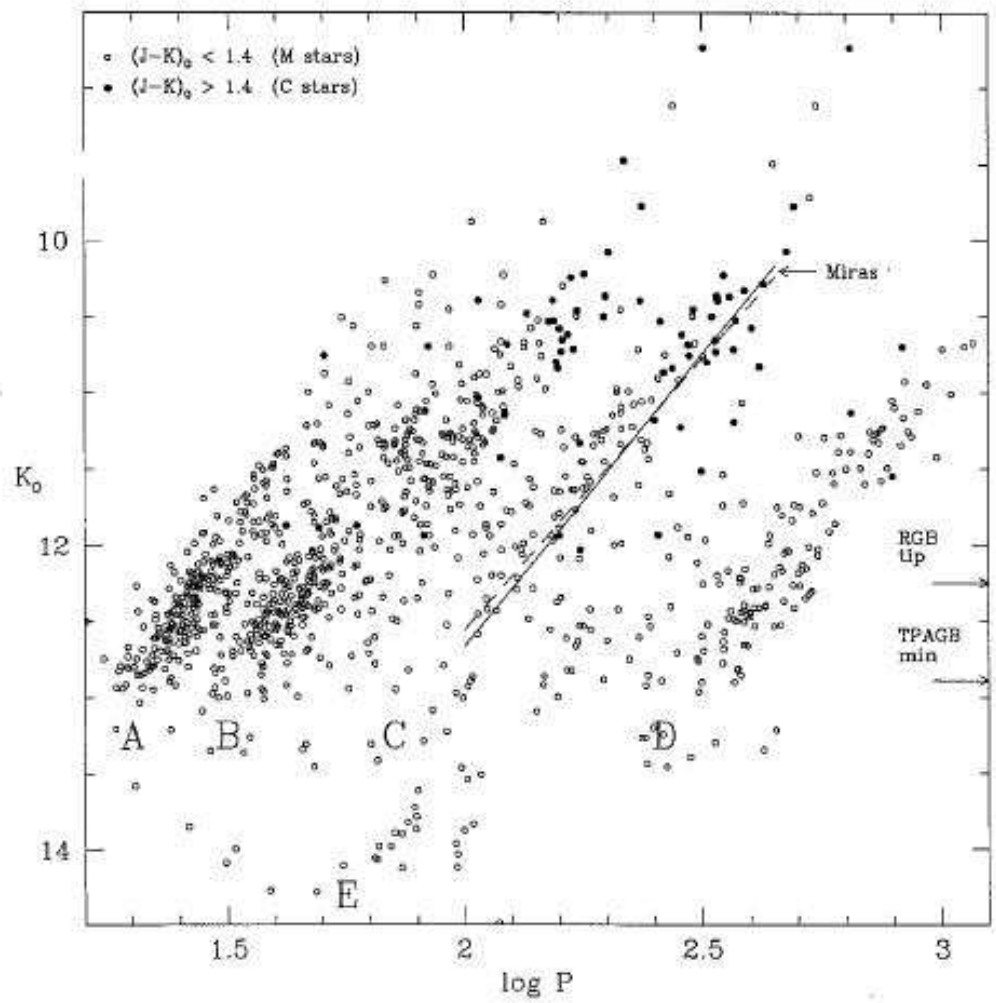


Figure A.11: The period-luminosity relations for optically visible red variables in a 0.5X0.5 degree area of the LMC plotted in the $(K_o, logP)$ plane.

stars (open circles). This may indicate that there are more carbon stars as the period grows. Another important observation is that the 'X-stars' which are dusty enshrouded stars made both O-stars and C-stars are found at the end of the Mira sequence and they decline in K magnitude because their dusty shells are so thick and cool and emit infrared at low K band. The interstellar extinction by dust is covered in section§ 5.2 of Chapter 5.

The main importance of P-L distribution is the derivation of Period -Luminosity

equation from the fit, like the one in case Miras,

$$H = -3.428 Log P_d + 1.54 < J - K > +15.637 \quad \text{(A.33)}$$

where H is the luminosity in the H band, $P_d$ is the period in days, and J−K is the infrared color for J band centered at 1.2 $\mu$m and K at 2.15 $\mu$m,

If the period can be determined, the intrinsic luminosity can be found. Once the luminosity is known the distance modulus relation can be used to measure the distance to the AGB star. The importances of knowing P-L relations (e.g Equation A.33) in Mira like stars in this work is that we can (1) determine the AGB luminosity which inturn can be used with Paczsynski relation ($M_{core} - L$) to estimate the mass of the core (see section§ 3.4.1) above; (2) estimate the distance to the star which becomes important in finding the dust mass around AGB stars and also for the early and post AGB.

## A.5 Post AGB Evolution

### A.5.1 The formation of Planetary Nebula and White Dwarfs

The burning of helium by the He-shell takes place under non-degenerate conditions, the extreme temperature dependence of the reaction, coupled with the thinness of the shell, causes thermal runaways to occur periodically. These can effect the observable evolution of the star (though not the core). Since helium shell burning occurs non-degenerately, the energy of the thermal pulse goes directly into heating the local area. This raises the pressure and causes rapid expansion of the shell. Eventually, after a few years, cooling sets in, and the helium burning begins to die down. However, during the pulse, the luminosity is raised to such an extent that convection occurs, and matter is circulated out to, and beyond, the hydrogen discontinuity. The expansion

lowers the density and temperature so much that hydrogen shell burning is effective shut off.

As the helium burning dies out, some of the matter that was propelled outward falls back towards the core. This compresses the hydrogen layer and re-ignites the hydrogen burning shell. The luminosity from hydrogen burning grows and, in a short period of time, it is once again the dominant source of energy in the star. This state continues for quite a while, with helium shell burning almost dormant, and the hydrogen shell providing the stars luminosity. After a critical amount of helium has been built up, the process will repeat. Models suggest that, very roughly, the timescale between pulses is given by equation 3.2. For $M_{core} \sim 0.5M_{\odot}$ , $T_{interpulse} \sim 10^5 years$; for $M_{core} \sim 1.4M\odot$ , $T_{interpulse} \sim 10 years$. An AGB star may undergo thousands of thermal pulses beforethe outer hydrogen shell runs out of mass i.e.,

$$M_{core} \simeq M_{\tau} - M_{env}$$

$M_{\tau} \sim M_H$ (mass contained within the hydrogen shell)

$M_{env} \sim 0.001M_{\odot}$ [6]

i.e the mass limit at the tip of the AGB when $t_{AGB-end} \simeq 10^6$ years, for $\dot{M} \sim 10^{-3}M_{\odot}yr^{-1}$, the estimated mass of the envelope is $0.001M_{\odot}$.

If the surface abundance of carbon in an AGB star is moder ately low, all the carbon will get locked up in the CO molecule. However, if the number of carbon atoms exceeds the number of oxygen atoms (which frequently occurs during dredge-up), the carbon will be quite visible, both through its molecular line blanketing and via the presence of graphite grains. These are Carbon Stars.

For stars with initial masses $M \sim 3M\odot$ , the luminosity of the hydrogen burning shell during the interpulse phase may be high enough to support convection. In this case, material from the entire envelope can be cycled through the hydrogen burning

[6]By $t_{AGB-end}$ means the end of AGB phase

shell, thereby enhancing the surface abundance of $^{14}$N and $^{4}$He even more (refer to section 3.6.4).

The luminosity of the star provided by hydrogen burning shell can be approximated by

$$L_H \propto M_{core}^{z}$$

where z $\sim$ 8. (There is also a weak dependence on the core radius). For hydrogen shell burning on the asymptotic branch, the luminosity is such that radiation pressure can no longer be neglected so we need to invoke equation A.17 in section§ A.1,i.e.,

$$P = \frac{\rho k_b T}{\mu m_H} + \frac{1}{3} a T^4$$

$$P = \frac{\rho k_b T}{\omega \mu m_H} \tag{A.34}$$

where $\omega = \frac{\mathbf{P_{gas}}}{\mathbf{P}}$. This changes the homology relations so that in the limit where $\omega - - > 0, L_H \approx M_{core}$ , (i.e., $z \sim 1$). Numerical modelling by Pazynski e.g. 3.1 confirns this.

Asymptotic Giant Branch stars continue to brighten, until their hydrogen shell approaches the stellar surface. Thus, the maximum brightness the star will achieve is a sensitive function of the star's initial mass and how much mass was lost throughout the star's history. Since the details of mass loss are poorly understood, the maximum brightness of an AGB stars is not well known.

Near the tip of the AGB, the mass loss rate from the star can be quite large, $\sim 10^{-5} M_{\odot} yr^{-1}$ or greater. This superwindcomes off at a velocity of $\sim 10 kms^{-1}$ , and forms a thick dusty envelope around the star. The envelope will probably not be spherically symmetric, however AGB envelopes are known to be spherical, therefore something have triggered this change of symmetry during the Post AGB phase. Since the envelope is bright in the IR and contains OH masers, the star is classified at this

time as an OH-IR star.

Bright AGB stars can also become unstable under radial pulsations, which take place with periods of the order of hundreds of days. Although these pulsations are poorly understood, the driving mechanism is undoubtably the partial ionization (and recombination) of hydrogen in the stars outer layers. It is important to note that Mira variables do not lie in the classical instability strip with Cepheids and RR Lyrae stars; they are supergiant AGB stars. Mira pulsations are moderately small (a factor of $\sim$ 2 in radius and $\sim$ 1 mag in bolometric luminosity over a period of$\sim$ 400 days), but the pulsations may be enough to enhance the rate of mass loss from their envelope, possibly to as high as $10^{-3} M\odot yr^{-1}$.

For example Mira a PPN researched in this thesis, has a low mass loss rate, $\dot{M} \sim 10^{-6} M_{\odot} yr^{-1}$ , but some OH-IR sources appear to have extremely high values of mass loss rate. Note also that, in the optical, Mira (o Ceti) varies from $m_V \sim 3$ to $m_v \sim 10$, but most of this change is due to a rapidly varying bolometric correction. Note: Mira pulsations are not strictly periodic. Typically, these stars have radii of $R_* \sim 300R$ , and luminosities $\sim 10^4 L_{\odot}$. Thus, their thermal timescales $\sim$ 10 years are comparable to their dynamical timescale ($\sim$ 25 years). Thus the star is never in hydrostatic or thermal equilibrium, and the structure of the star is different from pulse to pulse.

When the hydrogen shell approaches the stellar surface, the photosphere of the star begins to heat up. This moves the star to the left in the HR diagram and the surface can attain a temperature of $\sim 10^5$ K. The far UV photons emitted from the photo- sphere ionize the hydrogen which has been lost in early phases of mass loss. The star becomes a planetary nebulae.

For most stars, the thermal pulse has very little effect on the stars radius, effective temperature, and luminosity. This is simply because the event occurs well inside the star, and they are damped out by the large surrounding envelope; most of the energy

just goes into internal expansion. However, in low mass AGB stars ($M_{core} \sim 0.6 M\odot$ ), the pulse can occur near the surface, and the effects of the pulses can be seen. The star will brighten and fade over a timescale of months (or years) as the helium pulse first adds luminosity, then causes the star to fade (as the hydrogen shell burning is extinguished). Concurrently, as the hydrogen shell stops, the envelope contracts, moving the star to the left in Figure A.12. When the hydrogen shell re-ignites, the star moves back to the Hayashi line.

During the thermal pulse, the convective envelope temporarily retreats towards the surface. Once the pulse ends, however,convection again returns to the edge of the hydrogen burning shell. Because the thermal pulse convected the products of helium burning out past the hydrogen burning shell, the surface abundances will be affected. This is the Third Dredged-Up that accurs in all intermediate mass stars.

The nature of the processed material convected to the surface during the third dredge-up depends on many uncertain parameters. The thermal pulse itself synthesizes $^{14}$C and $^{16}$O. However, some (most?) of this material will be reprocessed in the hydrogen burning shell to $^{14}$N, and during the next thermal pulse, $^{14}$N can be fused to $^{18}$O and then to $^{22}$Ne. The most massive AGB stars may further fuse $^{22}$Ne to $^{25}$Mg in their later pulses.

This reaction liberates a neutron, which can then be captured in the s-process. Additionally, the reaction $^{13}\mathrm{C}(\alpha, n)^{16}\mathrm{O}$ is also one that produces a free neutron (refer to section 3.6.3.)

## A.6 Proto Planetary Nebula

During post-AGB stars excursion away from the Hayashi line, the hydrogen burning shell is still depositing material onto the helium core below it. Thus, it is possible that the star will experience one, final thermal pulse after it has left the AGB. By

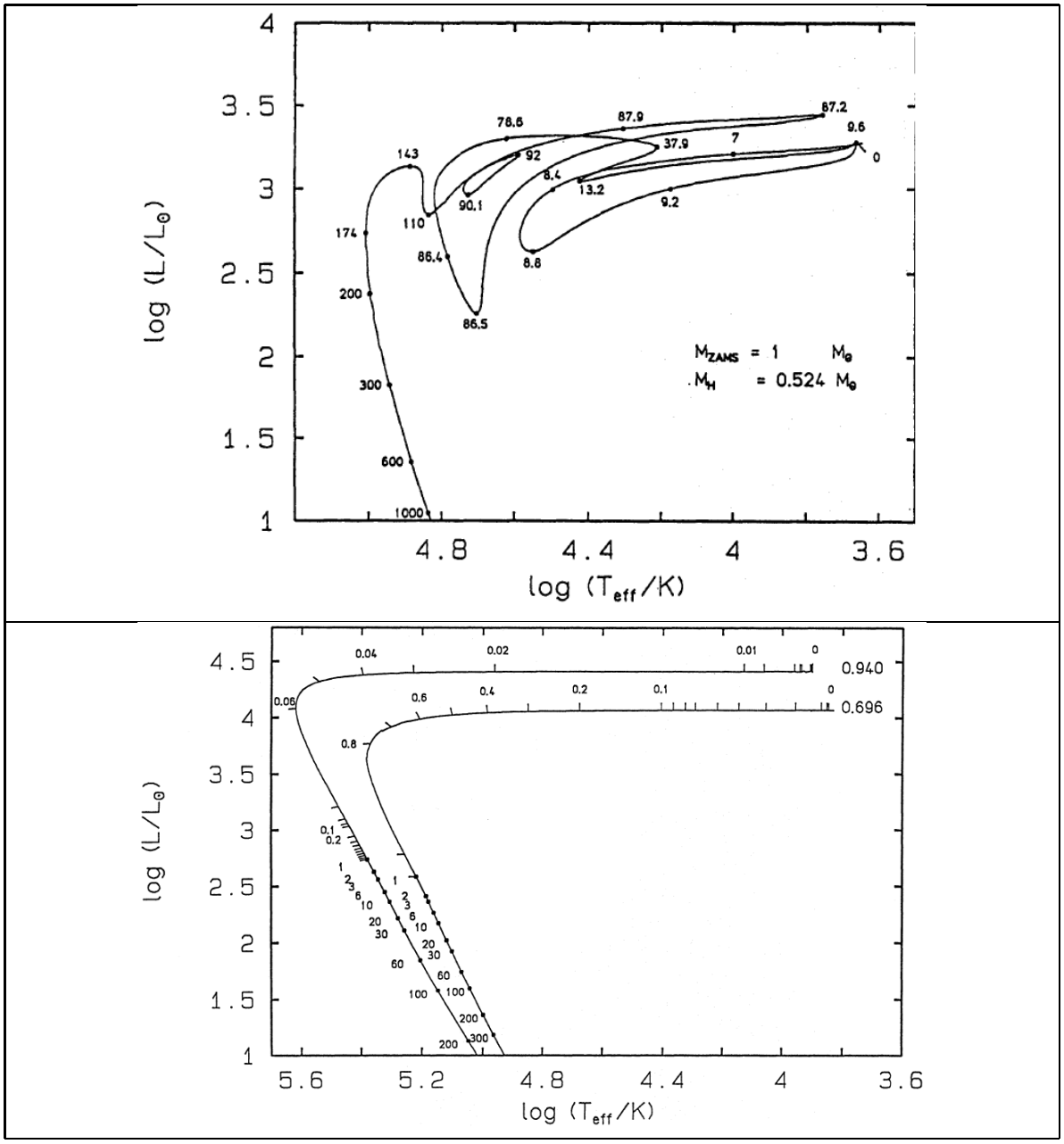


Figure A.12: *Top panel*:Evolutionary path of $0.6M_{\odot}$ PN central star which under - PN central star which undergoes a He-shell burning ($0.85 < \phi < 1.0$). *Bottom Panel*: Evolutionary path of $0.6M_{\odot}$ PN central star with He-shell while undergoing hydrogen burning ($0.15 < \phi < 0.75$).

some calculations e.g. Blöker 95, $\sim 10\%$ of all stars should do this. When this occurs, the helium shell mixes directly with the hydrogen rich envelope. Since the envelope mass is small and already hot, the energy of the pulse is not absorbed by the cool matter surrounding the shell. Consequently, a thermal runaway will will occure, due

to fresh hydrogen being cycled into the helium shell. All the remaining hydrogen will be destroyed through the re-action sequences

$$^{12}_{6}\mathrm{C}(p,\gamma)^{13}_{7}\mathrm{N}(\beta^{+},\nu_{e})^{13}_{6}\mathrm{C}(\alpha,n)^{18}_{6}\mathrm{O}$$

described bove in section 3.6.4.

Since the sequence also liberates a neutron, s- and possibly reprocess elements will also be formed. After the pulse, the surface of the star will contain no hydrogen. The energy liberated in the pulse will cause the intershell region expand. As the expansion proceeds, the temperature of the envelope will cool; this will increase the local opacity. The higher opacity will then cause the envelope to better absorb the input energy, further fueling the expansion. As a result, the photosphere will expand, and the star will for a short time return on the Hayashi track.

After another the pulse, the helium shell will return to its pre-pulse luminosity, and the star will repeat its journey across the blue-side of the HR diagram. The star appears to be 'born again' a scenario that is thought to be responsible for the origin of a number of hydrogen deficient stars, including the now so called R CrB stars, helium stars, hydrogen-deficient planetary nebulae nuclei and white dwarfs.

### A.6.1 The planetary nebula stage

As we discussed in section§ A.1, stars spend most of their lives on the main sequence burning hydrogen to helium, so, to the first-order, the main-sequence lifetime and therefore the total lifetime of the star can be approximated by

$$\tau_{nuc} = \frac{QM}{L} \tag{A.35}$$

The next level of approximation requires knowledge of the mass loss rates on the RGB and AGB, since these determine when the fuel (i.e., the envelope mass)

runs out. According to Iben & Laughlin (1989) [65], the total evolution time from the zero age main sequence to the end of the AGB phase (for stars with masses $0.6M_{\odot} < M_i < 10M_{\odot}$) can be approximated with a polynomial:

$$logt_{evol} = 9.921 - 3.6648\,(logM_i) + 1.9697\,(logM_i)^2 - 0.9369\,(logM)^3 \qquad \text{(A.36)}$$

where $M_i$ is the initial mass in solar masses. As the hydrogen burning shell of an AGB approaches the stellar surface, the effective temperature of the star will increase, and the star will move to the left in the HR diagram. The speed at which this occurs depends on the rate of shell burning, which, in turn, depends on the core mass. Low mass cores will evolve slowly and be relatively faint; conversely, high mass cores will be bright, and their evolution will be extremely rapid. Roughly speaking, $L \propto M_{core}^{3.5}$ , and $\tau_{nuc} \propto M_{core}^{9.5}$ . In theory, the evolution of $3M_{\odot}$ a low mass core may be so slow that the surrounding mass may disperse before the core gets hot enough to ionize the material.This is sometimes called a lazy PN central star. Similarly, the evolution of a high-mass ($> 5M_{\odot}$) core may occur so fast, that the star fades before the critical density is reached for forbidden emission lines. As the hot core of the planetary nebula is exposed, a very fast ($\sim 2000kms^1$ ) stellar wind appears with a mass loss rate of $\dot{M} \sim\ 10^{-7} - 10^{-9}M_{\odot}yr^{-1}$. This fast wind runs into the previously ejected shell, and is responsible for some of the ionization structures seen in nebulae. During this time, the spectra of the star is extremely similar to that of a Wolf-Rayet star.While shell hydrogen burning is proceeding, some shell helium burning may also exist. The ratio of these two energy sources depends on the progenitor, but typically, hydrogen burning will dominate.

The lifetime of a planetary nebula is $\sim$ 25, 000 yr. During the hydrogen burning stage, the star evolves to the left in the HR diagram at constant luminosity. When

the envelope becomes too small to support hydrogen burning, this source of energy vanishes, and the star begins to produce energy via gravitational contraction. This is the beginning of the white dwarf phase.

## A.7 Initial Masses and Luminosity Variations

In this part we want to explore the limits in mass and luminosity of AGB stars on the basis of observations of stars in globular clusters. Stars in globular clusters are very the old. The age of the cluster can be found at turnoff point of the cluster, which occurs because globular clusters lacks high mass stars that evolve faster and leave the main sequence. The low mass AGB stars in globular clusters must have had their initial mass to be about at turn-off point mass after leaving the main sequence. The minimum mass observed is set at about $0.85\,\mathrm{M}_{\odot}$ at a luminosity of about $M_{bol} = -3.6$. The higher mass observed is about $8M_{\odot}$ at $\mathrm{M}_{bol} = -7.1$.

Most stars in globular clusters are found to be oxygen rich meaning carbon has not appear to be dredge-up to the surface by thermal pulses. This trend is illustrated in Figure A.7 that shows observationally the distribution of initial mass (top axis) and the magnitude against the age of all long period variable stars in the Magellanic Cloud clusters. Large and Small Magellanic clouds are satellite galaxies clearly visible in the southern hemisphere, and they are good reservoirs of long period variable stars. Theire measured distances are 18.5 and 18.9 parsecs from the earth.

### A.7.1 Initial mass relations (IMF)

The fate of an intermediate mass star is determined by the competition betetween the growth of the core mass and mass loss by stellar winds. The core mass can grow up to the Chadrasekhar limit in which case a carbon ignition will occur as a result the star dies in the form of type I-1/2 supernovae. On the other hand mass loss by stellar

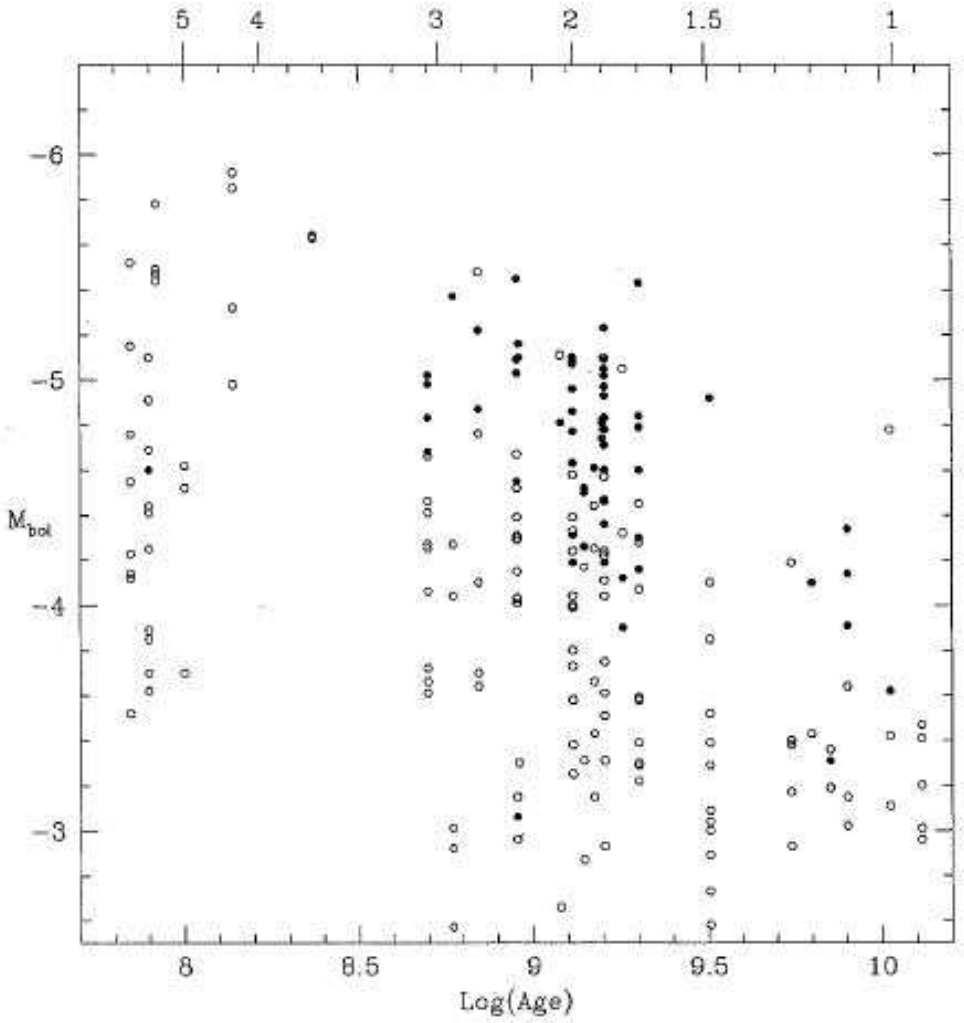


Figure A.13: AGB stars in the Magellanic Cloud (MC) clusters adapted from Lattanzio & Woods on [51].

winds can consume a lot of envelope such that the end product of intermediate mass stars ends up as a white CO-white dwarf. Therefore we need to establish a realation between the final mass ($M_f$) left at the end of the AGB to the initial mass $M_i$, of the progenitor star is of critical importance for various aspects related to both stellar evolution of intermediate mass stars and the galaxy the hosts them. The age of any stellar system (e.g. clusters in galaxies) can in principle be derived once the mass of white dwarfs detected in that particular system has been estimated. Thus we can argue that, for intermediate mass stars in clusters of different galaxies, their Initial Mass Function Relations (IMFR) can be used as an important tool to investigate the history of the hosting galaxy. For example (Iben, 1989 [65] and Wood, 1992[148]) used the information about the IMF for AGB stars to estimate the age of the local disk, i.e. a quote from Wood & Oswalt 1997 'The use of white dwarf (WD) stars as a probe of the Galactic age has a long history, dating to Schmidt's (1959) [116] realization that the Mestel (1954) [97] cooling law could be used to provide a lower limit to the age of the Galaxy if a downturn in the white dwarf luminosity function (WDLF) could be observationally detected.

The IMFR provides the information about the amount of mass that each star loses in the course of its entire evolution and hence on the evolution mass bugdet of stellar populations and galaxies e.g. Renzini, Chiosi & Dyson, 1986 [20]. Thus assesing the upper mass limit of white dwarf progenitors is of paramount importance since it affects the rate of type I-1/2 supernova events that are important for the star formation history, and the chemical enrichment of the interstellar medium, the birth-rate of neutron stars. Thus since in this thesis we also estimate the progenitor masses of intermediate mass stars, I will briefly discuss the IMF relations on the basis of synthetic AGB evolution. The analytic prescriptions presented in B the next paragraph only discuss the results of their usage in estimating the initial and final masses and how they impact our observations. This is based on the empirical

Wiedeman & Koester, 1983 [141](hereafter VK83) observations of white dwarf masses.

# Appendix B

# Initial Mass Function Relations

## B.1 Theoretical framework of IMF in AGB populations

For intermediate mass stars to be on the AGB, they must have been born some time ago, so under synthetic AGB evolution their mass distribution function $N(M_i)$ can be written as

$$N(M_i)dM_i \propto \int_0^{t_{AGB}} \theta(Mi)\psi(T_G - \tau(Mi, Z) - x)dx \tag{B.1}$$

where $\theta(Mi)$ is the initial mass function (IMF) that assumes the power law $Mi^{-\alpha}$, $\psi$ is the star formation rate, and $t_{AGB}$ is the lifetime of AGB, ($T_G$ is the age of the system and $\tau(Mi, Z)$ is the pre-AGB life time of a star with mass M, Z is the metalicity of the system. For AGB stars $t_{AGB} << \tau$, the we can estimate N, i.e.

$$N(M_i)dM_i \propto t_{AGB}\theta(Mi)\psi(T_G - \tau(Mi, Z)) \tag{B.2}$$

in the range $M_{low} = 0.8M_\odot < M < M_{high} = 8M_\odot$, for these stars to evolve up on the

AGB

# Appendix C

# General Radiative Transfer Equation

The general transfer equation for an isotropic scattering in a spherical, static circumstellar envelope (CSE) around a spherical radiative source is

$$\mu\frac{\partial I_\nu}{\partial r} + \frac{1-\mu^2}{r}\frac{\partial I_\nu}{\partial \mu} = \kappa_\mu \rho (I_\nu - J_\nu) \tag{C.1}$$

if we assume Eddington approximation i.e. the atmosphere is curved, then the transfere equation takes the form,

$$J - 3K + 1/2\Big(\sqrt{1-(R_*/r)^2}\Big).F = 0 \tag{C.2}$$

where J, K, F, are the zero - order, second moments of the intensity I. In a grey atmosphere Lucy, 1976 [86] intergrated equation C.2 to get

$$F(r) = (R_*/r)^2)F_*$$

$$J(r) = F_*\Big[W(r) + 3/4\int_0^{infty} \kappa_{tot}\rho(R_*/r)^2 dr\Big]$$

$\kappa_{tot} = kappa_{gas} + kappa_{dust}$

$$W(r) = \frac{1}{2}\left[1 - \sqrt{1 - \left(\frac{R}{r}\right)^2}\right]$$

In the atmosphere that is in radiative equilibrium,

$$J = B = \sigma/\pi)T^4.$$

Therefore solving Equation C.2

$$T_{eq}(r) = 1/2T_*\Big[2W(r) + 3/2\tau_{tot} \tag{C.3}$$

where the total optical depth is

$$\tau_{tot} = \int_r^\infty \kappa_{tot}(r')\rho(r')\Big(\frac{R_*}{r}\Big)^2 dr'$$

. The extiction mass absorption coefficient is

$\sim 2. \times 10^{-4} cm^2 g^{-1}$

## C.1 Spectroscopic Observations of Mass loss

We observe light coming from a star that has been reprocessed by a cloud of gas between the observer and the star to derive the spectra associated with the star. The spectral lines observed provide a wealth of information about the structure,dynamics, and the chemical composition of the intervening material. In the case of a cloud in motion, as it applies in stellar winds, observations of the stars with relatively high mass loss show that the widths or wavelengths are shifted due to outflowing motion of the gas in the wind. The spectra of a mass-losing star will appear to have emission lines, absorption lines, or the combination of the two cases in the so-called the P Cygni

profile. From the historical perspective of observations, the similarity in appearance of the Cygni profiles on the spectra of hot luminous stars to those dying stars with an expanding atmosphere in novae, gave rise to the idea that stars loose mass.

### C.1.1 P Cygni in hot stars

The most well known P Cygni profiles in the spectra of hot stars are formed by the process of resonance scattering of atom; in this case a line is formed when an atom absorb a photon that excites an electron to higher energy level, the photon with the same frequency is re-emitted when an electron returns to the ground state. In the presence of an expanding shell, the emission and part is red shifted making a bump in the continuum spectra towards the observer, while absorption part is blue shifted because of scattering of photons out of the line of sight with reference to the observer making a 'dip' in the continuum. A few examples of P Cygni profile lines on the UV spectra of O and early B stars that result from resonance lines of Si IV, C IV, Mg II. The velocity law of the expanding material can be derived from the P Cygni lines, and if the density in the shell is known, the rate at which the star loses mass can be found e.g Groenewegen 1989[46], Lamers 1995[78]. An example of P Cygni profile is presented in Figure 4.1.

### C.1.2 Atomic Emission lines

Atomic emission lines are good indicators that the star is loosing mass because of their broadness of FWHM (or width) that shows the Doppler shift of atoms that comes from the outflowing motion of the gas in the wind. These lines are formed through recombination process of line formation in stellar wind. Recombination occurs when an ion collides with an electron and produces an ion releases a photon when it return to the ground state. The emissivity of recombination is proportional to the density

of a gas, thus atomic line emission probe the denser regions in stellar winds. Stars with high mass loss rates $\sim 10^{-6}$ $M_{\odot} yr^{-1}$ show these emission lines in their spectra, the most well known lines are H$\alpha$, Paschen and Brackett lines of hydrogen atom.

The appearance of these lines in an atmosphere of a mass loosing star offers an insight on the physical conditions under which the ionised atoms in a gas interact with the photons.

### C.1.3 Molecular Emission lines

There are five processes associated with the line formation in stellar winds, namely; (a)Line scattering, in which an atom in a gas absorbs a photon causing the electron to excite into the higher energy level, as the atom cools because of expansion the electron can de-excite by emitting the same photon with same energy in a different direction. (b) Line emission by recombination, here the exited ion present into the stellar wind can recombine with an electron causing the ion to emit a photon as reaches the ground state. (c) Line emission from collision of atoms, a photon can be emitted when an an energetic atom returns to ground state after colliding with another atom, this process can occur in hot plasmas line corona and chromospheres. (d) Pure absorption, an atom absorbs a photo and get excited,the releases the photon(s) into lower levels destroying the initial photon. (e) Massering by stimulated emission, a photon in a stellar wind hits an excited atom or a molecule that causes the atom to release the same photon traveling the the same direction as the original photon.

# Appendix D

# Programs developed for data analysis

### D.0.4 Fitting Gaussian profiles

To make this code works, you wil need to be working under idl platform. These following files have to be in your working directory or included in your idl library: bvls.pro, numlines.pro,readcol.pro, strnumber.pro, gettok.pro repchr.pro, writespec.pro, PIKAIA.

```
; NAME:radialprofilefit
; ; PURPOSE:Fits a radial profile to an object in an astronomical image.
; ; CALLING SEQUENCE:Result = radialprofilefit(r,I)
; ; INPUTS:
; r = radial distance.
; I = intensity or flux.
; ; OUTPUTS:Result = the profile fit and it parameters plus errors.
; ; NOTES:(1) This routine is based on the routine MeasureFeatures.pro.
; ; MODIFICATION HISTORY:
;(November 4 2005) Original Version written in 2005, C. Dijkstra,
;and Menzi B. Mchunu at Department of Physics and Astronomy,
;University of Missouri, Columbia, USA
Email : dijkstrac@missouri.edu : bmmgd8@mail.missouri.
function radialprofilefit,r_in,f_in,min=min,max=max,
rmin=rmin,rmax=rmax,nrGaussians=nrGaussians,
show=show,slope=slope,poly=poly,muranges=muranges,
sigranges=sigranges,offsetranges=offsetranges,nrgenerations=nrge
nerations,nrpopulation=nrpopulation,outputfile=outputfile
forward_function integral,func
common common_pikaia_fit,r,f,show_intermediate,nr,diff0,boundlow,
boundmax,Param,
slope_option,poly_option,muranges2,sigranges2,offsetranges2
```

---

```
;Set the limits between which the fit parameters must be looked for.
if n_elements(min) eq 0 then boundlow=-2d4 else boundlow=min
if n_elements(max) eq 0 then boundmax=2d4 else boundmax=max
if not keyword_set(rmin) then rmin=-1000d0
if not keyword_set(rmax) then rmax=1000d0
if not keyword_set(nrGaussians) then nrGaussians=1d0
if keyword_set(show) then show_intermediate=1 else show_intermediate=0
if keyword_set(muranges) then muranges2=muranges else muranges2=0
if keyword_set(sigranges) then sigranges2=sigranges else sigranges2=0
if keyword_set(offsetranges) then offsetranges2=offsetranges
else offsetranges2=0
if not keyword_set(nrgenerations) then generations_pikaia=300
else generations_pikaia=nrgenerations
if not keyword_set(nrpopulation) then population_pikaia=100
else population_pikaia=nrpopulation
if not keyword_set(outputfile) then outputfile='radialprofilefit.tmp'
```

```
;Define the input radial profile.
r=r_in
f=f_in
idx=where((r ge rmin) and (r le rmax))
r=r[idx]
f=f[idx]
if not keyword_set(slope) then slope_option=0d0 else slope_option=r
if not keyword_set(poly) then poly_option=0d0 else poly_option=r^2
diff0=0d0
nr=nrGaussians
;Use pikaia to find the best-fit parameters.
openw,1,outputfile
pikaia,'func',2*nr,bestfitparameters,errorinfit,
generations=generations_pikaia,population=population_pikaia
close,1
;Calculate the errors on the best-fit parameters.
ErrorFile=read_ascii(outputfile)
diff_values=reform(ErrorFile.field01[0,*])
idx=where(abs((diff_values-diff_values[n_elements(diff_values)-1])
/diff_values[n_elements(diff_values)-1]) le 0.1d0)
scaling_values=dindgen(nr,n_elements(diff_values))
mu_values=dindgen(nr,n_elements(diff_values))
sig_values=dindgen(nr,n_elements(diff_values))
```

```
strength_values=dindgen(nr,n_elements(diff_values))
area_values=dindgen(nr,n_elements(diff_values))
offset_values=reform(ErrorFile.field01[6*nr+1,*])
slope_values=reform(ErrorFile.field01[6*nr+2,*])
poly_values=reform(ErrorFile.field01[6*nr+3,*])
scaling_range=dindgen(nr,2)
mu_range=dindgen(nr,2)
sig_range=dindgen(nr,2)
maximum_range=dindgen(nr,2)
strength_range=dindgen(nr,2)
area_range=dindgen(nr,2)
offset_range=[min(offset_values[idx]),max(offset_values[idx])]
slope_range=[min(slope_values[idx]),max(slope_values[idx])]
poly_range=[min(poly_values[idx]),max(poly_values[idx])]
for j=0,nr-1 do begin
scaling_values[j,*]=reform(ErrorFile.field01[1+6*j,*])
mu_values[j,*]=reform(ErrorFile.field01[2+6*j,*])
sig_values[j,*]=reform(ErrorFile.field01[3+6*j,*])
maximum_values[j,*]=reform(ErrorFile.field01[4+6*j,*])
strength_values[j,*]=reform(ErrorFile.field01[5+6*j,*])
area_values[j,*]=reform(ErrorFile.field01[6+6*j,*])
scaling_range[j,*]=[min(scaling_values[j,idx]),max(scaling_values[j,idx])]
mu_range[j,*]=[min(mu_values[j,idx]),max(mu_values[j,idx])]
sig_range[j,*]=[min(sig_values[j,idx]),max(sig_values[j,idx])]
maximum_range[j,*]=[min(maximum_values[j,idx]),max(maximum_values[j,idx])]
area_range[j,*]=[min(area_values[j,idx]),max(area_values[j,idx])]
endfor
e_range,poly_range:poly_range
;put a closed bracket on the previous line
spawn,'r m'+outputfile ;Put a backslash next to rm command to use aliases -i
;that is set in menzi'saliases file use your own setup.
```

```
;Plot the best-fit result.
plot,Param.r,Param.f,ps=0,chars=1.5,xtit='Radial distance',
ytit='Flux',tit='Best Fit',/nodata
oplot,Param.r,Param.f,ps=0,col=254,thi=2
oplot,Param.r,Param.fmodel,ps=0,col=75,thi=2
for i=0,n_elements(Param.maximum)-1 do oplot,Param.r,
(Param.r^2)*Param.poly+Param.r*Param.slope+Param
.offset+Param.fitcomponents[i,*],ps=0,linestyle=2,thi=2
;Return the best-fit parameters and their errors.
return,Param:Param,Param_Errors:Param_Errors
end
function func,n,p
common common_pikaia_fit,r,f,show_intermediate,nr,
diff0,boundlow,boundmax,Param,slope_option,poly_option,
muranges2,sigranges2,offsetranges2
fmodel=0d0*dindgen(n_elements(r))
;Define the standard deviation of the Gaussian.
if (n_elements(sigranges2) le 1) then begin
sig=(p[0:(n_elements(p)/2)-1])^4*50d0 endif else begin
sig=dindgen(nr)
for j=0,nr-1 do begin
sig[j]=sigranges2[2*j]+(sigranges2[2*j+1]-sigranges2[2*j])*p[j]
endfor
endelse
;Define the mean of the Gaussian.
if (n_elements(muranges2) le 1) then begin
mu=p[(n_elements(p)/2):2*(n_elements(p)/2)-1]*(r[n_elements(r)-1]-r[0])+r[0]
endif else begin
mu=dindgen(nr)
for j=0,nr-1 do begin
mu[j]=muranges2[2*j]+(muranges2[2*j+1]-muranges2[2*j])*p[(n_elements(p)/2)+j]
endfor
```

```
endelse
gaussians=dindgen(n_elements(r),nr+3)
;Define the Gaussians.
for j=0,nr-1 do begin
gaussians[*,j]=(1d0/(sig[j]*sqrt(2d0*!DPI)))*exp(-((r-mu[j])^2)/(2d0*sig[j]^2))
endfor
;Define the polynomial on top of which the Gaussian is located.
gaussians(*,nr)=1d0
gaussians(*,nr+1)=slope_option
gaussians(*,nr+2)=poly_option
;Do a least square fit.
x=dindgen(nr+3)
boundx=dindgen(2,nr+3)
boundx(0,0:nr-1)=boundlow
boundx(1,0:nr-1)=boundmax
if (n_elements(offsetranges2) le 1) then begin
boundx(0,nr)=-2d4 ;Lower bound offset.
boundx(1,nr)=2d4 ;Upper bound offset.
endif else begin
if n_elements(offsetranges2 ne 2) then begin
print,'Warning: The vector offsetranges may only contain 2 elements!'
stop
endif
boundx(0,nr)=offsetranges2[0] ;Lower bound offset.
boundx(1,nr)=offsetranges2[1] ;Upper bound offset.
endelse
boundx(0,nr+1)=-2d4 ;Lower bound slope.
boundx(1,nr+1)=2d4 ;Upper bound slope.
boundx(0,nr+2)=-2d4 ;Lower bound polynomial.
boundx(1,nr+2)=2d4 ;Upper bound polynomial.
```

### D.0.5 Calculation of emissivity and dust temperature

This code calculates beta if fluxes and temperatures are known

```
endelse
gaussians_in=gaussians
f_in2=f
bvls,gaussians_in,f_in2,boundx,x
;Define the total model.
for i=0,n_elements(r)-1 do begin
fmodel[i]=total(gaussians[i,*]*x)
endfor
maximum=dindgen(nr)
fitcomponents=dindgen(nr,n_elements(r))
for j=0,nr-1 do begin
maximum[j]=max(gaussians[*,j]*x[j])
fitcomponents[j,*]=gaussians[*,j]*x[j]
endfor
diff=1d0/(total((f-fmodel)^2d0))
if (diff gt diff0) then begin
diff0=diff
if (show_intermediate eq 1) then begin
plot,r,f,ps=0,chars=1.5,thi=2,xtit='Radial distance',ytit='Flux'
oplot,r,fmodel,ps=0,col=100
endif
poly=x[n_elements(x)-1]
slope=x[n_elements(x)-2]
offset=x[n_elements(x)-3]
scaling=x[0:n_elements(x)-4]
strength=0d0*dindgen(nr)
for k=0,nr-1 do strength[k]=max((fitcomponents[k,*]
+offset+slope*r+poly*r^2)/(offset+slope*r+poly*r^2))
area=0d0*dindgen(nr)
for k=0,nr-1 do area[k]=integral(r,scaling[k]*(1d0/(sig[k]
*sqrt(2d0*!DPI)))*exp(-((r-mu[k])^2)/(2d0*sig[k]^2)),n_elements(r))
```

```
Param=r:r,f:f,fmodel:fmodel,fitcomponents:fitcomponents,$
scaling:scaling,mu:mu,sig:sig,maximum:maximum,strength:strength,$
area:area,offset:offset,slope:slope,poly:poly
;Put a closed bracekts and the begining of Param and close it here
fmt = '(E15.7,A5,$)'
printf,1,format=fmt,diff,' '
for j=0,nr-1 do begin
fmt = '(E15.8,4X,E15.8,4X,E15.8,4X,E15.8,4X,E15.8,4X,E15.8,4X,A5,$)'
printf,1,format=fmt,scaling[j],mu[j],sig[j],maximum[j],strength[j],area[j],' '
endfor
fmt = '(E15.8,4X,E15.8,4X,E15.8,$)'
printf,1,format=fmt,offset,slope,poly
printf,1,""
endif
return,diff
end
function integral,x,y,n
;Calculation of an integral with the trapezium rule.
;Exact copy of integral from grow_mantleII.pro.
sum = 0d0
wgt = 0d0*dindgen(n)
if (n eq 1) then begin wgt[0] = 0.0d0
endif else begin
;wgt[0] = 0.5d0*abs(x[1]-x[0])
wgt[0] = 0.5d0*(x[1]-x[0])
sum = sum+wgt[0]
for i=1,n-2 do begin
;wgt[i] = 0.5d0*abs(x[i+1]-x[i-1])
wgt[i] = 0.5d0*(x[i+1]-x[i-1])
sum = sum+wgt[i]
endfor
;wgt[n-1] = 0.5d0*abs(x[n-1]-x[n-2])
wgt[n-1] = 0.5d0*(x[n-1]-x[n-2])
sum = sum+wgt[n-1]
endelse
integralout=total(wgt*y)
return,integralout end
```

; NAME:emissivity and Dust Temperature Calculation
; ; PURPOSE:This code calculates emissivity (beta) if fluxes and temperatures are known
; ; CALLING SEQUENCE: beta(f1,f2,T1,T2) ; ; INPUTS:Two Far infrared wavelenghts, two flux
; ; OUTPUTS:Table of emissivity and dust temperatures.
; ; NOTES:(1) The code is written in c++ programing, To run this programme you need to
eliminate spaces between  n”
; ; MODIFICATION HISTORY:
;(November 4 2005) Original Version written in 2007 by Menzi Basil. Mchunu
at Department of Physics and Astronomy,
University of Missouri, Columbia, USA
Email : dijkstrac@missouri.edu : bmmgd8@mail.missouri.
include stdio.h, math.h, locale.h, string.h
main()
float flux1, flux2;
float temp1,temp2;
float temp;
float frequency1,frequency2;
float beta;
printf(”Enter flux1 and flux2:n”);
scanf(”%f”,&flux1);
printf(” n”);
scanf(”%f”,&flux2);
printf(”nNow enter dust temperatures: inner temperature (higher)
and the outer temperature (lower)n”);
scanf(”%f”,&temp1);
printf(” n”);
scanf(”%f”,&temp2);
printf(”Great now enter the two frequencys (units of THz)
starting with the smallest n”);
scanf(”%f”,&frequency1);
printf(” n”);
scanf(”%f”,&frequency2);
printf(”You entered flux1 of %f and flux2 of %f
and dust temperatures %f and %f,
the first frequency is %f and the second is %f  n”,
flux1,flux2,temp1,temp2,frequency1,frequency2);
printf(”Now I shall try to compute Beta
for you within these temperatures  n”);
printf(”Temperature Beta  n”);
// The computation code goes here
for(temp = temp1;temp > temp2;temp-=0.5)

```
float expf(float s);
float logf(float t);
// beta = (flux1 / flux2)* (expf(48.01*frequency1 / temp) - 1);
beta = (log((flux1 / flux2) *(expf(48.01*frequency1 / temp) - 1) /
(expf(48.01*frequency2 / temp) - 1)) / log(frequency1 / frequency2)) - 3;
if (beta¿=0.8 && beta¡=2)
printf("%f %f  n",temp,beta);
return 0;
```

# VITA

I was born in South Africa at KwaZulu Natal, along the coastal area in place called St Faiths. I graduated with BSc in 1997 at the University of Zululand. I then continued to do an additional year of BSc Hons (Cum laude) in Physics in 1999 working on: Thermal annealing of Li with positron. In 1998 - 1999, I started working as intern Dr David Buckley on fiber - optics interface applications on one of South African Astronomical Observatory (SAAO). In 2000 I worked as as a student liaison officer, under Dr. Patricia Whitelock and Dr. Peter Martinez at SAAO. While working at SAAO I received the first prestigious scholarship award under South African large telescope (SALT) to do my Masters / PhD at Rutgers University in 2001 - 2003. At Rutgers worked on my masters with Prof. Theodore Williams on : Tracing of dust luminosities using far infrared radiation and calibration of the (SALT) etalon. I joined the University of Missouri in the fall of 2004 and started working with Prof. Angela Speck in 2005 on the project: Extremely extended dust shells around intermediate mass stars, tracing mass the histories of mass loss, thermal pulses and stellar evolution. In this project we used different in-space observational data e.g. ISO (ESA's Infrared Observatory)- presented in this thesis; Spitzer Space Telescope (SST), formerly the Space Infrared Telescope Facility (SIRTF) of NASA and AKARI (formerly ASTRO-F), the first Japanese satellite dedicated to infrared astronomy, from the Institute of Space and Astronautical Science (ISAS) of the Japanese Aerospace Exploration Agency (JAXA). I married my wife Heather Shawver in 2007, we have two wonderful children Rosemary Shawver, and Brianna Mchunu (who have been keeping me more busy while working on my thesis). I am planning to work on any research institution on a post - doctoral position or as an instructor in a field related to my research.